Experiments and Impedance Modeling of Liners Including The Effect of Bias Flow

Juan Fernando Betts

Dissertation submitted to the Faculty of the Virginia Polytechnic Institute and State University in partial fulfillment of the requirements for the degree of

Doctor of Philosophy

in

Mechanical Engineering

J. Kelly, Chairman

C. Fuller

W. Saunders

R. Thomas

M. Jones

T. Parrott

July 28, 2000

Hampton, Virginia

Key Words: Bias Flow, Impedance, Acoustic Liners, Perforated Plates

Experiments and Impedance Modeling of Liners Including The Effect of Bias Flow

Juan Fernando Betts

(ABSTRACT)

The study of normal impedance of perforated plate acoustic liners including the effect of bias flow was studied. Two impedance models were developed, by modeling the internal flows of perforate orifices as infinite tubes with the inclusion of end corrections to handle finite length effects. These models assumed incompressible and compressible flows, respectively, between the far field and the perforate orifice.

The incompressible model was used to predict impedance results for perforated plates with percent open areas ranging from 5% to 15%. The predicted resistance results showed better agreement with experiments for the higher percent open area samples. The agreement also tended to deteriorate as bias flow was increased.

For perforated plates with percent open areas ranging from 1% to 5%, the compressible model was used to predict impedance results. The model predictions were closer to the experimental resistance results for the 2% to 3% open area samples. The predictions tended to deteriorate as bias flow was increased.

The reactance results were well predicted by the models for the higher percent open area, but deteriorated as the percent open area was lowered (5%) and bias flow was increased.

A fit was done on the incompressible model to the experimental database. The fit was performed using an optimization routine that found the optimal set of multiplication coefficients to the non-dimensional groups that minimized the least squares slope error between predictions and experiments. The result of the fit indicated that terms not associated with bias flow required a greater degree of correction than the terms associated with the bias flow. This model improved agreement with experiments by nearly 15% for the low percent open area (5%) samples when compared to the unfitted model. The fitted model and the unfitted model performed equally well for the higher percent open area (10% and 15%).

To My Family and Friends

Acknowledgements

I would like to thank the following people for their guidance and support throughout this research effort.

1. Jeff Kelly
2. Tony Parrott
3. Mike Jones
4. Russ Thomas
5. Jesse Follet

These people have provided guidance support, insight, and time to insure success of this research. I would also like to thank

1. Carol Winbush
2. Brian Howerton

for their invaluable help with the experimental side of this study. Finally I would like to thank The Boeing Company and NASA Langley Research Center for funding this work.

Table of Contents

List of Variables

c	speed of sound in the normal incidence tube
c_c	speed of sound in the cavity
C_D	discharge coefficient (steady flow)
C_{drag}	grazing flow drag coefficient
d	perforate hole diameter
f	frequency
G	nonlinear Bernoulli parameter
H	orifice inertial length parameter
I	complex amplitude of incident acoustic wave
I.L.	insertion loss
J	momentum of the bias flow jet
J_0	Bessel function of zeroth order
J_1	Bessel function of first order
J_2	Bessel function of second order
k	wave number ($=\omega/c$)
k_r	wave number in the r-direction
L	length of cavity
M	Mach number in the cavity
M_c	bias flow Mach number in the cavity
M_{gf}	mean grazing flow Mach number ($=v_{gf}/c$)
M_h	bias flow Mach number in the holes of the perforate plates
M_H	effective Mach number in the holes of the perforate plates
M_{sa}	acoustic Mach number in the holes of the perforate plates
NIT	normal incidence tube
p	pressure in the fluid
$\langle p^2 \rangle$	mean squared pressure
p_a	acoustic pressure in the normal incidence tube
p_{ah}	acoustic pressure in perforate's orifice
p_i	incident acoustic wave on the liner

p_R	reflected acoustic wave from the liner
P_1	far field pressure
P_s	pressure in the perforate hole
R	complex amplitude of reflected acoustic wave
R_f	reflection coefficient
R.F.	reflection factor
S_{BL}	area of the boundary layer in perforate hole
S_s	perforate hole area
S_1	cavity area
t	perforate thickness
T	period
u	fluid particle velocity in the x direction
v	fluid particle velocity in the y direction
$\vec{v}$	fluid particle velocity
v_a	acoustic particle velocity in the normal incidence tube
v_{ah}	acoustic particle velocity in perforate's orifice
v_b	bias flow velocity in the normal incidence tube
v_{bh}	bias flow velocity in the perforate's orifice
v_e	effective velocity in the normal incidence tube
v_{eh}	effective velocity in the perforate's orifice
v_g	effective velocity through orifice due to grazing flow
v_{gf}	mean grazing flow velocity
v_{rms}	rms acoustic particle velocity
V_{BL}	velocity in the boundary layer of the perforate hole
w	fluid particle velocity in the z direction
$\langle W_{Iy} \rangle$	incident acoustic intensity to the liner
$\langle W_{Ty} \rangle$	reflected acoustic intensity from the liner
Z	dimensional impedance
α	absorption coefficient
χ	normalized reactance

δ^* boundary layer displacement thickness

ϕ angle of incident acoustic wave on the liner with respect to the normal incidence

Γ cavity propagation constant

γ $c_p/c_v \approx 1.4$ for air

κ_w shear stress from flow in the perforate duct.

μ absolute viscosity of fluid

μ' effective viscosity

θ normalized resistance

ρ density of fluid (air) in NIT

ρ_c density of fluid (air) in the cavity

ρ_h density of fluid in the holes of the perforate samples

σ percent open area

τ time

υ kinematic viscosity ($=\mu/\rho$)

ω circular frequency ($=2\pi f$)

ξ normalized impedance

ξ_c cavity characteristic impedance

Throughout this dissertation the word impedance means normalized impedance with respect to ρc and the sign convention $e^{+i\omega\tau}$ is used unless otherwise indicated. The words predicted and numerical are used interchangeably throughout this document.

1. Introduction

1.1 Objective

Due to the current and projected concerns about community noise annoyance from commercial air traffic, a number of innovative noise reduction concepts are being considered. Acoustic liner treatments for engine nacelles have been an effective means of suppressing turbomachinery noise for over three decades. In the search for even greater liner efficiency, due in-part to the need to suppress turbomachinery noise emanating from high bypass-ratio engines, in-situ (in place) control of liner impedance has been an on-going goal starting with the work of Dean who explored bias flow as a means of changing liner impedances. Bias flow is the introduction of airflow, blowing or suction, perpendicular to the acoustic liner as seen in Fig. 1-1. Figure 1-2 shows the location of acoustic liners in a turbofan engine.

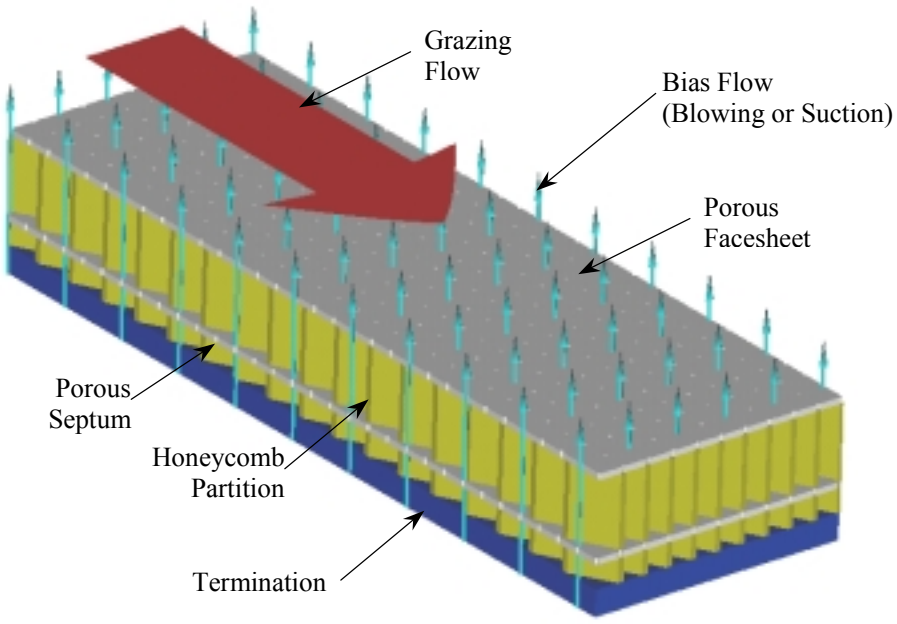

Figure 1-1. Typical double degree bias flow liner configuration[1].

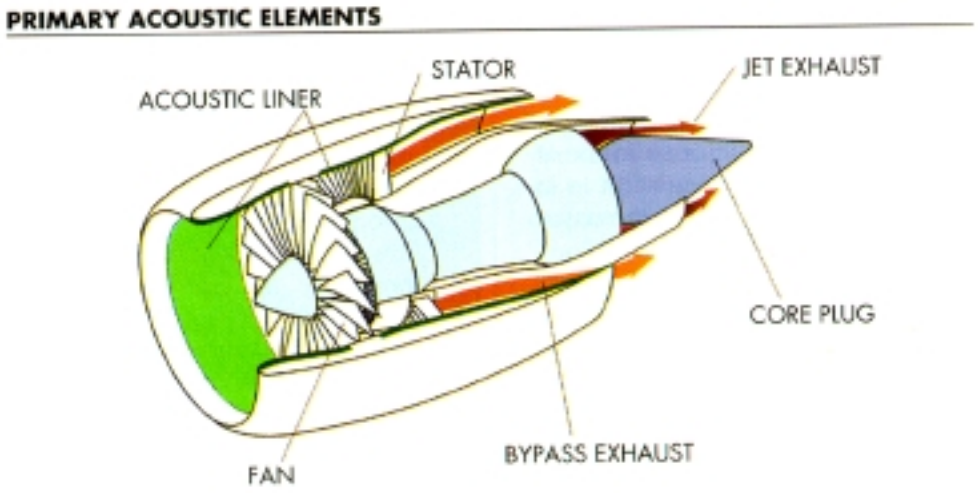

Figure 1-2. Primary Acoustic Elements of a Turbofan Engine[2].

Bias flow can be viewed as a mechanism for optimizing a liner either for developmental purposes in a scale model test or perhaps eventually for an operational full-scale engine.[3,4] Dean conducted an initial proof-of-concept study that showed several potential advantages[5]. The ability to control liner impedance "in-situ" (while the engine is operating) would allow several desirable possibilities including optimizing liner impedance to match different operating conditions or to more accurately match design conditions that could not be reached due to manufacturing tolerances.

There are four objectives to this study:

1. Acquire a quality experimental database of educed normal incidence impedances for perforates plates with and without bias flow
2. Develop improved impedance models for perforated plates in the presence of bias flow
3. Evaluate the models developed against the experimental database
4. Use the experimental database to improve the model's performance and evaluate the resultant model performance

To this end the dissertation is divided into nine chapters and eight appendices. Chapter 2 covers previous impedance modeling theory for perforated plates. Chapter 3 introduces new bias flow models, evaluation criteria, and other theoretical developments. This

chapter address objective 2. Chapter 4 describes the methods used to acquire the experimental database and therefore addresses objective 1. Chapter 5 shows impedance results of perforated plates without bias flow. This chapter is intended to analyze the performance of previous impedance models and to evaluate them against the evaluation error criteria to be used against the bias flow models. Chapters 6 and 7 present the impedance results of the experiments and two bias flow models developed assuming incompressible and compressible flow assumptions. This chapter addresses objective 3. Chapter 8 presents an experimentally fitted bias flow model. This chapter addresses objective 4.

1.2 Approach

An experimental database was produced which included perforate samples tested with and without bias flow in a single-degree-of-freedom (SDOF) liner configuration. The main trust of this dissertation work was the development and evaluation of bias flow impedance models for perforated plates. The database was used to evaluate the developed bias flow impedance models. After such evaluation was accomplished the models were "improved" through semi-empirical means to produce the best available frequency domain impedance model that includes the effect of bias flow. This approach permitted an assessment of how well a model "without" empiricism can predict experiments, and the relative improvement in the model's performance with empirical corrections included in the model.

The surface impedance predictions of the perforate-cavity system were obtained by way of a modified version of the NASA Langley Zwikker-Kosten Transmission Line Code (ZKTL) [6]. This computer program is based on Zwikker and Kosten's theory for sound propagation in channels[7]. In general, the model is composed of continuous arrays of multi-degree-of-freedom liner elements. For the geometry being modeled, the perforated plate model is the uppermost element of the continuous lumped element array, as seen in Fig. 1-3.

Matrix techniques are employed to compute the composite impedance due to the liner elements[8]. For the geometry of interest, these matrix techniques calculate the cavity

impedance (see Figure 1-3). Since flow is present in the cavity, wavenumber corrections were required and are presented in Section 3.5. Therefore, the total surface impedance is the sum of the cavity and perforated plate impedance.

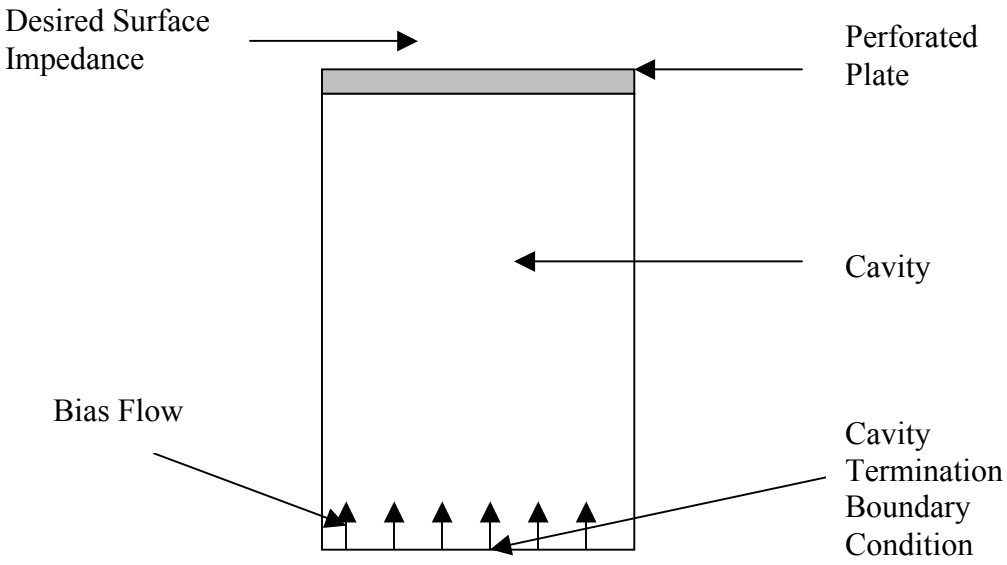

Figure 1-3. Domain geometry being modeled and tested.

In Chapter 3, new bias flow impedance models are developed for perforated plates. These impedance models are nonlinear, meaning that they are a function of the acoustic particle velocity. This can be expressed as

$$\xi = \frac{p_a}{\rho c v_a} = f(v_a) \tag{1-1}$$

where ξ, p_a, v_a, ρ, c, and $f(v_a)$ are the normalized impedance, acoustic pressure, acoustic particle velocity, fluid density, speed of sound, and an arbitrary function with respect to v_a, respectively. Since the impedance in Eq. (1-1) is nonlinear, an iteration scheme was required, given the incident sound-pressure level (SPL), to make both sides of Eq. (1-1) equal.

In this study, the NASA Langley Normal Incidence Tube (NIT) was treated as a distributed element (channel) and the liner sheets with the backing cavity as elements. The different perforate impedance models were implemented in the lumped element part of the modular structure of ZKTL. The cavity backing plate was made porous to allow passage of bias flow, but with a high acoustic resistance to make it highly reflective ("hard") as possible as seen in Fig. 1-3.

Least squares linear fits (with zero intercept) between the experiments and predicted results were performed. The slope of the fit indicated the difference (systematic error) between experimental and predicted values, and the correlation indicated whether they were following the same trend. A slope and correlation of one indicated a perfect match between experiments and predictions. Acceptable limits on the deviations of slope and correlation from one will be used as a basis for establishing the evaluation criteria for the various models.

Experiments were performed to determine the impedance of single degree of freedom liners with bias flow. The experimental data was obtained from the NIT. These liners were composed of nonlinear perforate facesheets followed by a 1.7 inch (4.32 cm) cavity and a high resistance fibermetal backing. Impedance data was acquired to determine the resistance of the fibermetal. It was determined that it had a minimal effect on the impedance of liner material. The bias flow was fed into a plenum chamber 3 inches (7.62 cm) in length with a cross sectional area 2x2 inches (5.08x5.08 cm) before flowing through the high resistance fibermetal.

Normal incidence impedance was measured using three stationary microphones. The first microphone was used to set the reference total sound pressure level (SPL) at the surface of the sample, and the other two microphones measured the transfer function between two points on the standing wave produced by the superposition of incident and reflected acoustic waves generated from the acoustic drivers and reflected from the perforate sample. The transfer function was then used to calculate the overall impedance of the sample-cavity system.

The perforate samples were discovered to exhibit structural resonances in the middle to upper range of the frequencies tested. A vibration inhibiting post was inserted through the fibermetal to support the perforate sample in the center. Preliminary data

suggested that the post support eliminated the resonance below 3 kHz, which was the frequency range of interest. A thin nut was used to constrain the fibermetal that also had resonant frequencies within the range tested. Other than eliminating the structural resonance, the data showed that the post and the nut supports had a minimal effect on the impedance measurements. This determination was achieved by observing the continuity in resistance and reactance of the experimental impedance results.

The perforate samples tested varied in open area from 1 - 15% with thickness to diameter ratios from 0.71 to 1.8. Twenty-three perforate samples were tested in all. The bias flow velocities tested ranged from 0 to 600 cm/s in the cavity. Tests were conducted over a frequency range from 1000 to 3000 Hz, one tone at a time (i.e., did not study frequency spectrum effects), in increments of 100 Hz. The reference SPL was set at 120, 130, and 140 dB for low flow rates and at 130 dB at high flow rates where changing SPL had no effect on measured impedance (based on a few measurements over the SPL range).

Acoustic resistance and reactance have been acquired for all samples. Overall, resistance increased with bias flow for all samples. At zero and low bias flow, increasing the reference SPL increased the resistance. Above a certain critical bias flow velocity; changing the reference SPL had no effect on the resistance. Therefore, the samples are said to exhibit linear behavior with respect to SPL at this critical bias flow rate. The reactance was minimally affected at low bias flow rates, but at high bias flow rates the reactance was significantly reduced. The effect was most noticeable as the velocity in the holes approached the choked condition.

References

1. Picture reprinted with permission of Jesse Follet.
2. Powell, C.A., and Preisser, J.S., "Research for Quieter Skies," Aerospace America. August 1999.
3. Follet, J.I., Betts, J.J., Kelly, J.J., Thomas R.H., "Experimental Impedance of Single Liner Elements with Bias Flow," AIAA-2000-1950. June 2000.
4. Follet, J.I., Betts, J.J., Kelly, J.J., "Improvement of One and Two-Layer Liner Design with Bias Flow," AIAA-2001. January 2001.
5. Dean, P. D., "On the In-Situ Control of Acoustic Liner Attenuation," ASME Paper No. 76-GT-61, Transactions of the ASME, *Journal of Engineering for Power.*

6. Kelly, J. J. and Abu-Khajeel, H., "A User's Guide to the Zwikker-Kosten Transmission Line Code (ZKTL)," NASA/CR-97-206901, December 1997.
7. Zwikker, C. and Kosten, C. W., *Sound Absorbing Materials*, Elsevier, Amsterdam, 1949.
8. Parrott, T. L. and Jones M. G., "Parallel-Element Liner Impedances for Improved Absorption of Broadband Sound in Ducts," *Noise Control Engineering Journal* 43(6), 183-195, November-December 1995.

2. Theory

2.1. No Bias Flow Impedance Models

2.1.1 GE Impedance Model

Description and Major Assumptions

- Incompressible Flow
- Linear Term derived assuming Poiseuille Flow (Fully Developed DC Duct Flow)
- Nonlinearity derived from non-dimensional analysis and empirical corrections

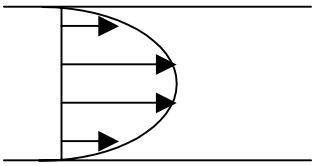

Figure 2-1. The velocity profile in the hole of the perforate associated with the linear resistance term in the GE model.

Motsinger and Kraft have discussed in detail the development of a Single-Degree-of-Freedom (SDOF) impedance model for perforate plates.[1] In their development they assumed a DC flow resistance equivalence with acoustic resistance, and therefore no frequency dependence in their impedance model, as seen in Fig. 2-1. Their resistance term was composed of three components; a linear viscous flow term, a nonlinear turbulent mixing loss component, and a grazing flow term. The GE resistance term, as described by Motsinger and Kraft, is

$$\theta_{GE} = \frac{32\upsilon t}{c\sigma C_D d^2} + \frac{1}{2c(\sigma C_D)^2} v_a + \frac{1}{\left(2 + 1.256\frac{\delta^*}{d}\right)\sigma} M_{gf} \qquad (2\text{-}1)$$

The linear resistance term in Eq. (2-1) can be derived by assuming Poiseuille flow in a duct, which for a Newtonian fluid creates a parabolic velocity profile within the duct as seen in Fig. 2-1. The velocity profile in the model is allowed to vary only in the radial

direction and the profile is fixed through the length of the duct. Motsinger and Kraft derived the nonlinear term through a non-dimensional analysis and an experimental fit.

The GE mass reactance is given by

$$\chi_{GE} = \frac{k}{\sigma C_D}\left[t + \in d\right] \tag{2-2}$$

where $\in$ is an experimentally determined end correction

$$\in = \frac{0.85(1 - 0.7\sqrt{\sigma})}{1 + 305\left(M_{gf}\right)^3} \tag{2-3}$$

C_D in the denominator of Eq. (2-2) was not included by Motsinger and Kraft, but it does appear when derived from a formal theoretical derivation. Kraft, Yu, and Kwan later corrected this problem.[2] Equation (2-2) can be derived by taking the one-dimensional momentum equation along the length of the duct and assuming the following: no viscosity, the velocity profile is constant through the cross section (i.e., "plug" flow), and the pressure field is only a function of the axial variation in the velocity field.

Notice that the set of assumptions for the resistance and reactance are different. Some of these conflicts in assumptions as well as the omission of the discharge coefficient in the model may have been alleviated through the empiricism in the development of the other previously described model parameters. The complete GE model using Eqs. (2-1) through (2-3) becomes

$$\xi = \frac{32\upsilon t}{c\sigma C_D d^2} + \frac{1}{2c\left(\sigma C_D\right)^2} v_a + \frac{1}{\left(2 + 1.256\frac{\delta^*}{d}\right)\sigma} M_{gf} + i\frac{k}{\sigma C_D}\left[t + \in d\right] \tag{2-4}$$

2.1.2 Crandall Impedance Model

Description and Major Assumptions

- Incompressible Flow

- Linear term derived assuming velocity profile has only radial variations and is constant through the length of the duct
- Interaction effect between the holes included
- Nonlinearity derived by assuming axial and radial variation in the velocity profile
- The velocity is assumed to have a simple harmonic time dependence (i.e., there are no higher harmonics produced by the nonlinearity)
- Acoustic parameters are replaced by their time averaged parameters for the nonlinear term

Melling analyzed and discussed in detail the derivation of Crandall's theory of acoustic propagation in perforates.[3] Crandall's model assumes an infinitely long duct, and end corrections are added to account for the finite length of the perforate's holes. Melling's analysis is more of a theoretical nature, and relies less on empiricism than Motsinger and Kraft. His analysis yielded the following impedance model

$$\xi = \frac{1}{c\sigma C_D}\left[\frac{i\omega t}{F\left(\frac{k_s' d}{2}\right)} + \frac{8d}{3\pi F\left(\frac{k_s d}{2}\right)\psi'(\sigma)}\right] + \frac{\left(1-\sigma^2\right)}{2c\left(\sigma C_D\right)^2} v_a \qquad (2\text{-}5)$$

where

$$F\left(\frac{k_s d}{2}\right) = 1 - \frac{2J_1\left(\frac{k_s d}{2}\right)}{k_s \frac{d}{2} J_0\left(\frac{k_s d}{2}\right)} \qquad (2\text{-}6)$$

Here J_0 and J_1 are the zero and first order Bessel functions.

$$k_s' = \sqrt{-\frac{i\omega}{\upsilon'}} \qquad (2\text{-}7)$$

is Stokes wave-number for a with highly conducting walls, and:

$$k_s = \sqrt{-\frac{i\omega}{\upsilon}} \tag{2-8}$$

is Stokes wave-number for a wall with thermally nonconducting walls. The Fok function ψ' is

$$\psi'(\sigma) = \sum_{n=0}^{8} a_n \left(\sqrt{\sigma}\right)^n \tag{2-9}$$

where

a_0=1.0	a_1=-1.4092	a_2=0.0
a_3=0.33818	a_4=0.0	a_5=0.06793
a_6=-0.02287	a_7=0.003015	a_8=-0.01614

The Fok function accounts for the acoustic interaction between the holes. According to Melling, Fok derived this solution of the impedance coupling between the perforate's holes for an infinitely thin plate.

Besides the acoustic interaction of the holes, the Crandall impedance model introduces frequency dependence to the acoustic impedance. The linear frequency dependence was lacking in the analysis by Motsinger and Kraft. The frequency dependence in the linear term of the Crandall model is due to the Bessel function solution.

Historically, Equation (2-5) was not normally used to calculate the impedance of a perforate, due to the difficulty in calculating the Bessel function with a complex-valued argument and separating the real and imaginary components of the impedance function. Although this impediment has been a problem in the past, current computers can easily handle the above-mentioned problems. However, the low and high frequency approximations to Eq. (2-5) are widely used, to provide additional physical insights to the Crandall impedance function.

The low frequency approximation (also called the **Poiseuille model**) is

$$\frac{d}{2}\sqrt{\frac{\omega}{\upsilon}} < 1 \qquad (2\text{-}10)$$

Making this approximation, Eq. (2-5) becomes

$$\xi = \frac{32\upsilon t}{c\sigma C_D d^2} + \frac{\left(1-\sigma^2\right)}{2c\left(\sigma C_D\right)^2} v_a + i\frac{k}{\sigma C_D}\left(\frac{4}{3}t + \frac{8d}{3\pi\psi'(\sigma)}\right) \qquad (2\text{-}11)$$

The first term in Eq. (2-11) is the same as the viscous DC linear term presented by Motsinger and Kraft for the GE model. Note that the first term in the reactance is 1/3 larger in the Crandall model than in the GE model. The effective mass in the Crandall model is larger because the viscosity within the hole increases the effective mass within the hole. This is due to the fact that the velocity profile is parabolic in the Crandall model, and not "plug-flow" as assumed for the reactance derivation in the GE model. The lower average velocity in the parabolic distribution leads to a higher effective mass because of conservation of momentum.

The high frequency approximation (also called the **Helmholtz model**) is valid if

$$\frac{d}{2}\sqrt{\frac{\omega}{\upsilon}} > 10 \qquad (2\text{-}12)$$

Making this approximation Eq. (2-5) becomes

$$\xi = 2.82\frac{\sqrt{\upsilon\omega}}{c\sigma C_d}\frac{t}{d} + \frac{\left(1-\sigma^2\right)}{2c\left(\sigma C_D\right)^2} v_a + i\left(\frac{\omega t}{c\sigma C_D} + 2.82\frac{\sqrt{\upsilon\omega}}{c\sigma C_d}\frac{t}{d} + \frac{8}{3\pi}\frac{d}{\psi'(\sigma)}\right) \qquad (2\text{-}13)$$

This approximation introduces frequency dependence in the linear term in the resistance that is absent in the GE model. Furthermore, the frequency independent term of the Poiseuille model vanishes. Also note that the effective mass is no longer a constant 1/3 higher, but contains an additional attached mass that is frequency dependent.

In practice neither the low nor high frequency approximations are used, because of the desire for a single model that works for all frequencies. Therefore, the high frequency model is usually corrected to account for low and intermediate frequencies. Kraft, Yu, and Kwan provide one such correction by adding half of the Poiseuille viscous term to the Helmholtz model.[2] This model is called the **GE-Rohr model**, and is given by

$$\xi = \frac{16\upsilon t}{c\sigma C_D d^2} + 2.82\frac{\sqrt{\omega\upsilon}}{c\sigma C_d}\frac{t}{d} + \frac{\left(1-\sigma^2\right)}{2c\left(\sigma C_D\right)^2}v_a + i\left(\frac{kt}{\sigma C_D} + 2.82\frac{\sqrt{\omega\upsilon}}{c\sigma C_D}\frac{t}{d} + \frac{8}{3\pi}\frac{d}{\psi'(\sigma)}\right) \qquad (2\text{-}14)$$

2.1.3 Hersh 75 Impedance Model

Description and Major Assumptions

- In the near field the flow moves in the radial direction and is axisymmetric.
- Within the near field the flow is incompressible and unsteady.
- At low sound pressure levels the linear regime dominates
- At high sound pressure levels the nonlinear regime dominates
- Core flow dominated by entrance effects

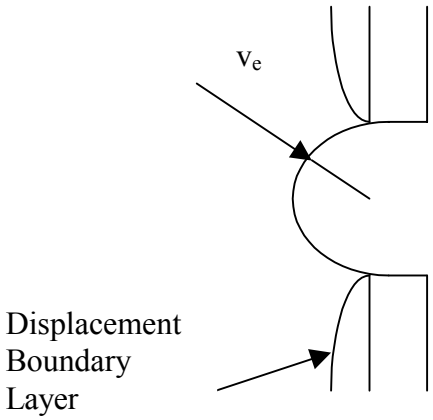

Figure 2-2. Velocity profile for Hersh 75 model for a perforate hole.

In 1975 Hersh and Rogers followed a different approach to modeling the impedance of the perforate from an impinging acoustic field.[4] According to them, perforate plates are too thin to assume fully developed duct flows through them as both

the linear components of the GE and Crandall models do. Hersh and Rogers concluded that since the orifice diameters are small in perforates, end corrections are not corrections, but a major component of the model's viscous losses. Major viscous losses do not occur inside the perforate's hole, but instead occur at the surface of the perforate. Consequently, their analysis focuses on modeling the near field of the perforate's hole rather than the interior, as seen in Fig. 2-2.

Hersh and Rogers developed their model by considering two regions, which they called the linear regime and nonlinear regime for low and high sound pressure levels respectively. In their model the linear and nonlinear regimes are determined by

$$\frac{v_a}{\sigma\omega d} \tag{2-15}$$

If this ratio is less or greater than one, the regime is linear or nonlinear respectively.

For the linear regime the impedance is

$$\theta_{\text{Hersh}\,75} = k(d+t)\left[\underbrace{\frac{4\frac{v_a}{\sigma\omega d}}{3\pi C_D^2\left(1+\frac{t}{d}\right)}}_{\text{Nonlinear loss}} + \underbrace{\frac{1}{\sqrt{2\,\text{Re}}}}_{\text{Viscous loss}}\right]\left[1+\sqrt{\frac{2}{\text{Re}}}-\frac{8\left(\frac{v_a}{\sigma\omega d}\right)}{3\pi C_D^2\left(1+\frac{t}{d}\right)}\right] \tag{2-16}$$

$$\chi_{\text{Hersh}\,75} = k(d+t)\left[1+\underbrace{\frac{1}{\sqrt{2\,\text{Re}}}}_{\text{Viscous loss}}\left(1-\underbrace{\frac{8\frac{v_a}{\sigma\omega d}}{3\pi C_D^2\left(1+\frac{t}{d}\right)}}_{\text{Nonlinear loss}}\right)\right] \tag{2-17}$$

where

$$\text{Re} = \frac{\omega(d+t)^2}{\upsilon} \tag{2-18}$$

The resistance term has two dominant terms, a nonlinear and a viscous loss term. These terms appear in both the resistance and reactance, indicating a linear and nonlinear coupling between resistance and reactance. This coupling is dominated by the viscous term when Ratio (2-15) is *less than one*. Rewriting Eq. (2-16) and (2-17) with Ratio (2-15) *much less than one* produces

$$\theta_{\text{Hersh}\,75} = k(d+t)\left(\frac{1}{\sqrt{2\,\text{Re}}}+\frac{1}{\text{Re}}\right)+ik(d+t)\left[1+\frac{1}{\sqrt{2\,\text{Re}}}\right] \tag{2-19}$$

Since the impedance is dominated by the viscous term, it is directly related to the displacement boundary layer along the surface of the perforate. Furthermore, the effects of viscosity increase the mass reactance. This result is in line with the Crandall model, where viscosity inside of the hole also increased the mass reactance. Therefore, the effect of viscosity increases the mass reactance both in the near field and within the hole.

For the nonlinear regime, Ratio (2-15) is larger than one. The impedance becomes

$$\theta_{\text{Hersh}\,75} = k(d+t)\left(\frac{0.64}{C_D^2}\right)\left(\frac{v_a}{\sigma\omega d}\right)\left(\frac{1}{1+\frac{t}{d}}\right)\left[1-\left(\frac{1.03C_D\omega\sigma(d+l)}{v_a}\right)^2\right] \tag{2-20}$$

$$\chi_{\text{Hersh}\,75} = k(d+t)\left(\frac{0.33}{C_D}\right)\left[1+2.6C_D\left(\frac{\sigma\omega d}{v_a}\right)\left(1+\frac{t}{d}\right)\right]\left[1-\left[1.03C_D\frac{\omega d\sigma}{v_a}\left(1+\frac{t}{d}\right)\right]^2\right] \tag{2-21}$$

In this regime nonlinear effects dominate the impedance, and the viscosity effects disappear in both the resistance and reactance.

2.1.4 Hersh 99 Impedance Model

Description and Major Assumptions

- Incompressible Flow
- Inviscid core flow with a viscous boundary layer inside the perforate hole
- Developing viscous boundary layer
- Unknown assumed model parameters determined through experiment
- t/d>>1

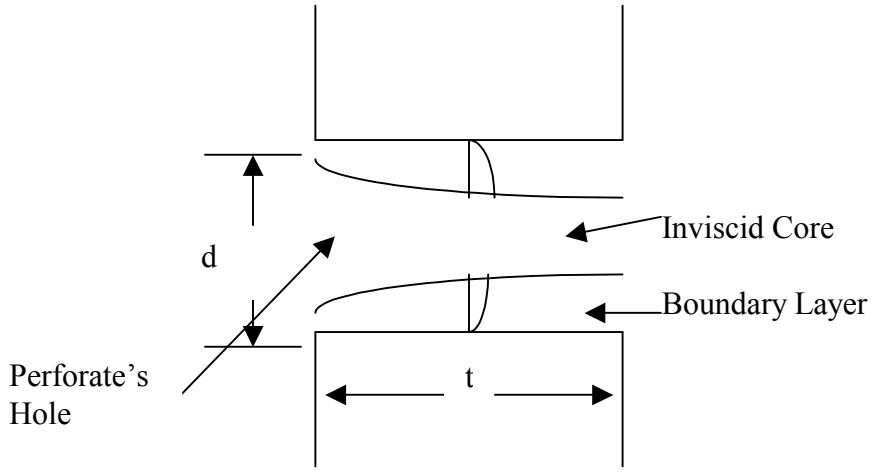

Figure 2-3. Velocity profile in the perforate for Hersh 99.

Hersh, Walker, and Celano[5] developed another impedance model in 1999, where they assumed an inviscid core with a boundary layer profile within the hole, as seen in Fig. 2-3. They developed this model from a control volume approach using the principles of conservation of mass and momentum. An assumed velocity and viscous loss was then inserted into these integral equations. The resultant equations become a function of unknown parameters that are themselves a function of geometrical variables. Then the functional relationship between the unknown parameters in the integral equations and geometrical variables is determined through experiments. A more detailed analysis will be presented in Appendix A, where a bias flow model using Hersh's ideas is presented.

2.2 Bias Flow Impedance Models

2.2.1 Dean's Bias Flow Model

Description and Major Assumptions

- Same assumptions as the Hersh 75 model
- Acoustic particle velocity replaced by bias flow velocity
- Additional impedance corrections determined empirically

Bias flow has been a concept for "in-situ" control of impedance in acoustic liners. Dean conducted an initial proof of concept in 1976[6] and developed a bias flow model based on the principles outlined by Hersh in his 1975 model. Dean, like Hersh, divided the flow region into two regions, the linear and nonlinear regimes respectively. He utilized the same terms as Hersh (Ratio (2-15)) to determine which impedance region was operating (linear or nonlinear), except that he replaced the acoustic particle velocity with the bias flow velocity in that term.

Therefore, the term that Dean used to determine the operating impedance regime was

$$\frac{v_b}{\sigma\omega d} \tag{2-22}$$

He also replaced the acoustic particle velocity with the bias flow velocity in both the linear and nonlinear impedance model regimes. Therefore his model ignores the effect of sound pressure change caused by changes in the acoustic particle velocity. He assumes the bias flow velocity to be much greater than the acoustic particle velocity, and therefore SPL effects are considered negligible. If the ratio (2-35) is less than one, his impedance model is

$$\theta_{Dean} = \frac{1}{\sigma}\left[k(d+t)\left(\frac{0.4244 v_b}{C_D^2(1.0+\frac{t}{d})} + \sqrt{\frac{1.0}{Re}} \right)\left[\frac{0.8488 v_b}{C_D^2(1.0+\frac{t}{d})} - 1.0 - \sqrt{\frac{2}{Re}} \right] \right. \tag{2-23}$$

$$\underbrace{\left. + \left\{ \frac{2 v_b}{c\sigma^2} \text{ or } \frac{M_{gf}}{0.845\sigma} \right\} \right.}$$

whichever is greater

$$\chi_{Dean} = \frac{k(d+t)}{\sigma}\left[1.0 + \sqrt{\frac{1}{2Re}}\left(1.0 - \frac{0.8488 v_b}{C_D^2\left(1+\frac{t}{d}\right)} \right) \right] \tag{2-24}$$

The last two terms in the resistance represent bias flow and grazing flow, respectively. Dean does not explain where these terms come from except to say "the effects of bias flow… has been experimentally investigated sporadically… and in broad terms the d-c flow resistance increases in direct proportion to the bias flow velocity and inversely to the square of the porosity." It appears that Dean might be alluding to a similar empirically determined nonlinear effect described by Motsinger and Kraft in the GE model previously discussed in this chapter. Dean's model has further differences to Hersh. Although the models are similar, they are not the same after accounting for the change in v_a by v_b. Dean does not explain these differences.

The nonlinear regime occurs when ratio (2-35) is greater than one as with Hersh. The impedance becomes

$$\theta_{Dean} = \frac{k(d+t)0.64v_b}{\sigma C_D^2\left(1.0+\frac{t}{d}\right)}\left[1.0-\left(\frac{1.03C_D\left(1.0+\frac{t}{d}\right)}{v_b}\right)^2\right] + \underbrace{\left\{\frac{2v_b}{c\sigma^2} \text{ or } \frac{M_{gf}}{0.845\sigma}\right\}}_{\text{whichever is greater}} \tag{2-25}$$

$$\chi_{Dean} = \frac{k(d+t)0.33}{\sigma C_D}\left[1.0+\frac{2.6C_D\left(1+\frac{t}{d}\right)}{v_b}\right] \times \left[1.0-\left(\frac{1.03C_D\left(1+\frac{t}{d}\right)}{v_b}\right)^2\right] \tag{2-26}$$

This impedance model is similar to the Hersh 75 model, and has the same bias and grazing flow corrections. Dean does not shed any more light into the development of this nonlinear regime impedance model.

2.2.2 Previous Bias Flow Corrections

The acoustic impedance models presented, except for Dean's Bias Flow model, do not account for the effect of bias flow. As seen in Dean's model, bias flow was accounted by replacing the acoustic particle velocity with the bias flow velocity and stating that the bias flow velocity was much greater than the acoustic particle velocity. As will be shown later, replacing the particle acoustic velocity with the bias flow velocity is questionable.

In the NASA Langley Zwikker-Kosten Transmission Line Code (ZKTL)[7], bias flow is accounted for by replacing the acoustic particle velocity in the impedance models with

$$v_a + v_b \tag{2-27}$$

This correction seems more reasonable than Dean's correction, especially at low bias flow velocities. Nevertheless, this bias flow correction as well as Dean's correction does not follow from basic principles. It is important to note that this correction has never been published, assessed or validated, and therefore was just a placeholder in ZKTL until a better correction was developed.

In another study, Premo derived a bias flow model using a time-domain approach. This approach yielded the following replacement for the acoustic particle velocity to include bias flow[8]

$$\sqrt{(1.15v_{rms})^2 + (2v_b)^2} \tag{2-28}$$

The relevance and comparison of this bias flow correction is further discussed in Section 3.1.

2.3 Grazing Flow

The effect of grazing flow on the acoustic impedance of perforates has been extensively studied for the past three decades. Rice developed an empirical acoustic resistance model for a single hole is given by[9]

$$\theta = 0.3M_{gf} \tag{2-29}$$

Equation (2-42) was modified in the same reference to account for percent open area (σ)

$$\theta = 0.3M_{gf}\left(\frac{3.15x10^{-2}}{\sigma} + 1.77\sigma + 0.3\right) \tag{2-30}$$

Since the development of this empirical model, there have been several grazing flow impedance models developed. Rice devised a model that assumed that vortices were formed when the fluid interacted with the acoustic jet exiting the perforate hole[10]. He presented an approximate simplified solution, where

$$\theta \propto \frac{dM_{gf}}{\sigma\delta} \tag{2-31}$$

This semi-empirical model showed that the grazing flow impedance was a function of boundary layer thickness (δ). Boundary layer thickness was ignored in the empirical model in Ref. 9. Armstrong, Beckemeyer, and Olsen devised a method of relating the acoustic propagation constant k_z along the length of the duct to the acoustic impedance in the presence of grazing flow using a "waveguide method."[11] This method took into account the boundary layer thickness through the velocity profile of v_{gf}.

Rice developed a theoretical model for grazing flow,[12] using the principles employed in the impedance model outlined by Hersh and Rogers (Hersh 75 model, see Section 2.1.3)[4]. Rice solves a simplified form of the Navier-Stokes equations assuming only a radial component of velocity entering the hole in a spherical coordinate system, and included grazing flow in his analysis. The resultant grazing flow part of the model was

$$\xi = \frac{1}{2}\left(M_{gf} + i\frac{kd}{2}\right) \tag{2-32}$$

Heidelberg, Rice and Homyak modified Eq. (2-45) to account for the effect of the grazing flow boundary layer thickness (δ)[13]. Their model is given as

$$\theta = \frac{M_{gf}}{\sigma\left(2 + 1.256\frac{\delta}{d}\right)} \qquad (2\text{-}33)$$

References

1. Motsinger, R.E. and Kraft, R.E., "Design and Performance of Duct Acoustic Treatment," Chapter 14, Volume 2, *Aeroacoustics of Flight Vehicles: Theory and Practice,* NASA RP-1258, August 1991.
2. Kraft, R.E., Yu J., and Kwan H.W., "Acoustic Treatment Design Scaling Methods," Volume 2, Advanced Treatment Impedance Models for High Frequency Ranges, NAS3-26617, May 1996.
3. Melling, T.H., "The Acoustic Impedance of Perforates at Medium and High Sound Pressure Levels," Journal of Sound and Vibration, 29(2-1), 1973.
4. Hersh, A. S. and Rogers, T., "Fluid Mechanical Model of the Acoustic Impedance of Small Orifices," AIAA 75-495, March 1975.
5. Hersh, A. S., Walker B.E., and Celano, J.W., "Semi-empirical Helmholtz Resonator Impedance Model," AIAA 99-1825. 1999.
6. Dean, P. D., "On the In-Situ Control of Acoustic Liner Attenuation," ASME Paper No. 76-GT-61, Transactions of the ASME, *Journal of Engineering for Power.*
7. Kelly, J.J. and Abu-Khajeel, H., "A User's Guide to the Zwikker-Kosten Transmission Line Code (ZKTL)," NASA/CR-97-206901, December 1997.
8. Premo, J., "The Application of a Time-Domain Model to Investigate the Impedance of Perforate Liners Including the Effects of Bias Flow," AIAA-99-1876. 1999.
9. Rice, E. J., "A Model for the Acoustic Impedance of a Perforated Plate Liner with Multiple Frequency Excitation," NASA TM X-67950, 1971.
10. Rice E. J., "A Model for the Pressure Excitation Spectrum and Acoustic Impedance of Sound Absorbers in The Presence of Grazing Flow," AIAA-73-995.
11. Armstrong, D.L., Beckemeyer, R. J., and Olsen, R.F. "Impedance Measurements of Acoustic Duct Liners with Grazing Flow," Acoustical Society of America. 1974.
12. Rice, E., "A Theoretical Study of the Acoustic Impedance of Orifices in the Presence of a Steady Grazing Flow," NASA TM X-71903. 1976.
13. Heidelberg, L. J., Rice, E. J., and Homyak, L., "Experimental Evaluation of a Spinning-Mode Acoustic Treatment Design Concept for Aircraft Inlets," NASA Technical Paper 1613, 1980.

3. New Theoretical Developments

There has been two major approaches to acoustic impedance modeling of perforate plates presented in Chapter 2. In the first approach, perforated plates were considered to be too thin for the orifices to be modeled as cylindrical ducts. Hersh and Sivian use this approach, where the end effects and boundary layer are significant. The second approach has been to model the perforate orifices as cylindrical ducts, an then to correct for "end effects." Crandall and Kraft have implemented this approach.

Although both of these approaches have been used to develop acoustic impedance models for perforates, the second approach has by far been more popular than the first. To date, the Crandall model as presented by Melling is the most comprehensive and complete impedance model study for perforated plates that I have found. This model contains fewer approximations, relies less on empiricism, and includes more effects than any of the other model studies. For this reason, the bias flow impedance models developed in this chapter will model the perforate orifices as cylindrical ducts. Chapters 6 through 8 evaluate these models using experimental results. Appendix A shows the development of a bias flow impedance model using the approach outlined by Hersh. This model is not evaluated in this dissertation.

3.1 Perforate Bias Flow (PBF) Model

The momentum equation for a viscous fluid is

$$\rho\left[\frac{\partial \vec{v}}{\partial t} + (\vec{v} \bullet \nabla)\vec{v}\right] = -\nabla p + \mu \nabla^2 \vec{v} \qquad (3\text{-}1)$$

where the compressibility term $\frac{1}{3}\mu\nabla(\nabla \bullet \vec{v})$ is assumed small and therefore is omitted from Eq. (3-1). Note, that by making this approximation, density disturbances are ignored. Let any fluid variable q be the sum of a mean flow q_b and an acoustic component q_a, that is

$$q(x,r,\tau) = q_b(x,r,\tau) + q_a(x,r,\tau) \tag{3-2}$$

Substituting Eq. (3-2) into (3-1) produces

$$\rho\left[\frac{\partial \vec{v}_a}{\partial t} + ((\vec{v}_b + \vec{v}_a)\bullet\nabla)(\vec{v}_b + \vec{v}_a)\right] = -\nabla p_b - \nabla p_a + \mu\nabla^2\vec{v}_b + \mu\nabla^2\vec{v}_a \tag{3-3}$$

where

$$\begin{aligned}\vec{v}_b &= v_v(x,r)\,\hat{e}_x \\ \vec{v}_a &= v_a(x,r,\tau)\,\hat{e}_x\end{aligned} \tag{3-4}$$

and simplifying yields

$$\begin{aligned}&\rho\left[\frac{\partial \vec{v}_a}{\partial t} + (\vec{v}_b\bullet\nabla)\vec{v}_b + (\vec{v}_b\bullet\nabla)\vec{v}_a + (\vec{v}_a\bullet\nabla)\vec{v}_b + (\vec{v}_a\bullet\nabla)\vec{v}_a\right] \\ &= -\nabla p_b - \nabla p_a + \mu\nabla^2\vec{v}_b + \mu\nabla^2\vec{v}_a\end{aligned} \tag{3-5}$$

This equation contains bias flow only, coupled bias flow/acoustic, and acoustic only components. The bias flow only components should balance, leaving only coupled and acoustic only components. Furthermore, assume that perforate holes can be modeled as cylindrical ducts, and that only a velocity component in the x-direction along the length of the perforate hole exists. This velocity component is assumed to vary in the x and radial directions. So far, the above description pertains to the interior of the perforate hole. To indicate this, the variables v_a and v_b will be subscripted with v_{ah} and v_{bh}. Making these approximations to Eq. (3-5) and letting v_{ah} and v_{bh} now represent the acoustic and bias flow velocity in the x direction inside the perforate's hole produces

$$\rho\left[\frac{\partial v_{ah}}{\partial t} + v_{bh}\frac{\partial v_{ah}}{\partial x} + v_{ah}\frac{\partial v_{bh}}{\partial x} + v_{ah}\frac{\partial v_{ah}}{\partial x}\right] = -\frac{\partial p_{ah}}{\partial x} + \mu\left(\frac{\partial^2 v_{ah}}{\partial r^2} + \frac{1}{r}\frac{\partial v_{ah}}{\partial r} + \frac{\partial^2 v_{ah}}{\partial x^2}\right) \tag{3-6}$$

Rewriting Eq. (3-6) and grouping linear and nonlinear coupling terms yields

$$\underbrace{\rho\frac{\partial v_{ah}}{\partial t}-\mu\left(\frac{\partial^2 v_{ah}}{\partial r^2}+\frac{1}{r}\frac{\partial v_{ah}}{\partial r}+\frac{\partial^2 v_{ah}}{\partial x^2}\right)}_{\text{Linear Terms}}+\underbrace{\rho\left[v_{bh}\frac{\partial v_{ah}}{\partial x}+v_{ah}\frac{\partial v_{bh}}{\partial x}+v_{ah}\frac{\partial v_{ah}}{\partial x}\right]}_{\text{Nonlinear \& Coupling Terms}}=-\frac{\partial p_{ah}}{\partial x} \quad (3\text{-}7)$$

The right hand side of Eq. (3-7) can be written as

$$-\frac{\partial p_{ah}}{\partial x}=-\left(\left.\frac{\partial p_{ah}}{\partial x}\right|_{linear}+\left.\frac{\partial p_{ah}}{\partial x}\right|_{nonlinear}\right) \quad (3\text{-}8)$$

Therefore the linear and nonlinear terms of Equation (3-7) balance their corresponding counterparts respectively, in Eq. (3-8). By utilizing the definition of impedance, the linear term of Eq. (3-8) can be rewritten in terms of the linear impedance by noting that

$$\left.-\frac{\partial p_{ah}}{\partial x}\right|_{linear}=\xi_{linear}\rho c\frac{\partial v_{ah}}{\partial x} \quad (3\text{-}9)$$

Substituting the above relationship in Eq. (3-7), assuming $\partial x=t$, $\partial p_{ah}=p_{ah}$, $p_{ah}=p_a$, and $\partial v_{ah}=v_{ah}$ produces

$$-\xi_{linear}\rho c v_{ah}-\rho\left(v_{bh}v_{ah}\right)-\frac{\rho v_{ah}^2}{2}=p_a \quad (3\text{-}10)$$

Figure 3-1 depicts a control volume where the incident and hole variables are defined.

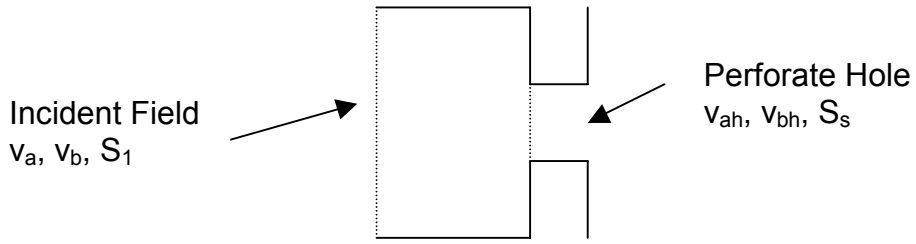

Figure 3-1. Control volume for the incident and hole regions.

From continuity, the relationship between the incident and hole velocities for an incompressible fluid is given by

$$\begin{aligned} v_a &= C_D \sigma v_{ah} \\ v_b &= C_D \sigma v_{bh} \end{aligned} \tag{3-11}$$

Inserting the relationships in Eq. (3-11) into Eq. (3-10) and multiplying by v_a produces

$$-\frac{\xi_{linear}\rho c v_a^2}{C_D\sigma} - \frac{\rho}{(C_D\sigma)^2} v_b v_a^2 - \frac{\rho v_a^3}{2(C_D\sigma)^2} = p_a v_a \tag{3-12}$$

The following procedure was used by Melling to relate the acoustic particle velocity to the rms velocity. Integrating both sides of Eq. (3-12) over the period yields

$$\frac{1}{T}\int_0^\tau \frac{\xi_{linear}\rho c v_a^2}{C_D\sigma} d\tau + \frac{1}{T}\int_0^\tau \frac{\rho}{(C_D\sigma)^2} v_b v_a^2 d\tau + \frac{1}{T}\int_0^\tau \frac{\rho |v_a| v_a^2}{2(C_D\sigma)^2} d\tau = \frac{1}{T}\int_0^\tau p_a v_a d\tau \tag{3-13}$$

where v_a^3 has been replaced by $|v_a| v_a^2$ in the third term to ensure that it remains positive. This is done for the following reason. A harmonic solution of the form $\text{Cos}(\omega\tau)$ is inserted for v_a into Eq. (3-13) in every term except the third term. Rewriting the resulting equation with the third term on the right hand side yields

$$\frac{\xi_{linear}\rho c}{C_D\sigma}v_{rms}^2+\frac{\rho}{(C_D\sigma)^2}v_b v_{rms}^2-\xi\rho c v_{rms}^2=-\frac{1}{T}\int_0^{\tau}\frac{\rho v_a^3}{2(C_D\sigma)^2}d\tau \qquad (3\text{-}14)$$

The left hand side of Eq. (3-14) is a constant regardless of the sign of v_a, yet the right hand side is either positive or negative depending on the sign of v_a (remember that a harmonic solution is assumed for v_a). This can be expressed mathematically as

$$\begin{aligned} &A = C \\ &\text{and} \\ &A = -C \end{aligned} \qquad (3\text{-}15)$$

where A and C are constants. The solution to Eq. (3-15) can be A=C=0, which is the trivial solution. Another solution is for the right hand side to be in absolute values. Therefore, in order to eliminate the trivial solution and for the equality to hold regardless of the sign of v_a, v_a^3 must be replaced by $|v_a|v_a^2$. Making this replacement into Eq. (3-13) produces

$$\frac{\xi_{linear}\rho c}{C_D\sigma}v_{rms}^2+\frac{\rho}{(C_D\sigma)^2}v_b v_{rms}^2+\frac{\rho}{2(C_D\sigma)^2}\frac{4}{3\pi}2\sqrt{2}v_{rms}^3=\xi\rho c v_{rms}^2 \qquad (3\text{-}16)$$

Dividing both sides by $\rho c v_{rms}^2$ produces

$$\xi=\frac{\xi_{linear}}{C_D\sigma}+\frac{1}{2c(C_D\sigma)^2}\left[2v_b+1.2v_{rms}\right] \qquad (3\text{-}17)$$

Melling notes that the pressure drop across a "sharp edge" orifice has been studied in some detail[1]. From these studies, a departure from the nonlinear term in Eq. (3-17) is suggested. Making the corrections indicated by Melling to Eq. (3-17) yields

$$\xi = \frac{\xi_{linear}}{C_D\sigma} + \frac{1-\sigma^2}{2c(C_D\sigma)^2}\left[2v_b + 1.2v_{rms}\right] \tag{3-18}$$

The linear impedance (ξ_{linear}) term is determined by solving Eq. (3-7) utilizing only the linear terms. Writing that equation leaving only the linear term yields

$$\rho\frac{\partial v_{ah}}{\partial t} - \mu\left(\frac{\partial^2 v_{ah}}{\partial r^2} + \frac{1}{r}\frac{\partial v_{ah}}{\partial r} + \frac{\partial^2 v_{ah}}{\partial x^2}\right) = -\left.\frac{\partial p_a}{\partial x}\right|_{linear} \tag{3-19}$$

The linear impedance of the Crandall model (see Section 2.1.2) is the harmonic solution of Eq. (3-19) assuming that the term $\frac{\partial^2 v_{ah}}{\partial x^2} \to 0$. This simplification effectively assumes there are no acoustic waves traveling along the length of the duct, or the wavelength is much greater than the perforate thickness since $\frac{\partial^2}{\partial x^2} \approx 0(k^2) << 1$. To solve Eq. (3-19) a harmonic solution of the following form is assumed:

$$\begin{aligned} v_{ah}(r,t) &= \hat{v}(r)e^{i(\omega t)} \\ p_{ah}(x,t) &= \hat{p}(x)e^{i(\omega t)} \end{aligned} \tag{3-20}$$

Inserting the above relations into Eq. (3-19) yields:

$$\frac{d^2\hat{v}}{dr^2} + \frac{1}{r}\frac{d\hat{v}}{dr} + \left(k_s^2\right)\hat{v} = -\frac{\phi}{\mu} \tag{3-21}$$

where

$$k_s^2 = -\frac{i\omega}{\upsilon} \tag{3-22}$$

$$\phi = -\frac{d\hat{p}}{dx} = \text{constant} \tag{3-23}$$

Equation (3-21) is the inhomogeneous Bessel equation of zero order. Assuming the pressure gradient in Eq. (3-23) to be constant, the solution of this equation is

$$\hat{v}(r) = -\frac{\phi}{\mu k_s^2}\left[1 - \frac{J_0[k_s r]}{J_0[k_s R]}\right] \tag{3-24}$$

where the no-slip condition at the tube wall, $\hat{v}(R) = 0$, has been imposed. R is the radius of the perforate hole. Averaging $\hat{v}$ over the cross-sectional area produces the mean velocity

$$\begin{aligned}\langle \hat{v} \rangle &= \frac{1}{\pi R^2}\int_0^R \hat{v}(r)(2\pi r)dr \\ &= -\frac{\phi}{\mu k_s^2}\left[1 - \frac{2J_1[k_s R]}{k_s R J_0[k_s R]}\right]\end{aligned} \tag{3-25}$$

From Eq. (3-23) $\Delta\hat{p}$ is:

$$\Delta\hat{p} = \phi t = \frac{i\omega\rho_o t\langle \hat{v} \rangle}{F[k_s R]} \tag{3-26}$$

where

$$F\left(\frac{k_s d}{2}\right) = 1 - \frac{2J_1\left(\frac{k_s d}{2}\right)}{k_s \frac{d}{2} J_0\left(\frac{k_s d}{2}\right)} \tag{3-27}$$

Using the fact that the acoustic impedance is $\xi = \frac{\Delta\hat{p}}{\rho c\hat{v}}$ and the diameter is twice the radius produces:

$$\xi = \frac{ikt}{F\left[\frac{k_s d}{2}\right]} \tag{3-28}$$

Sivian showed that the viscosity inside the perforate hole along a highly thermally conductive wall was different from the absolute viscosity outside the hole[2]. Sivian determined that for air over a wide range of temperatures the relationship between μ and μ' is:

$$\mu' = 2.179\mu \tag{3-29}$$

Noting that the analysis for the impedance was done within the perforate's hole k_s becomes k_s'. Equation (3-28) is the first term of the Crandall model as shown in Section 2.1.2. Tijdeman has studied extensively the propagation of sound waves in cylindrical tubes[3]. He presents results of acoustic propagation in ducts under less restrictive assumptions than what has been presented here. His analysis was not used for this study because a simpler model would provide a good initial understanding of the dynamics of the bias flow perforated plate. Furthermore, it was not known whether the approach of modeling the perforate orifices as ducts would work, and therefore given the resource constraints of this study a more complicated model was not warranted. Nevertheless, Tijdeman analysis could be used in future work as a starting point for developing a more comprehensive impedance model.

Melling also describes contributions by Sivian and Ingard for end effects to the perforate hole, and Fok's contribution to interaction effects between holes. His analysis is not going to be repeated here, but his results will be included. Therefore the Perforate Bias Flow model is:

$$\xi = \frac{1}{c\sigma C_D}\left[\frac{i\omega t}{F\left[\frac{k_s' d}{2}\right]} + \frac{8d}{3\pi F\left[\frac{k_s d}{2}\right]\psi'(\sigma)}\right] + \frac{\left(1-\sigma^2\right)}{2c\left(\sigma C_D\right)^2}\left[2v_b + 1.2v_{rms}\right] \tag{3-30}$$

where the Fok function $\psi'(\sigma)$ is defined in Eq. (2-9).

Note that the Perforate Bias Flow model is similar to the Crandall Impedance model. The Crandall Impedance model can be "corrected" to become the Perforate Bias Flow model by letting

$$v_a = 2v_b + 1.2v_{rms} \tag{3-31}$$

A problem arises when large enough negative bias flow rates would lead to negative impedance values. A recent study has experimentally shown the effect of negative bias flow rates of two degree-of-freedom liners.[4] The results of this suggest that increasing negative bias flow rates do not necessarily lead to lower or negative impedances. Consequently, Eq. (3-31) needs to be restricted to positive values. A possible method to accomplish this is to square Eq. (3-31) and take its square root. Doing this produces

$$v_a = \sqrt{(1.2v_{rms})^2 + (2v_b)^2 + 4.8v_{rms}v_b} \tag{3-32}$$

Thus the sign of v_b does affect the magnitude of impedance but cannot drive it negative. Therefore, blowing produces a different impedance result than suction. Comparing Eq. (3-32) to Premo's bias flow correction (Eq. (2-41)), it is noted that Premo's correction lacks the acoustic-bias flow coupling term $4.8v_{rms}v_b$ and therefore that model predicts the same resistance whether bias flow is provided via blowing or suction.

Equation (3-30) has a low and high frequency approximation. These approximations are valid if

$$\frac{d}{2}\sqrt{\frac{\omega}{\upsilon}} < 1 \qquad \frac{d}{2}\sqrt{\frac{\omega}{\upsilon}} > 10 \tag{3-33}$$

respectively. The low and high frequency approximations of Eq. (3-30) are

$$\xi = \frac{32\upsilon t}{c\sigma C_D d^2} + \frac{\left(1-\sigma^2\right)}{2c\left(\sigma C_D\right)^2}\left|2v_b + 1.2v_{rms}\right| + i\frac{k}{\sigma C_D}\left(\frac{4}{3}t + \frac{8d}{3\pi\psi'(\sigma)}\right) \qquad (3\text{-}34)$$

$$\xi = 2.82\frac{\sqrt{\omega\upsilon}}{c\sigma C_d}\frac{t}{d} + \frac{\left(1-\sigma^2\right)}{2c\left(\sigma C_D\right)^2}\left|2v_b + 1.2v_{rms}\right| + i\left(\frac{kt}{\sigma C_D} + 2.82\frac{\sqrt{\omega\upsilon}}{c\sigma C_d}\frac{t}{d} + \frac{8}{3\pi}\frac{d}{\psi'(\sigma)}\right) \qquad (3\text{-}35)$$

respectively. The PBF model runs into the problem that the Bessel functions in the linear component of the impedance obscure its physical relationship to geometrical parameters such as σ, t, and d. The low and high frequency approximations to the PBF model do not account for intermediate frequencies. Therefore, a single model that does not contain the Bessel functions, and "works" for all frequencies is desirable. One such correction similar to one done by Kraft, Yu, and Kwan, is[5]

$$\xi = \frac{16\upsilon t}{c\sigma C_D d^2} + 2.82\frac{\sqrt{\omega\upsilon}}{c\sigma C_D}\frac{t}{d} + \frac{\left(1-\sigma^2\right)}{2c\left(\sigma C_D\right)^2}\left|2v_b + 1.2v_{rms}\right| + i\left(\frac{kt}{\sigma C_D} + 2.82\frac{\sqrt{\omega\upsilon}}{c\sigma C_D}\frac{t}{d} + \frac{8}{3\pi}\frac{d}{\psi'(\sigma)}\right) \qquad (3\text{-}36)$$

Equation (3-36) will be called the **Perforate Bias Flow Intermediate Frequency model (PBFIF) model**. This is the model that will be evaluated against experiments. The exact model presented in Eq. (3-30) would be more accurate than Eq. (3-36). Nevertheless, during the evaluation process, using the PBFIF model provides better insight into the reasons for the good or bad agreement between the model and experiments. Using the PBFIF model also provides an extra degree of freedom for the experimental fit of this model presented in Section 3.6.

3.3 Perforate Compressible Bias Flow (PCBF) Model

The models studied so far, had a key assumption. These models assumed incompressible flow through the perforate holes. When bias flow is added, Mach

numbers within the perforate plate's hole can be substantial, and therefore fluid compressibility must be taken into account.

Compressibility corrections can be added to the models by allowing the incident field mean density to be different from that of the perforate's hole. During the derivation of both the PBF model and the PBLBF model the use of a control volume approach was employed. The control volume was used to relate the incident field acoustic and bias flow velocities to that of the perforate's hole, respectively. From the continuity principle, the incident and hole flow values can be related to each other. Therefore, Eq. (3-11) becomes

$$\begin{aligned} v_a &= \frac{\rho_h}{\rho}\sigma C_D v_{ah} \\ v_b &= \frac{\rho_h}{\rho}\sigma C_D v_{bh} \end{aligned} \tag{3-37}$$

where the mean hole density, ρ_h needs to be determined.

To determine the incident and mean perforate hole density, isentropic conditions can be employed. For an ideal gas assuming constant specific heat c_p, the first law of thermodynamics can be written as[6]

$$c_p T_o = c_p T + \frac{v^2}{2} \tag{3-38}$$

where T_o is the stagnation temperature. The speed of sound is given by

$$c^2 = \gamma R T \tag{3-39}$$

Inserting Eq. (3-39) into Eq. (3-38) and rewriting in terms of the incident and hole properties produces

$$\frac{c_h}{c} = \left(\frac{T_h}{T}\right)^{-\frac{1}{2}} = \left[\frac{1+\frac{1}{2}(\gamma-1)M_h^2}{1+\frac{1}{2}(\gamma-1)M^2}\right]^{-\frac{1}{2}} \tag{3-40}$$

For an isentropic fluid the following equation for a perfect gas can be written as[7]

$$\left(\frac{\rho}{\rho_o}\right)^{\gamma} = \left(\frac{T}{T_o}\right)^{\frac{\gamma}{(\gamma-1)}} \tag{3-41}$$

Inserting Eq. (3-41) into Eq. (3-40) and rearranging yields

$$\rho_h = \rho\left[\frac{1+\frac{1}{2}(\gamma-1)M_h^2}{1+\frac{1}{2}(\gamma-1)M^2}\right]^{-\frac{1}{\gamma-1}} \tag{3-42}$$

The principle of continuity can be written as

$$\frac{S}{S_h} = C_D\frac{\rho_h}{\rho}\frac{v_{bh}}{v_b} = C_D\frac{\rho_h}{\rho}\frac{M_h c_h}{Mc} \tag{3-43}$$

Substituting Eqs. (3-42) and (3-40) into Eq. (3-43) and assuming a circular jet produces

$$\frac{1}{\sigma} = C_D\left[\frac{1+\frac{1}{2}(\gamma-1)M^2}{1+\frac{1}{2}(\gamma-1)M_h^2}\right]^{\frac{\gamma+1}{2(\gamma-1)}}\left(\frac{M_h}{M}\right) \tag{3-44}$$

M_h is computed through iteration, and ρ_h is calculated from Eq. (3-42).

The compressible momentum equation with the simplifications given by Eqs. (3-1) through (3-9) yields

$$-\xi_{linear}\rho_h c v_{ah} - \rho_h\left(v_{bh}v_{ah}\right) - \frac{\rho_h v_{ah}^2}{2} = p_a \tag{3-45}$$

Inserting Eq. (3-37) into the above relation, multiplying by v_a and integrating over the period, noting that $|v_a|$ needs to be used in the third term to prevent it from being negative, produces

$$\xi = \frac{\xi_{linear}}{C_D\sigma} + \frac{1}{2c\left(C_D\sigma\right)^2}\frac{\rho}{\rho_h}\left|2v_b + 1.2v_{rms}\right| \tag{3-46}$$

Following a similar derivation as the one outlined in Section 3.1 produces

$$\xi = \frac{1}{c\sigma C_D}\left[\frac{i\omega t}{F\left[\frac{k_s' d}{2}\right]} + \frac{8d}{3\pi F\left[\frac{k_s d}{2}\right]\psi'(\sigma)}\right] + \frac{\rho}{\rho_h}\frac{\left(1-\sigma^2\right)}{2c\left(\sigma C_D\right)^2}\left|2v_b + 1.2v_{rms}\right| \tag{3-47}$$

where

$$k_s' = \sqrt{-\frac{i\omega}{\upsilon'}} \tag{3-48}$$

$$k_s = \sqrt{-\frac{i\omega}{\upsilon'}} \tag{3-49}$$

Notice that the compressibility term ρ/ρ_h only appears in the nonlinear term of Eq. (3-47). The corresponding low and high frequency approximations are

$$\xi = \frac{32\upsilon t}{c\sigma C_D d^2} + \frac{\rho}{\rho_h}\frac{\left(1-\sigma^2\right)}{2c\left(\sigma C_D\right)^2}\left|2v_b + 1.2v_{rms}\right| + i\frac{k}{\sigma C_D}\left(\frac{4}{3}t + \frac{8d}{3\pi\psi'(\sigma)}\right) \tag{3-50}$$

and

$$\xi = 2.82\frac{\sqrt{\omega\upsilon}}{c\sigma C_d}\frac{t}{d} + \frac{\rho}{\rho_h}\frac{\left(1-\sigma^2\right)}{2c\left(\sigma C_D\right)^2}\left|2v_b + 1.2v_{rms}\right| + i\left(\frac{kt}{\sigma C_D} + 2.82\frac{\sqrt{\omega\upsilon}}{c\sigma C_d}\frac{t}{d} + \frac{8}{3\pi}\frac{d}{\psi'(\sigma)}\right) \quad (3\text{-}51)$$

respectively. An intermediate frequency model such as Eq. (3-36) is

$$\begin{aligned}\xi = {} & \frac{16\upsilon t}{c\sigma C_D d^2} + 2.82\frac{\sqrt{\omega\upsilon}}{c\sigma C_d}\frac{t}{d} + \frac{\rho}{\rho_h}\frac{\left(1-\sigma^2\right)}{2c\left(\sigma C_D\right)^2}\left|2v_b + 1.2v_{rms}\right| \\ & + i\left(\frac{kt}{\sigma C_D} + 2.82\frac{\sqrt{\omega\upsilon}}{c\sigma C_d}\frac{t}{d} + \frac{8}{3\pi}\frac{d}{\psi'(\sigma)}\right)\end{aligned} \quad (3\text{-}52)$$

Equation (3-52) will be called **the Perforate Compressible Bias Flow Intermediate Frequency (PCBFIF) model**.

3.4 Grazing Flow Model

The following derivation uses some of the principles outlined by Rice[8]. It is important to note that although the general assumptions in this development follow from Rice, this model is more general and includes many more effects ignored by Rice. Moreover, this model includes bias flow, which was not included by Rice. Figure 3-1 shows the geometry of the model for the grazing flow-bias flow perforate hole interaction.

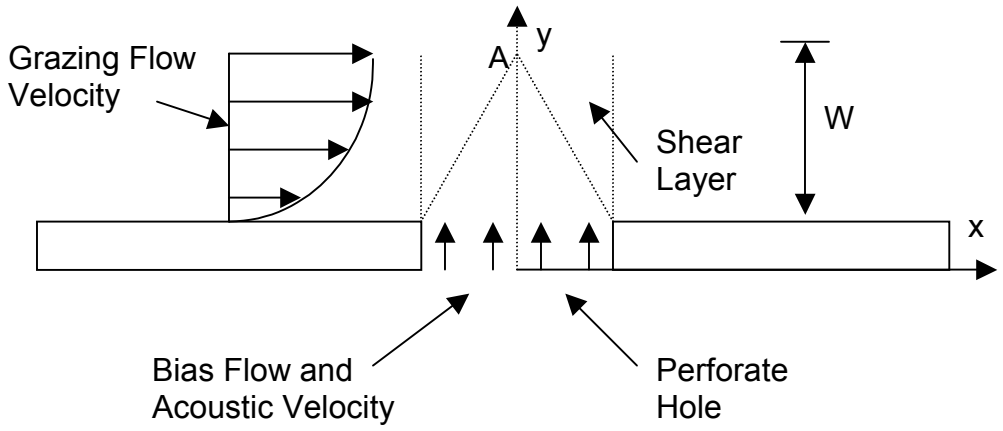

Figure 3-1. Grazing flow bias flow perforate hole interaction**.**

The jet emanating due to the bias flow interacts with the grazing flow. In the model that follows, the jet is treated as a rigid cone in the presence of grazing flow. The grazing flow generates vortices as it hits the cone. These vortices shed at a frequency given by the Strouhal number (St)[9]:

$$St = \frac{\omega d(y)}{V_g(y)} \tag{3-53}$$

Here d(y) and $V_g(y)$ are the diameter of the inviscid core, and the grazing flow velocity, respectively at some distance along the y-axis. $V_g(y)$ can be approximated by

$$V_g(y) = \frac{V_g y}{\delta} \tag{3-54}$$

where V_g is the free field grazing flow velocity and δ is the boundary layer thickness. The acoustic pressure generated by the vortices at point A is given by

$$p_A = \frac{C_{Drag}\rho V_g^2(W)e^{i\omega\tau}}{2} \tag{3-55}$$

where W is the distance that the jet emanates from the perforate hole into the grazing flow stream. To determine the radiated acoustic field, the convective wave equation is used. The convective wave equation in spherical coordinates assuming only radial variations is

$$c^2\left(\frac{\partial^2 p}{\partial r^2}+\frac{2}{r}\frac{\partial p}{\partial r}\right)=\left(\frac{\partial^2 p}{\partial t^2}+2v_r\frac{\partial^2 p}{\partial r\partial t}+v_r^2\frac{\partial^2 p}{\partial r^2}\right) \tag{3-56}$$

The assumed solution to Eq. (3-56) is

$$p=\frac{A}{r}e^{i(\omega t-k_r r)} \tag{3-57}$$

To determine the dispersion relationship, Eq. (3-57) is inserted into Eq. (3-56). This produces

$$\frac{\left(M_r^2-1\right)}{r}k_r^2-\frac{\left(i+2kM_r\right)}{r}k_r+\left(\frac{k^2}{r}-\frac{2M_r^2}{r^3}+i\frac{2k_r M_r}{r^2}\right)=0 \tag{3-58}$$

and M_r is the radial component of Mach number due to the bias flow. The roots of Eq. (3-58) are solved with respect to k to find the wave number corrections. Since the bias flow jet comes out with Mach number (M_y) in the y direction only, the radial component of this velocity needs to be computed to get M_r. It can be shown from Fig. 3-2 that M_r is related to M_y by

$$M_r=\frac{M_y\sqrt{x^2+W^2}}{W} \tag{3-59}$$

where M_y is the bias flow Mach number leaving the perforate hole. M_y is given by

$$M_y = \frac{v_b}{\sigma c} \tag{3-60}$$

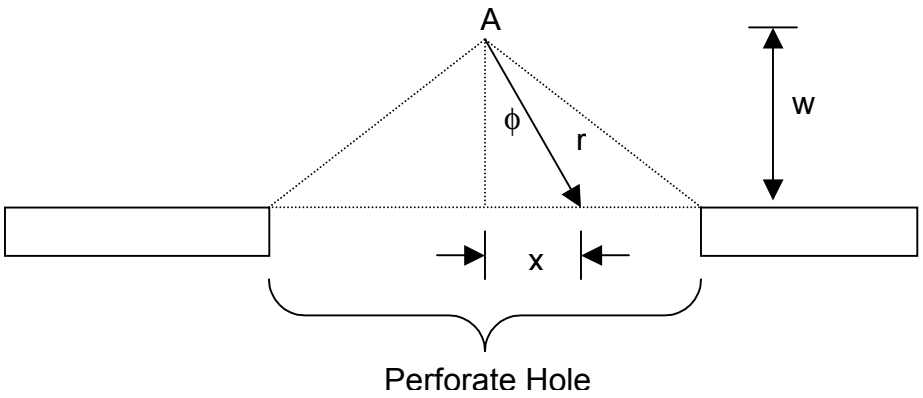

Figure 3-2. Geometry of Perforate Hole in Relation to the Acoustic Source.

Therefore, the radiated pressure field is

$$p_A(r) = \frac{C_{Drag} r_o \rho V_g^2(W)}{2r} e^{-ik_r r} \tag{3-61}$$

where $e^{i\omega\tau}$ has been omitted from Eq. (3-61) for clarity. At the perforate's hole surface, r is given by

$$r = \sqrt{W^2 + x^2} \tag{3-62}$$

Therefore the pressure field at the perforate hole surface is

$$p_A(x) = \frac{C_{Drag} r_o \rho V_g^2(W)}{2\sqrt{W^2 + x^2}} e^{-ik\sqrt{W^2+x^2}} \tag{3-63}$$

That distance W is due to the sum of the acoustic and bias flow fluid particle displacements and is given by

$$W = \frac{v_a}{i\omega} + W_b \tag{3-64}$$

where W_b is the jet displacement into the grazing flow due to the bias flow. To determine W_b the following analysis is made. The momentum and continuity equation for a circular jet can be written as[10]

$$v\frac{\partial v}{\partial y} + u\frac{\partial u}{\partial x} = \frac{\mu}{\rho}\frac{1}{x}\frac{\partial}{\partial x}\left(x\frac{\partial v}{\partial x}\right) \tag{3-65}$$

$$\frac{\partial v}{\partial y} + \frac{\partial u}{\partial x} + \frac{u}{x} = 0 \tag{3-66}$$

respectively. Velocity components along the x and y-axis are denoted by u and v, respectively. The y and x-axis are the lengthwise and radial components of the jet, respectively. The boundary conditions are

$$\begin{aligned} &x = 0: \quad u = 0; \quad \frac{\partial v}{\partial x} = 0 \\ &x = \infty: \quad v = 0 \end{aligned} \tag{3-67}$$

The solution to Eqs. (3-65), (3-66), and (3-67) is[11]

$$v = \frac{3}{8\pi}\frac{K}{\upsilon y}\frac{1}{\left(1 + 0.25\beta^2\right)^2} \tag{3-68}$$

$$u = 0.25\sqrt{\frac{3}{\pi}}\frac{\sqrt{K}}{y}\frac{\beta - 0.25\beta^2}{\left(1 + 0.25\beta^2\right)^2} \tag{3-69}$$

where

$$\beta = \sqrt{\frac{3}{16\pi}}\frac{\sqrt{K}}{\upsilon}\frac{x}{y} \tag{3-70}$$

$$K = \frac{J}{\rho} \tag{3-71}$$

J is the momentum of the jet given by

$$J = 2\pi\rho\int_0^{\infty} v^2 x\,dx \tag{3-72}$$

For the case of the perforate orifice, the equation for J becomes

$$J = 2\pi\rho\int_0^{d/2}\left(\frac{v_b}{\sigma}\right)^2 r\,dr = \frac{\pi d^2\rho v_b^2}{4\sigma^2} \tag{3-73}$$

At x=0, β=0, and v is

$$v = \frac{0.09375 d^2 v_b^2}{4\upsilon\sigma^2 y} \tag{3-74}$$

The distance the jet extends into the grazing flow stream is subjective. The fluid velocity continually slows down due to the viscosity in the surrounding fluid, and therefore where the jet is no longer affecting the grazing flow is debatable. Consequently, an assumption is made that the jet affects the grazing flow stream as long as it retains 10% of its original velocity. Inserting this assumption into Eq. (3-74) and simplifying yields

$$y = W_b = 0.2344\frac{d^2 v_b}{4\upsilon\sigma} \tag{3-75}$$

Equation (3-63) must be space averaged to get an approximate impedance at the hole surface. Therefore the average acoustic pressure at the surface of the perforate due to grazing flow p_g is

$$p_g = \frac{1}{d}\int_{-d/2}^{d/2} p_A(x)dx \tag{3-76}$$

The total acoustic pressure at the surface of the perforate p_{tot} is given by

$$p_{tot} = p_s + p_g \tag{3-77}$$

where p_s is another acoustic pressure source term present in the system. The bias flow impedance models presented previously give the acoustic particle velocity response. Therefore

$$\frac{p_{tot}}{\rho c v_a} = \xi_p + \xi_{cav} \tag{3-78}$$

where ξ_p and ξ_{cav} are the perforate bias flow impedance model and cavity impedance respectively. To solve Eq. (3-78) the left and right hand side of this equation must be equal. Therefore, through an iterative method an appropriate v_a is found that makes both sides of this equation equal.

3.5 ZKTL and Transmission Matrix Theory

Jones and Parrott first presented the Zwikker-Kosten Transmission Line code (ZKTL) in 1995.[11] The idea of this code was to use transmission matrices to calculate pressure and velocity at each section for a multi-element liner. The forward transmission matrix through a dissipative channel has the following form[12]

$$\begin{bmatrix} p_{m+1} \\ u_{m+1} \end{bmatrix} = \begin{bmatrix} T_{11} & T_{12} \\ T_{21} & T_{22} \end{bmatrix} \begin{bmatrix} p_m \\ u_m \end{bmatrix} \tag{3-79}$$

where

$$\begin{aligned} T_{11} &= T_{22} = \cosh(k\Gamma b) \\ T_{12} &= \zeta_c \sinh(k\Gamma b) \\ T_{21} &= \zeta_c^{-1} \sinh(k\Gamma b) \end{aligned} \tag{3-80}$$

Γ and ξ_c are the propagation constant and characteristic impedance, respectively. b is the length of the element between m+1 and m. In the ZKTL code, the Zwikker and Kosten low frequency solution of the propagation constant for shear wave numbers below 120 and the Kirchhoff "wide-tube" solution for shear wave numbers greater than 120 are used. The shear wave number is

$$s = \frac{d}{2}\sqrt{\frac{\omega}{\upsilon}} \tag{3-81}$$

The Zwikker and Kosten propagation constant and characteristic impedance are respectively

$$\Gamma = \sqrt{\frac{J_0\left(i^{3/2}s\right)}{J_2\left(i^{3/2}s\right)}}\sqrt{\frac{\gamma}{n}} \tag{3-82}$$

$$\xi_c = \frac{-i}{\Gamma}\frac{J_0\left(i^{3/2}s\right)}{J_2\left(i^{3/2}s\right)} \tag{3-83}$$

where

$$n = \left[1 + \frac{\gamma - 1}{\gamma} \frac{J_2\left(i^{3/2}\sigma s\right)}{J_0\left(i^{3/2}\sigma s\right)} \right]^{-1} \tag{3-84}$$

and γ is the specific heat ratio. The Kirchoff "wide-tube " solutions of the propagation constant and characteristic impedance for shear wave numbers greater than 120 are

$$\Gamma = \left\{ \frac{1}{\sqrt{2}} \left(\frac{\gamma - 1 + \sigma}{\sigma s} \right) + i \left[1 + \frac{1}{\sqrt{2}} \left(\frac{\gamma - 1 + \sigma}{\sigma s} \right) \right] \right\} \tag{3-85}$$

$$\xi_c = \frac{i}{\Gamma} \tag{3-86}$$

These transmission matrix elements were modified to account for the effect of the wave number shift caused by bias flow, which will effect cavity reactance. The elements in Eq. (3-80) become:

$$T_{11} = \frac{1}{2}\left(D^- e^{\Gamma k^- b} + D^+ e^{-\Gamma k^+ b} \right) \tag{3-87}$$

$$T_{12.} = \frac{iD^+ D^-}{2N\Gamma} \left(\frac{\rho_c c_c}{\rho c} \right) \left(e^{\Gamma k^- b} - e^{-\Gamma k^+ b} \right) \tag{3-88}$$

$$T_{21} = -\frac{iN\Gamma}{2} \left(\frac{\rho c}{\rho_c c_c} \right) \left(e^{\Gamma k^- b} - e^{-\Gamma k^+ b} \right) \tag{3-89}$$

$$T_{22} = \frac{1}{2}\left[D^+ e^{\Gamma k^- b} + D^- e^{-\Gamma k^+ b} \right] \tag{3-90}$$

where

$$k^{-} = \frac{\left(\omega / c_c\right)}{1 - M_c}$$

$$k^{+} = \frac{\left(\omega / c_c\right)}{1 + M_c} \tag{3-91}$$

$$D^{+} = 1 + (1 + i\Gamma)M_c$$
$$D^{-} = 1 - (1 + i\Gamma)M_c \tag{3-92}$$

$$b = x_{m+1} - x_m \tag{3-93}$$

where x_{m+1} and x_m are the x distance at locations m+1 and m, respectively. In this study these matrices model the cavity. Therefore, b is the length of the cavity L.

3.6 Error Criteria

The method of least squares can be employed to establish the error criteria for the model predictions. Let E_i and P_i be a set of experimental and predicted results, respectively. Assume that the following relationship exists between E_i and P_i[13]

$$P_i = SE_i + e_i \tag{3-94}$$

where e_i is the random error associated with experiment i and S is an arbitrary constant. Minimizing the square of the errors yields the linear regression of $N_{estimate}$ on E where

$$S = \frac{\sum_{i=1}^{m} P_i E_i}{\sum_{i=1}^{m} E_i^2} \tag{3-95}$$

and $N_{estimate}=SE_i$. Note that this regression curve has been forced through zero. S measures the ratio of predicted results to experimental results. If the ratio is equal to one then the experimental values equal the predicted results. Therefore, the deviation of this ratio from one is indicative of the least squares precision error between predictions and experiments as seen from Fig. 3-3.

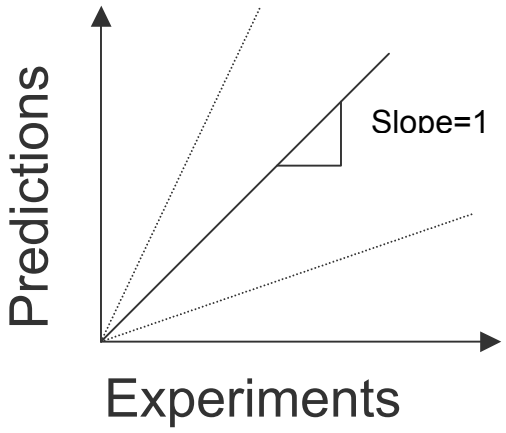

Figure 3-3. Sketch of least squares fit between predictions and experiments.

It is important to note that the least squares slope between predictions and experiments is not the same as taking the mean of the predictions divided by experiments. This is expressed in Eq. (3-96)

$$S \neq \frac{\sum_{i=1}^{N} \frac{P_i}{E_i}}{N} \tag{3-96}$$

where N is the number of points in the Prediction-Experiment plane of Fig. 3-3. The slope in the least squares sense is more sensitive than in the arithmetic sense, and therefore errors are larger using least squares procedure. For example, a slope of 0.9 in the least squares sense does not mean that on average the predictions are within 90% of the experiments. On an average sense the predictions may be within say 95% of the experiments.

Another measure of error used is the mean difference between experimental and predicted impedance results. To calculate the mean difference, the average predicted impedance in the frequency range is subtracted from the experimental counterpart as shown in Fig. 3-4. This difference is given in terms of ρc difference, since the impedance is normalized with respect to ρc.

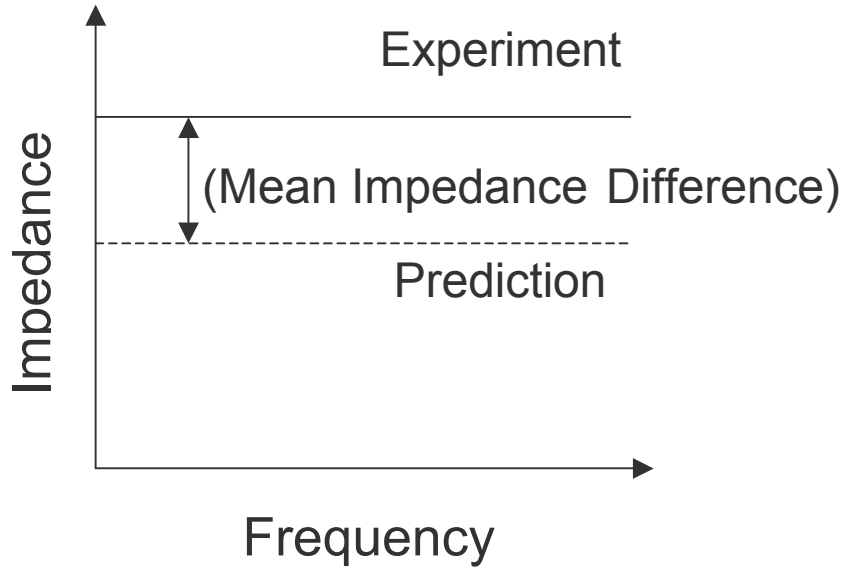

Figure 3-4. Sketch of difference between prediction and experiment.

The correlation coefficient is indicative of whether the predictions and experiments are following the same trend. This quantity is given by[14]

$$C = \frac{\sum_{i=1}^{m}\left(E_i - \overline{E}\right)\left(P_i - \overline{P}\right)}{\sqrt{\sum_{i=1}^{m}\left(E_i - \overline{E}\right)^2 \sum_{i=1}^{m}\left(P_i - \overline{P}\right)^2}} \qquad (3\text{-}97)$$

where, as before, E and P stand for experimental and predicted results, respectively. The correlation coefficient goes from –1 to +1 if the data is negatively or positively correlated, respectively. Note that for the correlation coefficient the regression curve has not been constrained to pass through P=E=0. This was done to avoid confusion, since the correlation coefficient is normally presented in the literature unconstrained.

3.7 Experimental Fit to Bias Flow Impedance Model

The impedance in the PBFIF model (Eq. (3-36)) can be written as

$$\xi = a_1 G_1 + a_2 G_2 + ... + a_n G_n \tag{3-98}$$

where a_1, a_2, …, a_n have values of one. G_1, G_2, …, G_n are the nondimensional group in that equation. For example in the PBFIF model G_1 and G_2 are

$$\begin{aligned} G_1 &= \frac{16\upsilon t}{c\sigma C_D d^2} \\ G_2 &= 2.82\frac{\sqrt{\omega\upsilon}}{c\sigma C_D}\frac{t}{d} \end{aligned} \tag{3-99}$$

To fit the model to the experiments an optimal set of a's is desired that minimizes the error between experiments and predictions. To this end an optimization procedure was developed and implemented. The optimization procedure was a constrained minimization routine that minimized an objective error function based on the slope error criterion[15]. Therefore, the setup for the optimization procedure was the following

$$\begin{aligned} &\text{minimize} \rightarrow \text{Objective Function} = \text{abs}(1 - \text{Slope}) \\ &\text{subject to (constraints)}: \\ &\\ &0 \le a_1 \le 3 \\ &0 \le a_2 \le 3 \\ &0 \le a_3 \le 3 \end{aligned} \tag{3-100}$$

where abs stands for absolute value and Slope is the slope error criterion described in Section 3.6. The optimal set of a_i only varied a_1 through a_3. This was done since bias flow only affects the resistance in the models developed in this chapter. This optimization

routine was used for the PBFIF model and the corresponding results are shown in Chapter 8. The fit was performed using the 5, 10 and 15% POA samples and all flow rates except the highest incident bias flow rate (600 cm/s). Other fitting methods were tried unsuccessfully and are addressed in Appendix C.

The ultimate goal of these impedance models is to be used to design a maximum absorptive liner. Appendix D addresses this ultimate goal.

References

1. Melling, T.H., "The Acoustic Impedance of Perforates at Medium and High Sound Pressure Levels," Journal of Sound and Vibration, 29(2-1), 1973.
2. Sivian. L. J., "Acoustic Impedance of Small Orifices," J. Acoustical Society of America, Vol. 7, October 1935, pp. 94-101.
3. Tijdeman, H., "On the Propagation of Sound Waves in Cylindrical Tubes," Journal of Sound and Vibration, 39(3-1), 1975
4. Cataldi, P., Ahuja, K. K., and Gaeta Jr., R. J., "Enhanced Sound Absorption Through Negative Bias Flow," AIAA 99-1879, 1999.
5. Kraft, R.E., Yu J., and Kwan H.W., "Acoustic Treatment Design Scaling Methods," Volume 2, Advanced Treatment Impedance Models for High Frequency Ranges, NAS3-26617, May 1996.
6. Shames, Irving H., Mechanics of Fluids, McGraw-Hill, New York, 1992.
7. Liepmann, H.W. and Roshko, A., Elements of Gas Dynamics, John Wiley & Sons, New York, 1957.
8. Rice, E. J., "A Model for the Acoustic Impedance of a Perforated Plate Liner with Multiple Frequency Excitation," NASA TM X-67950, 1971.
9. White, F. M., Fluid Mechanics, McGraw-Hill, New York 1979.
10. Schlichting, H., (Translated into English by Kestin, J), Boundary Layer Theory, McGraw-Hill, New York 1960.
11. Parrott, T.L. and Jones, M.G., "Parallel-element Liner Impedance for Improved Absorption of Broadband Sound in Ducts," Noise Control Eng. J., 43(3-6), 1995.
12. Samuel T., Elements of Acoustics (Wiley, New York, 1981) Chapter 6, Sec. 6.5, p.402.
13. James, M.L., Smith, G.M., and Wolford, J. C., *Applied Numerical Methods for Digital Computation*, Harper Collins College Publishers, 1993. pp. 302-305.
14. Bendat, J.S. and Piersol, A. G., *Random Data*, John Wiley & Sons, New York, 1986.
15. Arora, J., *Introduction to Optimum Design*, McGraw-Hill, New York, 1989. pp. 111

4. Experiments

Several perforate liner samples were tested using the NASA Langley Normal Impedance Tube (NIT) for the purposes of evaluating the acoustic impedance models discussed in Chapters 2 and 3. These samples were also tested in a raylometer for the purpose of determining the discharge coefficient associated with the perforate. Acoustic impedance was measured for the samples with and without bias flow for a frequency range of 1000 to 3000 Hz and sound pressure level (SPL) of 120 to 140 dB. After the completion of the tests, repeatability studies were performed to assess the validity of the experimental database.

The normal incidence tests were performed utilizing the Non-Switching Two-Microphone Method (NS-TMM)[1]. This method was preferred due to the higher speed of data collection it offered over the Switching Two-microphone Method (S-TMM). Although the NS-TMM method is an established method for measuring acoustic impedance, the NIT facility utilized the S-TMM method rather than the NS-TMM method to determine acoustic impedance. Consequently, the NS-TMM method had to be implemented.

In order to add bias flow to the liners, several experimental setup changes were required. These included the addition of a plenum chamber, the replacing of the hard backing plate with a high resistive mesh material, and the addition of a muffler at the end of the bias flow tube configuration. These and other issues involved in the testing of perforates in the presence of bias flow will be discussed in this chapter.

4.1 Experimental Setup

The NASA Langley Normal Incidence Tube (NIT) was used to make impedance measurements of lumped-element single-degree-of-freedom liners with bias flow (see Figures 4-1 and 4-2). Six acoustic drivers generate an acoustic plane-wave pressure field which, upon reflection from the perforate sample, sets up a standing wave along the axis of the 5.08-cm square tube. The perforate facesheet sample is placed at the end of the

tube and backed with a short 5.08-cm square cavity. This cavity is terminated with a high resistance fibermetal sheet designed to allow mean flow to pass through while reflecting almost all the acoustic signal. Three microphones are used in the test procedure. The microphone nearest the specimen is stationary, and is used to measure the sound pressure level near the surface of the specimen. Two other microphones measure the frequency dependent transfer functions (acoustic pressure magnitude and phase differences) between their respective locations. This information is equivalent to determining the standing wave pattern in the tube. Since the acoustic wave patterns are related to the surface impedance of the perforate-cavity system (test specimen), this impedance can then be determined.[2,3]

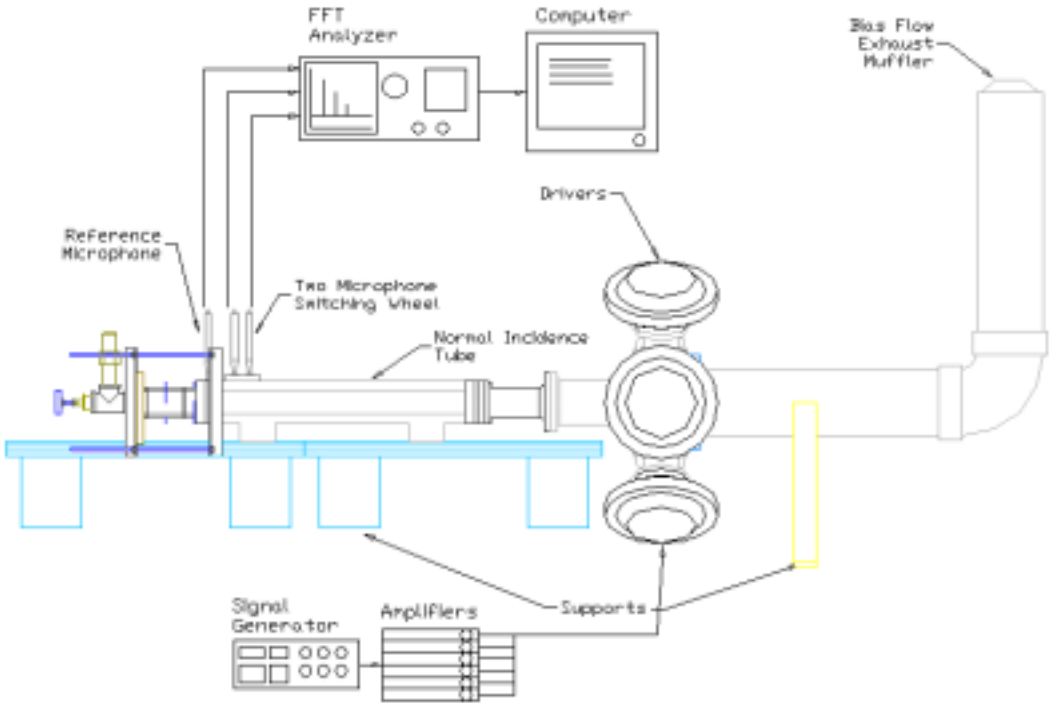

Figure 4-1. Sketch description of Normal Impedance Tube with bias flow, one degree of freedom liner installed.

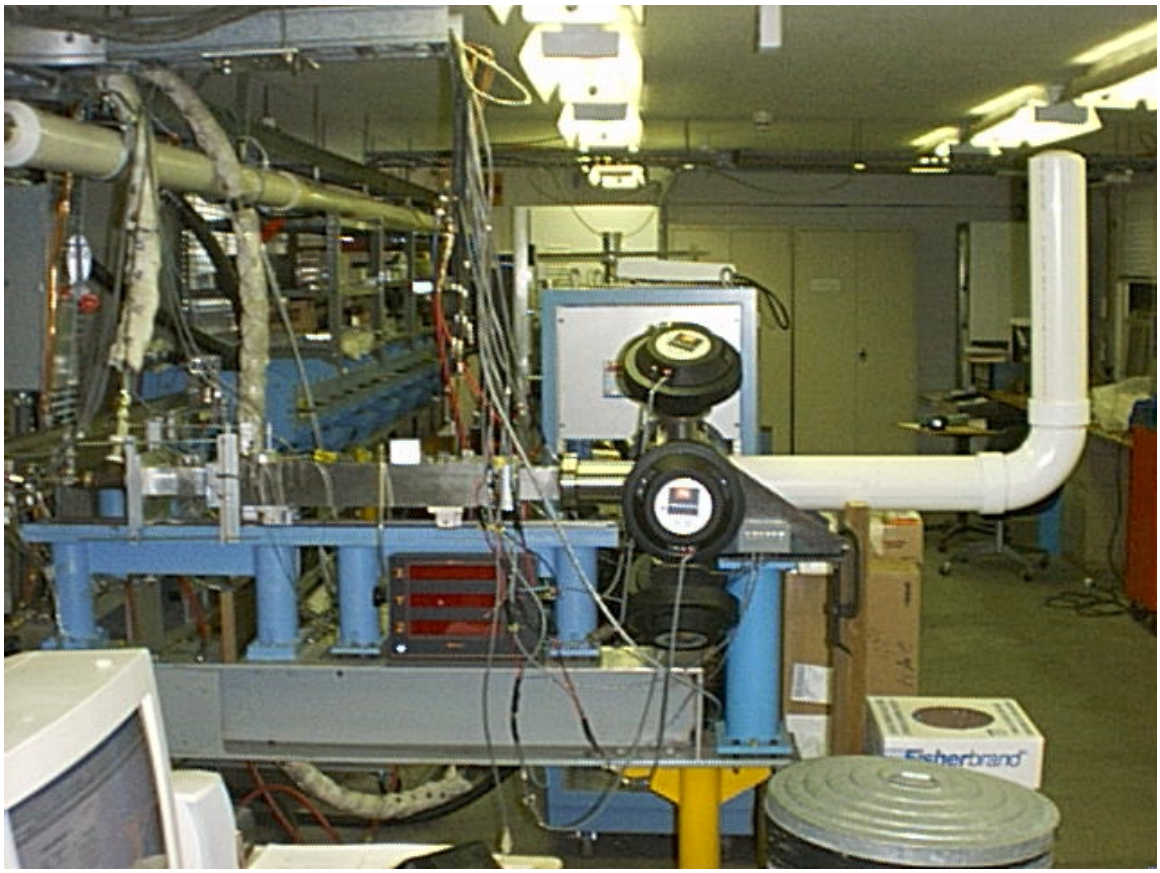

Figure 4-2. Picture of Normal Incident Tube.

The surface impedance of the specimen is given by

$$\xi = \frac{1+R}{1-R} = \theta + i\chi \tag{4-1}$$

where R is the complex reflection coefficient,

$$R = \frac{P_r}{P_i} \tag{4-2}$$

and θ and χ are the normalized resistance and reactance, respectively.

A signal generator is used to generate discrete frequency signals that are input to the power amplifiers. The amplified signals are then input to the acoustic drivers. Signals

from the microphones are sampled and averaged using an FFT analyzer and the data is stored on the computer.

Positive bias flow (blowing) is introduced through the 2.54-cm diameter inlet tee, shown in Figs. 4-3 and, 4-4 into a 5.08-cm square plenum chamber. The flow then continues through a high resistance (at least $10\rho c$) fibermetal sheet into the cavity section and through the perforate sample. The flow is exhausted through the muffler depicted in Figs. 4-1 and 4-2. A reference sample was tested in the NIT before and after the muffler was installed. Results showed the muffler had no effect on the measured impedance.

To adequately measure and control the bias flow velocity in each section, four pressure ports were installed along the sides of each duct section before and after each major pressure drop in the bias flow liner. To measure the velocity through each section, mass continuity and the ideal gas equation are used:

$$\begin{aligned} \rho_k V_k A_k &= \rho_{k+1} V_{k+1} A_{k+1} \\ \rho_k &= \frac{P_k}{RT} \end{aligned} \tag{4-3}$$

Here the index k indicates the section number (see Figure 2) and ρ, V, P, R, and T are the density, velocity, absolute pressure, ideal gas constant, and temperature, respectively. The mass flow is measured with a laminar flow meter upstream of the inlet tee. Using Eq. (4-3), the velocity is calculated in each section.

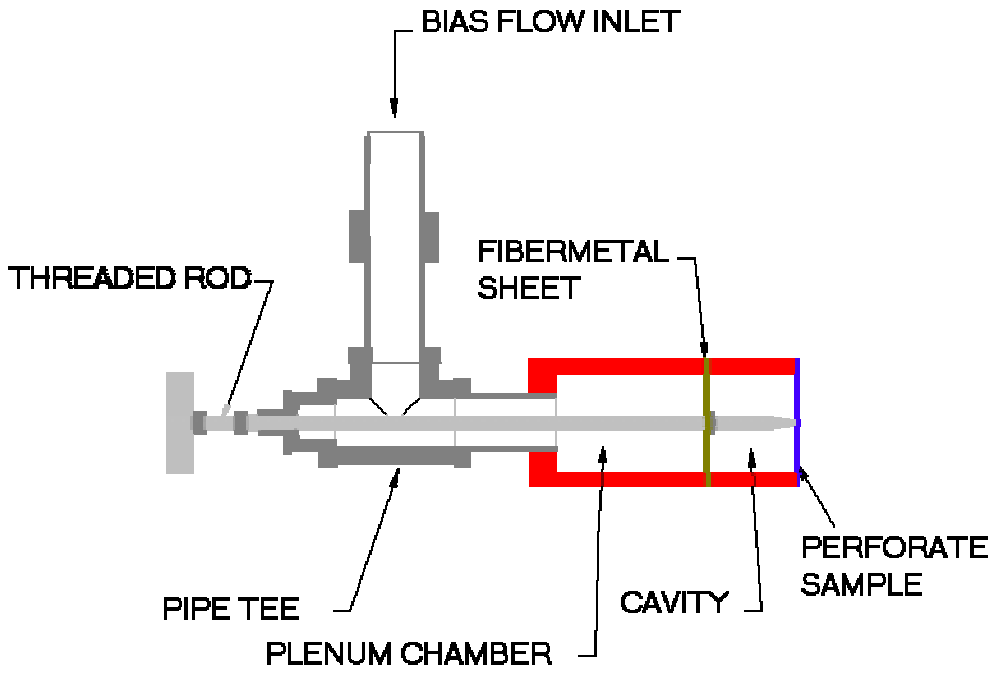

Figure 4-3. Sketch Description of bias flow one degree of freedom liner.

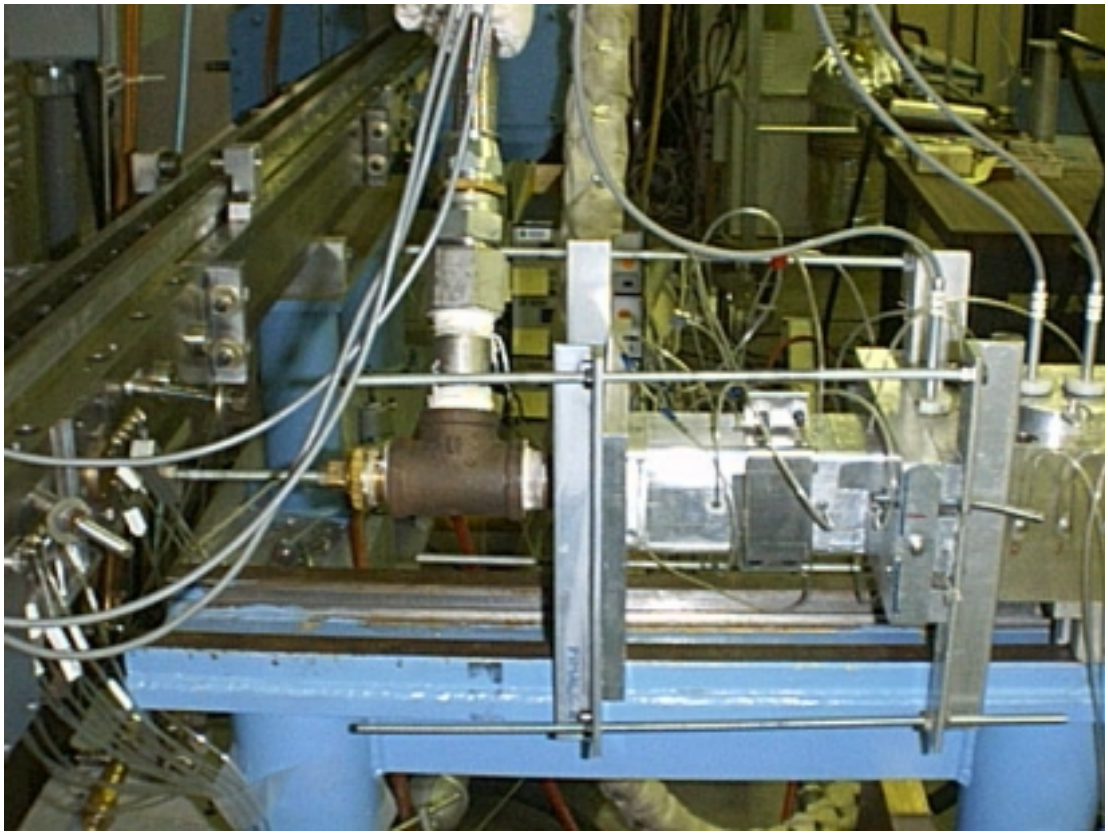

Figure 4-4. Picture of bias flow double degree of freedom liner.

Contamination of the intrinsic perforate impedance by a "shunt impedance" due to plate vibration is a recurrent problem in measurements of this type[4]. For this study, shunt impedance effects were clearly evident for some of the perforate samples. Consequently, special precautions were taken to inhibit this contamination. The measured impedance is always a combination of the plate mechanical impedance and the liner acoustic impedance, which can be modeled as parallel, lumped impedances. For most cases, the plate mechanical impedance is high enough, relative to the liner acoustic impedance, to cause minimal contamination. Near the plate mechanical resonance, however, it becomes a significant factor; i.e., in the range of the perforate impedance.

Near the resonant frequency of the plate, the impedance is transitioning from a stiffness-dominant to a mass-dominant system. Therefore, to counter resonance behavior exhibited in the acoustic impedance measurements, the effective plate stiffness was increased. This was achieved by the addition of a post support mechanism. Figure 4-5 shows a comparison of the acoustic impedance spectra for a single perforate sample when it is mounted with or without the post support mechanism. The unsupported plate (no post support) spectra shows the resonance frequency behavior, with a drop in impedance above the resonance frequency. The addition of the post support eliminates the structural resonances of the plate (perforated sheet sample) below 3kHz; thus, the resultant spectra is uncontaminated by plate resonance behavior in the current frequency range of interest.

In typical aircraft applications, this desired stiffness is achieved by permanently bonding a cellular honeycomb to the perforate sample. However, the honeycomb walls and the bonding agent cause perforate hole blockage. Since the purpose of this study was to study the effects of bias flow on the perforate, this blockage was unacceptable. Also, keeping the perforated plates unbonded allowed simple interchange of test materials. In contrast, the post blocked no more than one hole and it accounted for only 1.25% of the total cross-sectional area of the cavity.

Figures 4-3 and 4-4 show the post support mechanism. The post was centered through the fibermetal termination face into the cavity until it pushed against the perforate sample. A thin nut was installed on one side of the fibermetal to secure the fibermetal firmly.

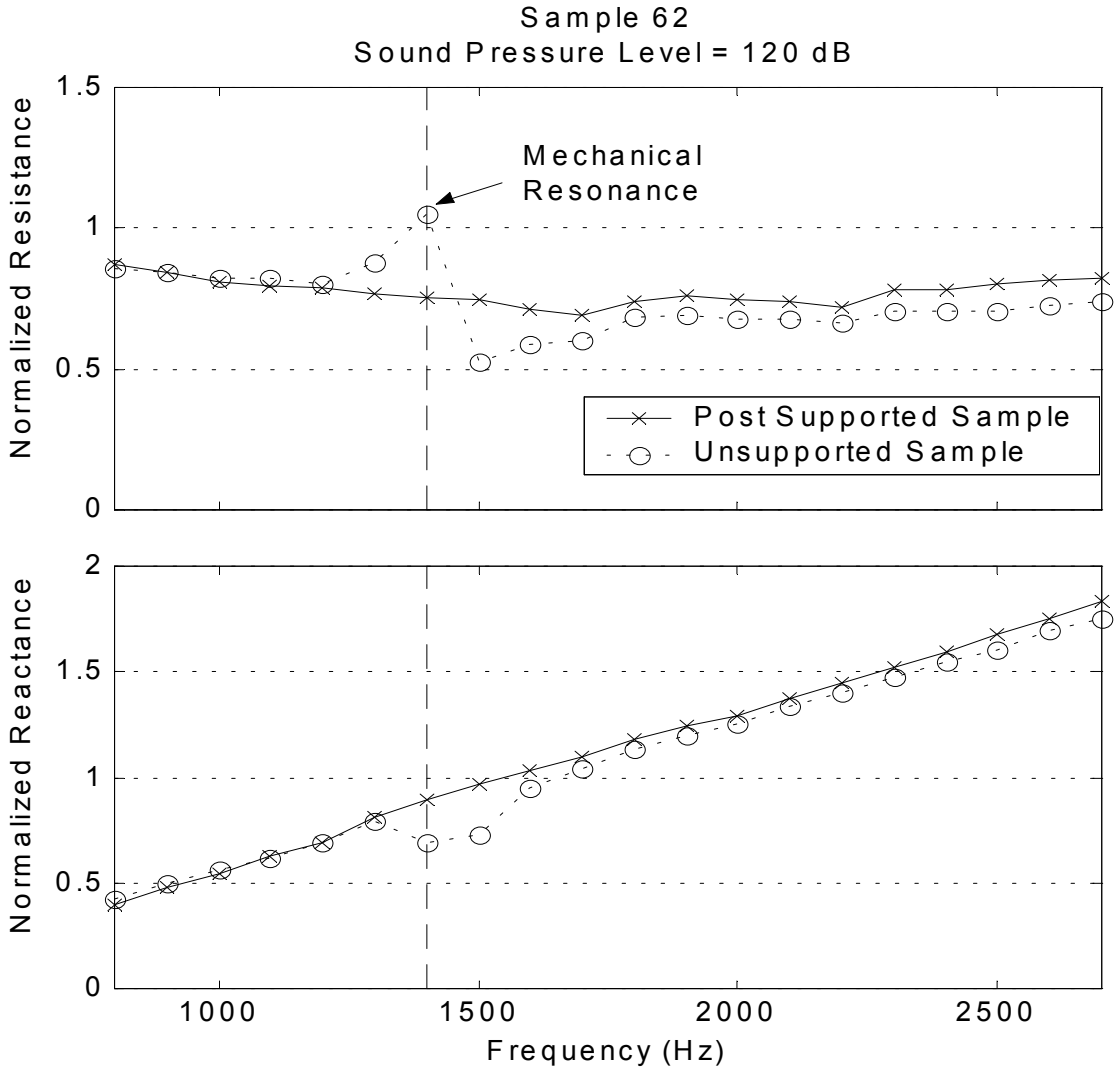

Figure 4-5. Example of structural resonance affecting liner impedance.

4.2 Repeatability and Error Estimation

To ensure data quality, Perforates 52-54 and 62 were used to conduct repeatability tests. These samples were each tested four times over the frequency range of 1300 to 2200 Hz (100 Hz increments) for SPL's of 100, 120 and 140 dB. These four perforates were used to represent the repeatability error for the full range of percent open areas being tested, with no bias flow. Thus, while providing helpful information regarding the

NS-TMM method, these results do not offer proof of the quality of the results acquired with bias flow.

For an individual sample at a fixed SPL, the mean acoustic resistance (similarly, for acoustic reactance) was computed from four measurements at each frequency. The percentage deviations (PD's) from the mean were then computed for each of the four measurements. Thus, for ten frequencies at four measurements per frequency, this gave 40 PD's. These 40 values of PD's were used to compute a global standard deviation for the selected sample and SPL, using

$$s = \sqrt{\frac{\sum_{i=1}^{N} (x_i - \bar{x})^2}{N-1}} \tag{4-4}$$

where x_i is the individual PD and N=40. Since the focus of this analysis was to quantify the repeatability (random) error, $\bar{x}$ was set to zero; i.e., the systematic error was ignored. The total error from the mean (% of data lying within 95% of the mean), which is ±2s, is provided in Table 4-1 for each sample and SPL.

A comparison of the Gaussian probability distribution with the measurement data (PD's discussed above) is shown in Fig. 4-6.[5] This figure shows the percentage of data lying below a certain mean for both the ideal Gaussian distribution and the measured data. Clearly, the distribution is "near" Gaussian in nature; thus, computing the repeatability error using the Gaussian mean and standard deviation should be sufficient for characterization of this data. Figure 4-6 also shows that 95% of the data is within ±7.25% of the mean.

Table 4-1 provides repeatability data for all of the samples, at each of the three SPL's tested. All twenty-four data sets show similar evidence of "near" Gaussian distributions of data. The measured data are shown to be off the mean value by a maximum of 7%. It should be noted that only 32 averages are sampled by the FFT analyzer for each microphone signal. In order to reduce data uncertainty, the number of averages could be increased. Regardless, with the data given in Table 4-1, it is reasonable to assume that overall measurement error is at most ±7%.

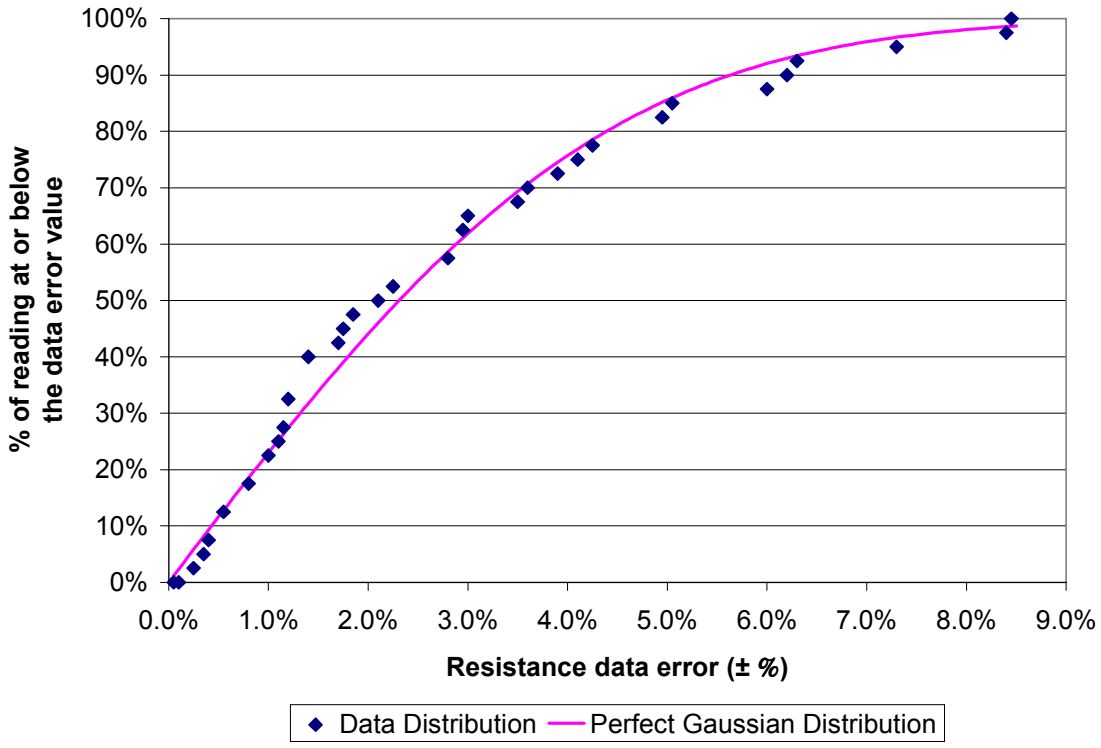

Figure 4-6. Comparison of ideal Gaussian distribution and data distribution (SPL of 100dB, 5 POA).

Table 4-1. Data acquisition repeatability percent error

	Resistance			Reactance		
SPL	5% POA	10% POA	15% POA	5% POA	10% POA	15% POA
100 dB	±2%	±6%	±7%	±1%	±4%	±4%
120 dB	±2%	±6%	±7%	±1%	±5%	±3%
140 dB	±2%	±5%	±5%	±1%	±3%	±6%

4.3 Sample Description

Each perforate was specially fabricated for this set of experiments. The samples are 6.35-cm square perforated plates, with rounded corners to conform to the NIT sample holder. The perforate's orifices were created by the punched method. The geometric parameters (plate thickness, hole diameter, and percent open area), as depicted in Figure 4, were varied for these plates over the respective ranges of

$$0.24 \text{ mm} < d < 1.48 \text{ mm}$$
$$0.51 \text{ mm} < t < 1.02 \text{ mm}$$
$$0.9\% < \text{POA} < 16.5\%$$

Table 4-2 gives the target and measured dimensions for the perforate liner samples. The target dimensions were chosen such that only one perforate dimension was varied at a time. Due to fabrication inconsistencies, the measured dimensions are slightly different from the desired values. The numbers quoted in the table represent an average of several measurements, with standard deviations being within ±2% of the means for each measured set. The ranges of perforate dimensions were chosen to encompass what is typically seen in current aircraft engine liners. Several groups of 5-15 POA perforates with constant plate thickness and hole diameter were selected. One group of 1-5 POA perforates was also selected.

A microscope was used to measure the individual hole diameters. Thirty holes were examined for the initial perforate. An analysis of those results concluded that only ten holes needed to be measured for successive samples. Perforate sheet thickness was measured using a micrometer, and the POA was determined by multiplying the number of holes in the perforate by the cross-sectional area per hole, then dividing by the total area of the sheet (5.08-cm square) exposed to the acoustic field in the NIT. As shown in the table, the fabrication process was better for the 5-15 POA perforates than for the 1-5 POA perforates.

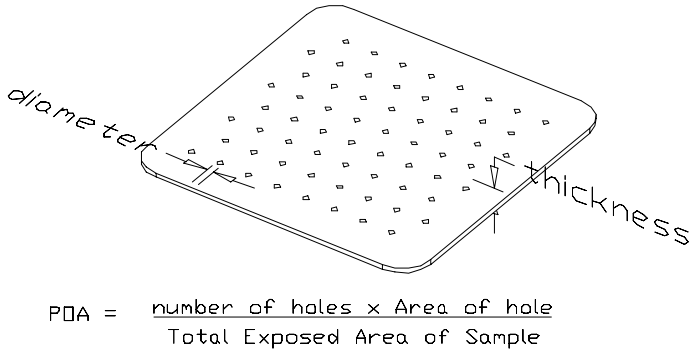

Figure 4-7. Geometric parameters of liner samples.

Table 4-2. Target and measured dimensions for fabricated perforated sheets.

Sample Number	Hole Diameter			Sheet Thickness			POA	
	Target (in)	Target (mm)	Measured (mm)	Target (in)	Target (mm)	Measured (mm)	Target	Measured
43	0.024	0.610	0.644	0.025	0.635	0.635	5%	5.7%
44	0.024	0.610	0.625	0.025	0.635	0.660	10%	10.5%
45	0.024	0.610	0.599	0.025	0.635	0.686	15%	14.5%
46	0.035	0.889	0.922	0.025	0.635	0.635	5%	5.4%
47	0.035	0.889	0.917	0.025	0.635	0.635	10%	10.7%
48	0.035	0.889	0.909	0.025	0.635	0.610	15%	15.6%
49	0.040	1.016	1.039	0.025	0.635	0.635	5%	5.3%
50	0.040	1.016	1.030	0.025	0.635	0.635	10%	10.2%
51	0.040	1.016	1.029	0.025	0.635	0.635	15%	15.5%
52	0.024	0.610	0.658	0.040	1.016	0.991	5%	5.9%
53	0.024	0.610	0.637	0.040	1.016	0.965	10%	10.9%
54	0.024	0.610	0.639	0.040	1.016	1.016	15%	16.5%
55	0.040	1.016	1.052	0.040	1.016	0.965	5%	5.4%
56	0.040	1.016	1.037	0.040	1.016	1.016	10%	10.3%
57	0.040	1.016	1.047	0.040	1.016	0.965	15%	16.0%

58	0.055	1.397	1.481	0.040	1.016	0.991	5%	5.7%
59	0.055	1.397	1.466	0.040	1.016	1.016	10%	11.0%
60	0.055	1.397	1.464	0.040	1.016	1.016	15%	16.6%
61	0.010	0.254	0.240	0.018	0.457	0.533	1%	0.9%
62	0.010	0.254	0.262	0.018	0.457	0.508	2%	2.2%
63	0.010	0.254	0.262	0.018	0.457	0.508	3%	3.1%
64	0.010	0.254	0.291	0.018	0.457	0.508	4%	5.2%
65	0.010	0.254	0.281	0.018	0.457	0.508	5%	6.1%

4.4 Non-Switching Two-Microphone Method

The NIT facility has traditionally utilized a switching two-microphone method[6] (S-TMM) that involves acquiring transfer function data between two microphone locations. The transfer functions between the two microphones are measured before and after the microphone positions are very accurately swapped by the usage of a rotating microphone plug. Appropriate averaging of the two readings eliminates the effects of any magnitude and phase differences between the two microphones. When this method is used with a discrete frequency source, the microphones must be swapped for each source frequency. While this eliminates the need for a separate calibration procedure, it is inefficient for the testing of a large number of test specimens. Thus, a modified version of the standard Two-Microphone Method[6,7], which does not require microphone switching during the test process, was used to significantly shorten the acquisition duration. This technique will be referred to as the Non-Switching Two-Microphone Method (NS-TMM).

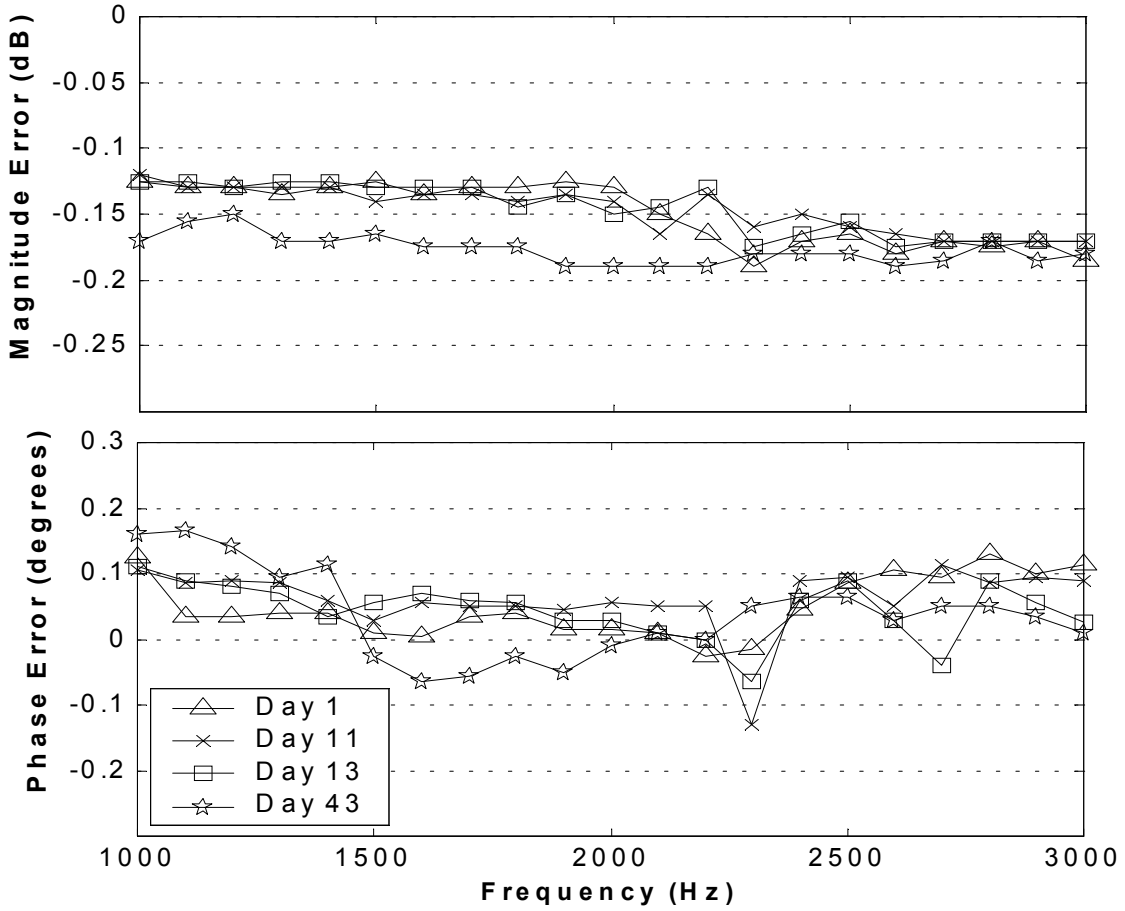

Figure 4-8. Magnitude and phase calibration constants for the non-switching method measured over a period several days to one month apart.

Proper implementation of the NS-TMM method requires accurate amplitude and phase calibration, for each microphone, across the entire frequency range of interest. To accomplish this, the plug containing two measurement microphones was rotated such that the microphones were positioned in a plane perpendicular to the duct axis. For frequencies below cut-on for the first higher order mode, measured amplitude or phase differences between the microphones are due to inherent differences between the microphones and signal conditioning. To account for these differences, the averaging process of the S-TMM method was used to acquire calibration constants at each frequency. These calibration constants were then used in the NS-TMM impedance determination method.

Figure 4-8 depicts the variability of the calibrations over an extended period of time. The magnitude calibration constants vary little from day to day, but over the course of the test there was a variability of approximately 0.1 dB. The phase calibration constants have somewhat more variability (approximately 0.3 degrees). Thus, for improved quality, calibration constants were acquired daily for the experimental database presented here.

Figure 4-9 shows a comparison of results acquired with the NS-TMM and S-TMM methods for a typical perforate liner. The results are almost identical. In fact, repeatability tests to be discussed later demonstrate more variability than shown here. Thus, the NS-TMM was determined to be acceptable for the current tests.

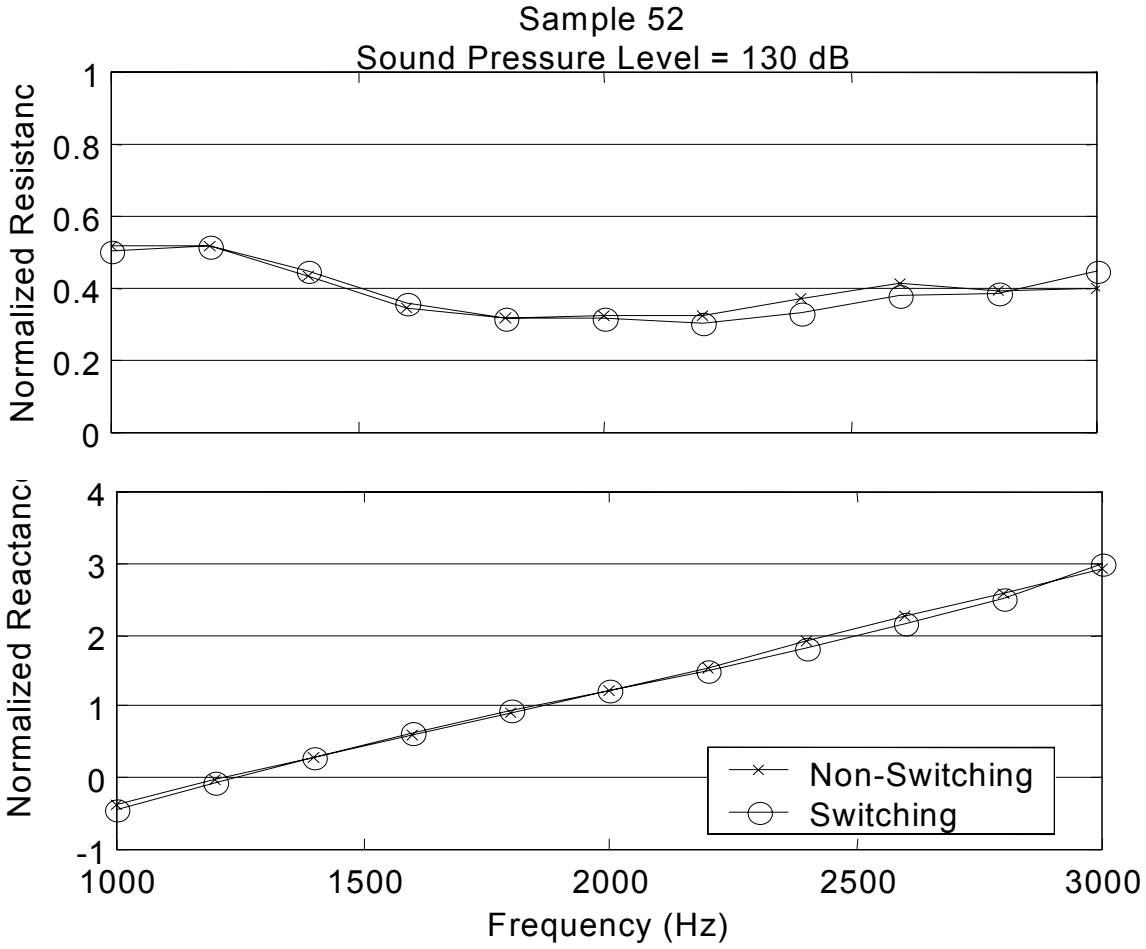

Figure 4-9. Sample impedance data comparing NS-TMM and S-TMM.

4.5 High Resistance Fibermetal

For the purposes of this study, it was important to design the experiment such that the bias flow effect on perforate samples could be analyzed with locally-reacting acoustic liner models. To achieve this, one of the key elements of the bias flow liner is the termination at the back of the cavity. For passive liners, the termination face for the acoustic wave in the cavity is a highly reflective surface. To add bias flow, this termination must be permeable while maintaining high reflectivity. A high resistance fibermetal was chosen to achieve this condition. Fibermetal is a dense mesh of metallic strands pressed and bonded together.

Premo[2] also used this approach, specifically applying a backing sheet with a nominal flow resistance of 190 cgs Rayls at 105 cm/s. There was no mention of whether this value was verified; however, his results showed 0.3ρc resistance difference from the hardwall measurement, which indicated the backing layer resistance, was not large enough to adequately simulate a hardwall.

Four different methods were used to evaluate the high resistance fibermetal sheet used in this experiment. In most acoustic liner models, the flow resistance (sometimes referred to as the direct current, or DC, flow resistance) is assumed to be equal to the acoustic resistance at low frequencies. As described below, the first three methods determine the acoustic resistance using complex acoustic pressure measurements in the normal incidence impedance tube. Of these, the first is an indirect method, which requires that the acoustic resistance be educed from measurements of multiple configurations. The other two methods allow the acoustic resistance to be determined directly. The last method uses a raylometer to measure the flow resistance. Appendix E contains a description of the methods.

The measured flow resistance of the fibermetal using the raylometer was 1200 cgs Rayls at 105 cm/s. This is much larger than the manufacturer's quoted value of 550 cgs Rayls. It is also substantially larger than 190 cgs Rayls, which was the flow resistance of the material used by Premo in a similar test.

The acoustic impedance measurements of the fibermetal consistently showed the acoustic resistance to be around 20 ρc. Thus, it was expected to provide sufficiently high acoustic reflection to simulate a rigid termination. Figure 4-10 shows the acoustic

resistance measured for a selected sample liner (Sample 43) with the high resistance fibermetal termination versus that measured with a hardwall (highly reflecting) termination. The high resistance fibermetal termination causes the acoustic resistance to be slightly higher in magnitude (~0.05 ρc) than that with the hardwall termination. This is significantly lower than the 0.3 ρc error observed by Premo. The measured acoustic reactance (not shown) of the sample liner was unchanged for each type of termination.

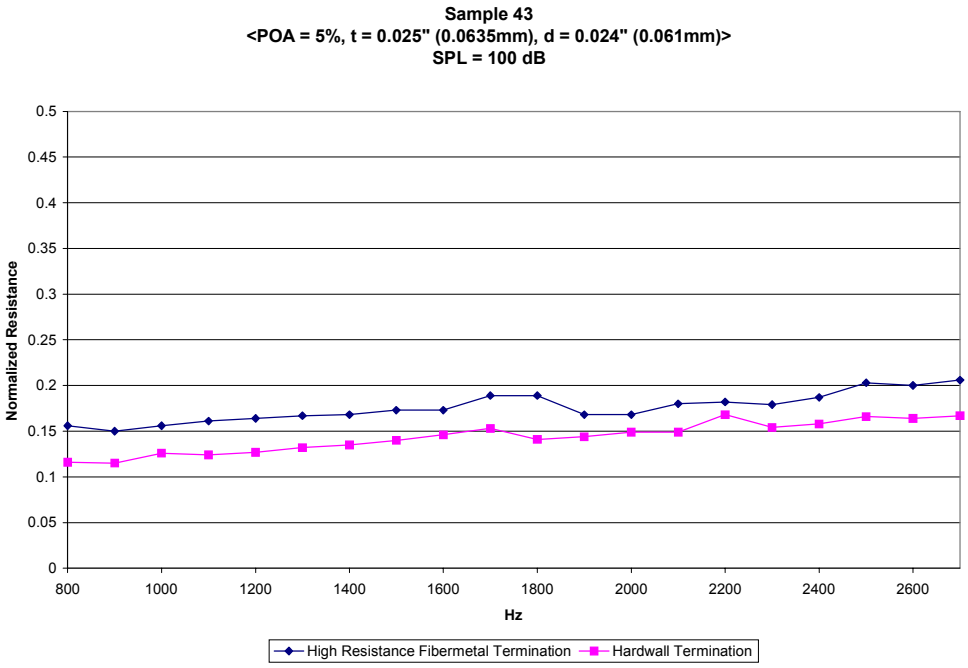

Figure 4-10. Measured difference between the hardwall termination and the high resistance fibermetal termination.

4.6 C_D determination

One parameter that plays an important role in all of the prediction models is the discharge coefficient, C_D. The discharge coefficient is defined as the product of the coefficient of contraction and the coefficient of velocity. The coefficient of contraction is

the ratio of the area of the vena contracta to the orifice area. The coefficient of velocity is the ratio of the ideal to the actual velocity of the vena contracta. The vena contracta is the minimum flow area of a jet formed by contraction of the streamlines at the point where streamlines become parallel.

The discharge coefficient can be determined by measurements of the flow resistance of a perforate sample compared with the flow velocity through it. The main device for measuring flow resistance vs. velocity is a raylometer (See Fig. 4-11). The pressure change caused by the sample is measured and plotted vs. the measured flow rate.

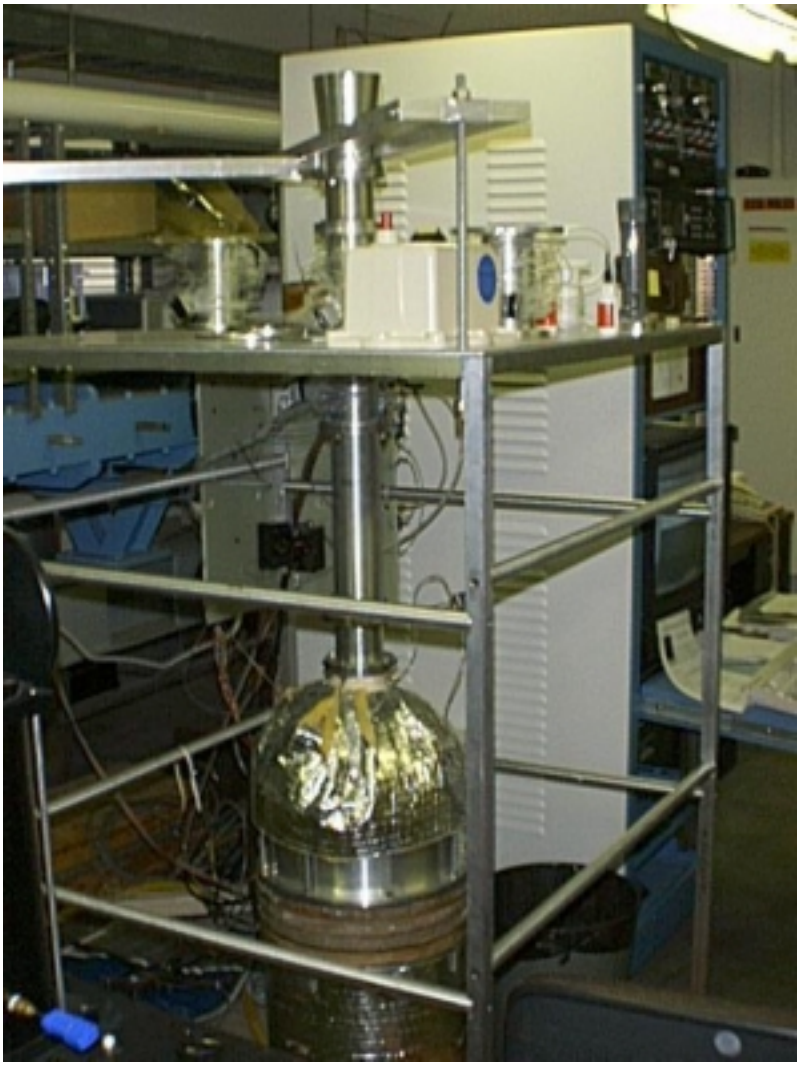

Figure 4-11. Picture of FITF Raylometer.

To determine the best discharge coefficient that fits the raylometer data a least squares error minimization can be applied. This least squares minimization is between the resistance measurements and the particular model. Let y_i and v_i be a set of resistance and velocity values measured by the raylometer denoted by the subscript i. Furthermore, let ϕ_i be our predicted resistance model at the same point. The GE resistance model (Eq. (2-1)) without grazing flow in cgs units becomes

$$\phi_i = v_i \frac{\rho}{2000\sigma^2 C_D^2} + \frac{3.2\mu t}{\sigma d^2 C_D} \tag{4-5}$$

where μ, ρ, σ, and C_D, are the viscosity, density, percent open area, and discharge coefficient, respectfully. Equation (4-5) can be rewritten in the following form

$$\phi_i = v_i \frac{c_2}{C_D^2} + \frac{c_1}{C_D} \tag{4-6}$$

where c_1 and c_2 are defined as

$$\begin{aligned} c_1 &= \frac{3.2\mu t}{\sigma d^2} \\ c_2 &= \frac{\rho}{2000\sigma^2} \end{aligned} \tag{4-7}$$

The square of the errors in resistance between the GE model and each measured resistance e_i is

$$e_i = (y_i - \phi_i)^2 \tag{4-8}$$

The sum of all these errors is given by

$$\sum_i e_i = \sum_i (y_i - \phi_i)^2 = \sum_i \left[y_i - \left(v_i \frac{c_2}{C_D^2} + \frac{c_1}{C_D} \right) \right]^2 \qquad (4\text{-}9)$$

In order to find the discharge coefficient that minimizes these errors, the derivative with respect to C_D in Eq. (4-9) must be set to zero which produces

$$\frac{d\sum_i e_i}{dC_D} = \sum_i \frac{2(c_1 C_D + 2C_D v_i)(C_D^2 y_i - c_1 C_D - c_2 v_i)}{C_D^5} = 0 \qquad (4\text{-}10)$$

Rearranging Eq. (4-20) yields

$$2c_1\left(\sum_i y_i\right)C_D^3 + 2\left(2c_2\left(\sum_i v_i y_i\right) - c_1^2\right)C_D^2 - 6c_1c_2\left(\sum_i v_i\right)C_D - 4c_2^2\left(\sum_i v_i^2\right) = 0 \quad (4\text{-}11)$$

Solving for the roots of this equation and making sure the second derivative of Eq. (4-10) is positive, produces the optimal value of the discharge coefficient that will satisfy the GE model for a set of experimental raylometer results.

The GE model in Eq. (4-5) is a good approximation if the density within the holes does not change very much. A more refined approximation takes into account the density changes due to pressure and temperature. For dry air assuming an ideal gas the density is related to the pressure and temperature through the following relationship[8]

$$\rho = 24.0213\frac{b}{T} \qquad (4\text{-}12)$$

where ρ, b, and T are the density, pressure and absolute temperature respectively. The units of ρ, b, and T are kilograms per cubic meter, psi, and Kelvins respectively. If Pascal instead of psi units for the pressure is used, then Eq. (4-12) becomes

$$\rho = 0.003484\frac{b}{T} \tag{4-13}$$

Inserting Eq. (4-12) into Eq. (4-5) produces

$$\phi_i = v_i \frac{24.0213 b_i}{2000 T \sigma^2 C_D^2} + \frac{3.2\mu t}{\sigma d^2 C_D} \tag{4-14}$$

where the fluid (air) is assumed to have constant temperature. Equation (4-14) can be rewritten as

$$\phi_i = v_i b_i \frac{c_2}{C_D^2} + \frac{c_1}{C_D} \tag{4-15}$$

where c_1 and c_2 now are given by

$$\begin{aligned} c_1 &= \frac{3.2\mu t}{\sigma d^2} \\ c_2 &= \frac{24.0213}{2000 T \sigma^2} \end{aligned} \tag{4-16}$$

Assuming the error e_i to be Eq. (4-8) and following the same optimization procedure outlined in Eqs. (4-9) through (4-11) yields the root equation

$$2c_1\left(\sum_i y_i\right)C_D^3 + 2\left(2c_2\left(\sum_i b_i v_i y_i\right) - c_1^2\right)C_D^2 - 6c_1c_2\left(\sum_i b_i v_i\right)C_D - 4c_2^2\left(\sum_i b_i^2 v_i^2\right) = 0 \tag{4-17}$$

Solving for the roots of this equation and making sure the second derivative of the equivalent of Eq. (4-10) is positive, produces the optimal value of the discharge coefficient that will satisfy the GE model for a set of experimental raylometer results assuming varying density.

References

1. Jones, M. and Stiede, P., "Comparison of Methods for Determining Specific Acoustic Impedance," Journal of the Acoustical Society of America, 101(5), May 1997, pp. 2694-2704
2. Jones, M.G. and Parrott, T.L., "Evaluation of a Multi-point Method for Determining Acoustic Impedance", *Mechanical Systems and Signal Processing*, 3(1), 1989, pp. 15-35.
3. Jones, M.G., and Steide, P.E., "Comparison of Methods for Determining Specific Acoustic Impedance", *J. Acoust. Soc. Am.* (5), Pt.1, May 1997.
4. Melling, T.H., "The Acoustic Impedance of Perforates at Medium and High Sound Pressure Levels", *J. Sound and Vibration.* (29), Pt.1, 1973.
5. Doebelin, E.O., *Measurement Systems: Application and Design*, McGraw-Hill, Inc., New York, 1990.
6. Chung, J.Y., and Blaser, D.A., "Transfer Function Method Of Measuring In-Duct Acoustic Properties: II. Experiment", *J. Acoust. Soc. Am.* (68), Pt.3, 1980.
7. Seybert, A.F., and Ross, D.F., "Experimental Determination Of Acoustic Properties Using A Two-Microphone Random-Excitation Technique", *J. Acoust. Soc. Am.* (61), Pt.5, 1977.
8. Avallone, E. and Baumeister, T., Marks Standard Handbook For Mechanical Engineers, McGraw-Hill, New York, 1996.

5. No Bias Flow Models Impedance Results

Figure 5-1 shows the experimental vs. the PBFIF (GE-Rohr) model impedance results for a representative sample with no flow. ***When there is no flow, the GE-Rohr model and the PBFIF model are the same model***. The numerical results approach the experimental results as the sound pressure level is increased in both the resistance and reactance. The mean slope and correlation error criteria for both the resistance and reactance show continuous improvements as the sound pressure level is increased (see Figs. 5-2 and 5-3). This indicates that the nonlinear term in the PBFIF model, which is associated with the acoustic particle velocity, better models the experiments than the linear component of this model.

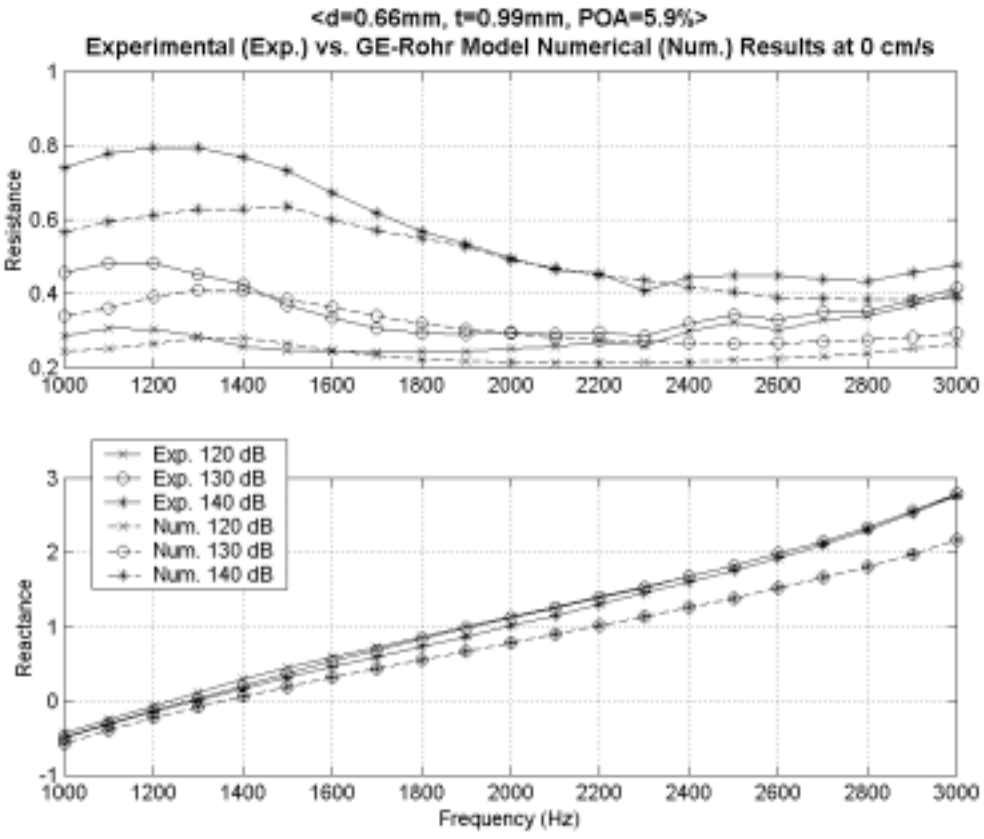

Figure 5-1. Experimental impedance vs. PBFIF (GE-Rohr) model numerical predictions for a sample with POA=5.9.

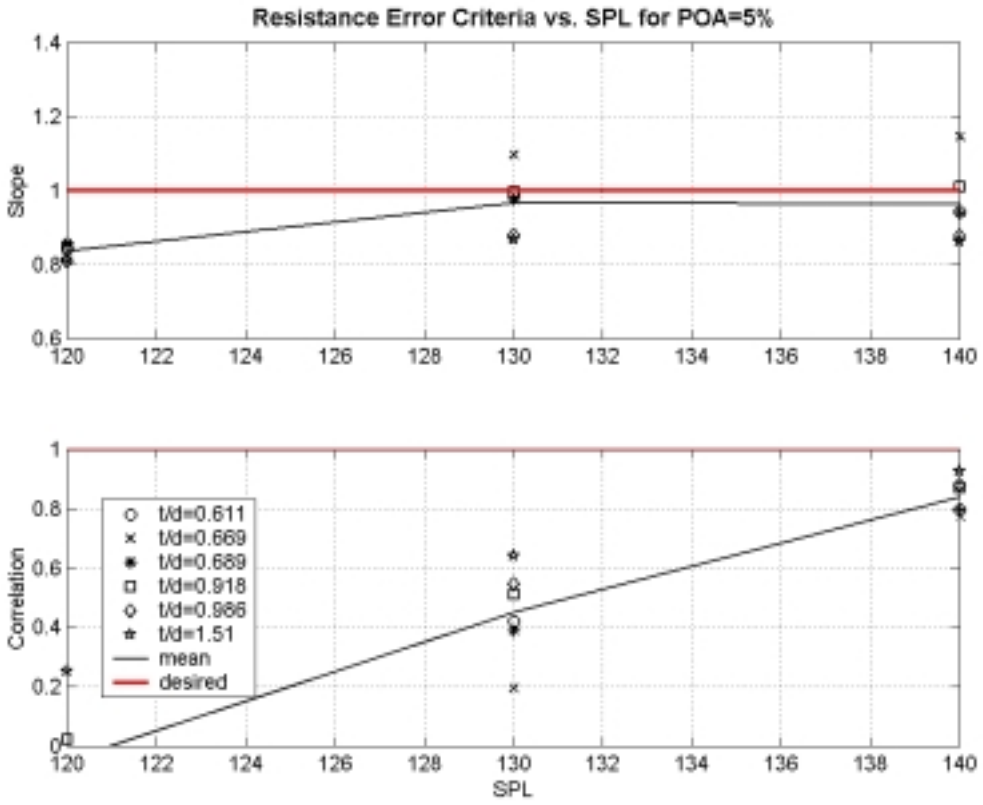

Figure 5-2. PBFIF model resistance error criteria for POA=5.

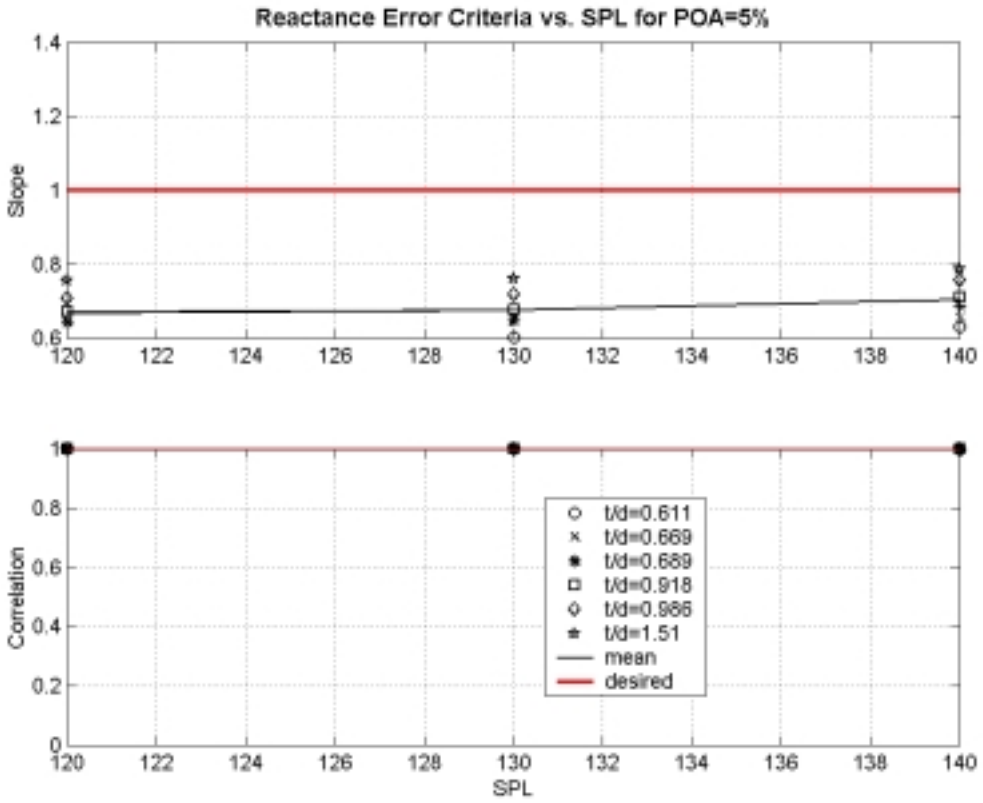

Figure 5-3. PBFIF model reactance error criteria for POA=5.

For the resistance (see Fig. 5-2), the mean slope error criteria starts at about 0.8 and increases to nearly one with increasing SPL. The mean correlation starts at nearly zero at 120 dB and continually increases up to about 0.85 at 140 dB. The spread of the slope error criteria with respect to the various t/d's increases from nearly zero at 120 dB to within 15% at 140 dB. For the reactance (see Fig. 5-3), the mean slope error criteria stays relatively constant at about 0.7 for all SPLs and the spread with respect to t/d is about 5%. The correlation is nearly equal to one for all SPLs with no spread in the data with respect to t/d.

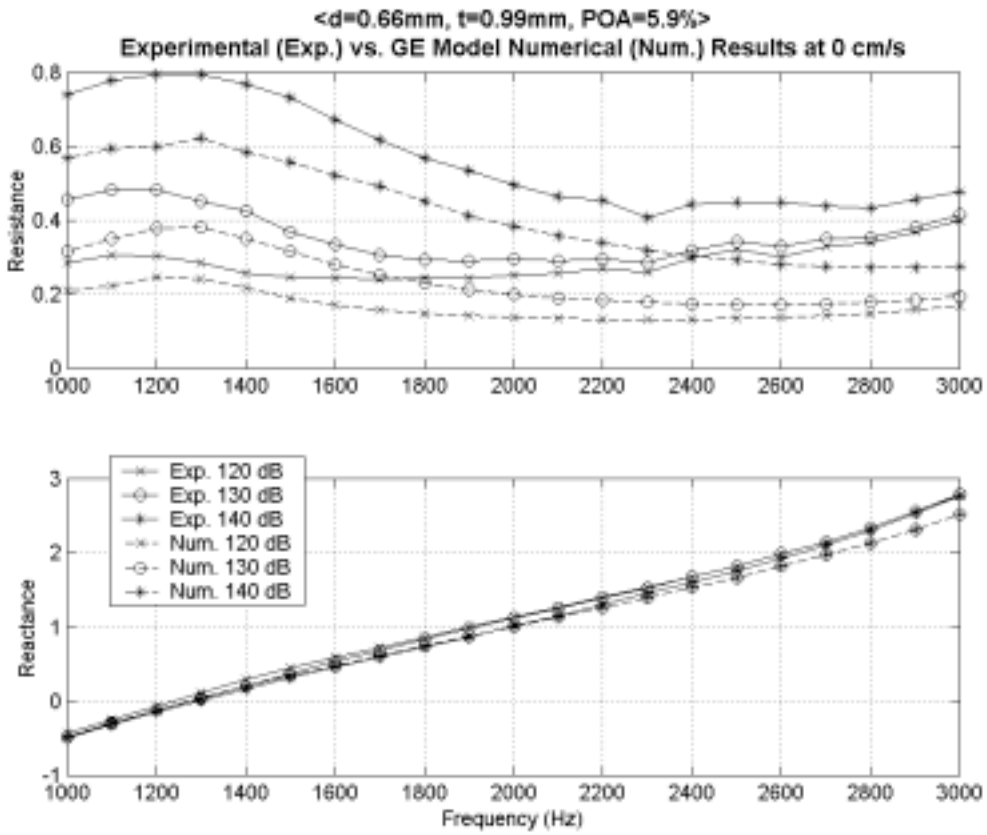

Figure 5-4. Experimental vs. GE model numerical impedance predictions for a sample with POA=5.92.

Figure 5-4 shows the experimental vs. the GE model impedance results for a representative sample with no flow. Both the GE and PBFIF model numerical results approach the experimental results as the sound pressure level is increased in both the resistance and reactance. For the resistance (see Fig. 5-5), the mean slope and correlation error criteria for both the resistance and reactance show continuous improvements as the sound pressure level is increased. The slope error criterion starts at about 0.6 for 120 dB and increases to about 0.8 at 140 dB. Comparing this result to that of the PBFIF model, indicates that the PBFIF model is about 20% better at predicting the experimental results with a mean slope error criteria of about 1 for the PBFIF model vs. 0.8 for the GE model at the higher SPL's.

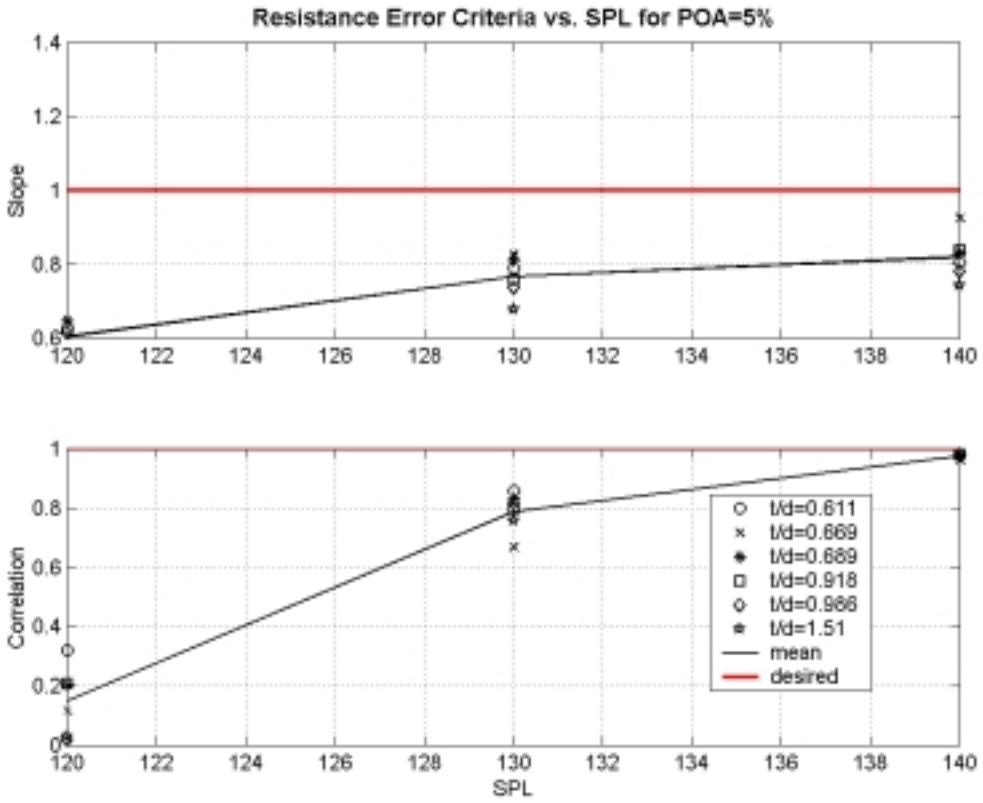

Figure 5-5. GE model resistance error criteria for POA=5.

The reactance for the GE model numerical impedance predictions (see Fig. 5-6) fares better than the PBFIF model with a slope error criteria of nearly 1 vs. 0.7 for all SPLs. It is important to note that for both the GE and PBFIF models the reactance prediction is the sum of the perforate and cavity reactance. Consequently, since the cavity reactance is much larger in magnitude than that of the perforate, the reactance prediction is in large part due to the ability of the transmission matrices in ZKTL to model the cavity.

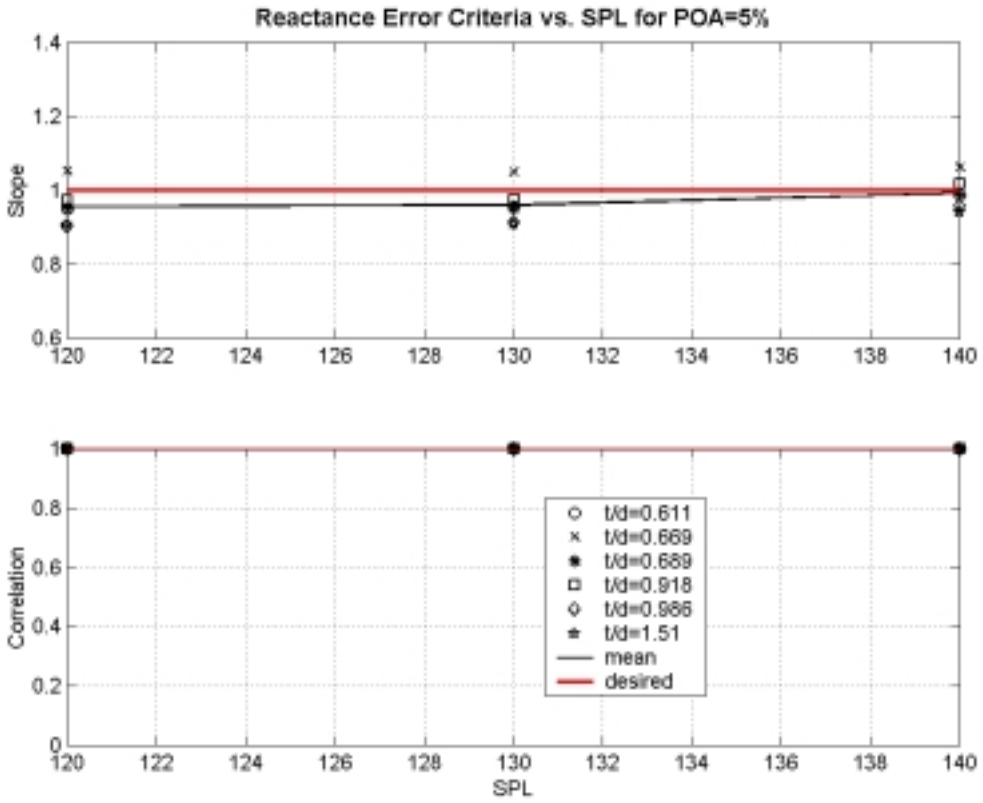

Figure 5-6. GE model reactance error criteria for POA=5.

The next couple of figures are impedance contour plots of t/d vs. frequency at various percent open areas. It is important to note that each t/d point in the t/d-frequency plane is a sample. Each of these samples had specified geometrical parameters such as percent open area. Nevertheless, each of these geometrical parameters varied because the specified and actual geometrical parameters were not the same. Besides percent open area the, C_D also varies from sample to sample because a single C_D is calculated for each sample and these values are given in Appendix G. Therefore it is important to recognize that as t/d increases other geometrical parameters also vary, because of manufacturing tolerances.

Another word of caution, realize that t/d is the part of the second nondimensional group in the PBFIF model (see Section 3.1). These contour plots are provided to evaluate how the experimental and model impedance trends against this nondimensional group. It is important to realize that these groups in the model are not independent of each other.

For example, in the PBFIF model varying t/d affect groups one, two, four, and five (see Section 3.1). For more information on this topic see Appendix B.

Figure 5-7 is the impedance contour plot of t/d vs. frequency at 10% percent open area with no bias flow for the experiment. This figure shows how changes in t/d and sound pressure level, respectively affect the impedance. At low sound pressure levels changes in the resistance seem to be dominated more by changes in t/d rather than frequency, except at the high end of the frequency range. As the sound pressure is increased the opposite effect occurs. The resistance is now more affected by changes in frequency than t/d.

These effects were expected. At low sound pressure levels the impedance is dominated by the linear component of the resistance, which is a function of t/d. As the sound pressure level rises, the impedance becomes dominated by the nonlinear component of the resistance. Since the acoustic particle velocity is a function of frequency, the resistance becomes more dependent on frequency changes.

This figure also shows two distinctive regions of high resistance, at around 1400 and 3000 Hz, as sound pressure level is increased. The reactance for all three sound pressure levels is increasing as a function of frequency, yet it is relatively constant as a function of t/d. This effect is due to the cavity reactance, whose resonance and anti-resonance occur at 2000 and 4000 Hz, respectively.

Figure 5-8 is the GE model impedance contour plot of t/d vs. frequency at 10% percent open area with no bias flow. This model tends to predict similar iso-resistance shapes when compared to the experimental results for the lower frequency range. It also under-predicts the magnitude of the resistance for the entire frequency range, but the problem seems to be worse at the higher end of the frequency range. As the sound pressure level is increased, this trend seems to stay fairly constant.

For middle and higher frequency ranges, the impedance is not predicted well. The model simply predicts a low resistance value through the entire region independent of frequency or t/d. The reactance, in contrast, is predicted fairly well for the entire frequency range.

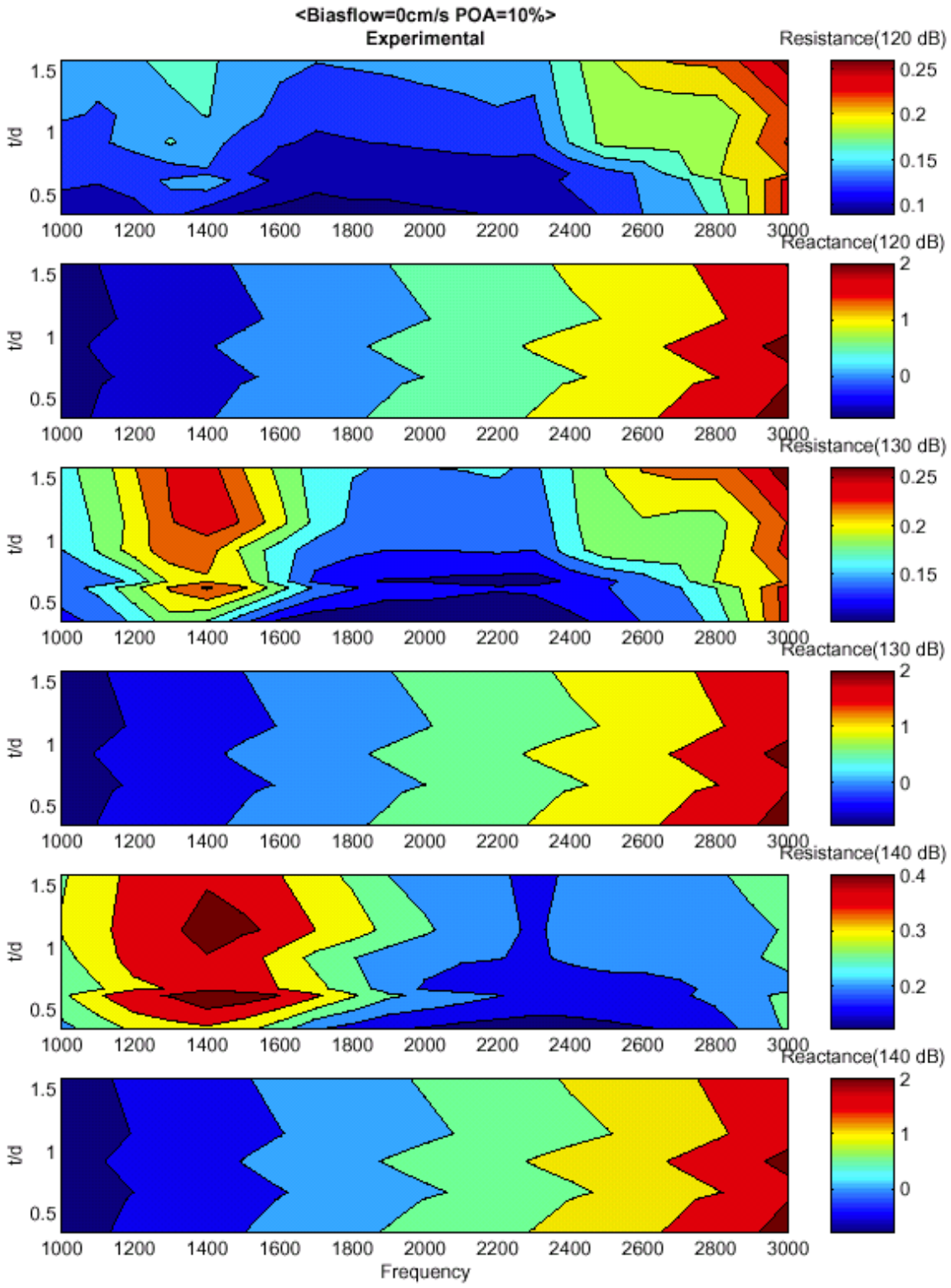

Figure 5-7. Experimental impedance contour plot.

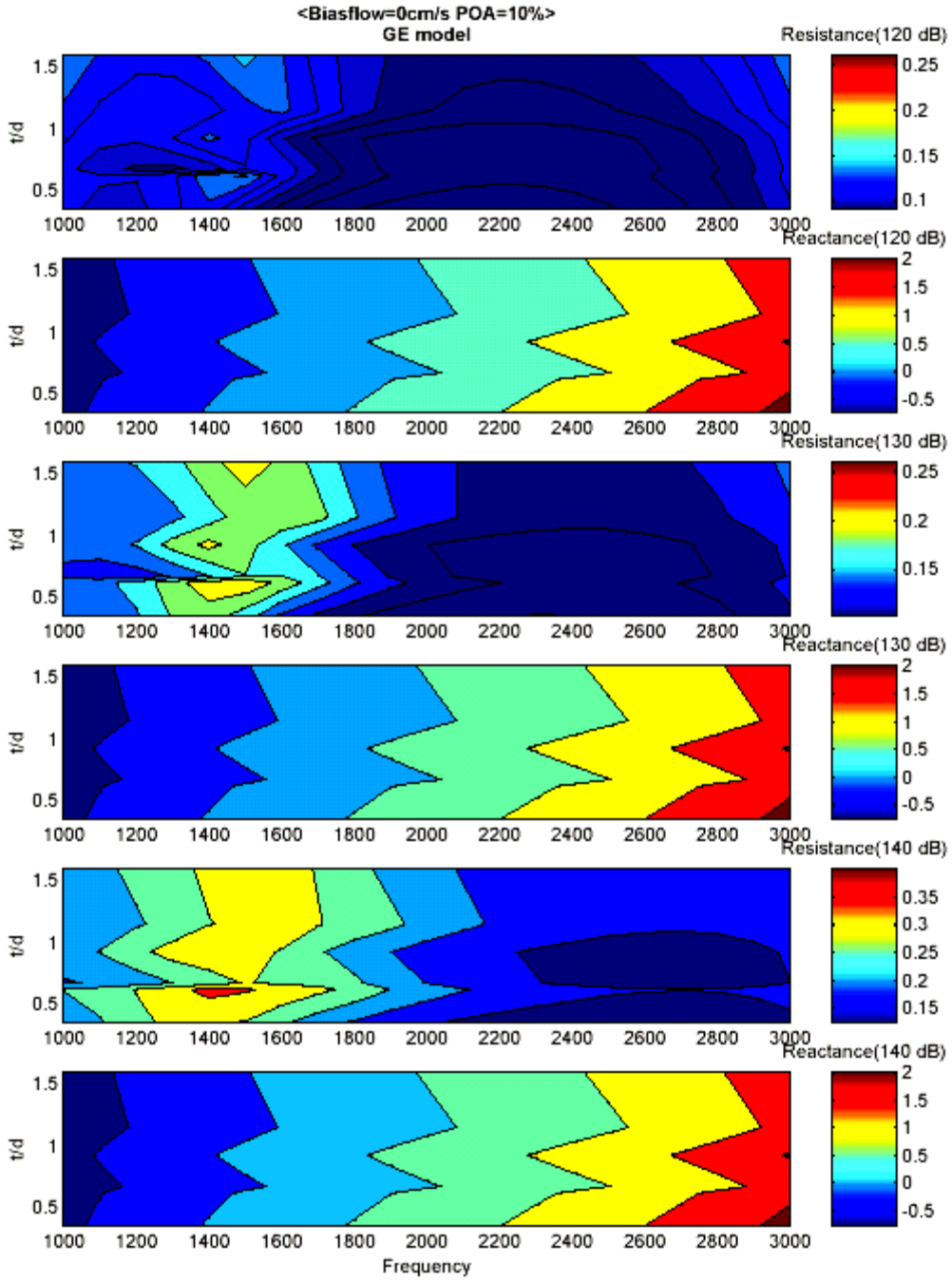

Figure 5-8. GE impedance contour plot.

These results were expected, since the resistance in the GE model was derived assuming DC or Poiseuille flow (zero frequency) through the perforate. Therefore, it is expected that the GE model would approximate the experimental results well in the lower frequency range. The higher frequency effects in the perforate's holes, which are ignored in the GE model, are lost, and consequently produce a low predicted resistance value throughout the middle and higher spectral ranges.

Figure 5-9 is the PBFIF (GE-Rohr) model impedance contour plot of t/d vs. frequency at 10% percent open area with no bias flow. The resistance predicted in this model approximates fairly well the experimental results for the low and middle frequencies for this range of t/d. This model tends to predict better the magnitude of the resistance especially at the higher frequency range than the GE model.

The reactance in the PBFIF model is in better agreement than the GE model. The PBFIF and experimental reactances are higher than that predicted by the GE model. This result was anticipated, as discussed in *section 2.1.2*, due to the effect of viscosity in the mass reactance.

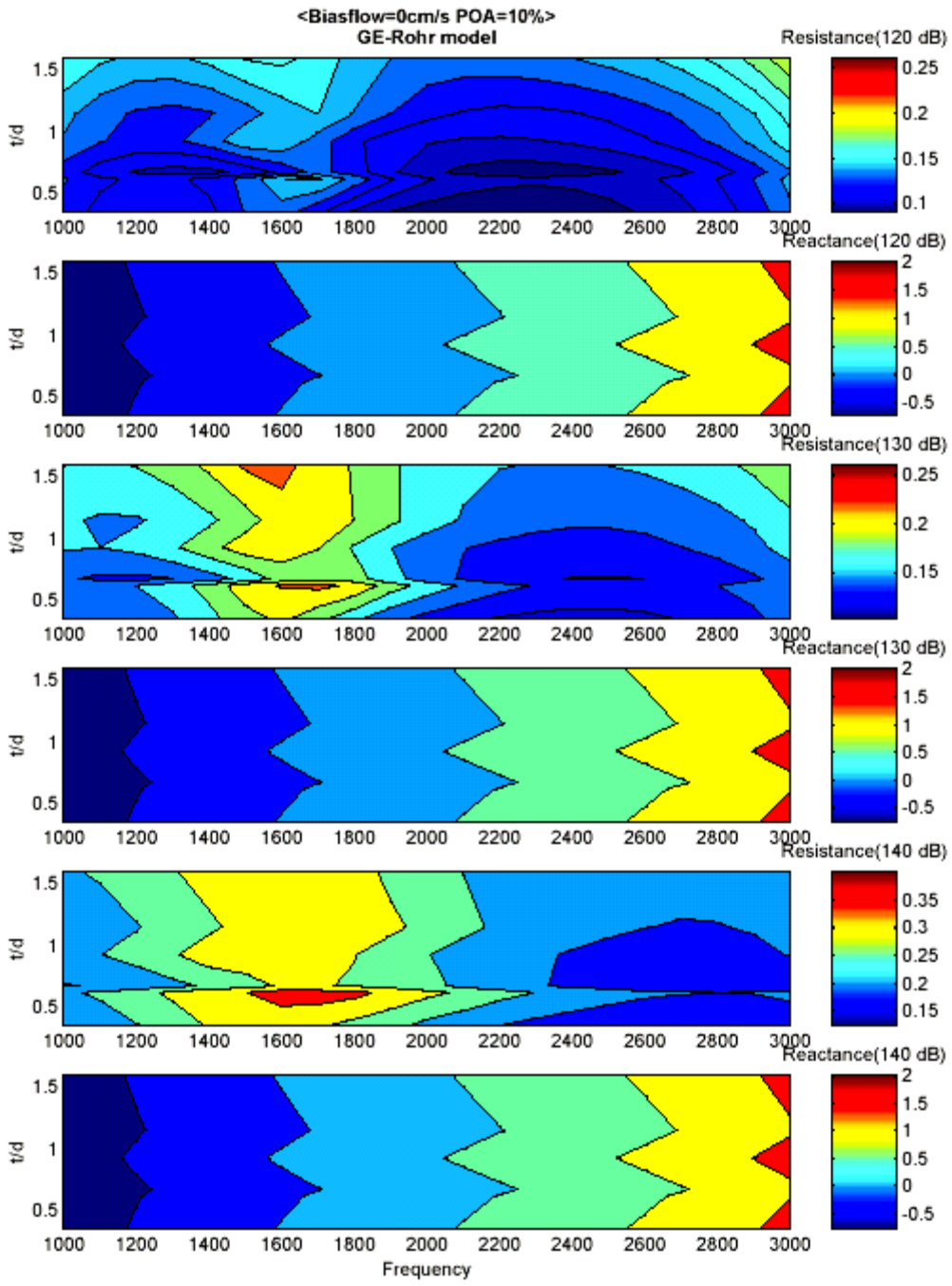

Figure 5-9. PBFIF (GE-Rohr) model impedance contour plot.

6. Incompressible Bias Flow Model Impedance Results

M_H is the effective Mach number (incompressible flow) at the perforate hole. It is defined as

$$M_H = \frac{v_{ah} + 2v_{bh}}{2c} \tag{6-1}$$

This Mach number equation is extracted from the PBFIF model's nonlinear term (Eq. (3-36)). The problem with using this equation is that the actual v_{ah} is unknown as far as the impedance models are concerned. In fact that is what the impedance models are trying to find. The experimental v_{ah} could be acquired from the experimental results and an assumed relationship between the incident and perforate hole acoustic particle velocities. Although this method would be the most accurate, a simplified approach suffices for this study.

It is of interest determine what level of bias flow is required such that changes in M_H due to SPL changes do not affect the overall acoustic impedance. Consequently, for a plane wave, the relationship between the acoustic particle velocity and pressure can be used to determine an approximate magnitude of v_{ah}. Therefore, the relationship between the acoustic particle velocity and the SPL is

$$|v_a| = \frac{P_{ref} 10^{SPL/20} \sqrt{2}}{\rho c} \tag{6-2}$$

Using the continuity principle for an incompressible fluid to relate the incident velocity and the hole velocity yields

$$|M_H| = \frac{1}{2c\sigma C_D} \left[\frac{P_{ref} 10^{SPL/20} \sqrt{2}}{\rho c} + 2v_b \right] \tag{6-3}$$

where $|M_H|$ is used to indicate the magnitude of the Mach number in the perforate.

The error criteria used for the resistance, was the slope and difference criterion, respectively. The correlation criterion was not used for the resistance, since resistance results showed little variation with respect to frequency. Remember that the correlation measures the percent change (variability) in the experiments that can be explained by the numerical results. Consequently, due to the small scale of variations, the correlation results will be of little use. The reactance, on the other hand, does have significant variation with respect to frequency, and therefore the correlation is meaningful.

The discharge coefficient used for the model predictions was measured using a raylometer and the values are provided in Appendix G using the procedure outlined in Section 4.6. A discussion on the appropriateness of this procedure for determining C_D and a sensitivity analysis is provided in Appendix F. Sample prediction results of the PBFIF model is presented in this chapter. For a complete database of including all the sample results see Appendix H.

Figure 6-1 shows a sample experimental and PBFIF model impedance at 130 dB and 5.9% POA for various bias flow velocities. The figure shows increasing resistance with increasing bias flow rates. The resistance seems to stay constant with frequency except for the high bias flow rates, where it tends to decrease with increasing frequency. The reactance increases with frequency due to the cavity reactance. The experimental reactance tends to decrease as bias flow is increased. The model was not able to account for this effect.

Figure 6-2 shows the slope and difference error criteria for the resistance for various t/d samples. The flow rates are given in cm/s and M_H (Hole Mach Number) for the NIT and hole velocities, respectively, on the x-axis. The slope error criterion shows a mean slope starting at one for no flow then decreasing to 0.7 and increasing back to 0.9 as flow rate is increased. Therefore, the resistance numerical and experimental results are staying within 30% of each other in a least squares sense.

The mean difference starts at nearly zero and increases to about one and decreases slightly after that. The maximum difference is about 2.5ρc occurring at around 300 cm/s for t/d=0.689. These errors are significant; the model's performance leaves a lot to be desired for this percent open area case.

The model underpredicts the resistances for all bias flow rates. At the higher flow rates the slope error improves because the experimental resistance decreases with increasing frequency at these flow rates (see Fig. 6-1). Since the model underpredicts the resistance, the decrease with frequency places the experimental resistance closer to the model results, and therefore decreases the measured slope error.

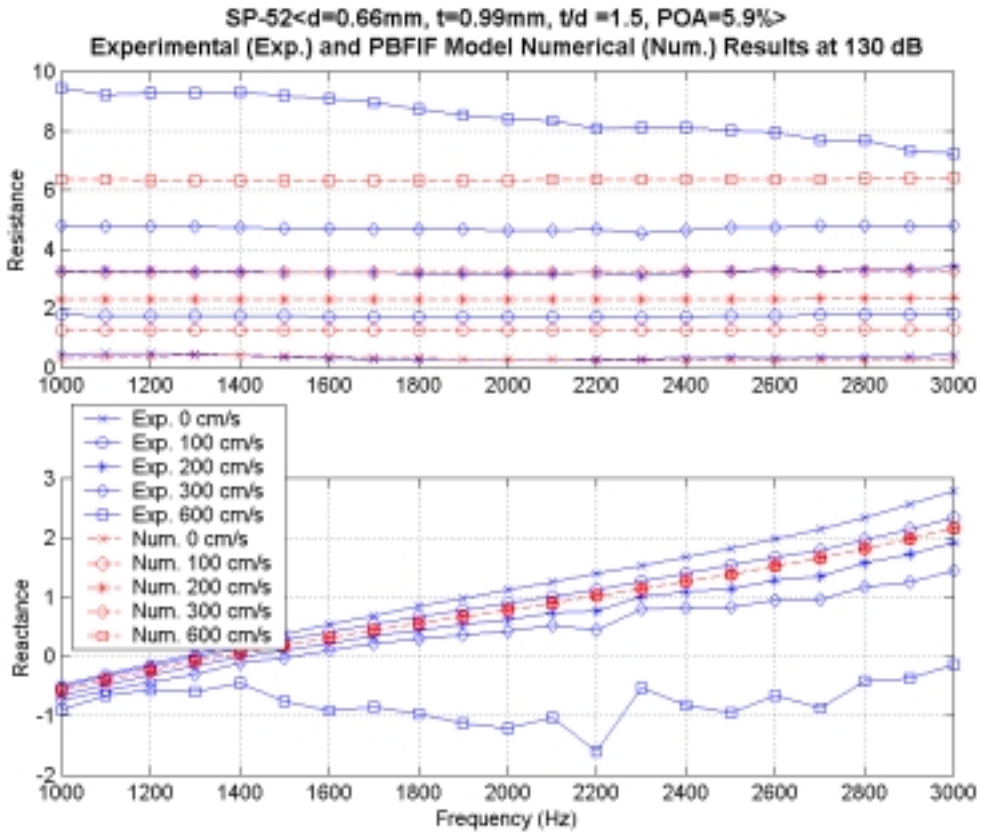

Figure 6-1. Experimental impedance and PBFIF model numerical predictions for a sample with POA=5.9.

Figure 6-3 shows the slope and correlation error criteria for the reactance of the same t/d samples. The mean reactance slope starts at 0.7, goes to 1.1, and then decreases to negative values as bias flow is increased. The mean correlation on the other hand stays close to one at the lower bias flow rates and then sharply decreases to 0.65.

Note that there is significant scatter in Figs. 6-2 and 6-3 for the various t/d samples. This scatter is low at no flow, but significant for nearly all the flow rates. This

result indicates that there is some sort of interaction between t/d and bias flow velocities not accounted for by the PBFIF model.

Jing and Sun[1] provide possible explanations for the scatter in error associated with various t/ds, and the impedance values at higher bias flow rates. They developed a model that accounted for bias flow.

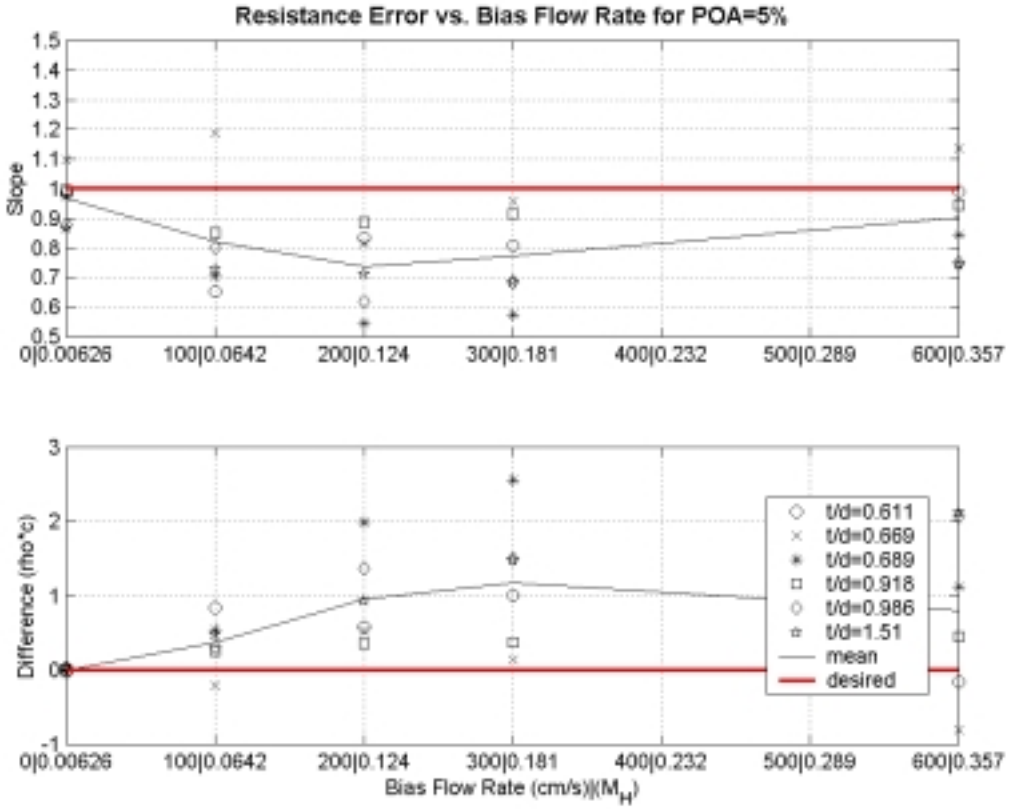

Figure 6-2. PBFIF model resistance error criteria for POA=5.

Jing and Sun[1] developed a boundary element bias flow model from Euler's Equation, where the Kutta condition was applied to generate unsteady vortices due to the bias flow. Their model showed that different t/d and hole Mach numbers had a significant impact in the resistance and reactance. Their model successfully predicted a decrease in reactance as bias flow was increased. Since the PBFIF model does not take into account vortex creation in the perforate's holes, it fails to predict the decrease in reactance, as well as some of the interaction between hole Mach number and changes in t/d. This

possibly explains the scatter seen in the error plots with t/d, which suggests that the models are not accounting for some physical phenomena associated with t/d.

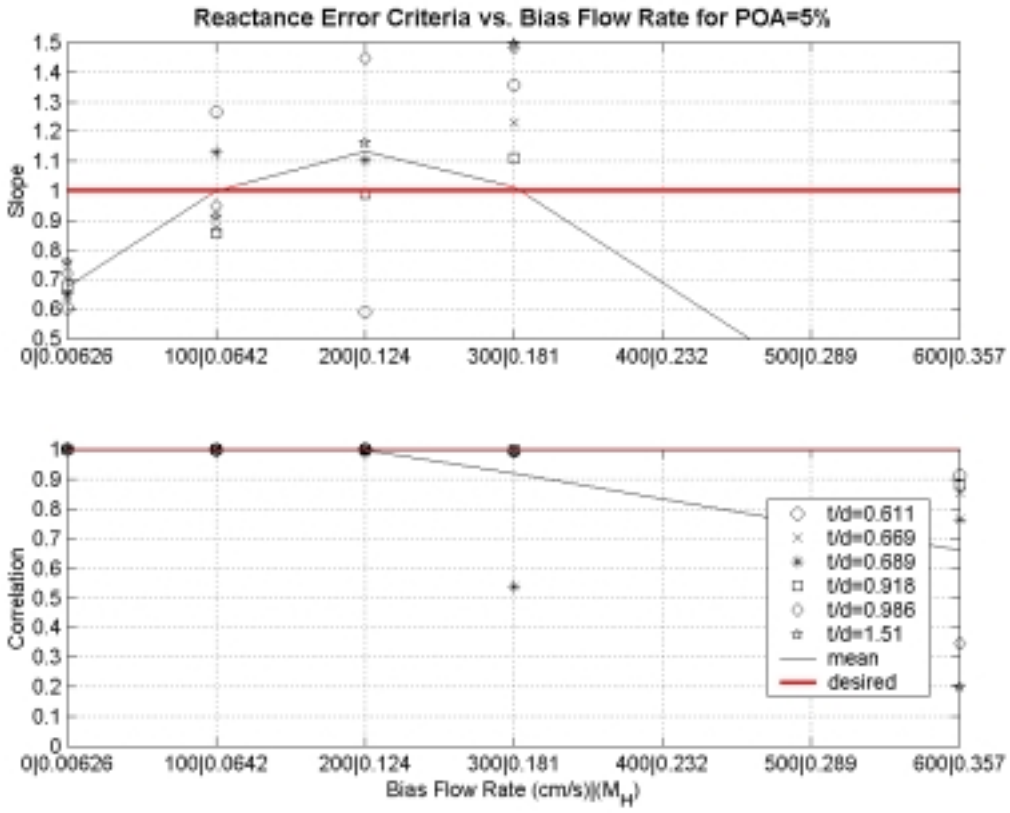

Figure 6-3. PBFIF model reactance error criteria for POA=5.

The PBFIF model improves its prediction as POA is increased. Figure 6-4 shows a sample experimental and PBFIF model impedance at 130 dB and 10.9% POA for various bias flow velocities. The figure shows the experimental and numerical results are closer at 10% than at 5% (Fig. 6-1) POA.

The error criteria for both the resistance and reactance show significant improvements as seen in Figs. 6-5 and 6-6. For the resistance, the mean slope starts at about 0.92 at zero flow, increases to about 1.18, then decreases to about 0.82. There is a general tendency of improving results as t/d is increased. This result was expected, since increasing t/d makes the modeling of perforate holes as tubes more appropriate. The difference error criteria for the resistance starts at nearly zero for no flow, and increases steadily to about 0.5ρc at 600cm/s bias flow rate. Comparing the 10% vs. the 5% POA

difference error plots; there is significant reduction in scatter due to varying t/d for the 10% POA case.

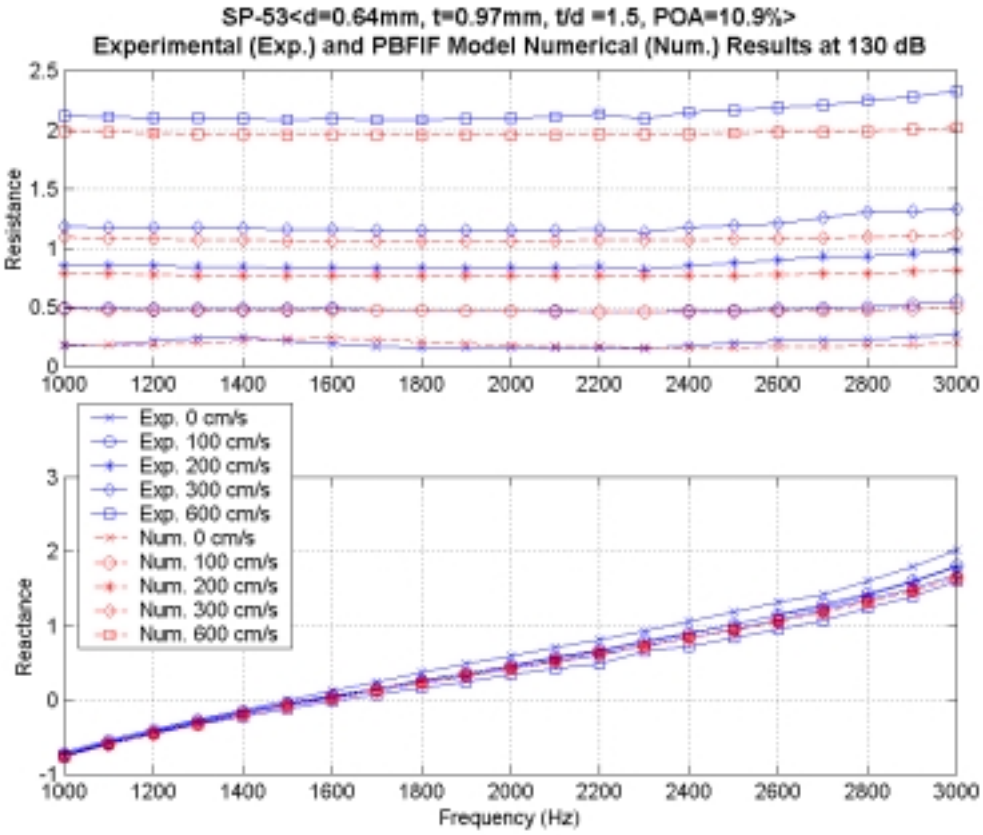

Figure 6-4. Experimental impedance and PBFIF model numerical predictions for a sample with POA=10.9

The reactance error criteria shows the mean slope starting at around 0.8 at zero bias flow rate and increasing steadily to around 1 as the bias flow rate is increased. The scatter around this mean with respect to t/d increases as bias flow is increased. Nevertheless, the same general trend exists. That is, the slope error for the resistance improves as t/d is increased. The reactance correlation also shows some slight improvement; especially at the 600cm/s bias flow rate. This result is probably due to the lower bias flow rate in the perforate hole at 10% vs. 5% POA.

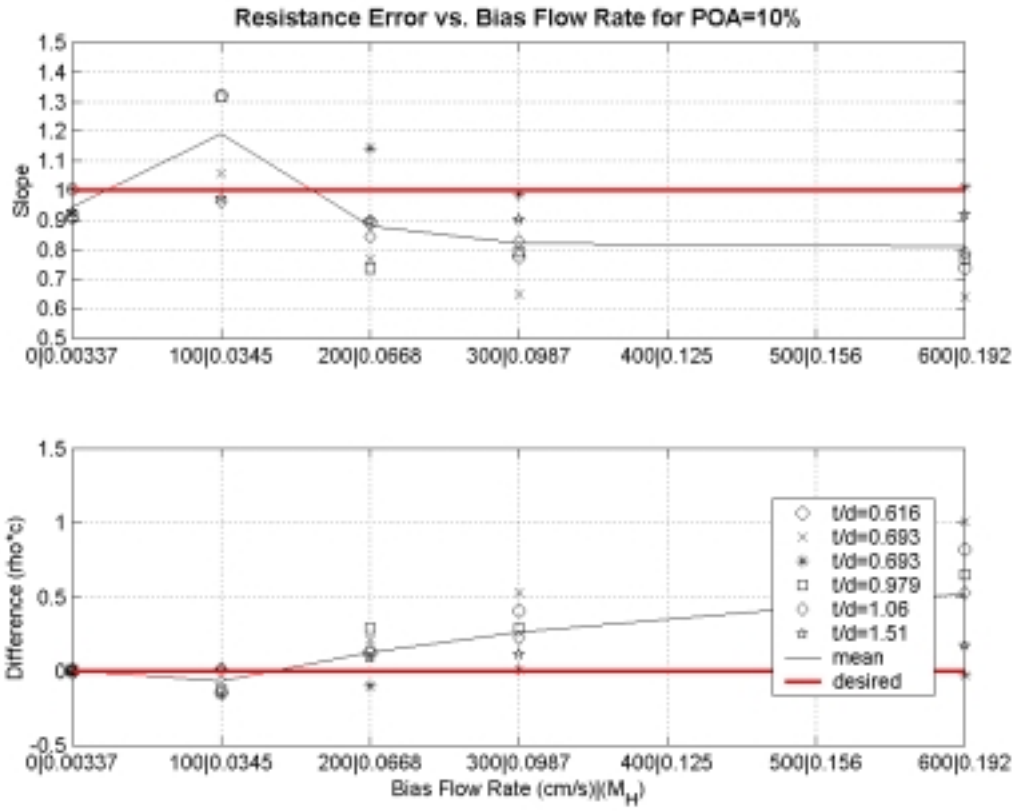

Figure 6-5. PBFIF model resistance error criteria for POA=10.

There is a possible explanation for the PBFIF model's improved performance as POA is increased. As POA is increased, the effective bias flow Mach number in the perforate hole decreases. For example, the highest Mach numbers achieved with the 15% and 5% POA samples were 0.126 (see Figs. 6-8 and 6-9) and 0.357 (See Figs. 6-2 and 6-3), respectively. The PBFIF model performs better at lower flow velocities, because the formation of unsteady vortices is a function of the fluid velocity, given constant viscosity and hole diameter. At low flow velocities, vortices are not formed, and the perforate's hole physics follow the principles outlined in the PBFIF model. As the bias flow velocity in the hole increases, unsteady vortices start forming and the assumptions and principles outlined in the PBFIF model start to break down. At higher perforate bias flow rates a model such as that outlined in Ref. 1 should be used.

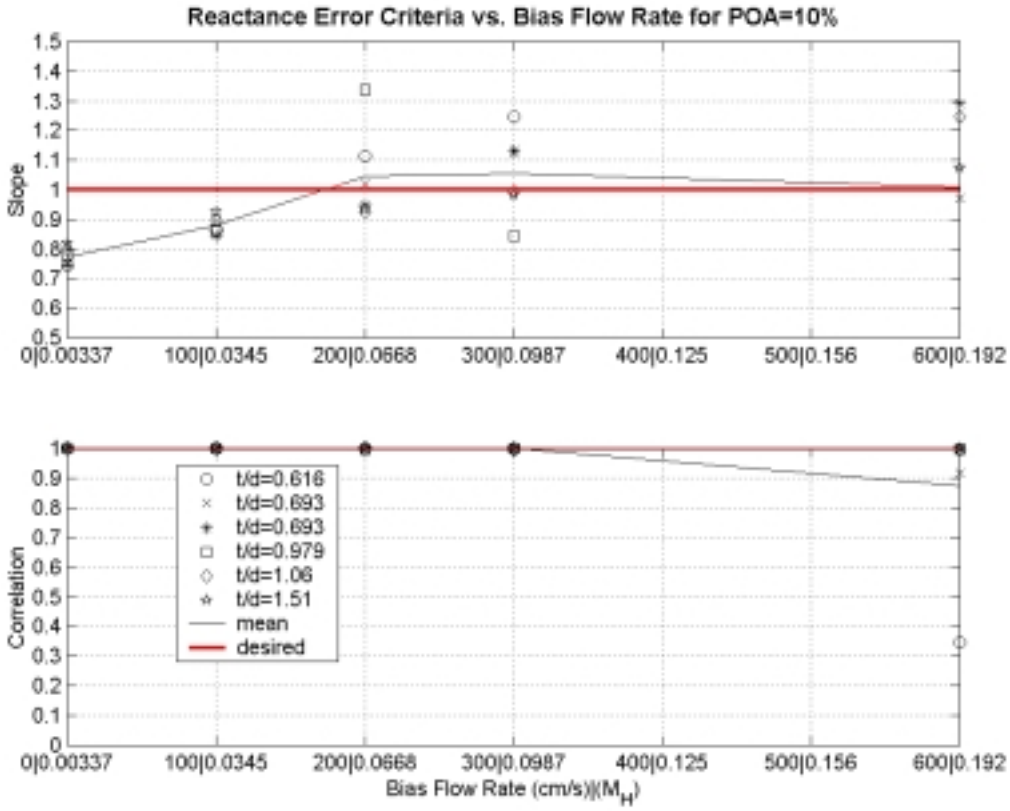

Figure 6-6. PBFIF model reactance error criteria for POA=10.

Figure 6-7 shows a sample experimental and PBFIF model impedance at 130dB and 16.5% POA for various bias flow velocities. Comparing the sample resistance impedance plots for the 10% (Fig. 6-4) and 15% (Fig. 6-7) POA samples, the results look very similar. The resistance prediction seems to do no better in approximating the experimental results. The reactance, on the other hand, does show some improvement when going from 10% to 15% POA.

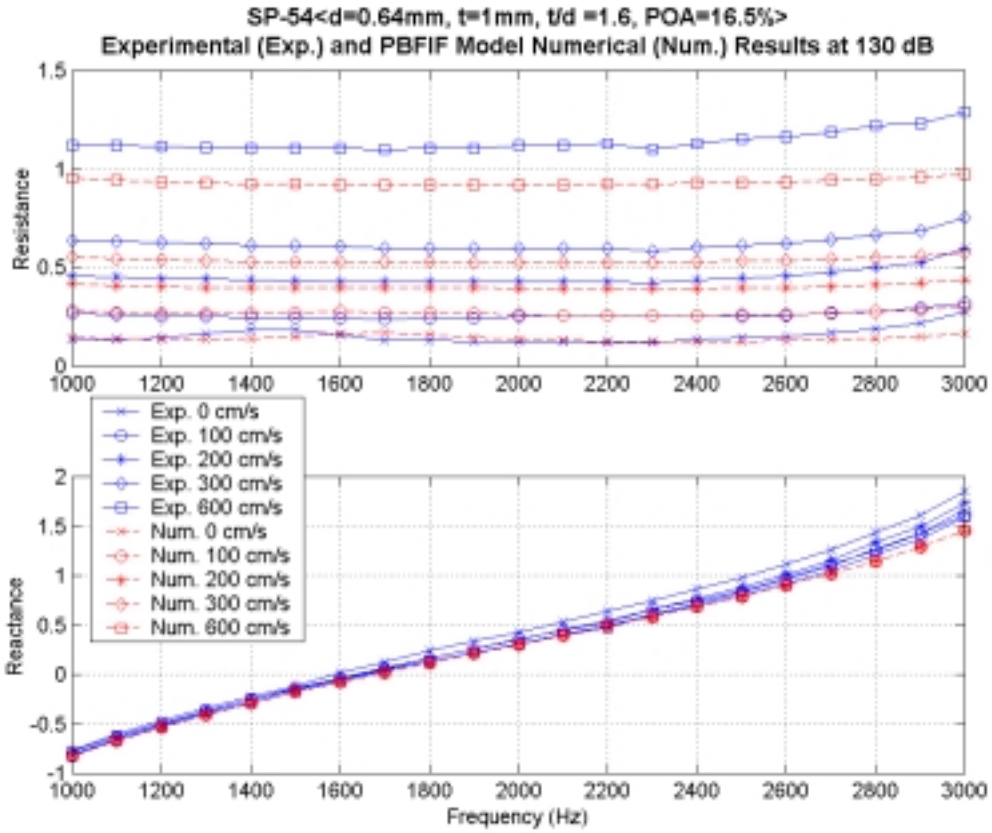

Figure 6-7. Experimental impedance and PBFIF model numerical predictions for a sample with POA=16.5%.

The error criteria plot for the 15% POA samples confirms the visual trend comparison between the experimental and predicted results. Figure 6-8 shows the resistance error criteria for various t/d samples and bias flow rates. The mean slope criteria starts at around 0.9 at zero flow, increases to 1.2 as bias flow is increased, and decreases to 0.8 as bias flow is increased further. On average the numerical and experimental results stay within 20% of each other in a least squares sense. This trend is very similar to the 10% POA samples resistance slope error criteria. The resistance difference error criteria for the 15% POA samples starts at nearly zero at no bias flow and increases to about 0.3ρc at 600cm/s bias flow rate. This result is slightly lower than the 10% POA resistance error difference. The spread in difference error with respect to different t/d is also larger at 10% than at 15% POA.

The reactance slope criteria for the 15% POA samples starts around 0.8 and steadily increases to one, indicating that the reactance curves are within 20% of the experiments in a least squares sense. The reactance correlation is about one for all flow rates indicating a nearly perfect correlation between the experimental and numerical results.

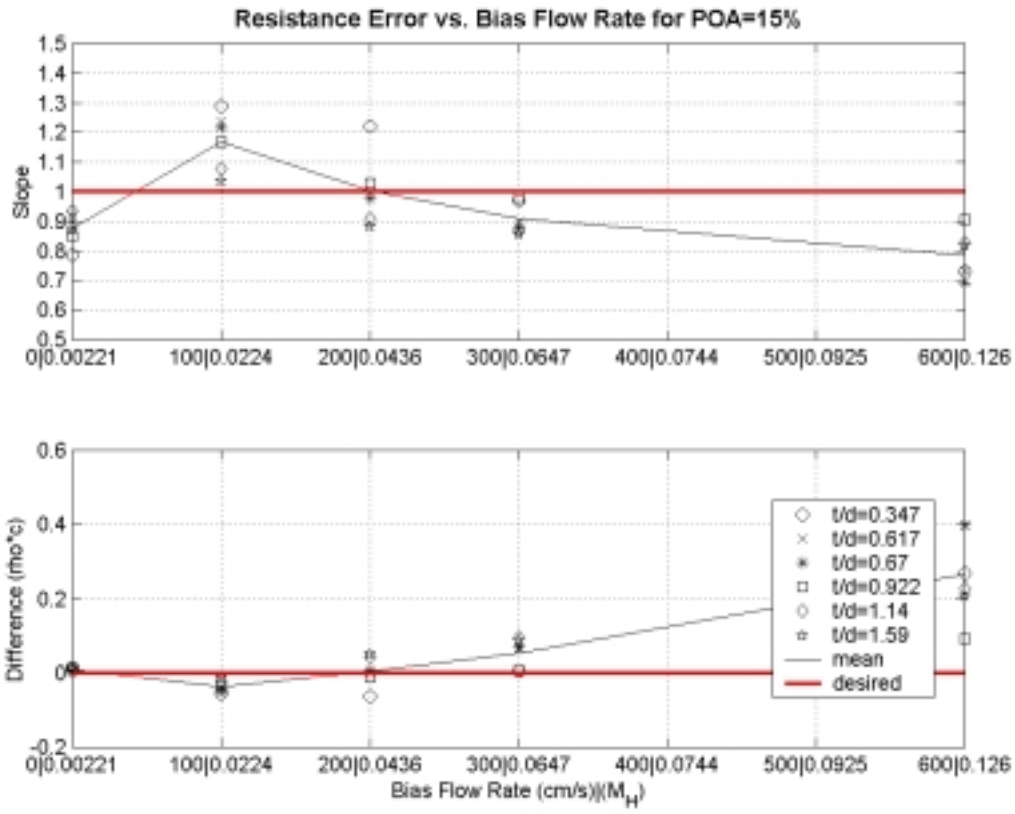

Figure 6-8. PBFIF model resistance error criteria for POA=15.

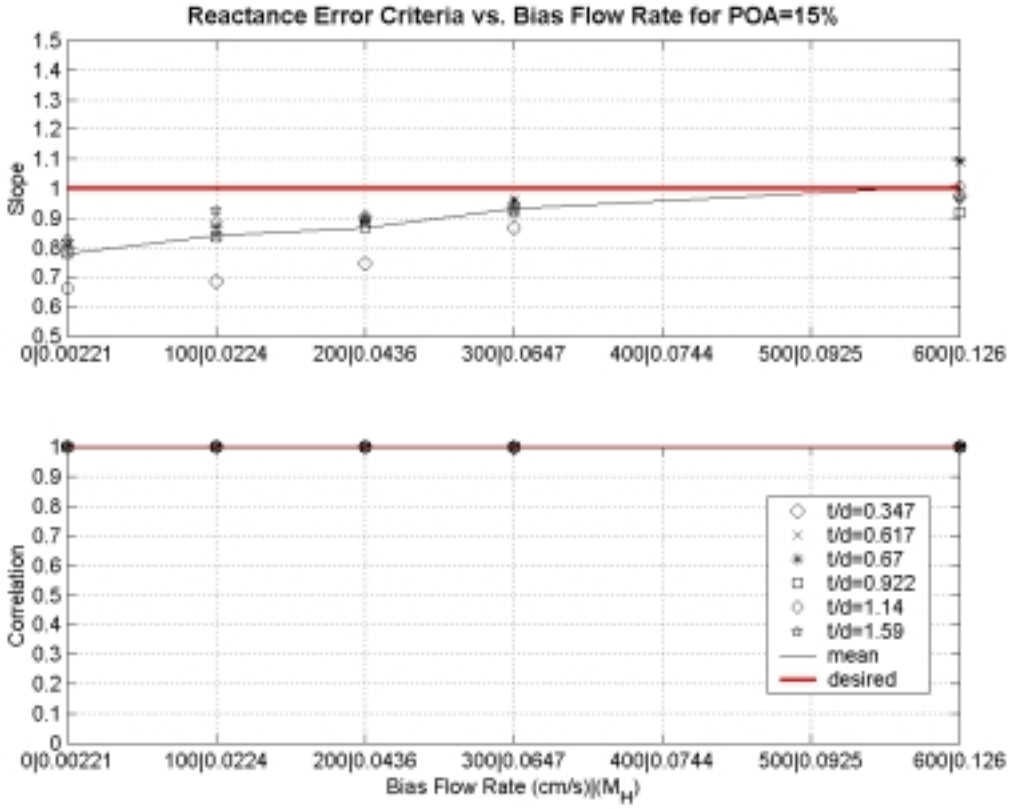

Figure 6-9. PBFIF model reactance error criteria for POA=15.

The next couple of figures are impedance contour plots of t/d vs. frequency at various percent open areas. It is important to note that the each t/d point in the t/d-frequency plane is a sample. Each of these samples had specified geometrical parameters such as percent open area. Nevertheless, each of these geometrical parameters varied because the specified and actual geometrical parameters were not the same. Besides percent open area the C_D also varies from sample to sample because a single C_D is calculated for each sample and these values are given in Appendix G. Therefore it is important to recognize that as t/d increases other geometrical parameters also vary, because of manufacturing tolerances.

Another word of caution, realize that t/d is the part of the second nondimensional group in the PBFIF model (see Section 3.1). These contour plots are provided to evaluate how the experimental and model impedance trends against this nondimensional group. It is important to realize that these groups in the model are not independent of each other.

For example, in the PBFIF model varying t/d affect groups one, two, four, and five (see Section 3.1). For more information on this topic see Appendix B.

Figure 6-10 shows the experimental impedance for varying t/d at 100 cm/s bias flow for 15 percent open area. This figure shows increasing spans of constant resistance throughout the frequency range, especially at the lower sound pressure levels. Also note that increasing the sound pressure level from 120 to 130 dB does not change the iso-resistance distribution in the t/d and frequency plane. Therefore, bias flow has linearized the resistance with respect to sound pressure level at these dB levels.

These results should be expected. Looking at the Perforate Bias Flow (PBF) model in *section 3.1*, we note that the addition of bias flow increases the nonlinear component of resistance. Therefore, increasing the bias flow component makes the nonlinear component more significant than the linear component, which depends on t/d. Furthermore, bias flow makes the nonlinear resistance term more dependent on the bias flow component than the acoustic particle velocity component. This produces the dual effect of reducing the resistance frequency variation, since the bias flow rate is constant through the frequency range, and making the resistance independent of sound pressure level, because the bias flow velocity is larger in magnitude than the acoustic particle velocity.

Figure 6-11 shows the experimental impedance for varying t/d at 100 cm/s bias flow for 5 percent open area. Comparing Figs. 6-10 and 6-11 the resistance becomes more constant throughout the t/d and frequency range as percent open area is decreased. Furthermore, the resistance is now independent of sound pressure level for all three levels.

The reactance does not seem to change very much between zero and 100 cm/s bias flow. Nevertheless, the reactance seems to be affected more by changes in percent open area. The 5 % open area reactance experiences a jigsaw shape with increases in t/d, while the 15 % open area reactance is constant with respect to t/d.

.

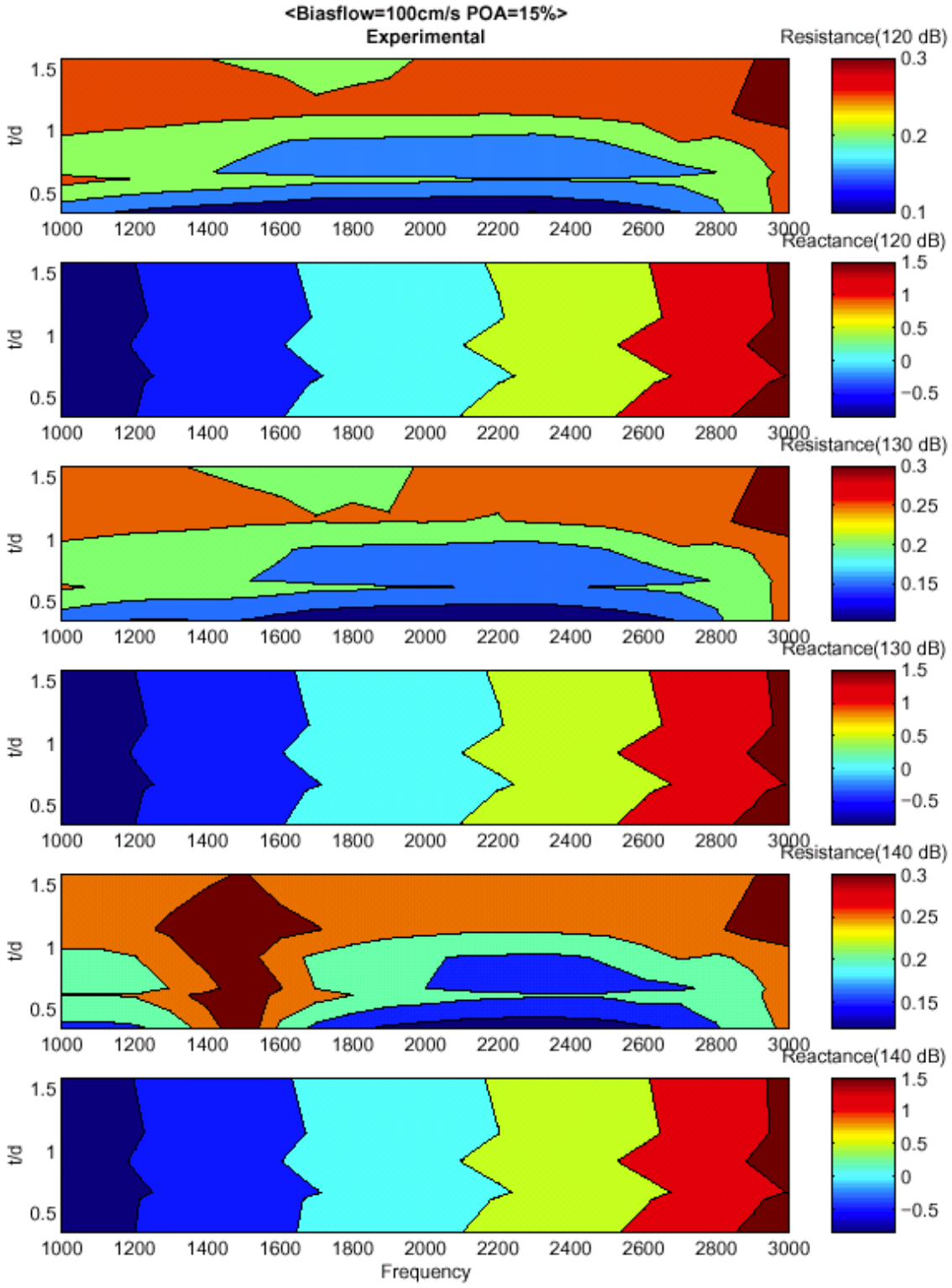

Figure 6-10. Experimental impedance contour plot.

Another trend to note is the effect of decreasing the percent open area at a constant flow rate. As the percent open area is decreased, bias flow becomes more significant. Decreasing the POA increases the effect of the nonlinear component of resistance in both the experiment and prediction. This is due to the $1/\sigma^2$ factor in the nonlinear component vs. the $1/\sigma$ factor in the linear component in all of the incompressible models.

Figure 6-12 shows the PBFIF model impedance for varying t/d at 100 cm/s bias flow for 15 percent open area. Comparing this model to the experimental results, the PBFIF model tends to over-predict the magnitude of the resistance. Furthermore, the iso-resistance shapes somewhat follows a similar trend to the experimental results, yet improvements are needed. The effect of sound pressure level changes on this model is in better agreement with the experimental results. This model tends to overstate slightly the effect of sound pressure level changes on the resistance. The reactance is in better agreement with the experimental results.

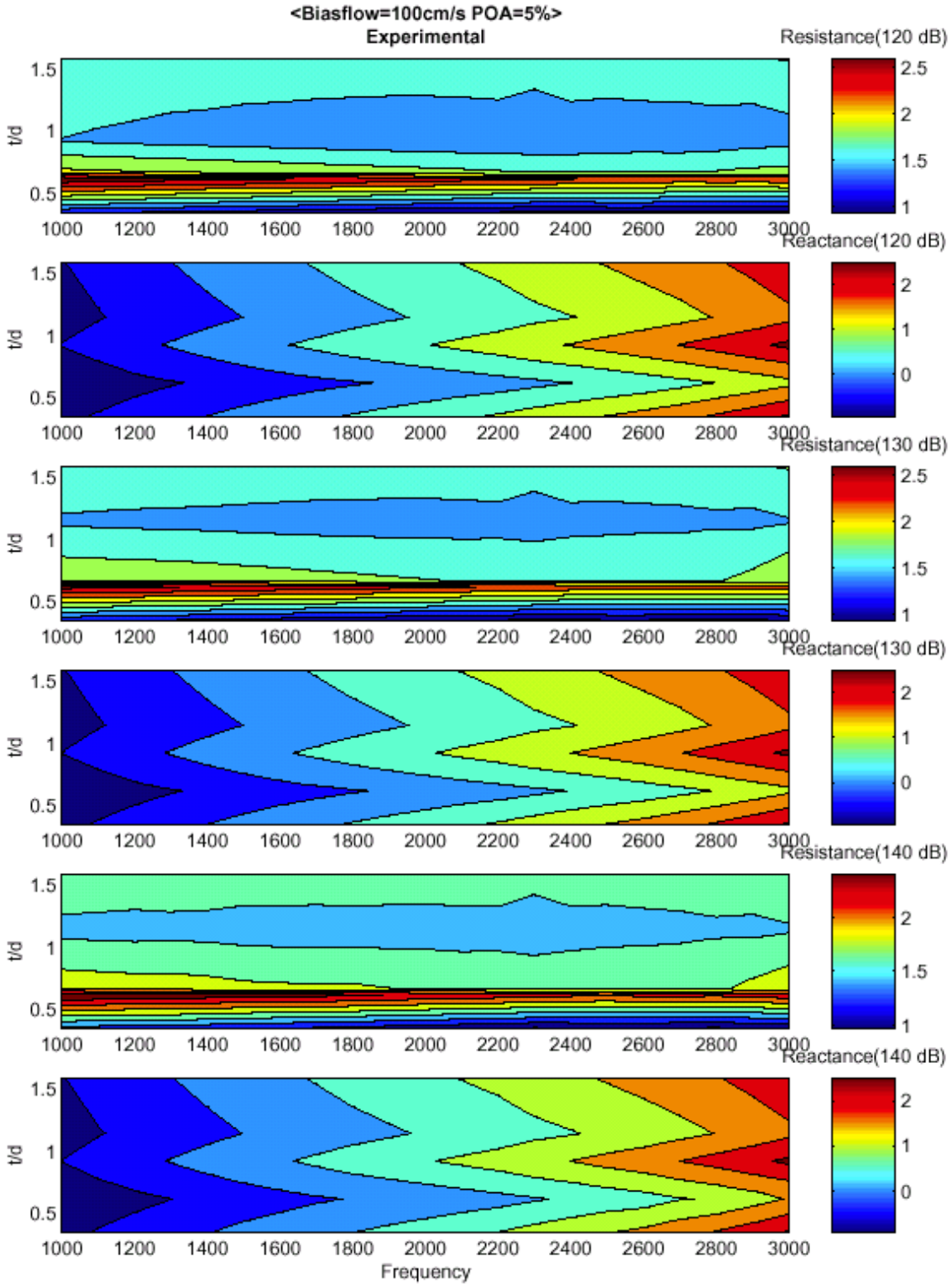

Figure 6-11. Experimental impedance contour plot.

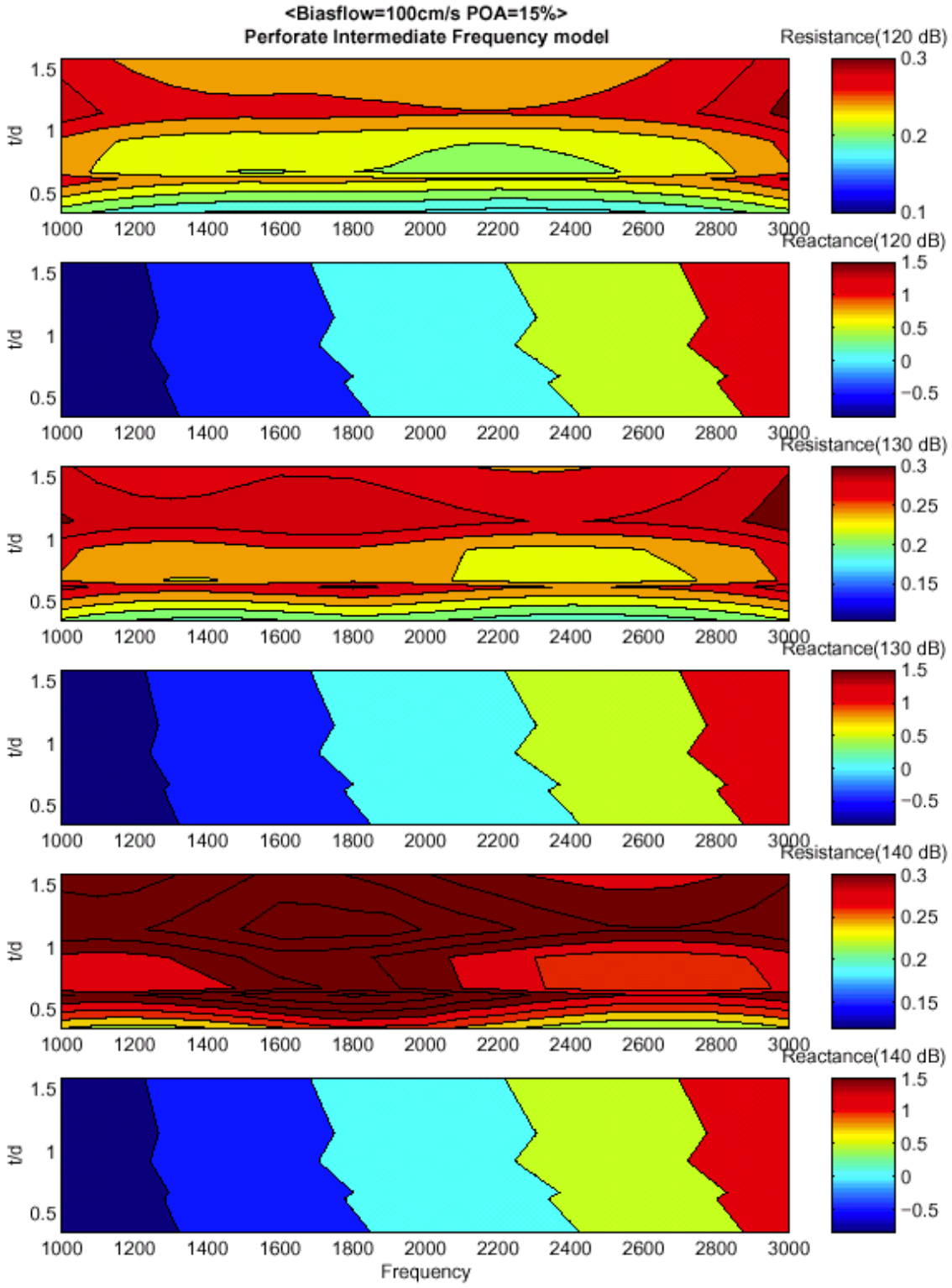

Figure 6-12. Perforate Intermediate Frequency model impedance contour plot.

The PBFIF model includes a bias flow correction given in Section 3.1. This correction, which was derived using a frequency domain approach, is similar to that developed by Premo using a time domain approach (See Section 2.2.2). Figures 6-13 and 6-14 show resistance comparisons between the models for 5% and 15% POA sample perforates. The reactance is not shown because bias flow only affects the resistance in both Premo's and the PBFIF model. These figures show almost identical resistance values for all bias flow rates.

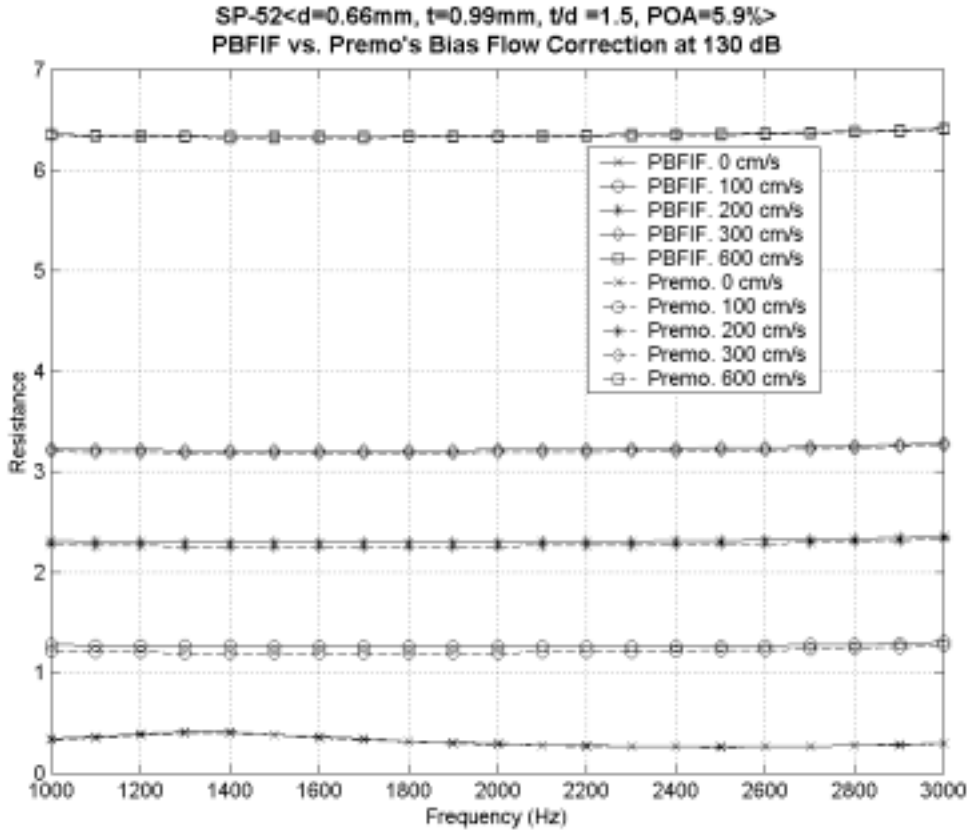

Figure 6-13. PBFIF vs. Premo's impedance model predictions at POA=5.9.

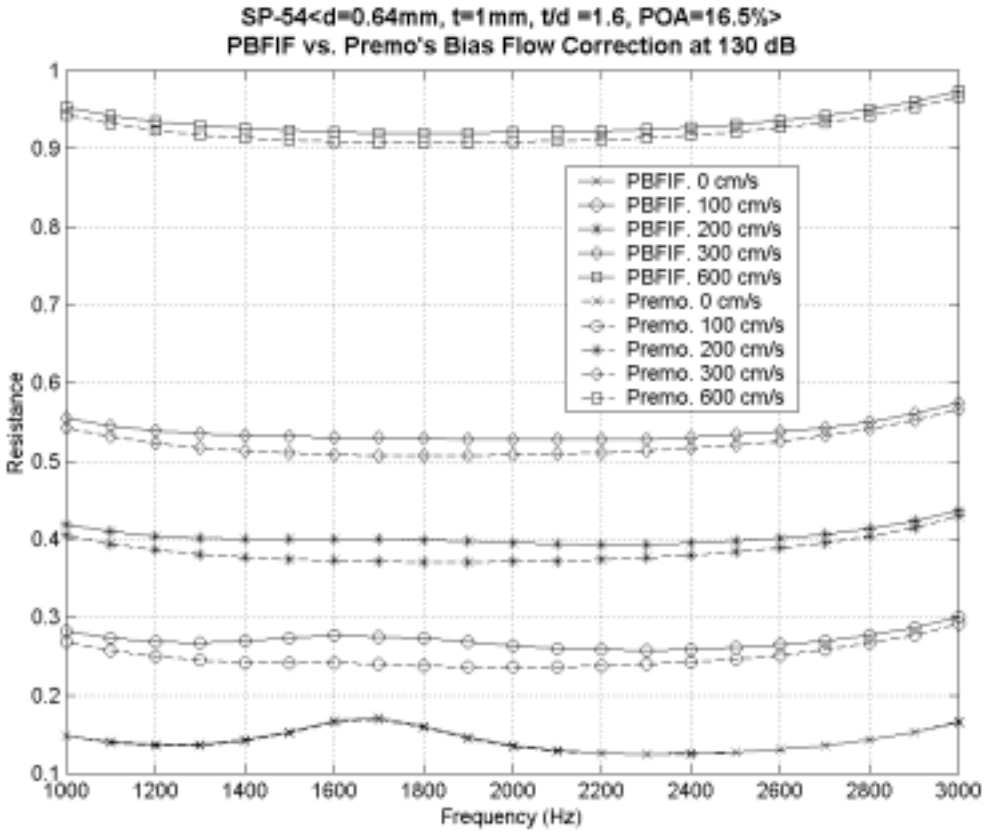

Figure 6-14. PBFIF vs. Premo's impedance model predictions at POA=16.5.

1. Jing, X. and Sun, X., "Effect of Plate Thickness on Impedance of Perforated Plates with Bias Flow," AIAA-99-1877.

7. Compressible Bias Flow Model Impedance Results

In Section 3.2, a compressible impedance model was derived and called the PCBFIF model. This model was developed for compressibility effects as the hole Mach number approached one. Figs 7-1 and 7-2 show resistance comparisons between the PBFIF and PCBFIF model predictions for samples of 5.9 and 16.5 POA. Only the resistance is plotted, because the reactance model is the same for both models. The symbol with the solid line is the PCBFIF model while the symbol alone is the PBFIF model. These plots are plotted for increasing hole Mach numbers. The hole Mach number was calculated using Eq. (3-44) derived in Section 3.3 rather than Eq. (6-1), due to the fact that Eq. (3-44) accounts for fluid compressibility while Eq. (6-1) does not.

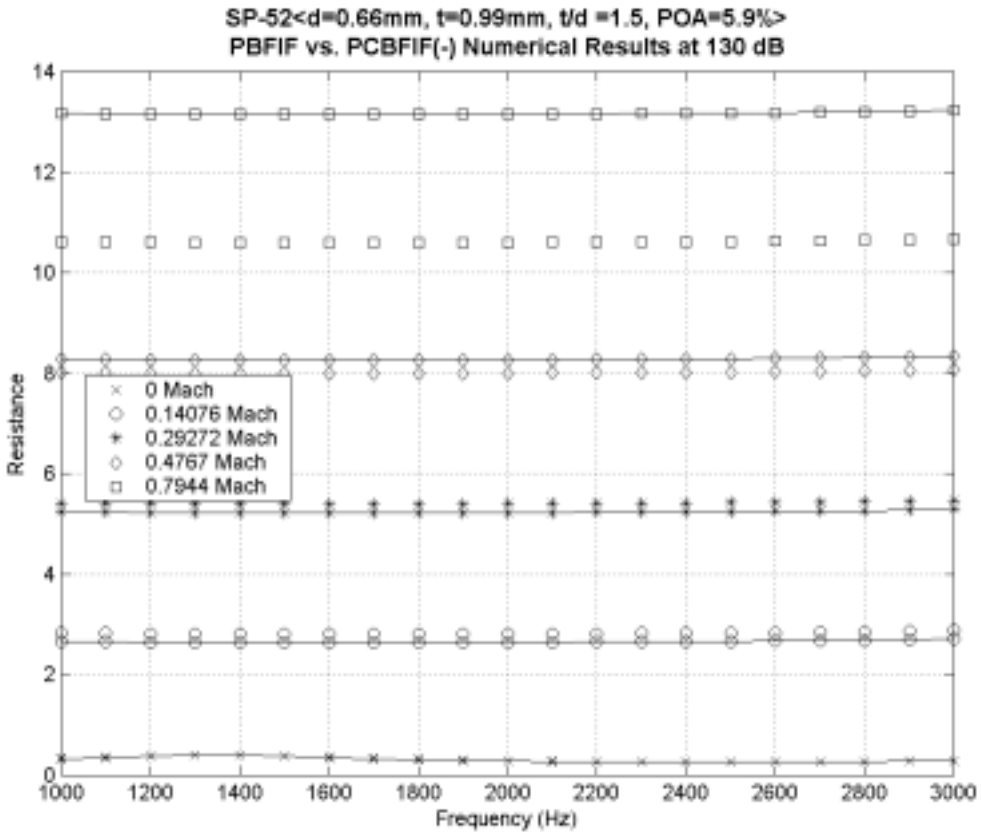

Figure 7-1. PBFIF vs. PCBFIF impedance model predictions at POA=5.9.

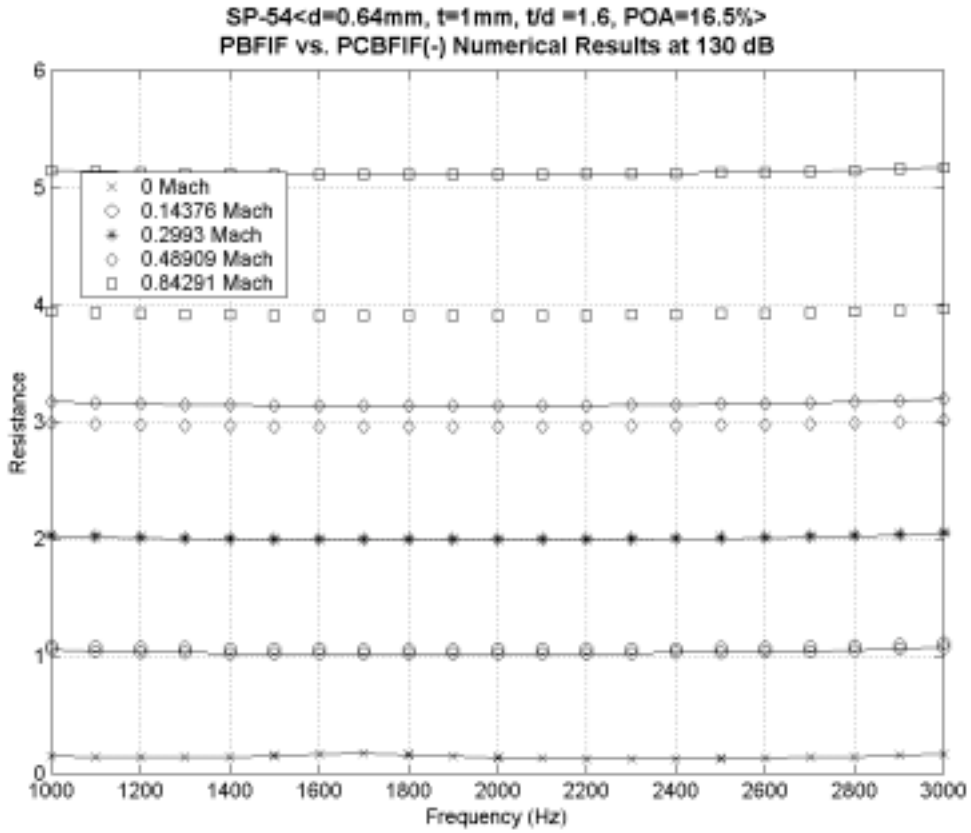

Figure 7-2. PBFIF vs. PCBFIF impedance model predictions at POA=16.5.

The resistance results indicate that the PBFIF and PCBFIF models predict nearly the same results for the low hole Mach numbers. As the hole Mach number increases, the resistance results start diverging, with the PCBFIF model predicting higher resistance results. This trend is independent of the sample POA. As the hole Mach number increases, fluid compressibility effects become more prevalent. Fluid compressibility can occur due to pressure variations and entropy variations. For the PCBFIF model an isentropic relationship was used, therefore only pressure variations can cause compressibility in this model. For incompressibility the following relationship must hold

$$\left(-\nabla \bullet \mathrm{v}\right) = \frac{1}{\rho}\frac{\mathrm{D}\rho}{\mathrm{Dt}} \approx 0 \qquad (7\text{-}1)$$

Using the momentum equation and ignoring entropy variations, unsteady effects, viscous, and body forces produces

$$\left(-\nabla \bullet v\right) = \frac{1}{\rho}\frac{D\rho}{Dt} = -M^2 \frac{1}{c^2} v \bullet \nabla \frac{1}{2} v^2 \qquad (7\text{-}2)$$

As M becomes small, the left side of Eq. (7-2) also becomes small, and approaches the incompressibility relation in Eq. (7-1). Conversely, as M becomes large, Eq. (7-1) no longer holds and the fluid behaves as a compressible fluid.

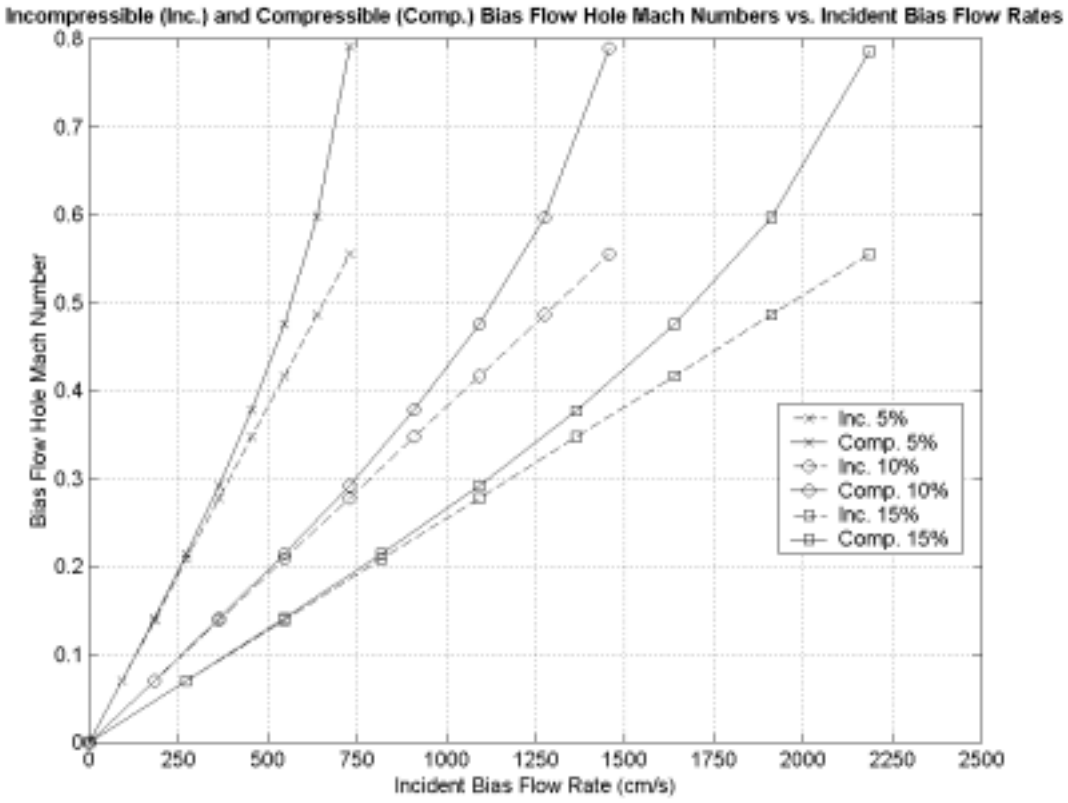

Figure 7-3. Incompressible and Compressible Bias Flow Hole Mach Numbers vs. Incident Bias Flow Rates at 5%, 10%, and 15% POA using C_D=0.76.

Figure 7-3 shows the calculated bias flow hole Mach Number vs. incident bias flow rate using compressible and incompressible flow assumptions for 5%, 10%, and 15% open areas, respectively. The incompressible hole Mach Number is calculated using Eq. (6-3), ignoring the acoustic term. The compressible hole Mach Number was

calculated by solving Eq. (3-44) through an iterative method. The discharge coefficient (C_D) used for these calculations was 0.76.

This figure shows that the predicted hole Mach numbers using compressible and incompressible flow assumptions are the same for the low incident bias flow rates for three percent open areas as expected. As the incident bias flow rate increases, the incompressible and compressible flow assumptions start diverging in terms of terms of their prediction of the hole Mach number. This divergence starts occurring at around a hole Mach Number of 0.35 for all three percent open areas. From this figure a hole Mach number of 0.35 corresponds to an incident bias flow rate of 450, 875, and 1250 cm/s for a 5, 10, and 15% open area perforate, respectively. Therefore, except for the highest bias flow rate and the lowest percent open area, fluid compressibility is not an effect.

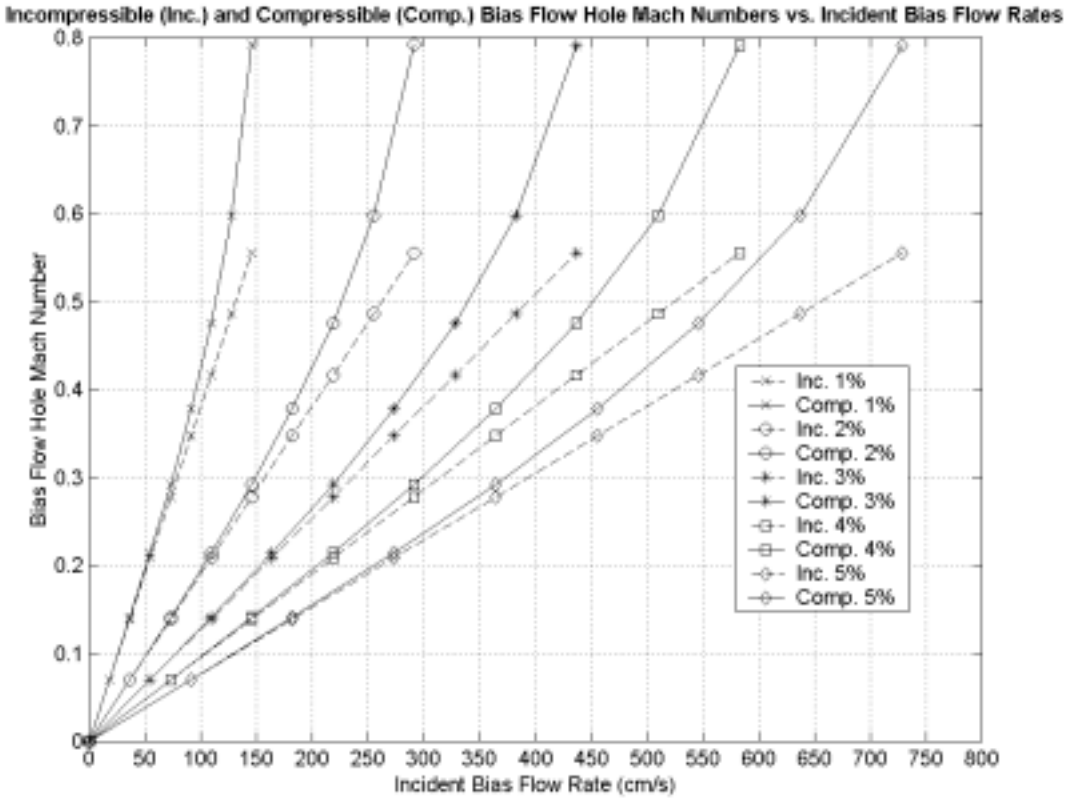

Figure 7-4. Incompressible and Compressible Bias Flow Hole Mach Numbers vs. Incident Bias Flow Rates at 1% through 5% POA using C_D=0.76.

Samples 61 through 65 are common septum perforated plates for multi-degree-of–freedom liners. These septum plates range from 1% to 5% POA. Figure 7-4 shows the calculated bias flow hole Mach Number vs. incident bias flow rate using compressible and incompressible flow assumptions for 1% to 5% open area samples. As seen from this figure, fluid compressibility is significant at these POAs. The test range of these samples had to be limited to low bias flow rates to avoid choked conditions in the perforate's orifices. Notice that as the POA is decreased, not only does fluid compressibility occur at lower flow rates, but also the rate of divergence between the incompressible and compressible hole Mach number predictions is greater. Therefore analysis of these samples must be done using the compressible bias flow model (PBCFIF) rather than the incompressible model (PBFIF).

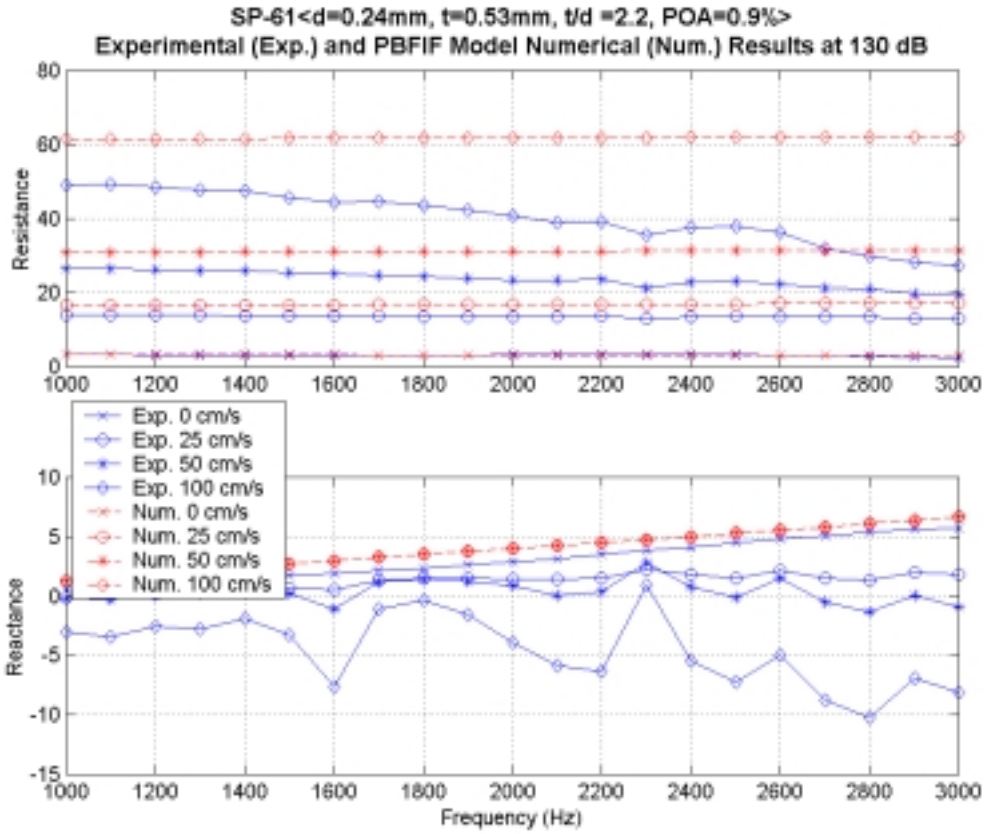

Figure 7-5. Experimental impedance and PBFIF model numerical predictions for a sample with POA=0.9.

For the analysis of these samples the discharge coefficient used was 0.76 rather than the calculated C_D given in Appendix G. The reason for this is that the fit used to determine C_D (see Section 4.6) assumes incompressible flow and therefore does not apply for these samples. More discussion on C_D may be found in Appendix F.

Figure 7-5 shows a sample experimental and PBFIF model impedance at 130 dB and 0.9% POA for various bias flow velocities. This figure shows a rapid increase in resistance with increasing bias flow. The experimental resistance also shows a decreasing trend with frequency at the higher bias flow rates. The prediction's agreement with the experimental results deteriorates as the bias flow is increased. The resistance model results follow the same trend as the experiments of increasing resistance with increasing bias flow, but tend to over-predict its values over the frequency range.

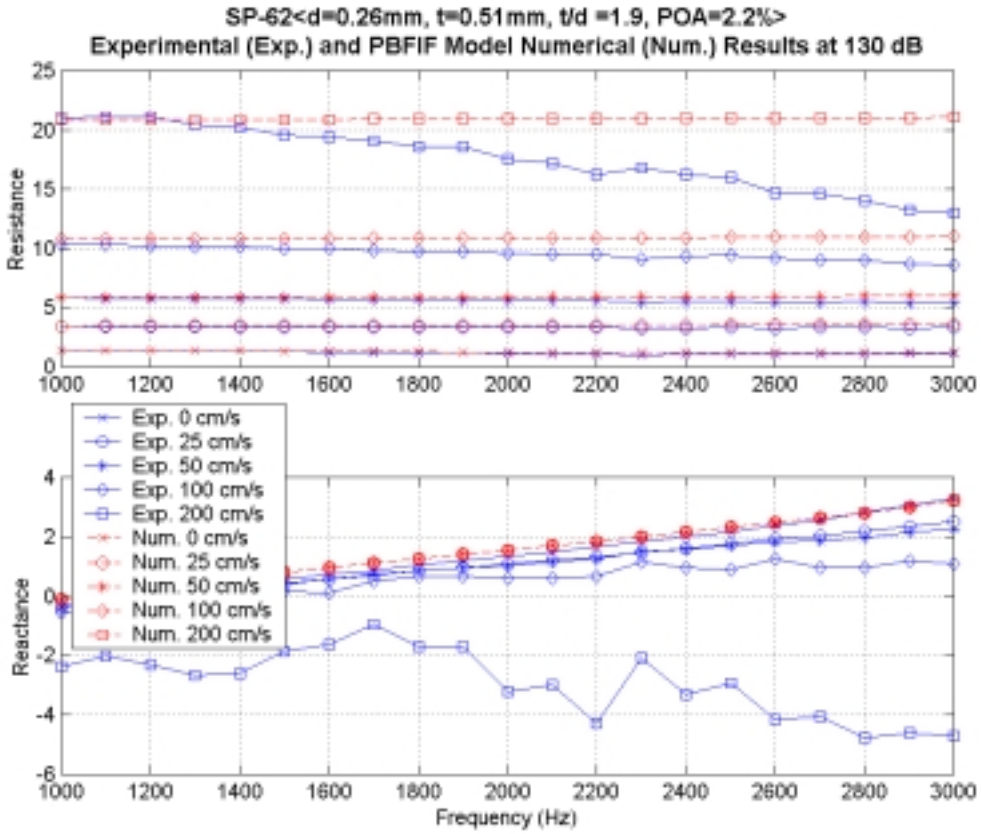

Figure 7-6. Experimental impedance and PBFIF model numerical predictions for a sample with POA=2.2.

The experimental reactance results show a decreasing trend as bias flow is increased. This trend is more pronounced as the frequency is increased. The model predictions do not account for this effect. This effect was seen before (although less accentuated) for higher percent open areas (5%), and more discussion on this is provided in Chapter 6.

Figures 7-6, 7-7, and 7-8 show sample experimental and PBFIF model impedance results at 130 dB and 2.2%, 3.1%, and 5.2% POA, respectively, for various bias flow velocities. As with the 0.9% POA sample, the resistance results for these samples show deteriorating agreement between model predictions and experiments as bias flow is increased. The 2.2% and 3.1% samples show better agreement between the predictions and experiments than the 0.9% and 5.2% samples.

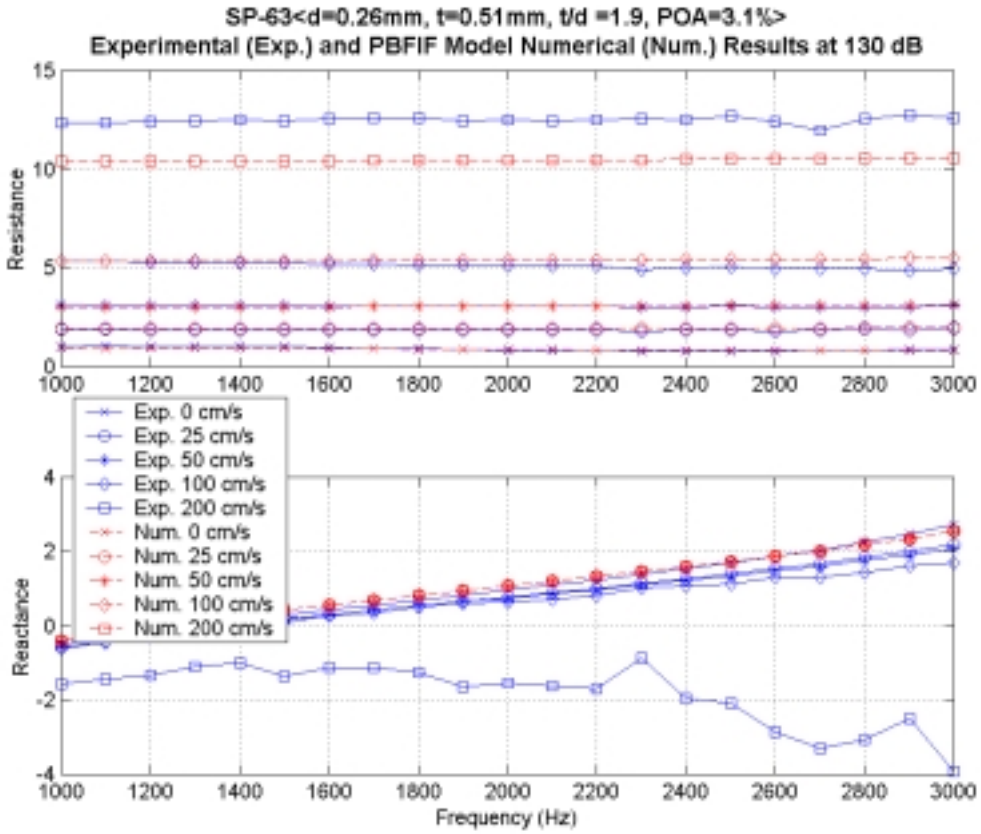

Figure 7-7. Experimental impedance and PBFIF model numerical predictions for a sample with POA=3.1.

These higher percent open area samples also show the trend of decreasing experimental resistance with frequency at the highest bias flow rates. This trend was also seen in Chapter 6 for the 5% open area sample. It is important to note that this effect occurs usually only at the highest flow rate and seems to be independent of the resulting resistance value. Therefore, this problem may be due to the loss of backpressure in the experiments during the test at these low POA and high bias flow rates and not an inherit physical phenomena. Consequently, the model predictions will not account for this effect.

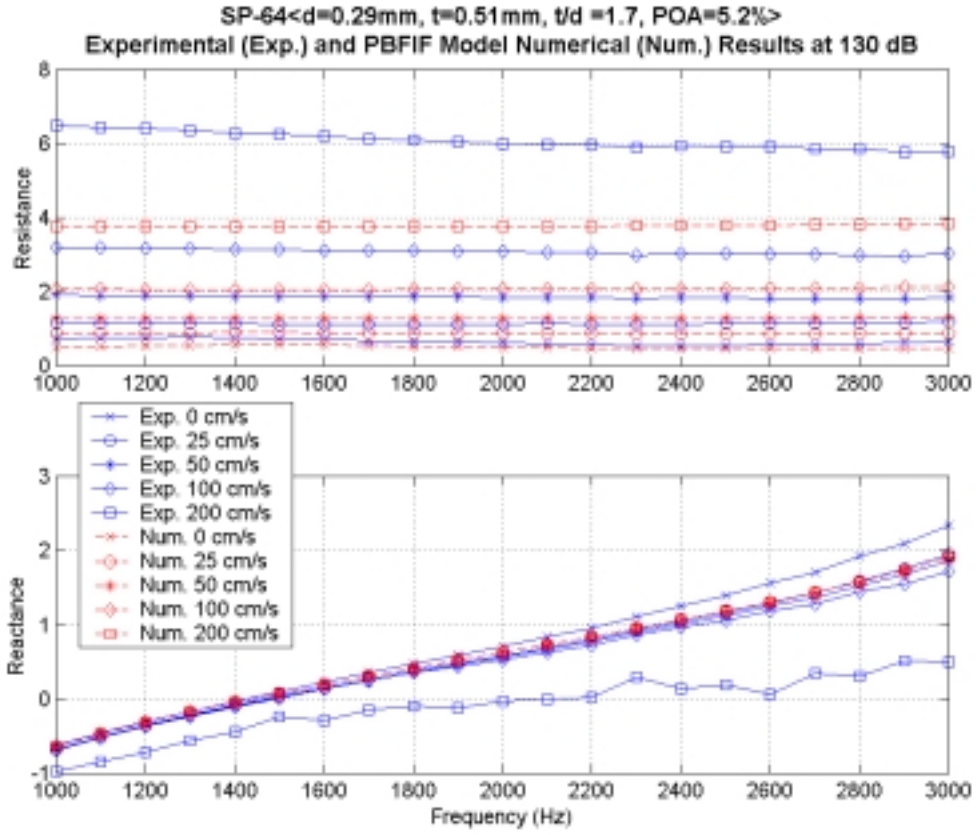

Figure 7-8. Experimental impedance and PBFIF model numerical predictions for a sample with POA=5.2

8. Experimentally Fitted Bias Flow Model Impedance Results

In Section 3.6 a method of experimentally fitting (correcting) the numerical model to better approximate the experimental results was described. In this chapter, the PBFIF model is fitted using the method described in that section, with the slope error criteria used as the optimizing objective function. Only the resistance terms in the PBFIF model were fitted to the experiments. The resulting fitted model is

$$\xi = (1)\frac{16\upsilon t}{c\sigma C_D d^2} + (0.4)2.82\frac{\sqrt{\omega\upsilon}}{c\sigma C_D}\frac{t}{d} + (1.2)\frac{\left(1-\sigma^2\right)}{2c\left(\sigma C_D\right)^2}\left|2v_b + 1.2v_{rms}\right| + i\left(\frac{kt}{\sigma C_D} + 2.82\frac{\sqrt{\omega\upsilon}}{c\sigma C_D}\frac{t}{d} + \frac{8}{3\pi}\frac{d}{\psi'(\sigma)}\right) \tag{8-1}$$

This model will be called the Fitted Perforate Bias Flow Intermediate Frequency (FPBFIF) model. The similarity between the PBFIF and FPBFIF models is striking. The optimal multiplication constant to fit the model to the experiments were 1, 0.4, and 1.2 for the linear dc (first term), linear ac (second term), and nonlinear (third term) resistance terms, respectively, as seen in Eq. (8-1). Most of the correction predicted by the optimization routine was in the second term, reducing its influence in the model by nearly 60%.

Figure 8-1 shows a sample experimental and FPBFIF model resistance at 130 dB and 5.9% POA for various bias flow velocities. Only the resistance is plotted since the reactance of the FPBFIF and PBFIF model is the same. The reader is referred to Chapter 6 for experimental and predicted reactance plots. The FPBFIF model shows good agreement between experimental and predicted results at the low bias flow rates. This agreement, as with the PBFIF model, deteriorates as the bias flow rate is increased. Nevertheless, the FPBFIF model seems to be closer to experimental results than the PBFIF model results shown in Chapter 6 and Appendix H.

Figure 8-2 shows the error in terms of slope and difference between the experimental and predicted results for all nominal 5% open area samples using the FPBFIF model. The error plots indicate that the worst slope criterion is about 0.65, but

the mean hovers between 0.9 and 1 excluding the highest flow rate (600 cm/s). This is a significant improvement when compared to the PBFIF model, where the worst point and mean slope is about 0.5 and 0.7, respectively (see Chapter 6 or Appendix H). The spread of the slope with respect to different t/d is significant, although reduced when compared to the PBFIF model. There is a about a 15% improvement in terms of worst point slope between the FPBFIF and PBFIF model.

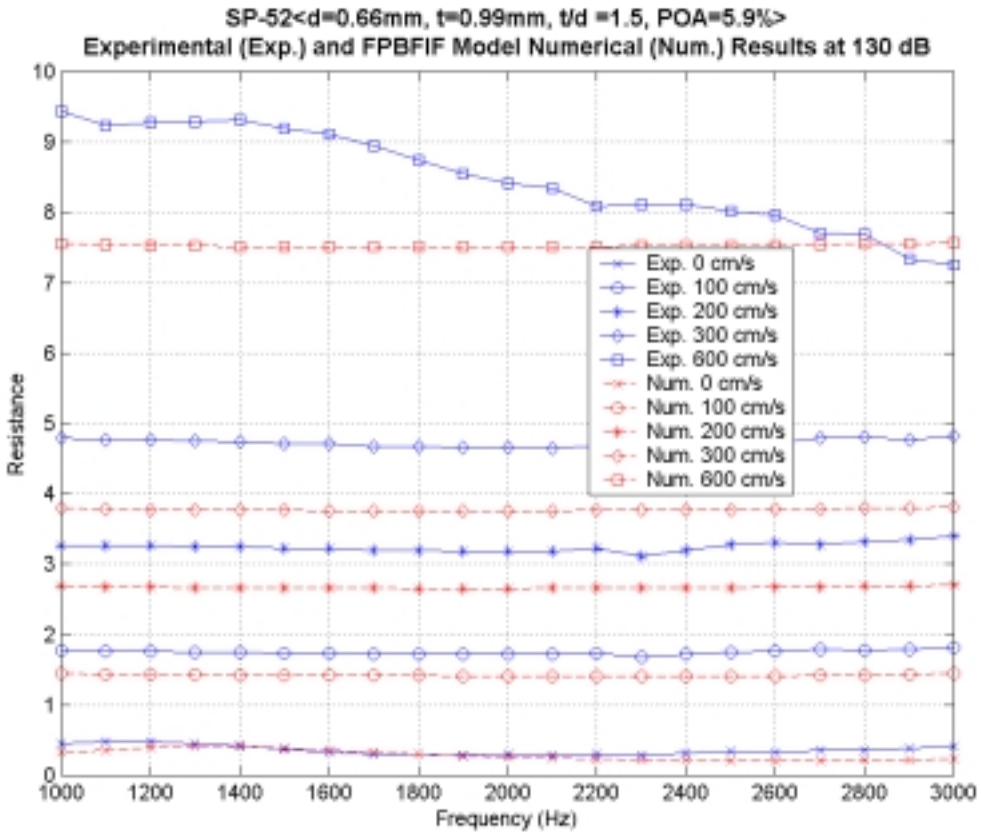

Figure 8-1. Experimental and FPBFIF model impedance for a sample with POA=5.9.

The maximum mean difference between the experiments and the FPBFIF model is about 2ρc, although the mean is generally within 0.5ρc. Comparing these results to the worst difference in the PBFIF model (about 2.5ρc), the FPBFIF model performs about 20% better. Although there is a significant improvement in model agreement with experimental results using the FPBFIF model, there is still considerable improvement

required. The proper modeling of the combination of low percent open area with bias flow is still a problem that even with an experimentally fitted model remains aloof.

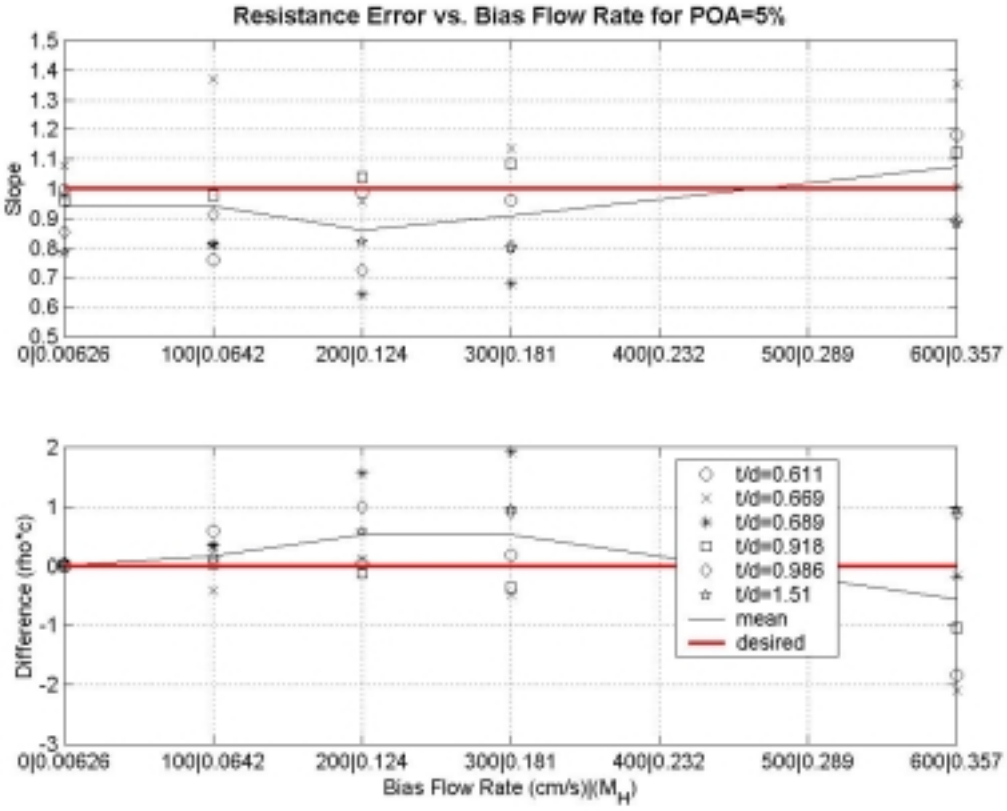

Figure 8-2. FPBFIF model resistance error criteria for POA=5.

Figure 8-3 shows a sample experimental and FPBFIF model resistance at 130 dB and 10.88% POA for various bias flow velocities. The results in this plot show significant improvement between the experimental and numerical results. As with the 5% open area sample, the agreement between numerical and experimental results deteriorates as bias flow increases. Nevertheless, the deterioration rate is significantly reduced for the nominal 10% vs. 5% open area sample.

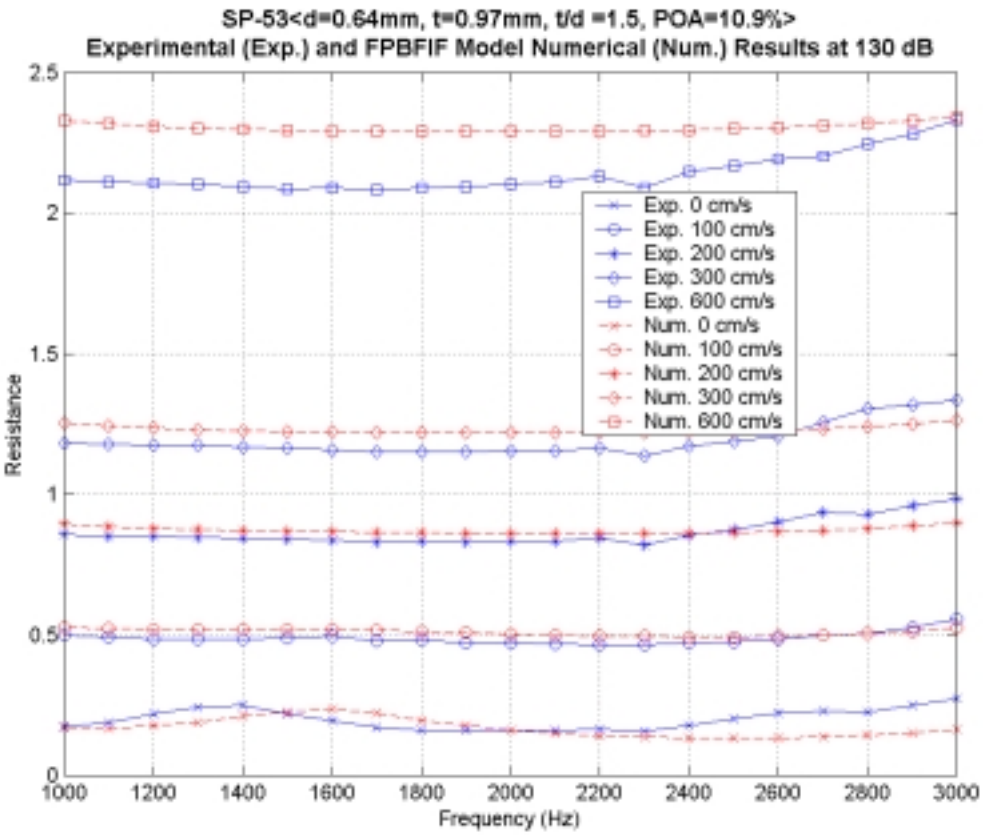

Figure 8-3. Experimental and FPBFIF model impedance for a sample with POA=10.9.

Figure 8-4 shows the error in terms of slope and difference between the experimental and predicted results vs. bias flow rate for nominal 10% open area samples with various t/d's using the FPBFIF model. The mean slope starts at about 0.9 for zero bias flow, increases to 1.3 at 100 cm/s, then decreases to about 1.0 as the bias flow rate is increased to 600 cm/s. The spread about the mean is about 0.4 (or +/- 0.2 about the mean) and is fairly constant for all the flow rates. In general, as the t/d is increased the slope approaches one. This is expected since the perforate holes were modeled as tubes. Compared to the PBFIF model (see Chapter 6) the FPBFIF model fares slightly worse, especially for the 100 cm/s bias flow rate.

Figure 8-4 also shows the difference between experiments and predictions. The mean difference tends to increase with increasing bias flow rate. It starts at nearly zero for no flow to about 0.5ρc for the highest bias flow rate. The spread in the difference (maximum minus minimum difference) with varying t/d also follows this trend of

increasing with bias flow increase. The spread starts at nearly zero and increases to about 1ρc (or +/-0.5ρc about the mean).

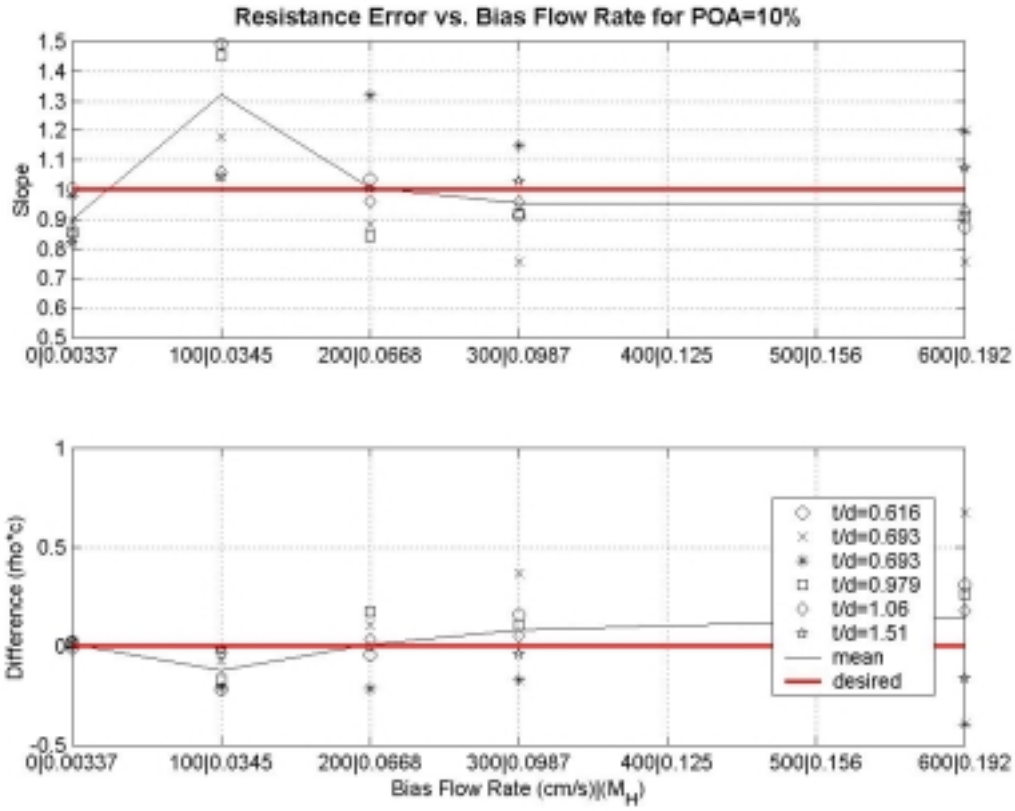

Figure 8-4. FPBFIF model resistance error criteria for POA=10.

Figure 8-5 shows a sample experimental and FPBFIF model resistance at 130 dB and 16.48% POA for various bias flow velocities. The results at the for the 15% open area sample are similar to the 10%, and both show better agreement than the 5% open area sample.

The slope error criteria of the 15% nominal POA is very similar to that of the 10% POA (see Figs. 8-4 and 8-6), although the spread about this mean seems to be reduced for the 15% vs. 10% POA. The mean difference error criteria for the nominal 15% POA is less than 0.1ρc for all bias flow rates, and less than 0.05ρc excluding the highest bias flow rate (600cm/s). The spread of the difference error is also within 0.1ρc (+/- 0.05ρc) excluding the highest bias flow rate (600cm/s).

Comparing these results with the PBFIF model (Chapter 6), both the slope and difference error criteria for the nominal 15% POA samples are very similar. The FPFIF model performs somewhat better than the PBFIF model, especially at the higher bias flow rates. For example, the mean slope error at 600cm/s bias flow rate is about 0.8 for the PBFIF vs. 0.9 for the FBFIF model, a 10% improvement in the least squares sense.

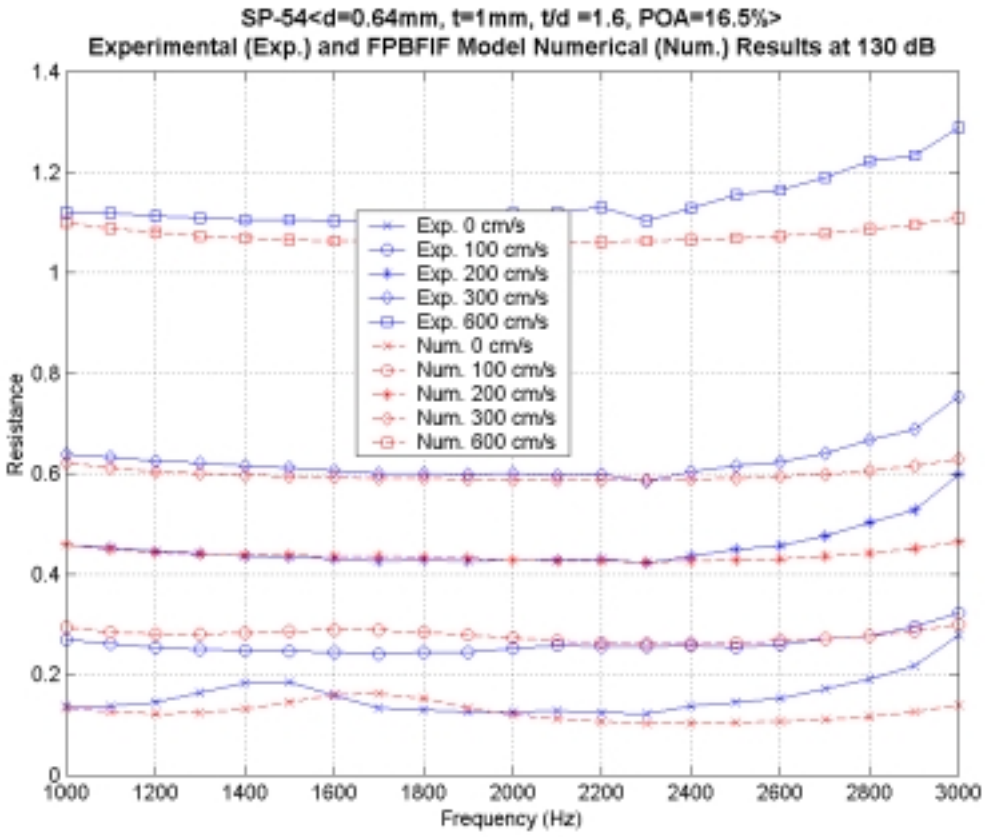

Figure 8-5. Experimental and FPBFIF model impedance for a sample with POA=16.5.

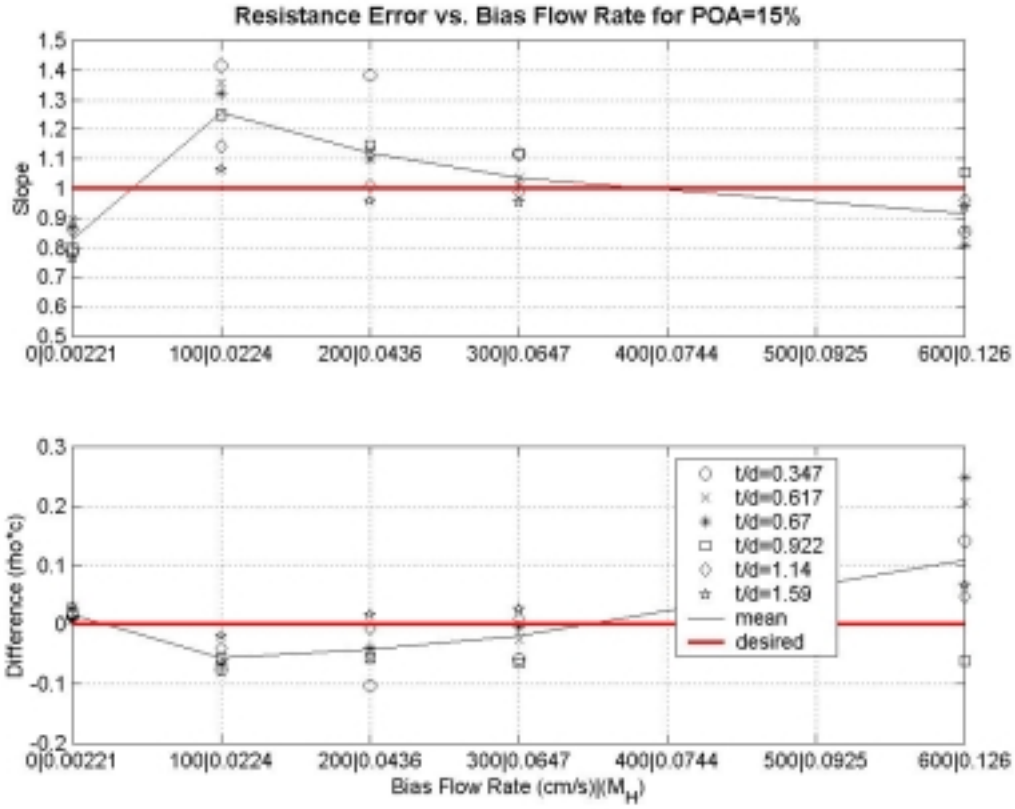

Figure 8-6. FPBFIF model resistance error criteria for POA=15.

9. Conclusions and Future Work

There were four objectives to this study:

1. Acquire a quality experimental database of educed normal incidence impedances for perforates plates with and without bias flow
2. Develop improved impedance models for perforated plates in the presence of bias flow
3. Evaluate the models developed against the experimental database
4. Use the experimental database to improve the model's performance and evaluate the resultant model performance

To achieve objective one, normal incident impedances were experimentally educed from perforated samples in the presence of bias flow. These samples were tested in the NASA Langley Normal Incident Tube (NIT), where several experimental issues were addressed to test these samples.

These issues included the modifications to the NIT to introduce bias flow, the repeatability of the experiments, the implementation of a non-switching two-microphone method, mechanisms to eliminate the perforates plate resonances, the accurate determination of bias flow speeds through the perforates, and the impedance determination of the high resistance fibermetal between the plenum chamber and the cavity. Figures 4-1 and 4-3 show the NIT experimental setup. Having addressed these issues, a quality database of educed perforated plate impedances was acquired, and therefore objective one was achieved.

Objective two was addressed by first determining the previous impedance modeling methods. These methods mainly involved the determination of the impedance of perforated plates without bias flow. Three impedance models, which included the effect of bias flow, were developed. Two of the impedance models were developed by modeling the perforate orifices as infinite tubes with the inclusion of end corrections. These models assumed incompressible and compressible flow assumptions, respectively, between the far field and the perforate orifice. The incompressible and compressible

models were called the PBFIF (Eq. (3-36)) and PCBFIF (Eq. (3-52)) model, respectively. These models were implemented and their results were evaluated against experiments. The third model was developed following a similar approach to Hersh99. This model was not implemented and more information on this model may be found in Appendix A.

The PBFIF and PCBFIF models were evaluated against experiments to address objective three. The frequency range for which this model was evaluated was from 1000 to 3000 Hz. The PBFIF model performed better for higher (15%) rather than lower (5%) percent open area (POA) samples. Based on the slope error criteria, the model's resistance predictions were on average within 20% and 30% for the higher and lower POA's, respectively. The mean difference between the experiments and predictions started at nearly zero for the low flow rates and increased to about 1ρc and 0.5ρc for 5% and 15% open area respectively, at the highest incident bias flow rate of 600cm/s. The numerical model predictions of lower POA perforates contained more scatter, with respect to varying t/d's, than at higher POA. This was true regardless of whether the slope, difference or correlation error criterion was used. The scatter also tended to increase as the flow velocity was increased for any given POA.

Results at zero flow indicated the linear terms required more correction than the nonlinear terms for the PBFIF model. When this model was compared to GE's model, which lacked the linear resistance frequency dependent term, the PBFIF model outperformed the GE model when compared to experiments in the middle and higher frequency range.

As flow was added the nonlinear term became more important than the linear terms. The resistance of the perforate became more independent of t/d, SPL, and frequency as bias flow was increased (perforate linearization). The point where this linearization occurred was a function of the bias flow rate and percent open area. For example, the 15% POA samples experienced linearization at 100cm/s incident bias flow velocity for the SPL's of 120dB and 130dB, but not 140dB, while the 5% POA sample was linearized for these SPL's at this incident bias flow rate.

The experimental reactance results showed a decreasing trend as bias flow was increased. This trend was more pronounced at the lower percent open areas (<5%) and higher frequency range. The PBFIF model was not able to account for this effect on the

reactance. A possible explanation for this shortcoming in the model was that this model did not account for the formation of unsteady vortices. Another model by Jing and Sung[1] that accounted for this effect was able to predict the decrease in reactance as bias flow was increased. The PBFIF model showed good agreements with Premo's bias flow correction.

The PCBFIF model and the PBFIF predicted nearly the same results for low hole Mach numbers. As the hole Mach number was increased the PCBFIF model predicted higher resistance values than the PBFIF model. It was shown that the predicted hole Mach number was the same using the compressible and incompressible flow assumptions except for the highest bias flow rate (600cm/s) and lower percent open area (5%).

The septum perforates with POAs between 1% and 5% were also analyzed. The results showed that the rate of divergence between the predicted hole Mach number using compressible and incompressible flow assumptions increased as the POA was lowered. Therefore, the PCBFIF model was used to analyze these samples. The septum perforate results showed decreasing agreement between model results and experiments as bias flow was increased. The 2.2% and 3.1% samples show better agreement between the predictions and experiments than the 0.9% and 5.2% samples.

To address objective four, a fit of the PBFIF model was performed using the experimental data. The fit was performed using an optimization routine that found the optimal set of multiplication constants to the non-dimensional groups that minimized the least squares slope error between predictions and experiments. The fitted model indicated that most of the correction required to better approximate the measured results was in the frequency dependent linear term of the resistance. The fitted model results showed significant improvement over the original model for the low percent open area 5% samples. The fitted model performed about the same as the original model for the 10% POA sample and slightly better for the 15% POA sample.

There are several potential research areas for future work in the modeling of bias flow acoustic perforated plate liners. The determination of a suitable grazing flow model that accounted for bias flow was only preliminarily addressed in this dissertation. There are several other parameters that have future research potential in the area of bias flow acoustic liners. These include the effects of broadband acoustic signals and temperature

variation, to name a few. Another important area of future research is the determination of C_D. Appendix F discusses some of the issues associated with the methods used to determine C_D in this study, and provides a sensitivity study of the effect on the resistance results due to the uncertainty in C_D. There are also several experimental fluid mechanical visualization studies that could be performed to complement the development of other theoretical models.

---

1. Jing, X. and Sun, X., "Effect of Plate Thickness on Impedance of Perforated Plates with Bias Flow," AIAA-99-1877.

Appendix A: Perforate Boundary Layer Bias Flow (PBLBF) Model

The Perforate Boundary Layer Bias Flow model is based on the principles outlined by the Hersh99 model[1]. The original model includes cavity reactance and needs to be modified for this study since ZKTL calculates the cavity reactance in a separate module. Hersh99 utilizes a control volume approach, where they write the conservation of vertical momentum within the holes.

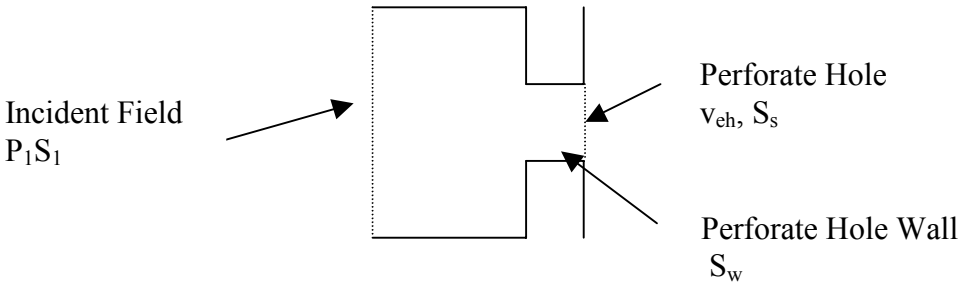

Figure A-1. Control volume for perforate hole.

The momentum equation from Fig. A-1 for the modified model is

$$\rho_h S_1 H \frac{dv_e}{dt} + \rho_h \int_0^R 2\pi r v_{eh}^2 dr - \rho v_e^2 S_1 = P_1 S_1 - P_1 (S_1 - S_s) - \kappa_w S_w \qquad \text{(A-1)}$$

where R is the radius of the perforate orifice. Hersh uses a similar equation to Eq. (A-1)[1] except that he includes the cavity reactance. He then groups terms, simplifies, and rewrites that equation in terms of semi-empirical parameters, which produces

$$\rho_h S_1 H \frac{dv_e}{dt} + \rho_h S_1 \left(\frac{G}{\sigma} - 1 \right) v_e^2 + K_{vis} v_e = P_s S_s \qquad \text{(A-2)}$$

where the parameters G, H, and K_{vis} are determined semi-empirically. Hersh demonstrates that G can be related to the viscous boundary layer profile by

$$G = \frac{\kappa_{BL}^2}{(1 - S_{inv})} + \frac{(1 - \kappa_{BL})^2}{S_{inv}} \tag{A-3}$$

where κ_{BL} is given by

$$\kappa_{BL} = \frac{v_{BL} S_{BL}}{v_e} \tag{A-4}$$

Let v_e be a harmonic acoustic disturbance with a superimposed mean bias flow velocity of the following form

$$v_e = v_a e^{i\omega t} + v_b \tag{A-5}$$

and let

$$v_e^2 = \left[v_a^2 + 2 v_b v_a\right] e^{i\omega t} + v_b^2 \tag{A-6}$$

where Eq. (A-6) forces nonlinear and linear oscillations to be of the same frequency. Let's further assume that

$$P_s = p_a e^{i\omega t} + p_b \tag{A-7}$$

Substituting Eqs. (A-5) through (A-7) into Eq. (A-2) yields

$$i\rho_s S_1 H \omega v_a e^{i\omega t} + \rho_s S_1 \left(\frac{G}{\sigma} - 1\right)\left(v_a e^{i\omega t} + v_b\right)^2 + K_{vis}\left(v_a e^{i\omega t} + v_b\right) = \left(p_a e^{i\omega t} + p_b\right) S_s \tag{A-8}$$

Rearranging and collecting terms produces

$$\underbrace{\left[(iA + B + 2v_b)v_a + v_a^2 - Cp_a\right]e^{i\omega t}}_{=0} + \underbrace{\left[v_b^2 + Bv_b - Cp_b\right]e^0}_{=0} = 0 \qquad \text{(A-9)}$$

where

$$A = \frac{H\omega}{\left(\frac{G}{\sigma} - 1\right)} \qquad \text{(A-10)}$$

$$B = \frac{4\sigma K_{vis}}{\pi d^2 \rho_s \left(\frac{G}{\sigma} - 1\right)} \qquad \text{(A-11)}$$

$$C = \frac{\sigma}{\rho_s \left(\frac{G}{\sigma} - 1\right)} \qquad \text{(A-12)}$$

In order for Equation (A-9) to be satisfied the coefficients of the terms in that equation must be zero. For the first coefficient this produces

$$(iA + B + 2v_b)v_a + v_a^2 - Cp_a = 0 \qquad \text{(A-13)}$$

Multiplying Eq. (A-13) by v_a produces

$$iAv_a^2 + Bv_a^2 + 2v_b v_a^2 + v_a^3 = Cp_a v_a \qquad \text{(A-14)}$$

Integrating both sides over the period yields

$$\frac{1}{T}\int_0^\tau iAv_a^2 d\tau + \frac{1}{T}\int_0^\tau Bv_a^2 d\tau + \frac{1}{T}\int_0^\tau 2v_b v_a^2 d\tau + \frac{1}{T}\int_0^\tau |v_a| v_a^2 d\tau = \frac{1}{T}\int_0^\tau Cp_a v_a d\tau \qquad \text{(A-15)}$$

where v_a^3 has been replaced by $|v_a|v_a^2$ in the fourth term to ensure that it remains positive. Assuming a harmonic solution for v_a of the form $\mathrm{Cos}(\omega\tau)$ and simplifying yields

$$iAv_{rms}^2 + Bv_{rms}^2 + 2v_b v_{rms}^2 + \frac{4}{3\pi}2\sqrt{2}v_{rms}^3 = \xi C\rho c v_{rms}^2 \qquad \text{(A-16)}$$

Dividing both sides by $C\rho c v_{rms}^2$ produces

$$\xi = \frac{1}{\rho c C}\left[B + 1.2v_{rms} + 2v_b + iA\right] \qquad \text{(A-17)}$$

Variables A, B, and C depend on K_{vis}, H, and G. These variables must be related to the geometrical parameters of the perforate that produces them. Hersh developed these relationships in his paper through semi-empirical means. These relationships are

$$K_{vis} = \frac{\pi d\mu}{\sigma}\left[\left(\frac{t}{d}\right)K_{ss} + \left(\sqrt{\frac{\omega t^2}{\upsilon}}\right)K_{ac}\right] \qquad \text{(A-18)}$$

$$K_{ss} = 13 + 50.35\left(\frac{t}{d}\right)^{-1.35} \qquad \text{(A-19)}$$

$$K_{ac} = 3.2 + 1.95\left(\frac{t}{d}\right)^{-1.07} \qquad \text{(A-20)}$$

The parameter H becomes

$$H = \left[a + (1-a)e^{-bP_{non}^2}\right]d_e \qquad \text{(A-21)}$$

where

$$a = \frac{5.564\left(\frac{t}{d}\right)}{1+5.564\left(\frac{t}{d}\right)} \tag{A-22}$$

$$b = 1.537 + 6.532\left(\frac{t}{d}\right) - 1.693\left(\frac{t}{d}\right)^2 + 0.179\left(\frac{t}{d}\right)^3 \tag{A-23}$$

$$d_e = t + 0.85d \tag{A-24}$$

$$P_{non} = \left[\frac{p_a}{\rho(2\pi f)^2}\right]^{\frac{1}{2}} \tag{A-25}$$

The parameter G becomes

$$G = a\left[1 - e^{-nPnon}\right] \tag{A-26}$$

where a and b are redefined as follows

$$a = \frac{0.76 + 0.129\left(\frac{t}{d}\right)^2}{1+0.161\left(\frac{t}{d}\right)^2} \tag{A-27}$$

$$b = \frac{11.876 + 4.484\left(\frac{t}{d}\right)^2}{1+0.159\left(\frac{t}{d}\right)^2} \tag{A-28}$$

These semi-empirical relationships assume a viscous boundary layer profile with an inviscid core in the perforate's hole. The boundary layer thickness has been assumed to be equal to the diameter of the perforate hole.

References

1. Hersh, A. S., Walker B.E., and Celano, J.W., "Semi-empirical Helmholtz Resonator Impedance Model," AIAA 99-1825, 1999.

Appendix B: Non-dimensional Analysis and Functional Determination

The impedance of liners can be analyzed numerically and experimentally by using principles of non-dimensional analysis. Let the experimentally determined non-dimensional impedance ξ be expressed as

$$\xi = F(G_1, G_2, ..., G_n) \tag{B-1}$$

where F is a function and G_1, G_2,…, G_n are non-dimensional groups. In general these groups are complex, and are themselves a function of dimensional geometric and physical parameters.

Theoretical impedance models, such as those developed by Crandall and Kraft, have claimed that the function F is separable. This means Eq. (B-1) can be rewritten as

$$\xi = F_1(G_1) + F_2(G_2) + ... + F_n(G_n) \tag{B-2}$$

The different theoretical models assume different F's and G's depending on the assumptions and approximations of each model. In general G_1, G_2, …, G_n are not independent of each other; i.e., they may be functions of each other. Nevertheless the functions F_1, F_2, …, F_n can be approximated from the experimental results through the following procedure. Taking the derivative of Eq. (B-2) with respect to G_1 yields

$$\frac{\partial \xi}{\partial G_1} = \frac{dF_1(G_1)}{dG_1} + \frac{dF_2(G_2)}{dG_2}\frac{\partial G_2}{\partial G_1} + ... + \frac{dF_n(G_n)}{dG_n}\frac{\partial G_n}{\partial G_1} \tag{B-3}$$

Rearranging and integrating both sides produces

$$F_1(G_1) = \int_{G_{1i}}^{G_{1f}} \left[\frac{\partial \xi}{\partial G_1} - \frac{dF_2}{dG_2}\frac{\partial G_2}{\partial G_1} - ... - \frac{dF_n}{dG_n}\frac{\partial G_n}{\partial G_1} \right] dG_1 \tag{B-4}$$

where G_{1i} and G_{1f} are the initial and final G_1, respectively. Consequently the functions F_i are

$$
\begin{aligned}
F_1(G_1) &= \int_{G_{1i}}^{G_{1f}} \left[\frac{\partial \xi}{\partial G_1} - \frac{dF_2}{dG_2}\frac{\partial G_2}{\partial G_1} - \ldots - \frac{dF_n}{dG_n}\frac{\partial G_n}{\partial G_1} \right] dG_1, \\
F_2(G_2) &= \int_{G_{2i}}^{G_{2f}} \left[\frac{\partial \xi}{\partial G_2} - \frac{dF_1}{dG_1}\frac{\partial G_1}{\partial G_2} - \ldots - \frac{dF_n}{dG_n}\frac{\partial G_n}{\partial G_2} \right] dG_2, \\
&\ldots, \\
F_n(G_n) &= \int_{G_{ni}}^{G_{nf}} \left[\frac{\partial \xi}{\partial G_n} - \frac{dF_1}{dG_1}\frac{\partial G_1}{\partial G_n} - \ldots - \frac{dF_{n-1}}{dG_{n-1}}\frac{\partial G_{n-1}}{\partial G_n} \right] dG_n
\end{aligned}
\qquad \text{(B-5)}
$$

If the functions G_i are independent or weakly dependent, Equation (B-5) becomes

$$
F_1(G_1) = \int_{G_{1i}}^{G_{1f}} \frac{\partial \xi}{\partial G_1} dG_1,\ F_2(G_2) = \int_{G_{2i}}^{G_{2f}} \frac{\partial \xi}{\partial G_2} dG_2,\ \ldots,\ F_n(G_n) = \int_{G_{ni}}^{G_{nf}} \frac{\partial \xi}{\partial G_n} dG_n \qquad \text{(B-6)}
$$

Therefore experimental impedance results should be plotted against each of these non-dimensional groups G_1, G_2, …, G_n.

Appendix C: Alternate Experimental Fit to Bias Flow Impedance Model

Another method of determining the functions $F_i(G_i)$ is to assume their form and use a least squares fit criterion. Assume the following form for F_i [1]

$$F_i(G_i) = a_i G_i + e_i \tag{C-1}$$

where a_i and e_i are an unknown constant and random error corresponding to the non-dimensional group i, respectively, to be determined from experimental results. Double subscripted notation is now introduced, where the first and second index indicates the non-dimensional group number and experiment number, respectively. For example G_{12} indicates the value of dimensionless group 1 for the second experiment. In what follows the subscript in the single subscripted quantities indicate parameter variations. For example, ξ_i indicates non-dimensional experimental value i and a_j indicates a constant associated with group j. Notice, that although both indices are the first indices in these variables, they mean different things. Letting the square of the errors be e^2 and applying the relationships just mentioned produces

$$\begin{aligned} e^2 = {} & (\xi_1 - a_1 G_{11} - a_2 G_{21} - \ldots - a_n G_{n1})^2 + (\xi_2 - a_1 G_{12} - a_2 G_{22} - \ldots - a_n G_{n2})^2 \\ & + \ldots + (\xi_m - a_1 G_{1m} - a_2 G_{2m} - \ldots - a_n G_{nm})^2 \end{aligned} \tag{C-2}$$

for n dimensionless groups, and m experimental values. To minimize these errors, the partial derivative of e^2 with respect to a_i is taken and set to zero. Doing this yields

$$\begin{aligned} \frac{\partial e^2}{\partial a_i} = {} & 2(\xi_1 - a_1 G_{11} - a_2 G_{21} - \ldots - a_n G_{n1}) G_{i1} + 2(\xi_2 - a_1 G_{12} - a_2 G_{22} - \ldots - a_n G_{n2}) G_{i2} \\ & + \ldots + 2(\xi_m - a_1 G_{1m} - a_2 G_{2m} - \ldots - a_n G_{nm}) G_{im} = 0 \end{aligned} \tag{C-3}$$

Rewriting Eq. (C-3) in summation notation results in

$$a_1 \sum_{j=1}^{m} G_{1j} G_{ij} + a_2 \sum_{j=1}^{m} G_{2j} G_{ij} + \ldots + a_n \sum_{j=1}^{m} G_{nj} G_{ij} = \sum_{j=1}^{m} \xi_j G_{ij} \qquad \text{(C-4)}$$

This is the equation for group i. For n dimensionless groups Eq. (C-4) in matrix form becomes:

$$\begin{bmatrix} \sum_{j=1}^{m} G_{1j} G_{1j} & \sum_{j=1}^{m} G_{2j} G_{1j} & \ldots & \sum_{j=1}^{m} G_{nj} G_{1j} \\ \sum_{j=1}^{m} G_{1j} G_{2j} & \sum_{j=1}^{m} G_{2j} G_{2j} & \ldots & \sum_{j=1}^{m} G_{nj} G_{2j} \\ \ldots & \ldots & \ldots & \ldots \\ \sum_{j=1}^{m} G_{1j} G_{nj} & \sum_{j=1}^{m} G_{2j} G_{nj} & \ldots & \sum_{j=1}^{m} G_{nj} G_{nj} \end{bmatrix} \begin{Bmatrix} a_1 \\ a_2 \\ \ldots \\ a_n \end{Bmatrix} = \begin{Bmatrix} \sum_{j=1}^{m} \xi_j G_{1j} \\ \sum_{j=1}^{m} \xi_j G_{2j} \\ \ldots \\ \sum_{j=1}^{m} \xi_j G_{nj} \end{Bmatrix} \qquad \text{(C-5)}$$

Letting G, A, and Z be the first, second and third matrices respectively, of Eq. (C-5) produces

$$[G]\{A\} = \{Z\} \qquad \text{(C-6)}$$

Therefore, A can be found from

$$\{A\} = [G]^{-1}\{Z\} \qquad \text{(C-7)}$$

where $[G]^{-1}$ is the inverse of matrix $[G]$.

Using the least squares approach proved to be difficult to implement. The problem stemmed from the fact that the difference between largest and lowest magnitude dimensionless groups in $[G]$ varied significantly (high matrix condition). Techniques such as singular value decomposition (SVD)[2] were tried and found to be unsuccessful. Therefore another fitting technique was used.

References

1. James, M.L., Smith, G.M., and Wolford, J. C., Applied Numerical Methods for Digital Computation, Harper Collins College Publishers, 1993. pp. 302-305.
2. Strang, G., *Introduction to Applied Mathematics*, Wellesley-Cambridge Press, Wellesley, 1986. pp. 78-79.

Appendix D: Absorption Coefficient

The idea behind modeling bias flow acoustic liners is to be able to use these models to generate an optimally designed absorptive liner. In what follows, it will be shown that absorption coefficients, reflection factors and insertion losses are related to the acoustic intensity. The liner was designed using an incident plane wave analysis as shown in Fig. D-1.

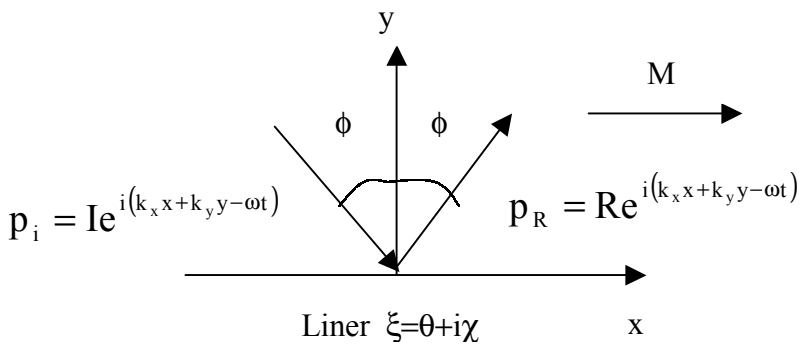

Figure D-1. Plane Wave Model in ZKTL.

I and R in Fig. D-1 stand for the incident and reflected acoustic wave, respectively. M stands for the grazing flow Mach number and note that the $e^{-i\omega\tau}$ convention is now being used for this section only. Using continuity of particle displacement at y=0 results in the following relation for the reflection coefficient, R_f,

$$R_f = \frac{\zeta(1+M\sin\phi)\cos\phi - 1}{\zeta(1+M\sin\phi)\cos\phi + 1} \tag{D-1}$$

where

$$R_f = \frac{R}{I} \tag{D-2}$$

For the normal incidence tube, design M will be zero. For each spectral component, the mean squared pressure is given by

$$\left\langle p^2 \right\rangle = \frac{|I|^2}{2}\left[1 + 2|R_f|\cos\left(\frac{4\pi f}{c}\cos\phi y + \delta\right) + |R_f|^2\right] \tag{D-3}$$

where δ is the phase of R_f. Since the reflected wave is coherent with the incident wave, there is a mixed term as shown in Eq. (D-3) that contributes to the SPL. This causes the pressure field to vary spatially because of interference effects. At y=0, Eq. (D-3) corresponds to the input pressure for ZKTL which is the total acoustic pressure that is held constant during the iteration algorithm. Thus, for a given SPL, changing the liner parameters/configuration changes the ratio of reflected energy to incident energy but has no effect on the SPL values. Minimizing the reflected energy is the goal of the liner design procedure.

The acoustic intensity (time-averaged energy flux) of the incident wave normal to the liner must be conserved which is[1]

$$\left\langle W_{Iy} \right\rangle = \frac{(1 + M\sin\phi)|I|^2\cos\phi}{2\rho c} \tag{D-4}$$

The difference between the incident and reflected intensities represents the energy absorbed by the liner:

$$\left\langle W_{Ty} \right\rangle = \frac{(1 + M\sin\phi)|I|^2\cos\phi}{2\rho c}\left(1 - |R_f|^2\right) \tag{D-5}$$

The absorption coefficient is defined as[2]

$$\alpha = \frac{\left\langle W_{Ty} \right\rangle}{\left\langle W_{Iy} \right\rangle} = 1 - |R_f|^2 \tag{D-6}$$

Substituting Equation (D-1) into Equation (D-6) produces

$$\alpha = \frac{4\theta(1 + M\sin\phi)\cos\phi}{[\theta(1 + M\sin\phi)\cos\phi + 1]^2 + [\chi(1 + M\sin\phi)\cos\phi]^2} \tag{D-7}$$

which is the relation used in ZKTL to compute the absorption coefficient. Also, in ZKTL the "R.F." that is computed is equivalent to

$$\text{R.F.} = 1 - \alpha = |R_f|^2 \tag{D-8}$$

which is the ratio of reflected energy to incident energy, $\langle W_{Ry} \rangle / \langle W_{Iy} \rangle$. The insertion loss, "I. L.", computed by the code is

$$\text{I.L.} = 10\log\left(|R_f|^2\right) = 10\log\left(\frac{\langle W_{Ry} \rangle}{\langle W_{Iy} \rangle}\right) \tag{D-9}$$

Thus, an optimum liner requires maximum α, minimum R.F. and maximum I.L.

References

1. Kelly, J. J., "A Generalized Approach to Acoustic Intensity," *Journal of the Acoustical Society of America*, Vol. 83, No. 6, June 1988.
2. Pierce, A. D., Acoustics: An Introduction to Its Physical Principles and Applications, McGraw-Hill, New York, 1981, p. 109.

Appendix E: High Resistance Fibermetal Determination Methods

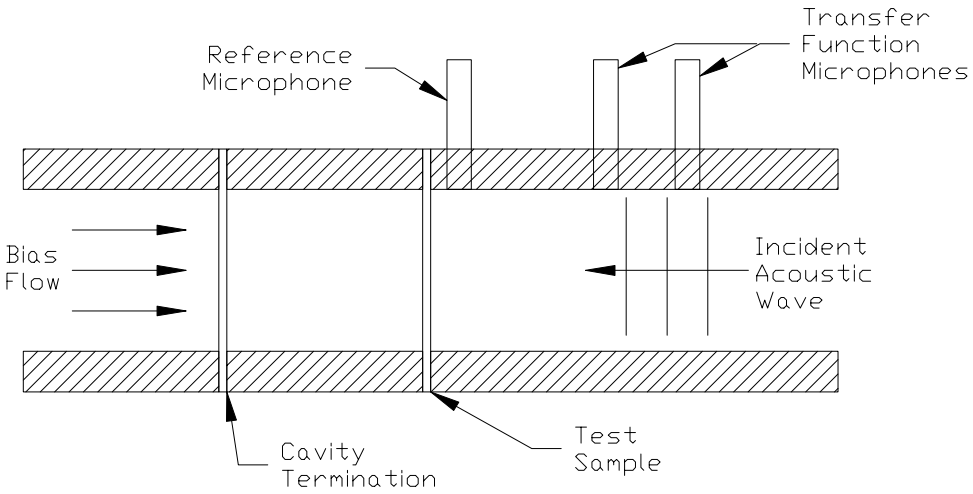

	Indirect Method
Test 1:	
Test Sample:	Perforate sheet
Cavity Termination:	Hardwall
Bias Flow:	Off
Test 2:	
Test Sample:	Perforate sheet
Cavity Termination:	High resistance fibermetal sheet
Bias Flow:	On
	Direct Method I
Test Sample:	High resistance fibermetal sheet
Cavity Termination:	Hardwall
Bias Flow:	Off
	Direct Method II
Test Sample:	Open (no sample installed)
Cavity Termination:	High resistance fibermetal sheet
Bias Flow:	On

Figure E-1. Summary sketch of three methods used to determine acoustic resistance of fibermetal sheet.

4.5.1 Indirect Acoustic Method

A low resistance perforate was tested in the normal incidence tube using two configurations. For the first configuration, the perforate had a cavity with a hardwall termination. For the other, the termination was the high resistance fibermetal under investigation, which could allow bias flow to be passed through the tube. Using the NS-TMM method described earlier, the acoustic impedance of the perforate sample was determined for each of these configurations.

The impedance measured at the surface of the perforated plate for the hardwall termination is given as ξ_{s1}. Similarly, the impedance measured with the fibermetal termination is ξ_{s2}. These two impedances are the sum of the individual impedances of each liner element; i.e.,

$$\xi_{s1} = \xi_p + \xi_{cw} \tag{E-1}$$

$$\xi_{s2} = \xi_p + \xi_{cf} \tag{E-2}$$

where ξ_p is the perforate impedance, and ξ_{cw} and ξ_{cf} are the cavity impedances with the hardwall and fibermetal terminations, respectively. For this method to work ξ_p must be independent of the test configuration. The only way to assure ξ_p is constant is for the perforate to be linear (independent of SPL and bias flow). Tests were conducted over the bias flow and SPL range of interest in this study with the high resistance fibermetal termination installed. The results of these tests indicated that the selected perforate sample was acceptably linear.

Subtracting Eq. (E-1) from (E-2) and solving for ξ_{cf} produces

$$\xi_{cf} = \xi_{cw} + \xi_{s2} - \xi_{s1} \tag{E-3}$$

This is the cavity impedance with the fibermetal backing. The cavity impedance due to the hardwall is given by

$$\xi_{cw} = -iCot(kL) \tag{E-4}$$

where L is the cavity length, and k the wave number. The lumped-element impedance of the fibermetal ξ_f is related to the cavity impedance with the fibermetal termination ξ_{cf} by the following relationship

$$\xi_f = -\frac{(\xi_{cf}-1)e^{i(k_i+k_r)L} + (\xi_{cf}+1)}{(\xi_{cf}-1)e^{i(k_i+k_r)L} - (\xi_{cf}+1)} \tag{E-5}$$

where the wave numbers k_i and k_r are

$$k_i = \frac{k}{1+M}$$
$$k_r = \frac{k}{1-M} \tag{E-6}$$

and M is the Mach number in the duct.

The major advantage of this method is that ξ_{s1} and ξ_{s2} can be measured accurately. Measurements near nulls of large standing waves are avoided by properly choosing the perforate material, consequently improving the accuracy of the measurement. Perhaps more importantly, bias flow effects on the fibermetal impedance can be studied. The major disadvantage of this method is that more measurements and calculations are required to determine the impedance of the fibermetal.

4.5.2 Direct Acoustic Methods

There are two ways to measure the fibermetal impedance directly. In Method I the fibermetal sheet under investigation is installed as the "test sample" in the NIT, with a

hardwall termination. The NS-TMM method is then used to measure the normal incidence acoustic impedance. This method offers the advantage of requiring only a single measurement, and consequently is a fast method for determining the impedance properties of the fibermetal. Its main disadvantage is the inability to measure how bias flow affects the fibermetal impedance.

In Method II the fibermetal under investigation is used as the cavity termination. For this method, no sample is installed; thus, the cavity is left open. The fibermetal impedance is determined using Eq. (E-5), where ξ_{cf} and ξ_f are the measured impedance at the standard test plane (where sample surface is typically located) and fibermetal lumped-element impedance, respectively. The advantage of Method II is the single-step process in measuring the impedance of the fibermetal. Furthermore, this method allows for the determination of bias flow effects on the impedance of the fibermetal. The major disadvantage to this method is the potential for measuring near nulls of large standing waves, with the accompanying increased potential for measurement error due to large changes in SPL over the diameter of the measurement microphone.

4.5.3 Raylometer Method

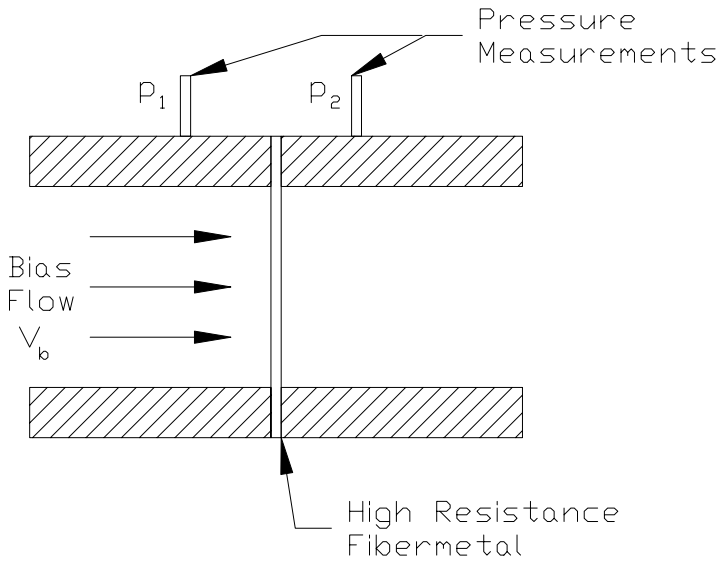

Figure E-2. Raylometer experimental setup for determining fibermetal resistance (Raylometer Method).

The raylometer measures the DC flow resistance of the high resistance fibermetal backing. Figure E-2 shows the typical experimental setup utilized for this experiment. The non-dimensional resistance, θ, is

$$\theta = \frac{p_1 - p_2}{\rho c V_b} \tag{E-7}$$

where p_1, p_2, V_b, ρ, and c are the pressure reading before the fibermetal, pressure reading after the fibermetal, velocity in the duct, fluid density, and the speed of sound, respectively. The flow resistance is assumed to be a linear function of velocity of the form

$$\theta = A + B\frac{V_b}{c} \tag{E-8}$$

Several values of flow resistance versus flow velocity were acquired in this experiment. These values were then curve-fitted to determine A and B.

The advantage of using the raylometer is the speed of acquiring the data. The disadvantage is the assumption that the resistance of a DC flow measurement is equivalent to the real part of the acoustic impedance. This assumption is not entirely correct because frequency dependence is ignored.

Appendix F: Dynamic C_D

Jing and Sun[1] took issue with the empirical nature of the determination of C_D. Their model showed that the formation of the vena contracta is a time dependent problem in the presence of an acoustic field, and determined an approximate steady state value of 0.61 for C_D. This value of C_D is lower than the normally measured experimental value of 0.76 or higher. Jing and Sun did not account for the presence of mean flow, and therefore the variation of C_D with increasing bias flow is not known and is an area of potential future research.

For this study, the C_D used for the model predictions, except for the compressible model results, was a measured raylometer C_D. This approach may be questionable but it has been ingrained in this field for nearly three decades. The value of C_D greatly affects the predicted results and in general it is a function of frequency, SPL, etc. Tradition and the empirical nature of this field (more than physics) has generally resulted in the use of a constant C_D in previous studies. Figures F-1 to F-9 show the PBFIF model resistance error criteria sensitivity to C_D's of 0.76, 0.66, and 0.86 for 5, 10, and 15 POA, respectively. These plots show significant variation in the results depending on the value of C_D used. Therefore, the accurate determination of this variable and consequently an increased understanding of the physics of this variable in the presence of an acoustic field with mean flow is an important area of future research.

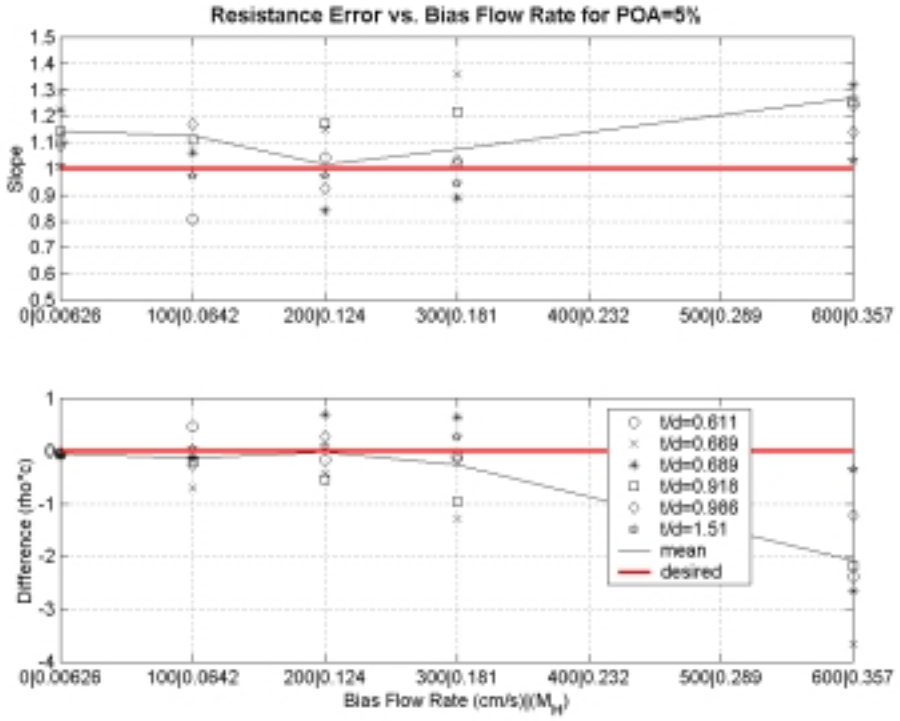

Figure F-1. PBFIF model resistance error criteria for POA=5 and C_D=0.76.

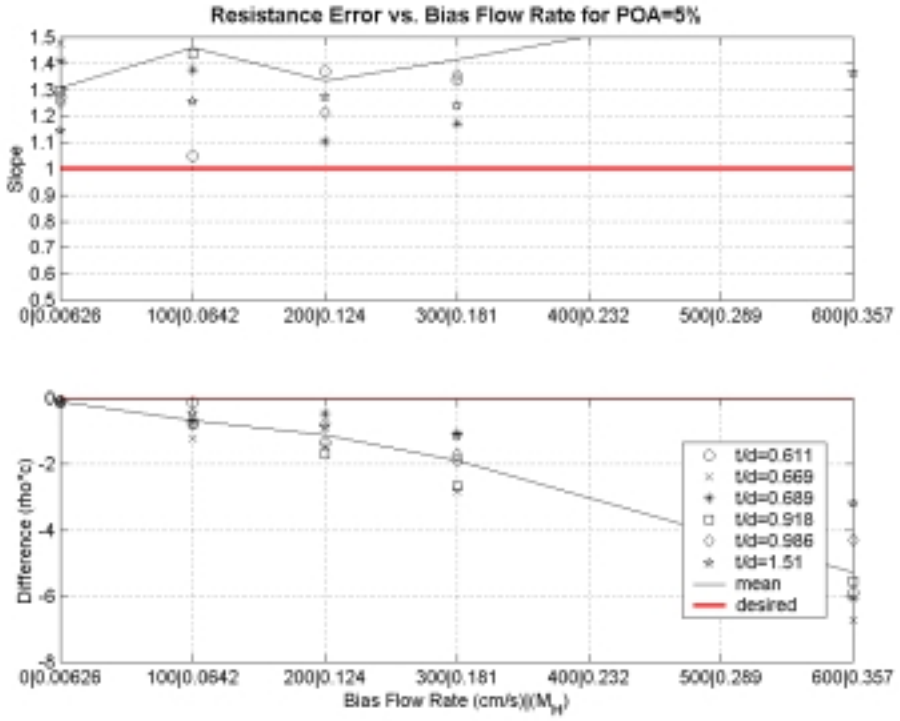

Figure F-2. PBFIF model resistance error criteria for POA=5 and C_D=0.66.

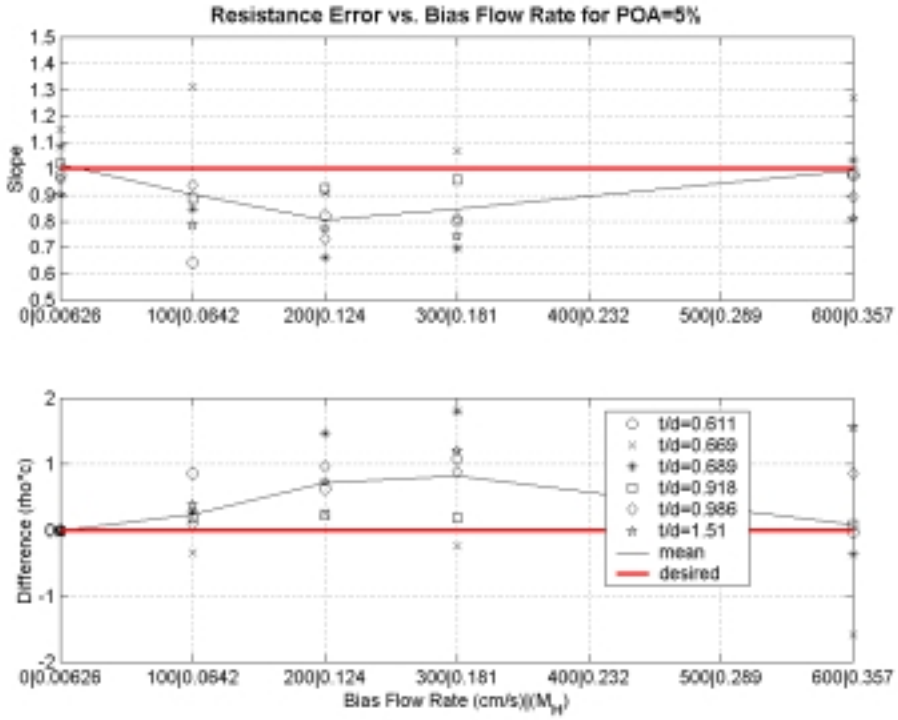

Figure F-3. PBFIF model resistance error criteria for POA=5 and C_D=0.86.

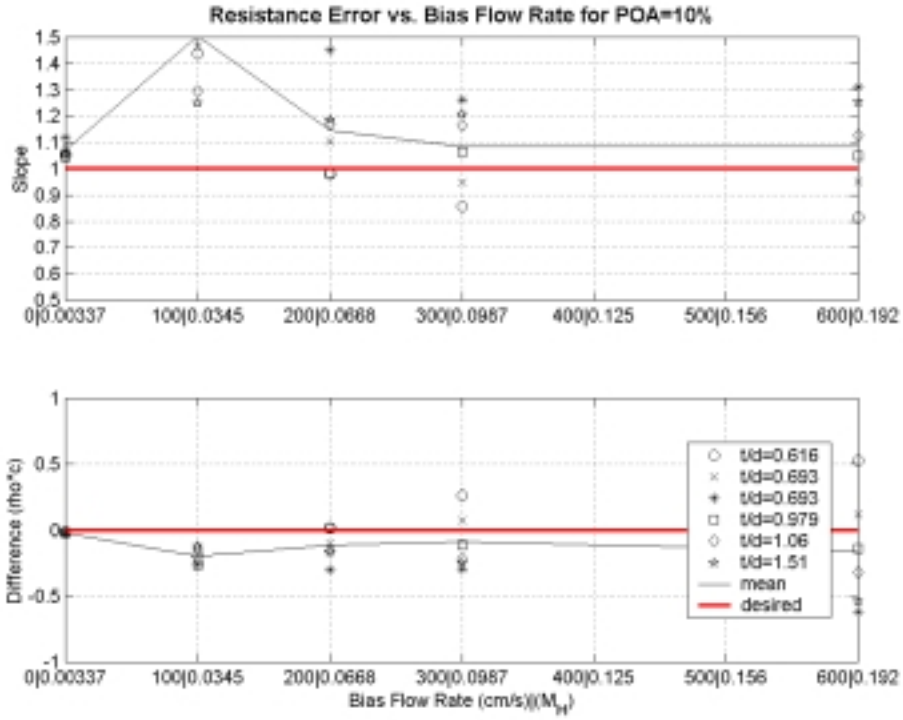

Figure F-4. PBFIF model resistance error criteria for POA=10 and C_D=0.76.

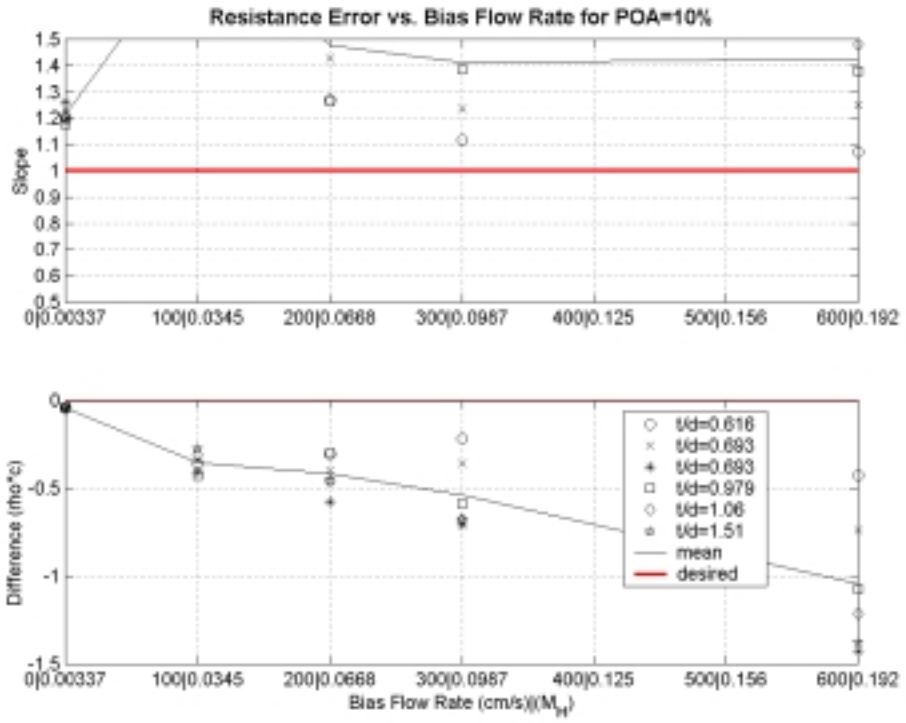

Figure F-5. PBFIF model resistance error criteria for POA=10 and C_D=0.66.

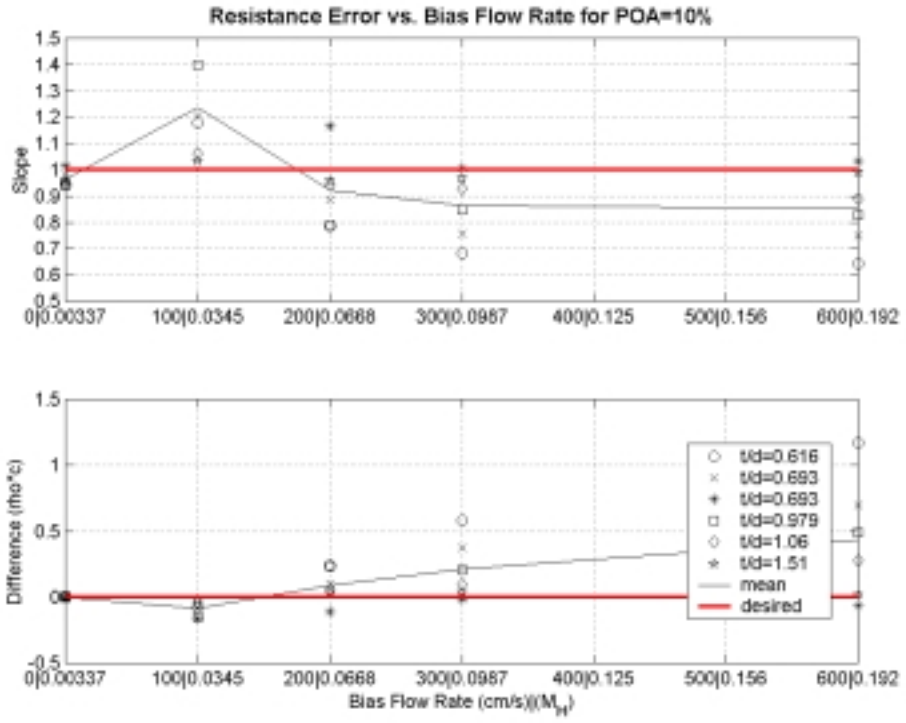

Figure F-6. PBFIF model resistance error criteria for POA=10 and C_D=0.86.

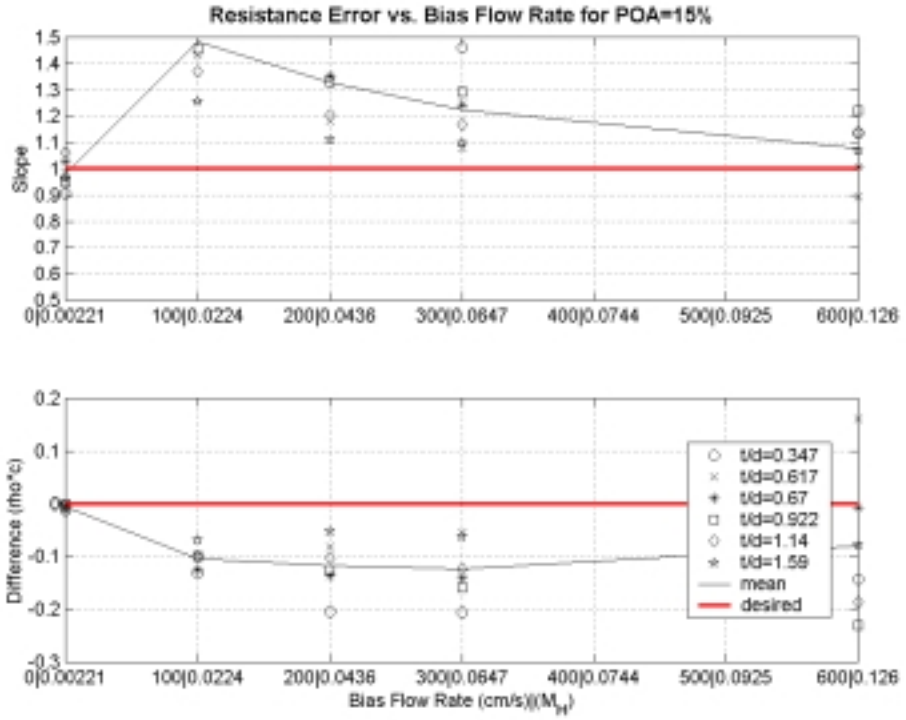

Figure F-7. PBFIF model resistance error criteria for POA=15 and C_D=0.76.

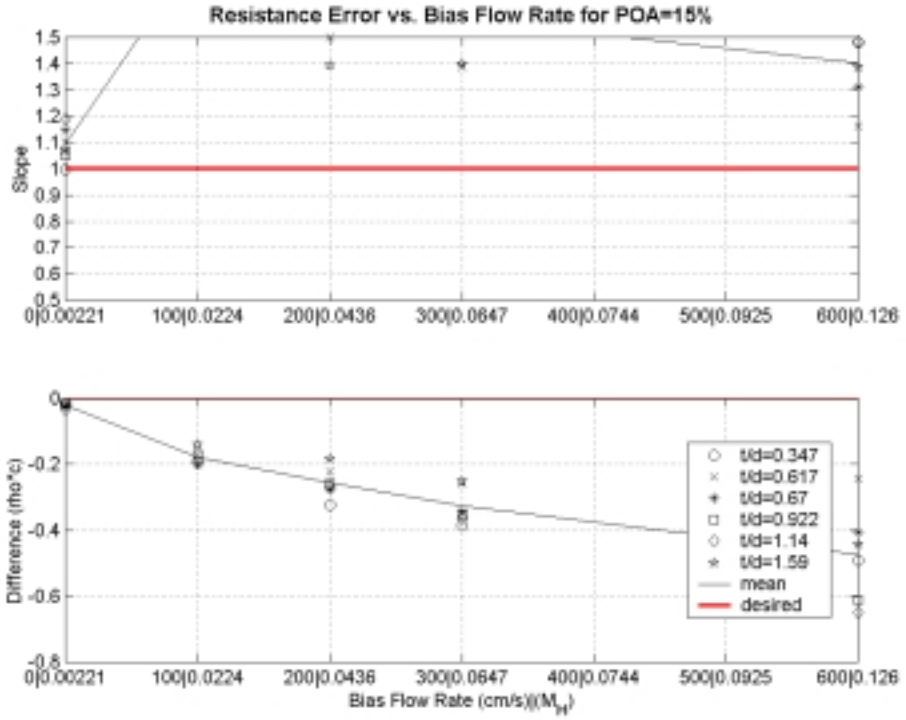

Figure F-8. PBFIF model resistance error criteria for POA=15 and C_D=0.66.

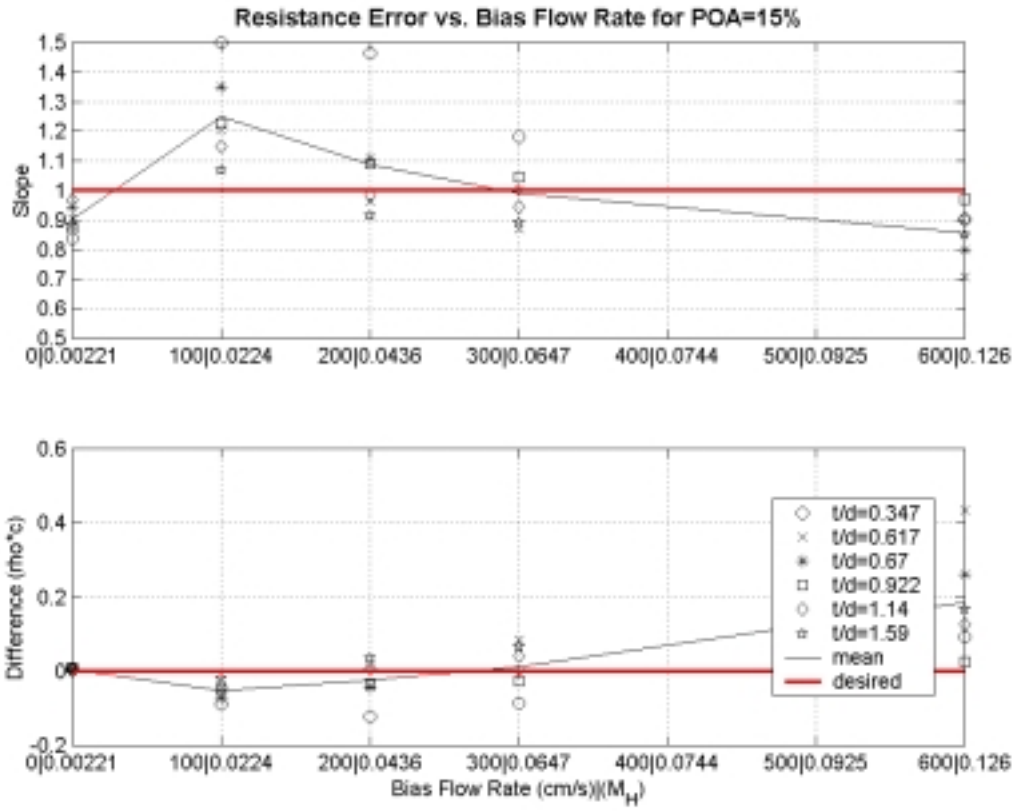

Figure F-9. PBFIF model resistance error criteria for POA=15 and C_D=0.86.

References

1. Jing, X. and Sun, X., "Numerical Simulation on the Nonlinear Acoustic Properties of an Orifice," AIAA-99-1878.

Appendix G: Kluge and FITF Raylometer Database

Kluge is an assembled raylometer or "old" raylometer. This raylometer contains four pressure ports to measure the pressure drop across the sample.

FITF is a high-end raylometer with 160 measurement locations, statistical measurement outliers elimination, and curve fitting to minimize tailing effects* near the sample.

The pages that follow provide plots of resistance vs. velocity for the perforated plates samples. Each page contains three plots, where the first, second and third plots provide results using the Kluge, FITF, and Kluge & FITF raylometer results, respectively. C_{DA} and C_{DB} are the calculated by doing a linear regression of the plots, and equating the resultant intercept and slope to (c_1/C_D) and (c_2/C_D), respectively, in Eq. (4-6). This creates two equations, where C_{DA} and C_{DB} are obtained by of solving C_D in the resulting intercept and slope equation, respectively. C_{DBST} is calculated using the procedure outlined in Section 4.6. The C_D used for the prediction was the C_{DBST} of the FITF raylometer.

* Tailing effects is near field effects close to the sample. The pressure field starts tailing (curving) near the sample.

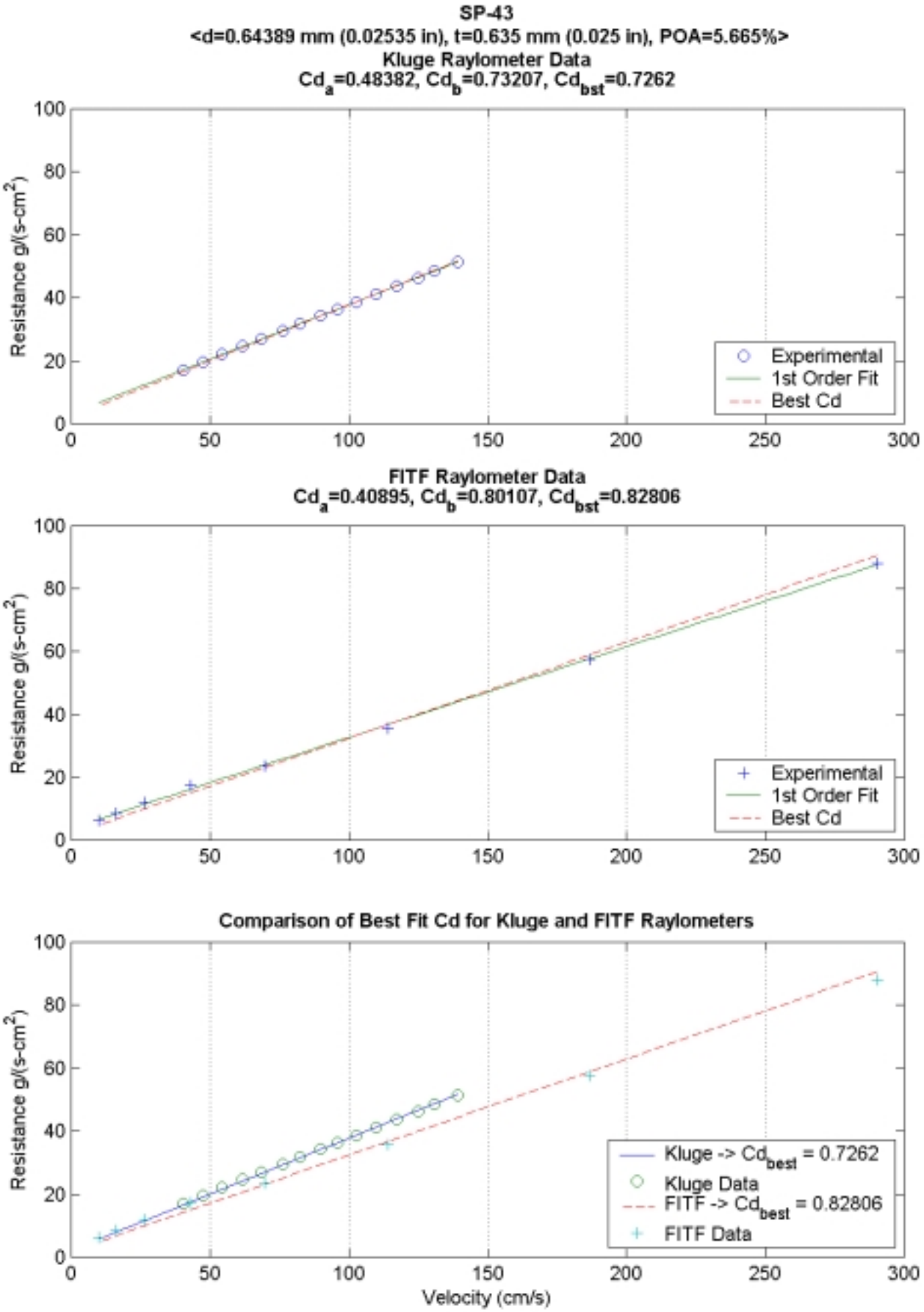
SP-43
<d=0.64389 mm (0.02535 in), t=0.635 mm (0.025 in), POA=5.665%>
Kluge Raylometer Data
Cd_a=0.48382, Cd_b=0.73207, Cd_bst=0.7262
Resistance g/(s-cm^2)
Experimental
1st Order Fit
Best Cd
FITF Raylometer Data
Cd_a=0.40895, Cd_b=0.80107, Cd_bst=0.82806
Resistance g/(s-cm^2)
Experimental
1st Order Fit
Best Cd
Comparison of Best Fit Cd for Kluge and FITF Raylometers
Resistance g/(s-cm^2)
Kluge -> Cd_best = 0.7262
Kluge Data
FITF -> Cd_best = 0.82806
FITF Data
Velocity (cm/s)

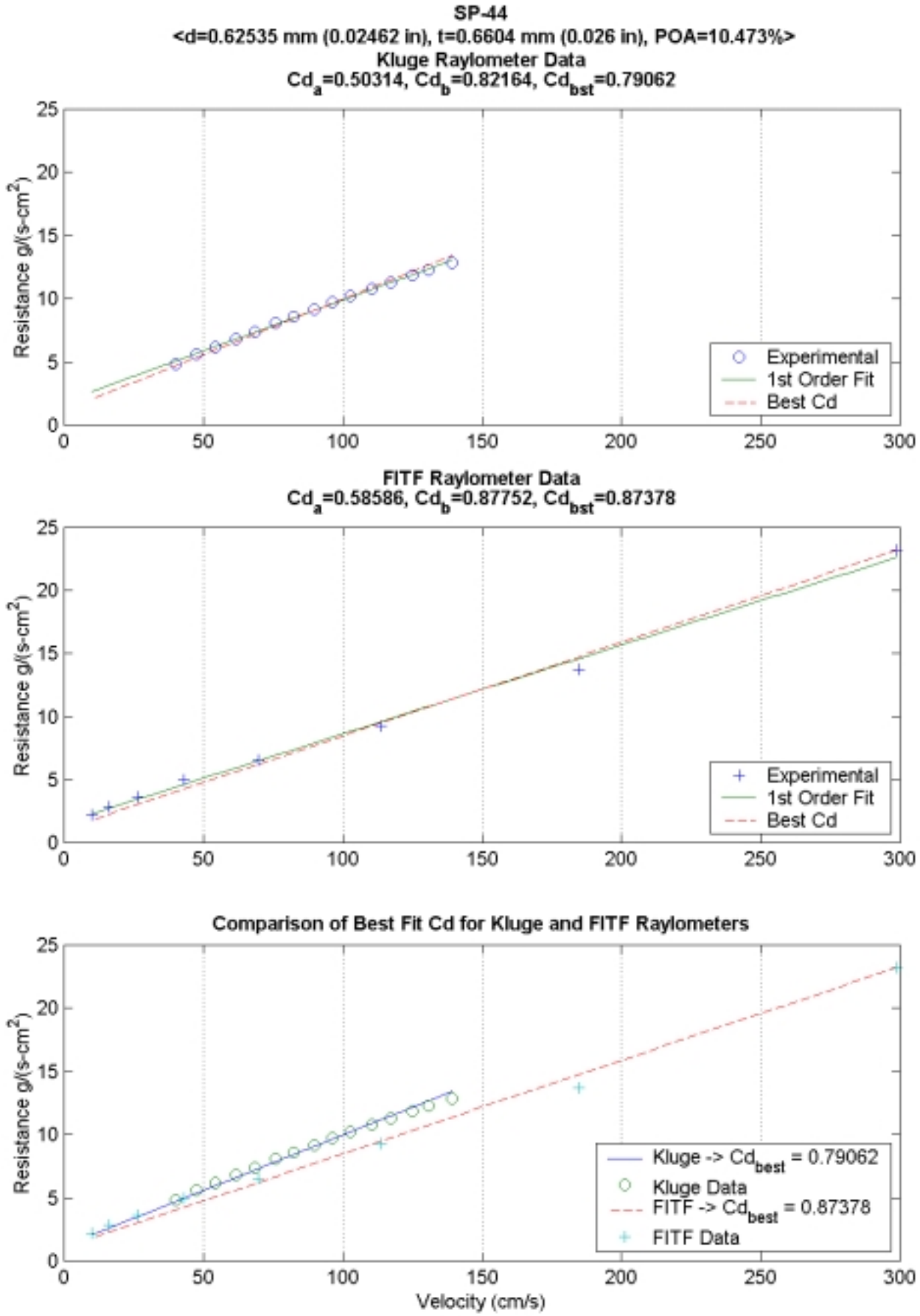
SP-44
<d=0.62535 mm (0.02462 in), t=0.6604 mm (0.026 in), POA=10.473%>
Kluge Raylometer Data
Cd_a=0.50314, Cd_b=0.82164, Cd_bst=0.79062
Resistance g/(s-cm^2)
Experimental
1st Order Fit
Best Cd
FITF Raylometer Data
Cd_a=0.58586, Cd_b=0.87752, Cd_bst=0.87378
Resistance g/(s-cm^2)
Experimental
1st Order Fit
Best Cd
Comparison of Best Fit Cd for Kluge and FITF Raylometers
Resistance g/(s-cm^2)
Kluge -> Cd_best = 0.79062
Kluge Data
FITF -> Cd_best = 0.87378
FITF Data
Velocity (cm/s)

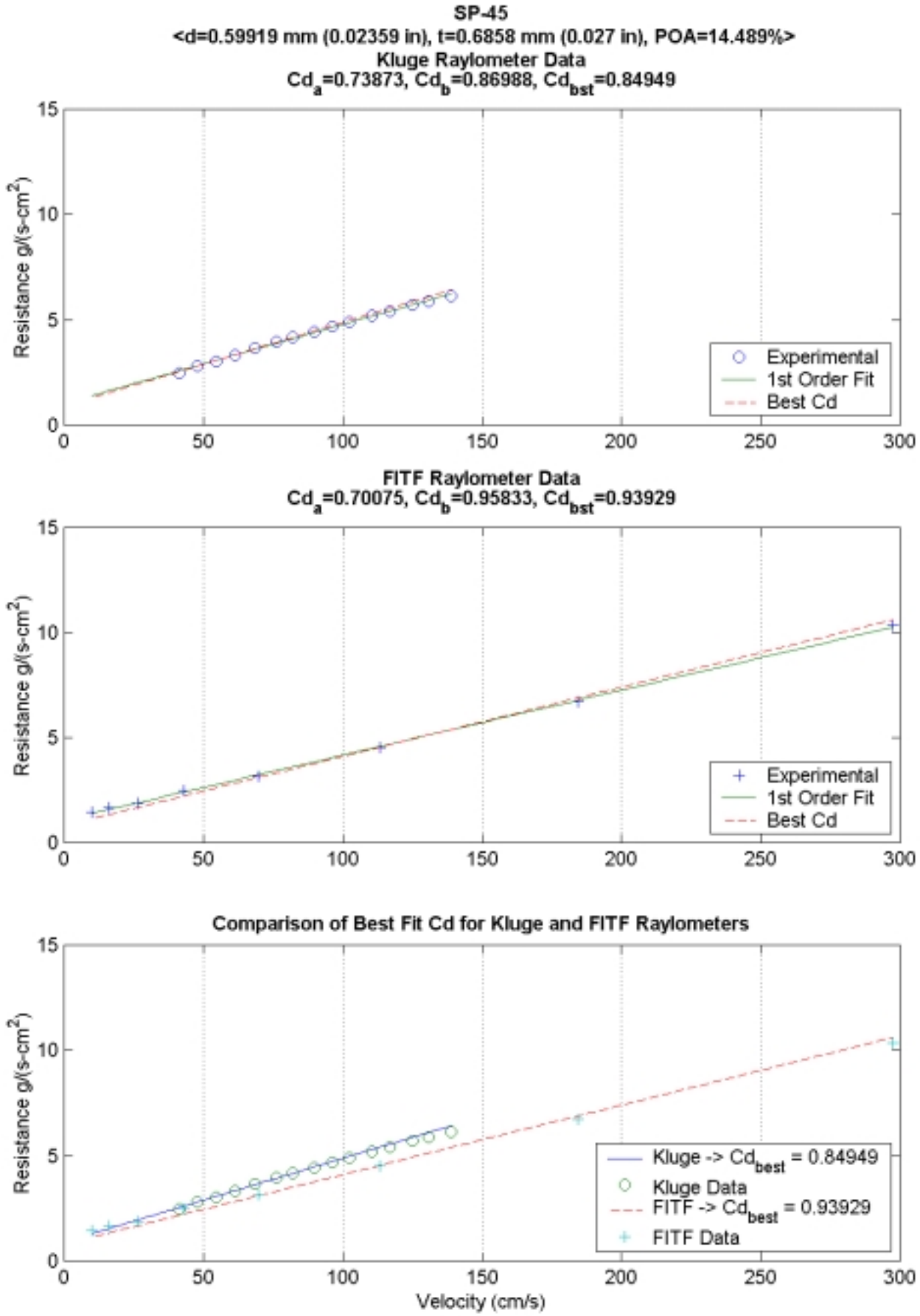
SP-45
<d=0.59919 mm (0.02359 in), t=0.6858 mm (0.027 in), POA=14.489%>
Kluge Raylometer Data
Cd_a=0.73873, Cd_b=0.86988, Cd_bst=0.84949
Resistance g/(s-cm^2)
Experimental
1st Order Fit
Best Cd
FITF Raylometer Data
Cd_a=0.70075, Cd_b=0.95833, Cd_bst=0.93929
Resistance g/(s-cm^2)
Experimental
1st Order Fit
Best Cd
Comparison of Best Fit Cd for Kluge and FITF Raylometers
Resistance g/(s-cm^2)
Kluge -> Cd_best = 0.84949
Kluge Data
FITF -> Cd_best = 0.93929
FITF Data
Velocity (cm/s)

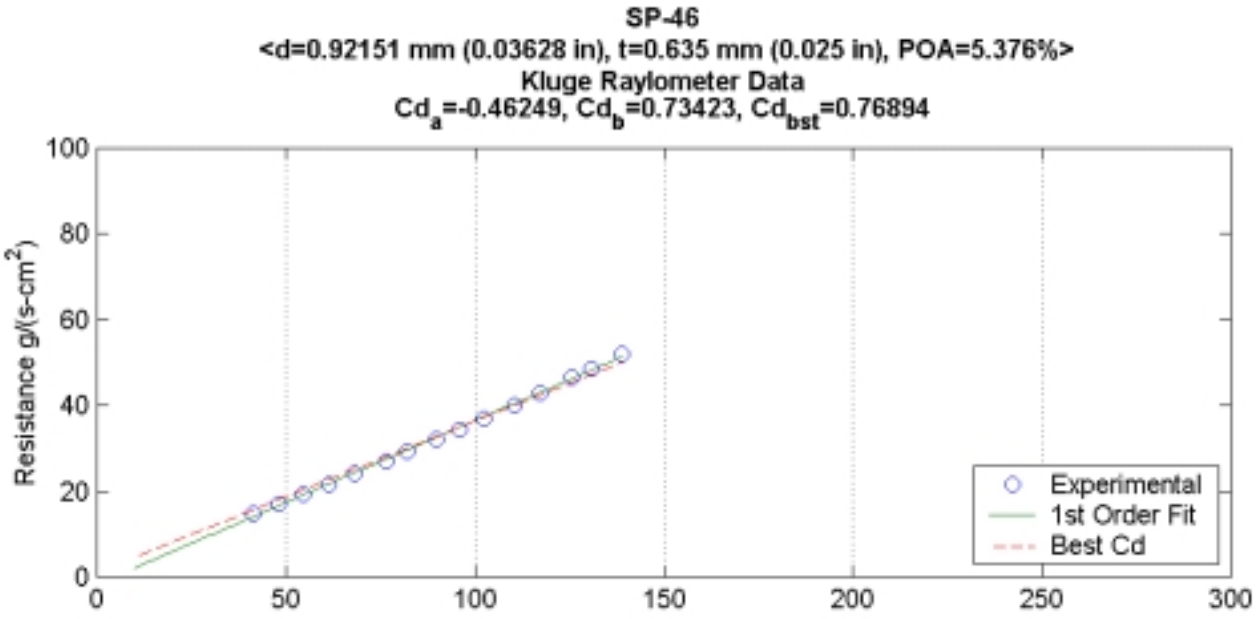
SP-46
<d=0.92151 mm (0.03628 in), t=0.635 mm (0.025 in), POA=5.376%>
Kluge Raylometer Data
Cd_a=-0.46249, Cd_b=0.73423, Cd_bst=0.76894
Resistance g/(s-cm^2)
Experimental
1st Order Fit
Best Cd

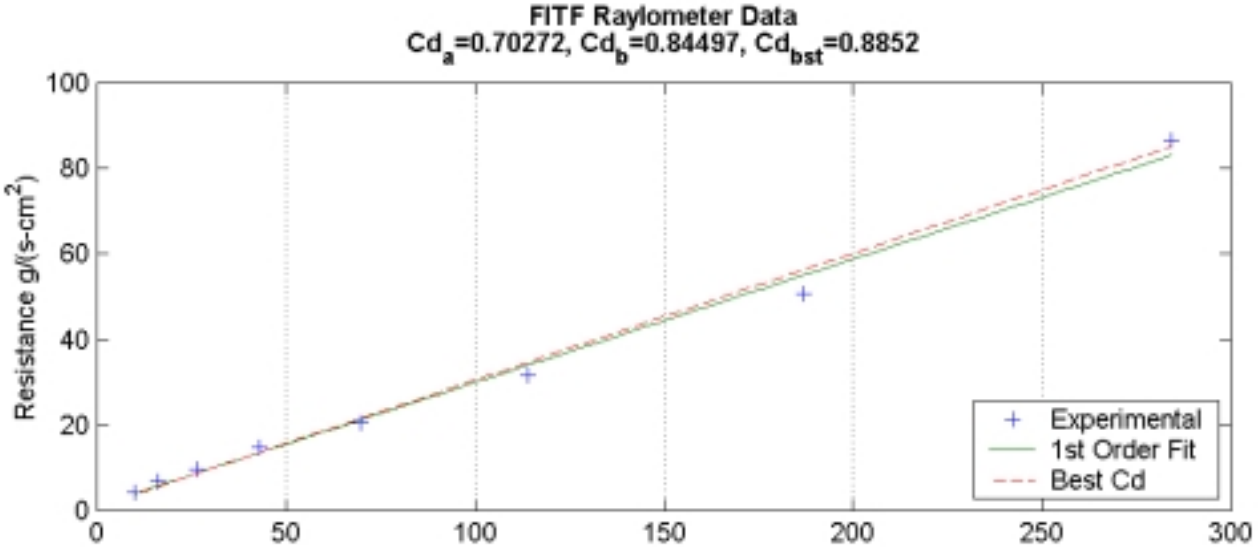
FITF Raylometer Data
Cd_a=0.70272, Cd_b=0.84497, Cd_bst=0.8852
Resistance g/(s-cm^2)
Experimental
1st Order Fit
Best Cd

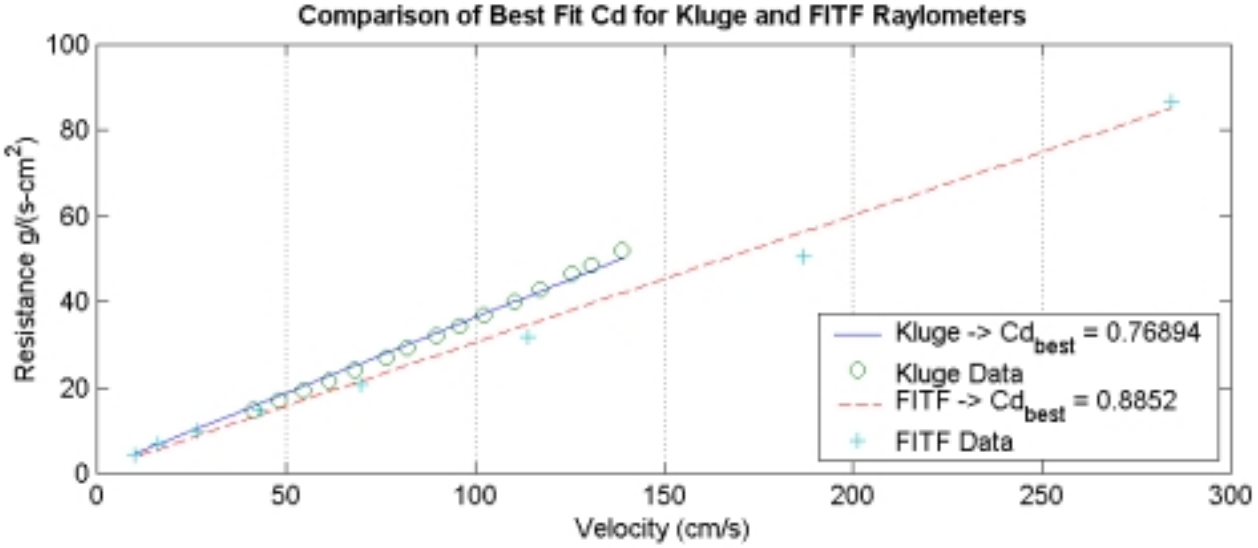
Comparison of Best Fit Cd for Kluge and FITF Raylometers
Resistance g/(s-cm^2)
Velocity (cm/s)
Kluge -> Cd_best = 0.76894
Kluge Data
FITF -> Cd_best = 0.8852
FITF Data

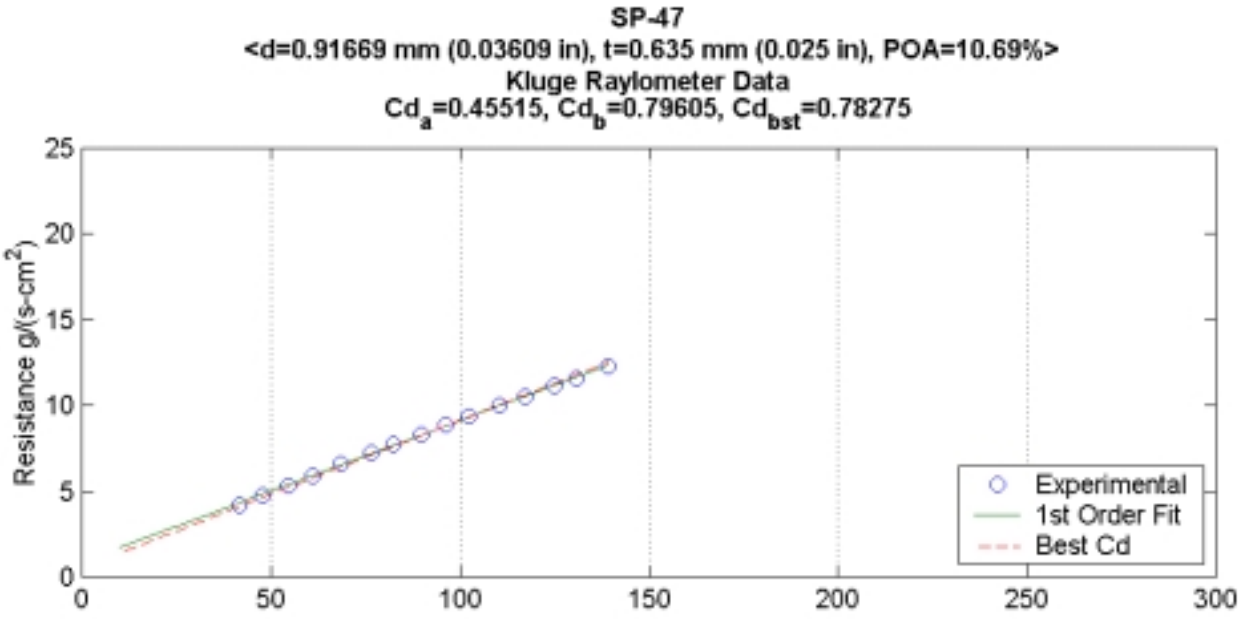
SP-47
<d=0.91669 mm (0.03609 in), t=0.635 mm (0.025 in), POA=10.69%>
Kluge Raylometer Data
Cd_a=0.45515, Cd_b=0.79605, Cd_bst=0.78275
Resistance g/(s-cm^2)
Experimental
1st Order Fit
Best Cd

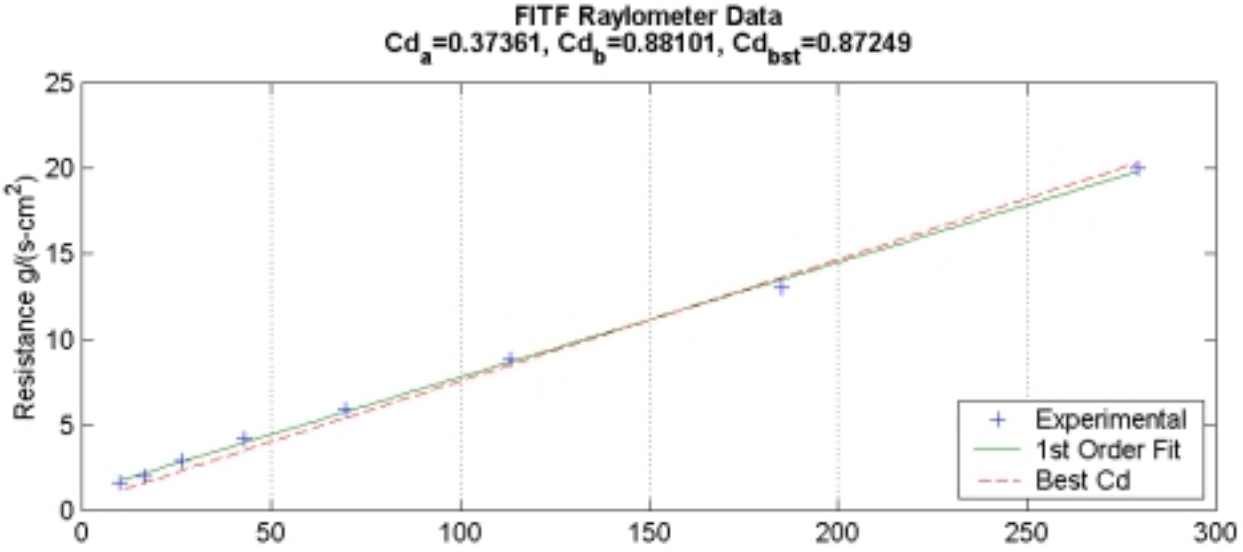
FITF Raylometer Data
Cd_a=0.37361, Cd_b=0.88101, Cd_bst=0.87249
Resistance g/(s-cm^2)
Experimental
1st Order Fit
Best Cd

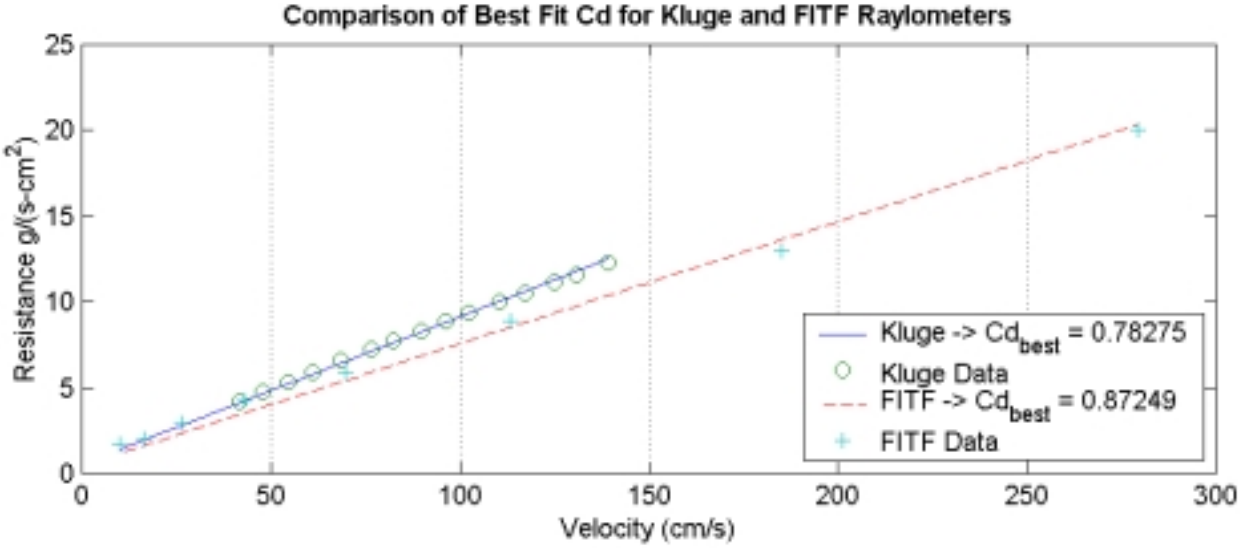
Comparison of Best Fit Cd for Kluge and FITF Raylometers
Resistance g/(s-cm^2)
Kluge -> Cd_best = 0.78275
Kluge Data
FITF -> Cd_best = 0.87249
FITF Data
Velocity (cm/s)

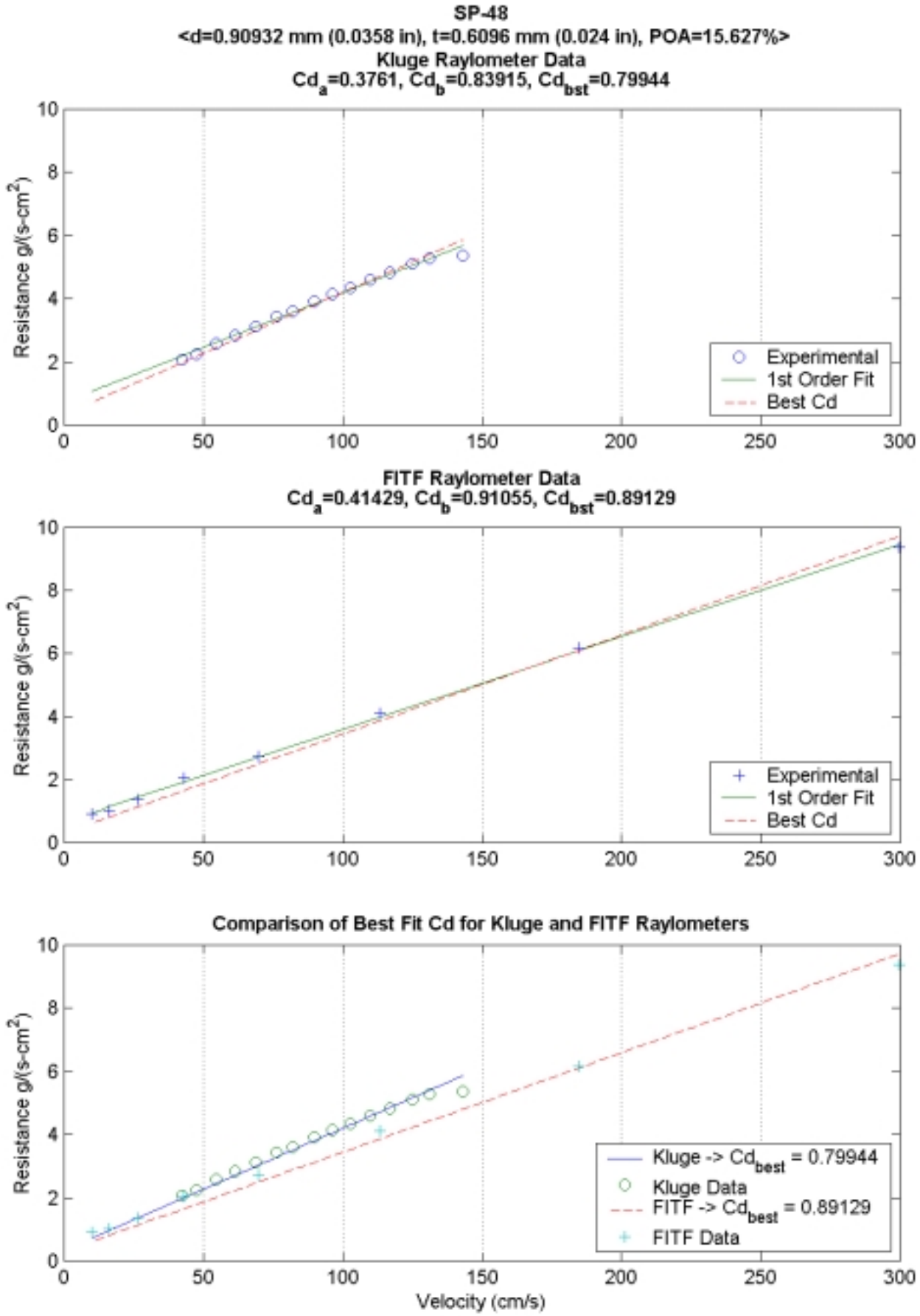
SP-48
<d=0.90932 mm (0.0358 in), t=0.6096 mm (0.024 in), POA=15.627%>
Kluge Raylometer Data
Cd_a=0.3761, Cd_b=0.83915, Cd_bst=0.79944
Resistance g/(s-cm^2)
Experimental
1st Order Fit
Best Cd
FITF Raylometer Data
Cd_a=0.41429, Cd_b=0.91055, Cd_bst=0.89129
Resistance g/(s-cm^2)
Experimental
1st Order Fit
Best Cd
Comparison of Best Fit Cd for Kluge and FITF Raylometers
Resistance g/(s-cm^2)
Kluge -> Cd_best = 0.79944
Kluge Data
FITF -> Cd_best = 0.89129
FITF Data
Velocity (cm/s)

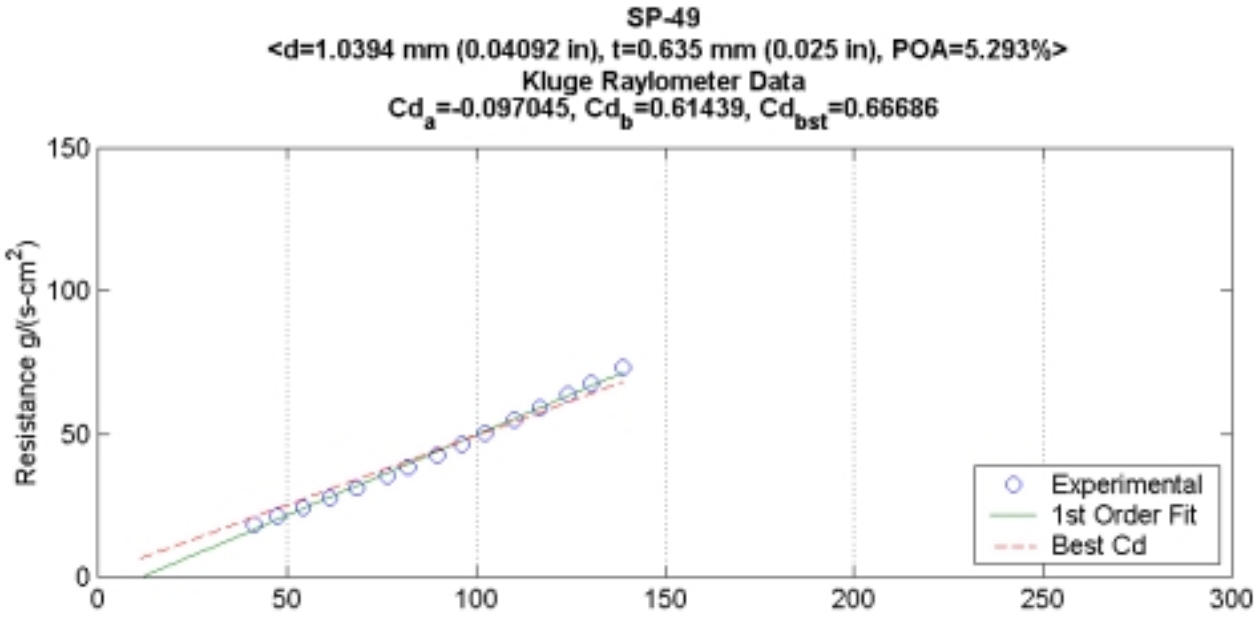
SP-49
<d=1.0394 mm (0.04092 in), t=0.635 mm (0.025 in), POA=5.293%>
Kluge Raylometer Data
Cd_a=-0.097045, Cd_b=0.61439, Cd_bst=0.66686
Resistance g/(s-cm^2)
Experimental
1st Order Fit
Best Cd

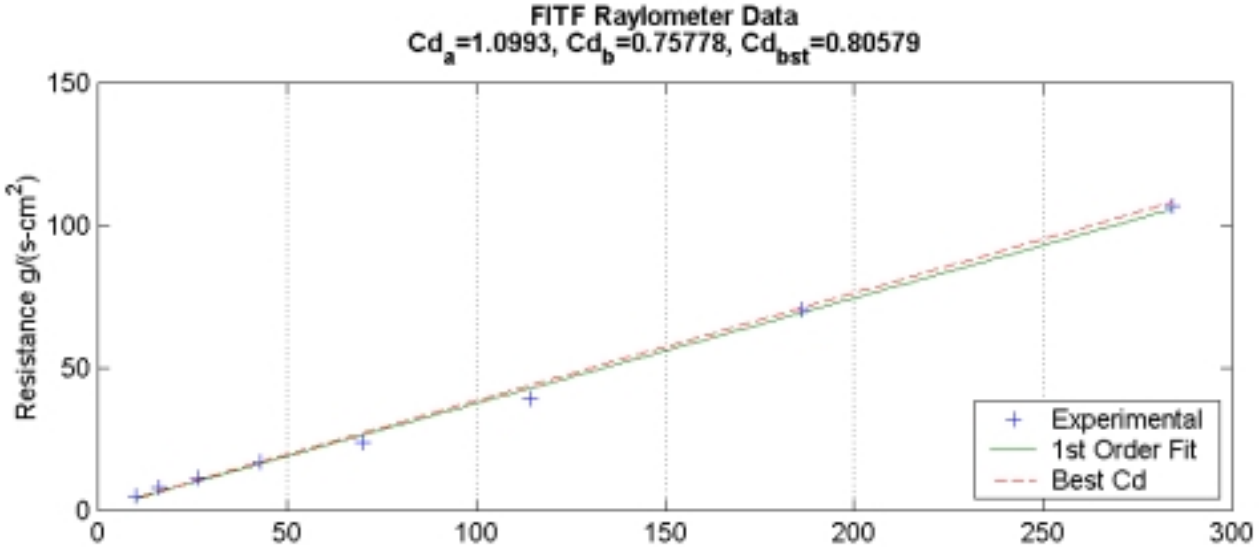
FITF Raylometer Data
Cd_a=1.0993, Cd_b=0.75778, Cd_bst=0.80579
Resistance g/(s-cm^2)
Experimental
1st Order Fit
Best Cd

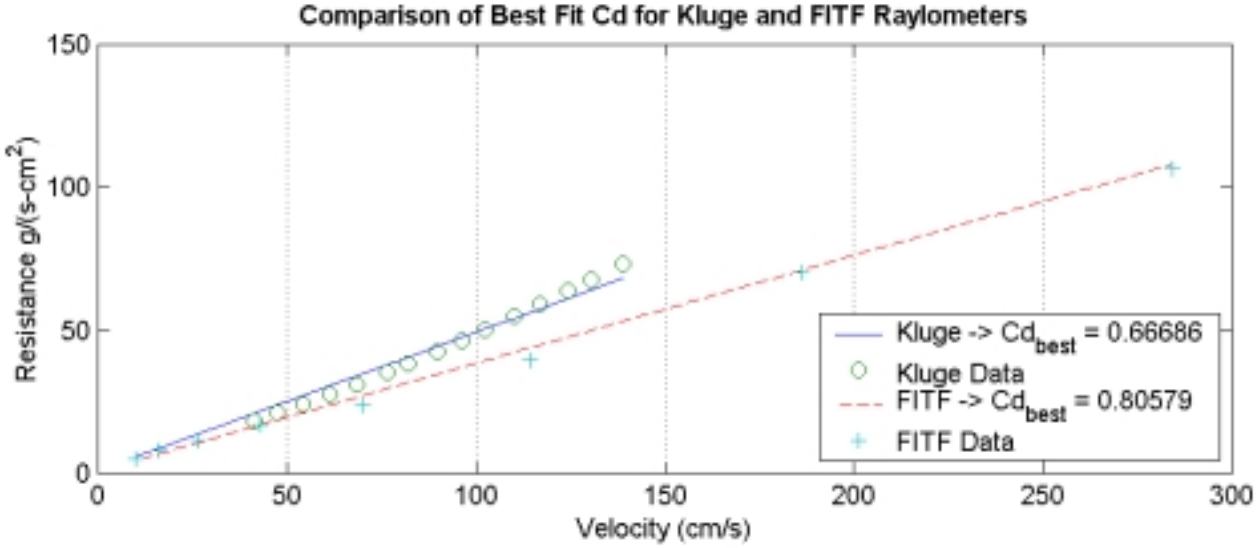
Comparison of Best Fit Cd for Kluge and FITF Raylometers
Resistance g/(s-cm^2)
Kluge -> Cd_best = 0.66686
Kluge Data
FITF -> Cd_best = 0.80579
FITF Data
Velocity (cm/s)

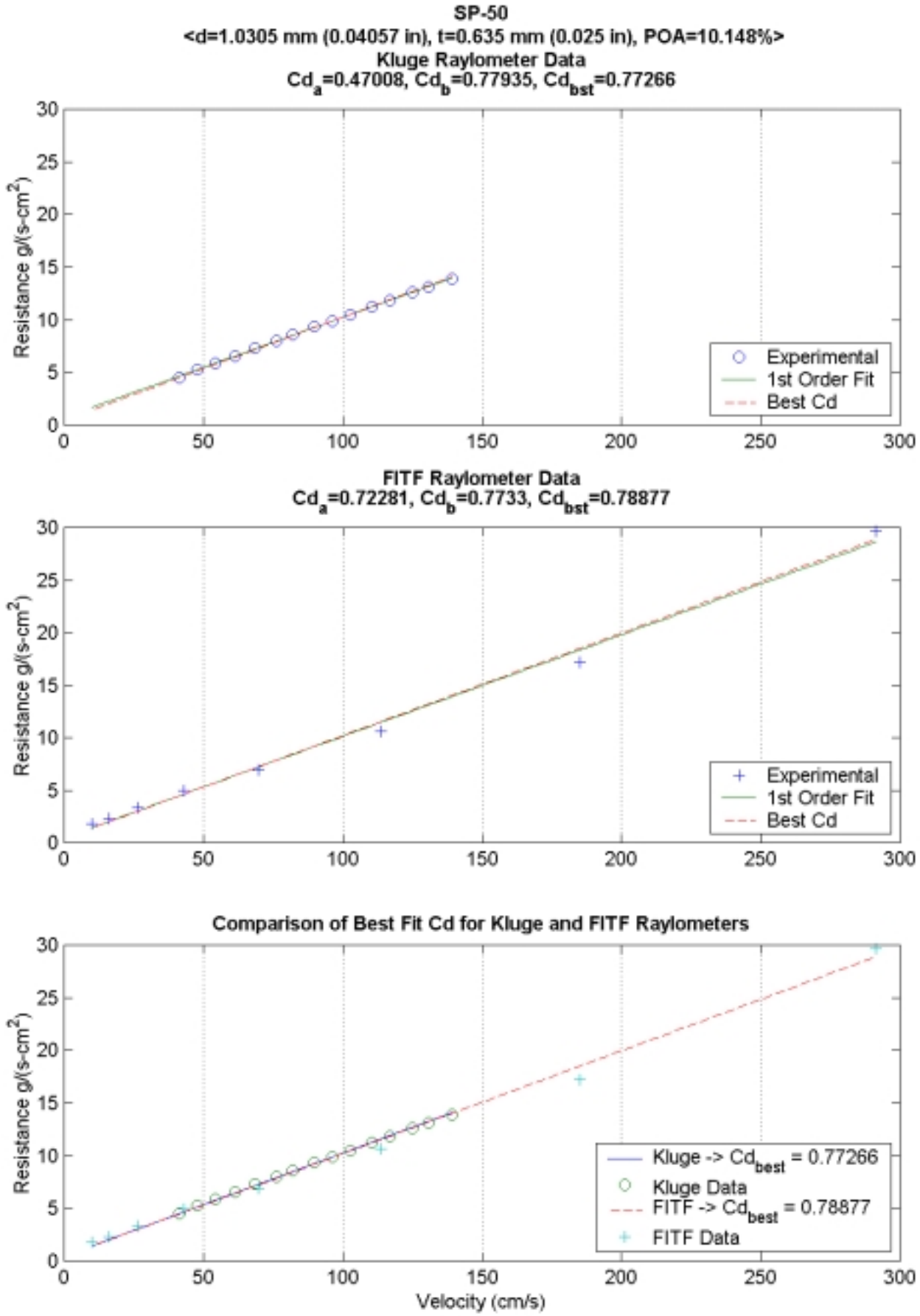
SP-50
<d=1.0305 mm (0.04057 in), t=0.635 mm (0.025 in), POA=10.148%>
Kluge Raylometer Data
Cd_a=0.47008, Cd_b=0.77935, Cd_bst=0.77266
Resistance g/(s-cm^2)
Experimental
1st Order Fit
Best Cd
FITF Raylometer Data
Cd_a=0.72281, Cd_b=0.7733, Cd_bst=0.78877
Resistance g/(s-cm^2)
Experimental
1st Order Fit
Best Cd
Comparison of Best Fit Cd for Kluge and FITF Raylometers
Resistance g/(s-cm^2)
Kluge -> Cd_best = 0.77266
Kluge Data
FITF -> Cd_best = 0.78877
FITF Data
Velocity (cm/s)

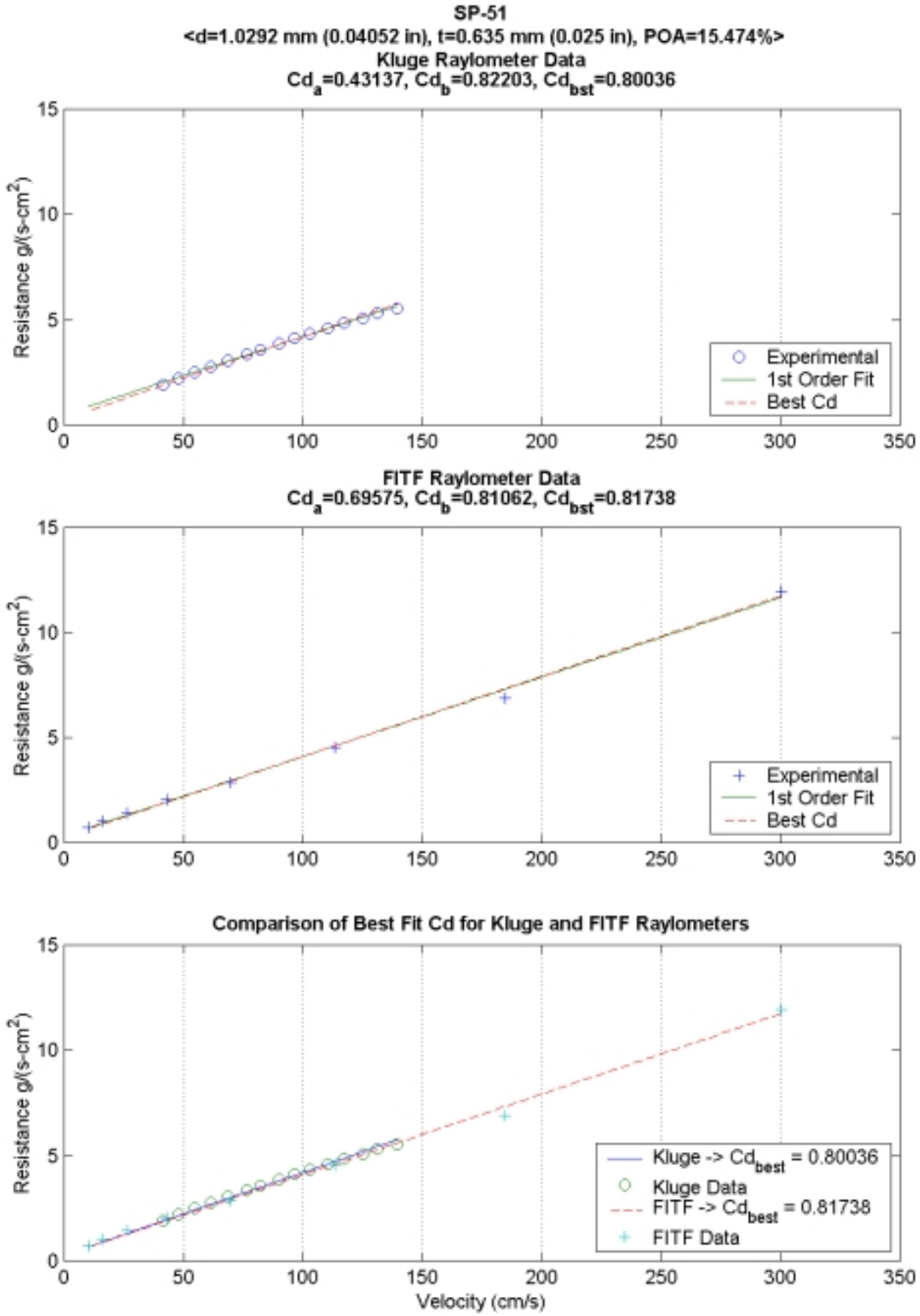
SP-51
<d=1.0292 mm (0.04052 in), t=0.635 mm (0.025 in), POA=15.474%>
Kluge Raylometer Data
Cd_a=0.43137, Cd_b=0.82203, Cd_bst=0.80036
Resistance g/(s-cm^2)
Experimental
1st Order Fit
Best Cd
FITF Raylometer Data
Cd_a=0.69575, Cd_b=0.81062, Cd_bst=0.81738
Resistance g/(s-cm^2)
Experimental
1st Order Fit
Best Cd
Comparison of Best Fit Cd for Kluge and FITF Raylometers
Resistance g/(s-cm^2)
Kluge -> Cd_best = 0.80036
Kluge Data
FITF -> Cd_best = 0.81738
FITF Data
Velocity (cm/s)

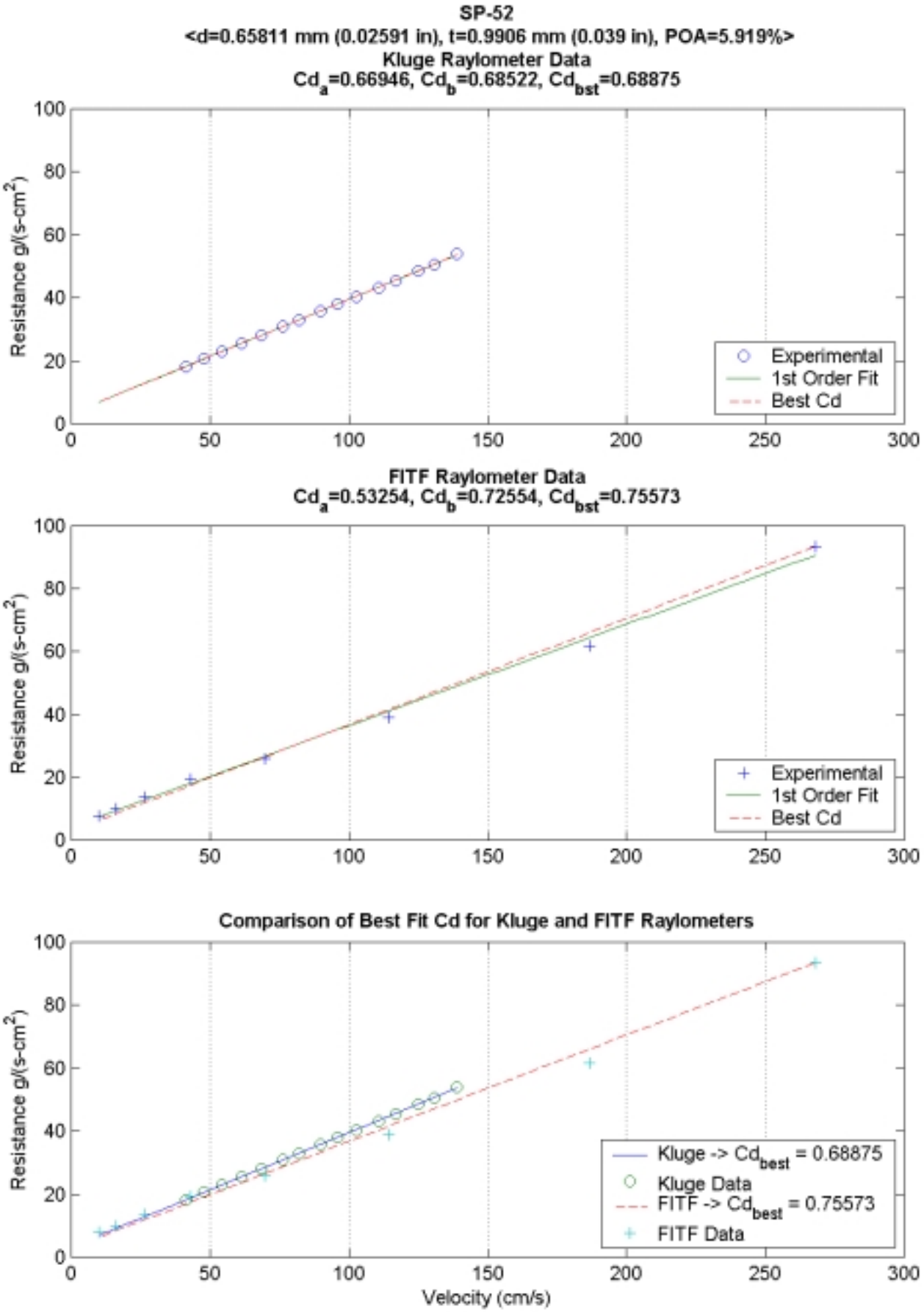
SP-52
<d=0.65811 mm (0.02591 in), t=0.9906 mm (0.039 in), POA=5.919%>
Kluge Raylometer Data
Cd_a=0.66946, Cd_b=0.68522, Cd_bst=0.68875
Resistance g/(s-cm^2)
Experimental
1st Order Fit
Best Cd
FITF Raylometer Data
Cd_a=0.53254, Cd_b=0.72554, Cd_bst=0.75573
Resistance g/(s-cm^2)
Experimental
1st Order Fit
Best Cd
Comparison of Best Fit Cd for Kluge and FITF Raylometers
Resistance g/(s-cm^2)
Kluge -> Cd_best = 0.68875
Kluge Data
FITF -> Cd_best = 0.75573
FITF Data
Velocity (cm/s)

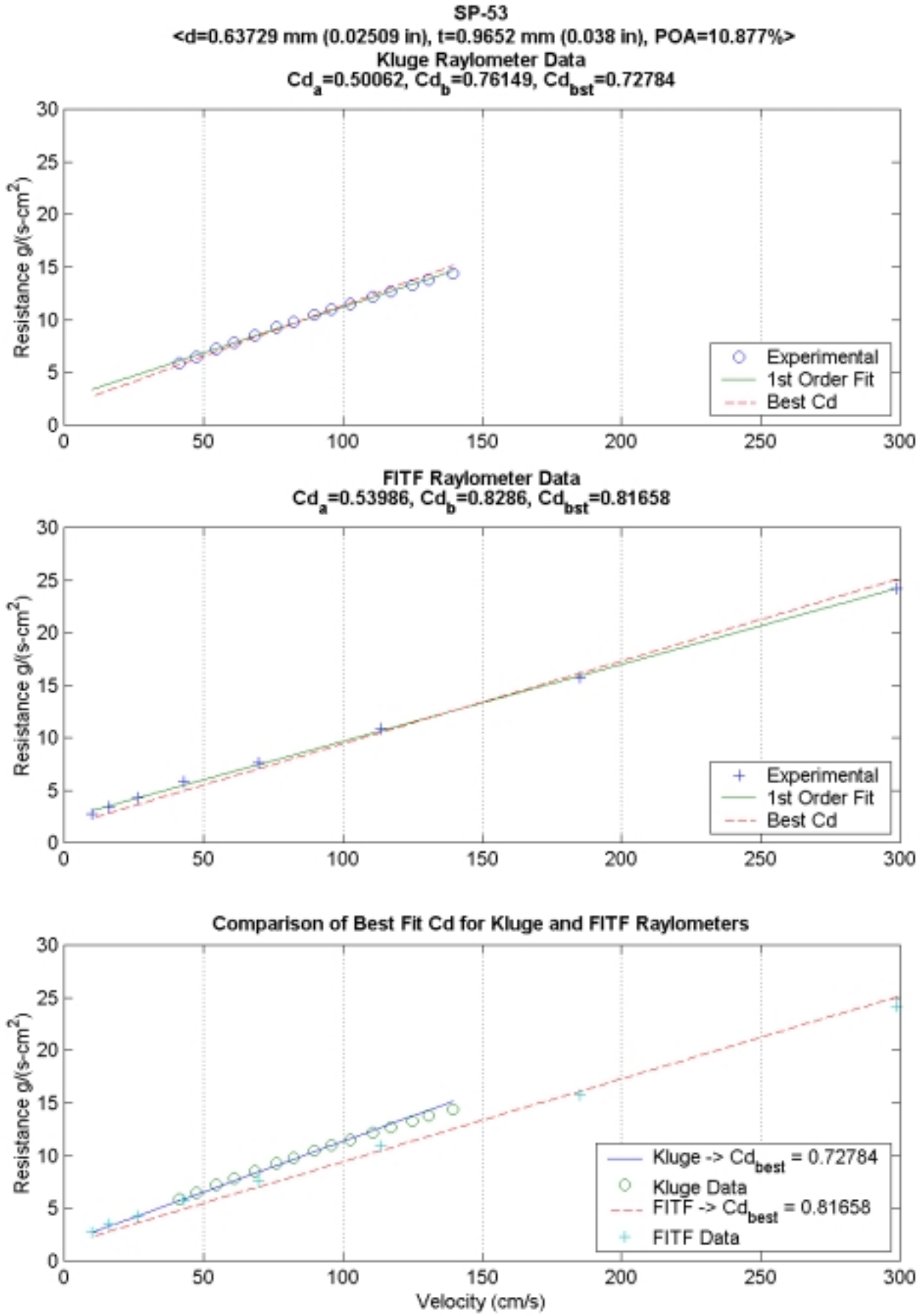
SP-53
<d=0.63729 mm (0.02509 in), t=0.9652 mm (0.038 in), POA=10.877%>
Kluge Raylometer Data
Cd_a=0.50062, Cd_b=0.76149, Cd_bst=0.72784
Resistance g/(s-cm^2)
Experimental
1st Order Fit
Best Cd
FITF Raylometer Data
Cd_a=0.53986, Cd_b=0.8286, Cd_bst=0.81658
Resistance g/(s-cm^2)
Experimental
1st Order Fit
Best Cd
Comparison of Best Fit Cd for Kluge and FITF Raylometers
Resistance g/(s-cm^2)
Kluge -> Cd_best = 0.72784
Kluge Data
FITF -> Cd_best = 0.81658
FITF Data
Velocity (cm/s)

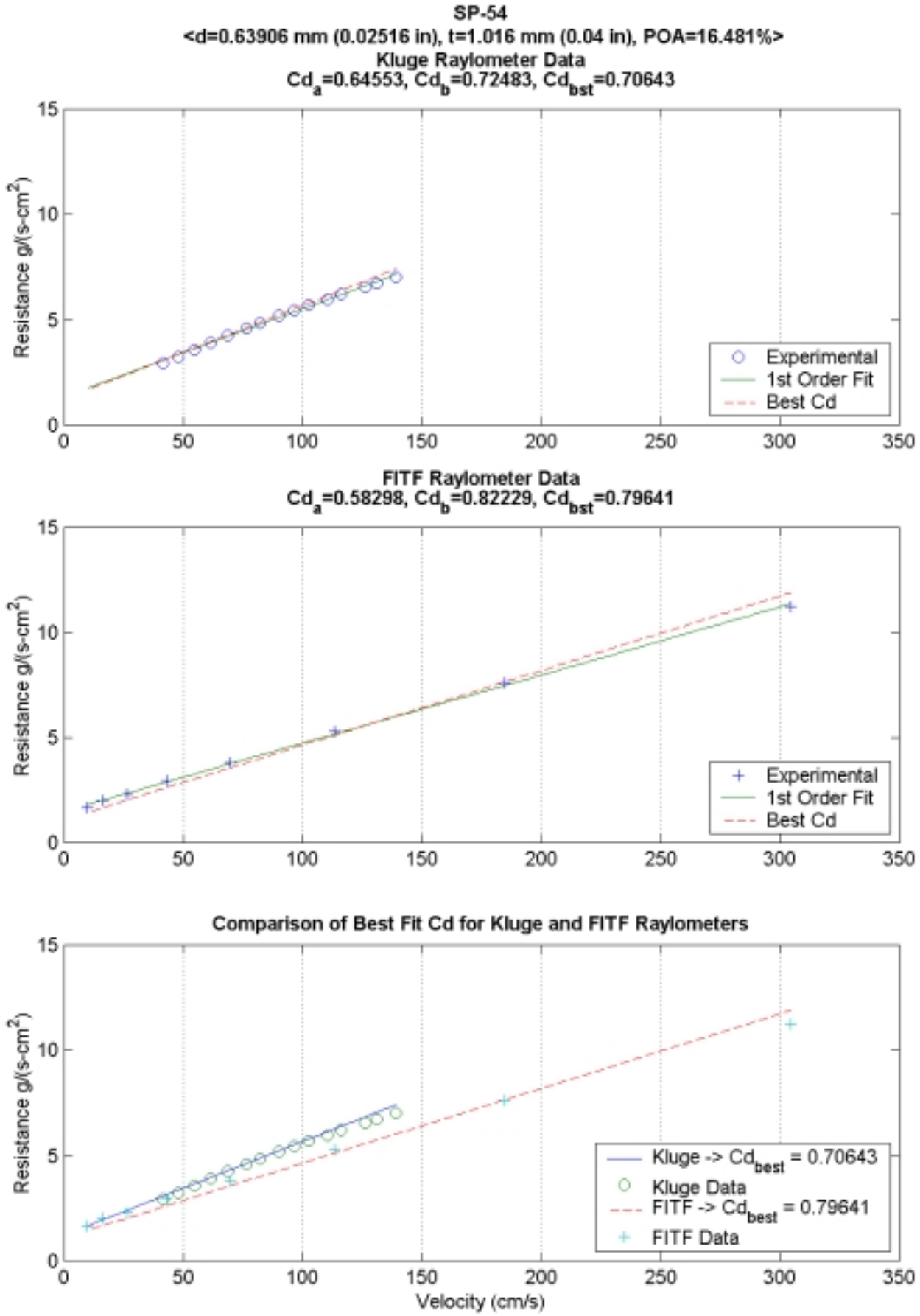
SP-54
<d=0.63906 mm (0.02516 in), t=1.016 mm (0.04 in), POA=16.481%>
Kluge Raylometer Data
Cd_a=0.64553, Cd_b=0.72483, Cd_bst=0.70643
Resistance g/(s-cm^2)
Experimental
1st Order Fit
Best Cd
FITF Raylometer Data
Cd_a=0.58298, Cd_b=0.82229, Cd_bst=0.79641
Resistance g/(s-cm^2)
Experimental
1st Order Fit
Best Cd
Comparison of Best Fit Cd for Kluge and FITF Raylometers
Resistance g/(s-cm^2)
Kluge -> Cd_best = 0.70643
Kluge Data
FITF -> Cd_best = 0.79641
FITF Data
Velocity (cm/s)

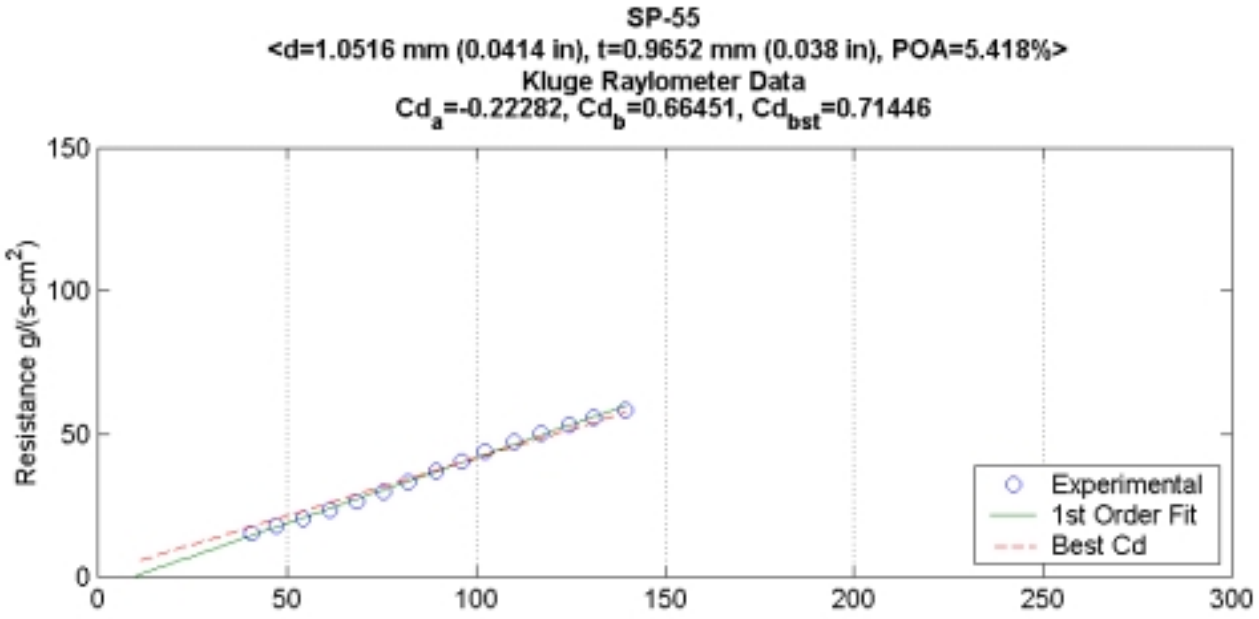
SP-55
<d=1.0516 mm (0.0414 in), t=0.9652 mm (0.038 in), POA=5.418%>
Kluge Raylometer Data
Cd_a=-0.22282, Cd_b=0.66451, Cd_bst=0.71446
Resistance g/(s-cm^2)
Experimental
1st Order Fit
Best Cd

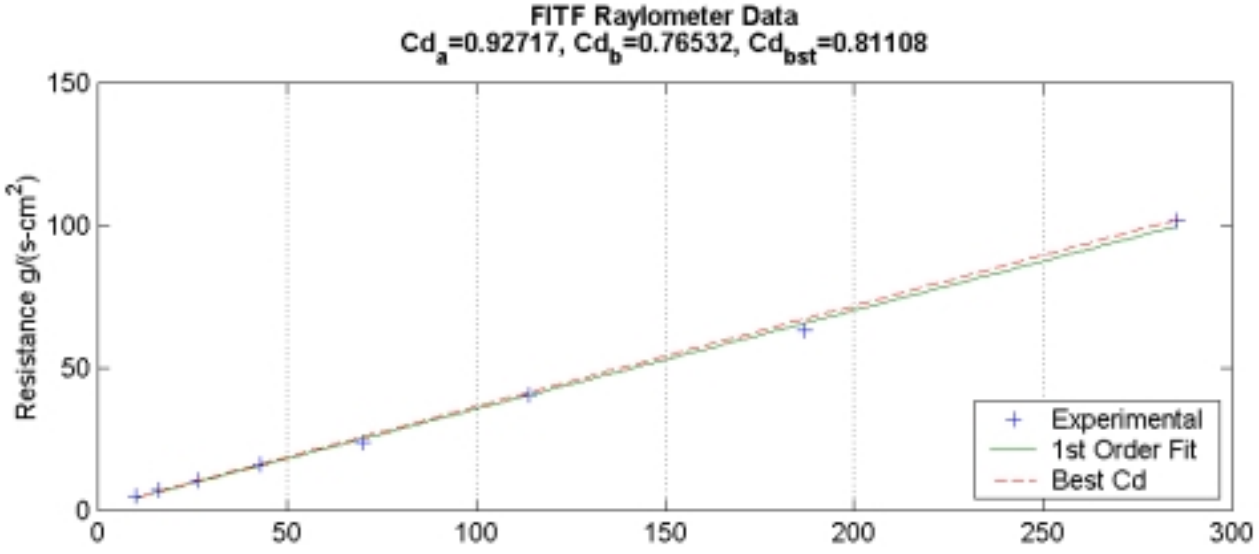
FITF Raylometer Data
Cd_a=0.92717, Cd_b=0.76532, Cd_bst=0.81108
Resistance g/(s-cm^2)
Experimental
1st Order Fit
Best Cd

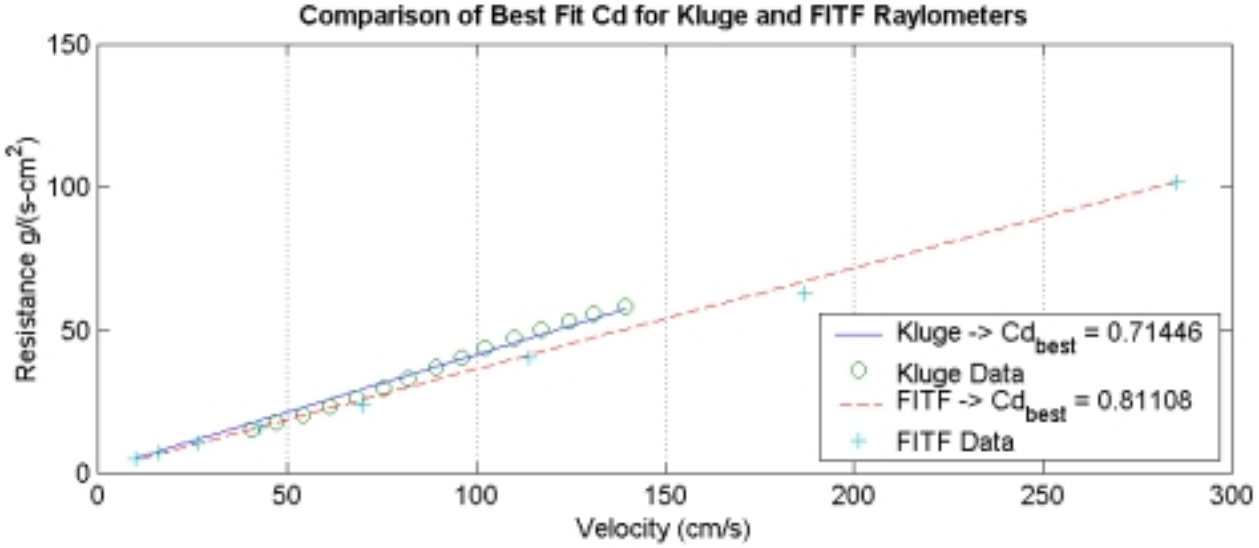
Comparison of Best Fit Cd for Kluge and FITF Raylometers
Resistance g/(s-cm^2)
Velocity (cm/s)
Kluge -> Cd_best = 0.71446
Kluge Data
FITF -> Cd_best = 0.81108
FITF Data

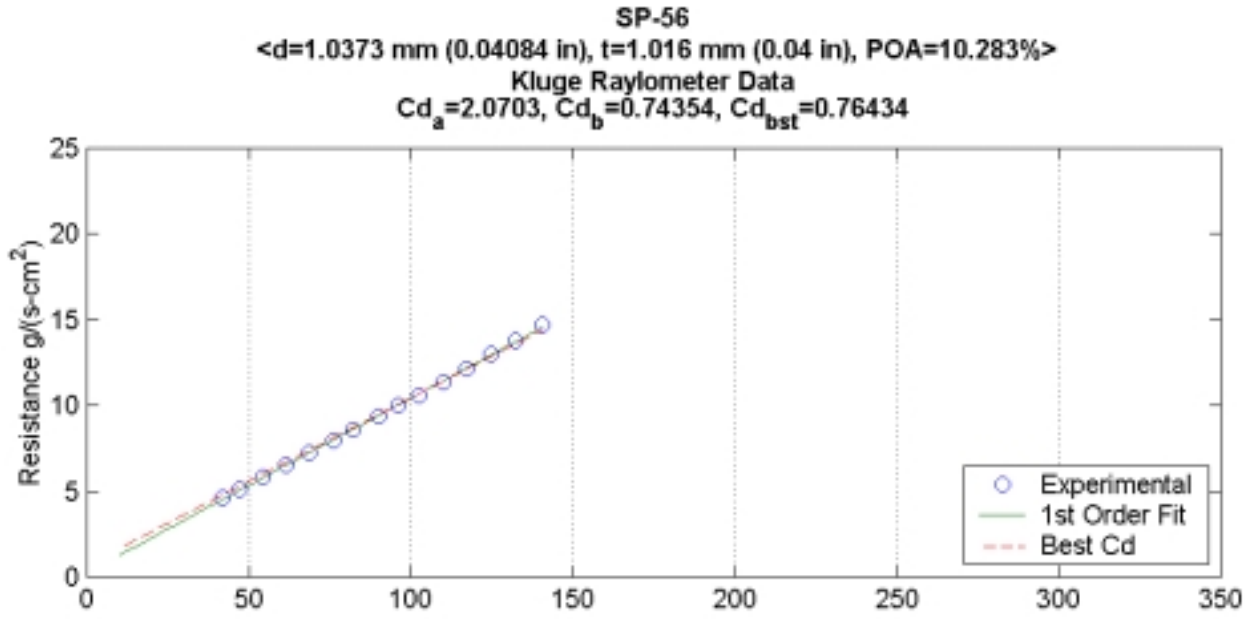
SP-56
<d=1.0373 mm (0.04084 in), t=1.016 mm (0.04 in), POA=10.283%>
Kluge Raylometer Data
Cd_a=2.0703, Cd_b=0.74354, Cd_bst=0.76434
Resistance g/(s-cm^2)
Experimental
1st Order Fit
Best Cd

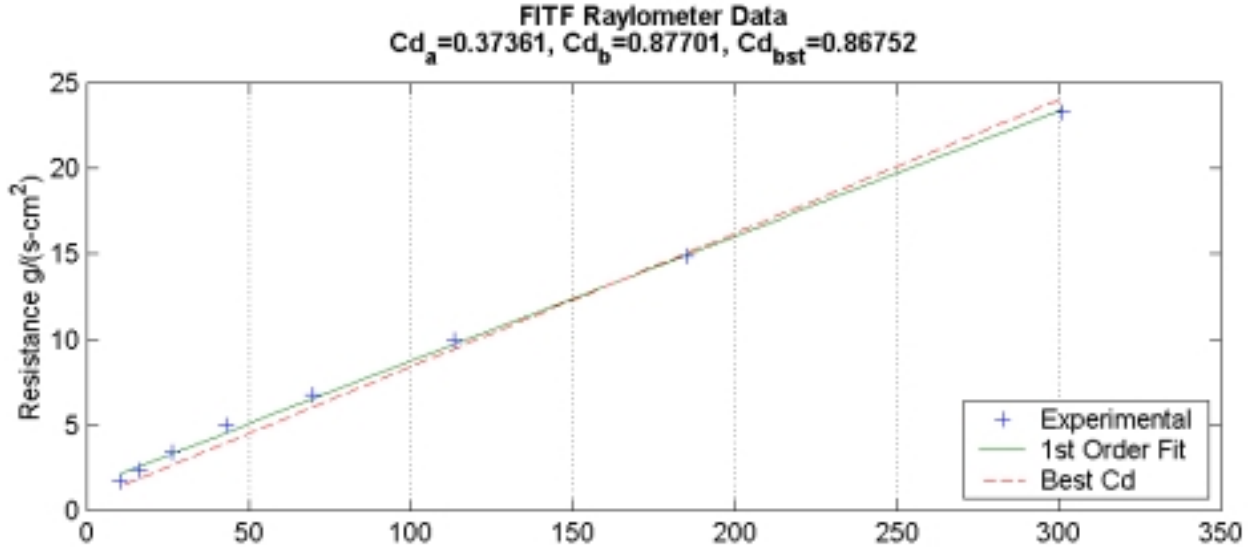
FITF Raylometer Data
Cd_a=0.37361, Cd_b=0.87701, Cd_bst=0.86752
Resistance g/(s-cm^2)
Experimental
1st Order Fit
Best Cd

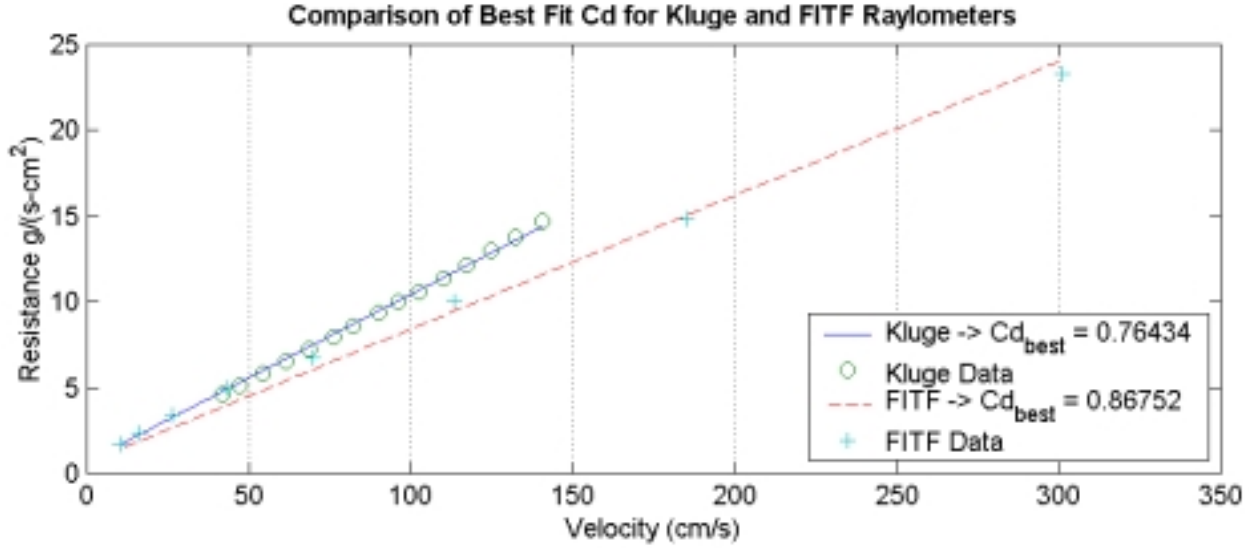
Comparison of Best Fit Cd for Kluge and FITF Raylometers
Resistance g/(s-cm^2)
Velocity (cm/s)
Kluge -> Cd_best = 0.76434
Kluge Data
FITF -> Cd_best = 0.86752
FITF Data

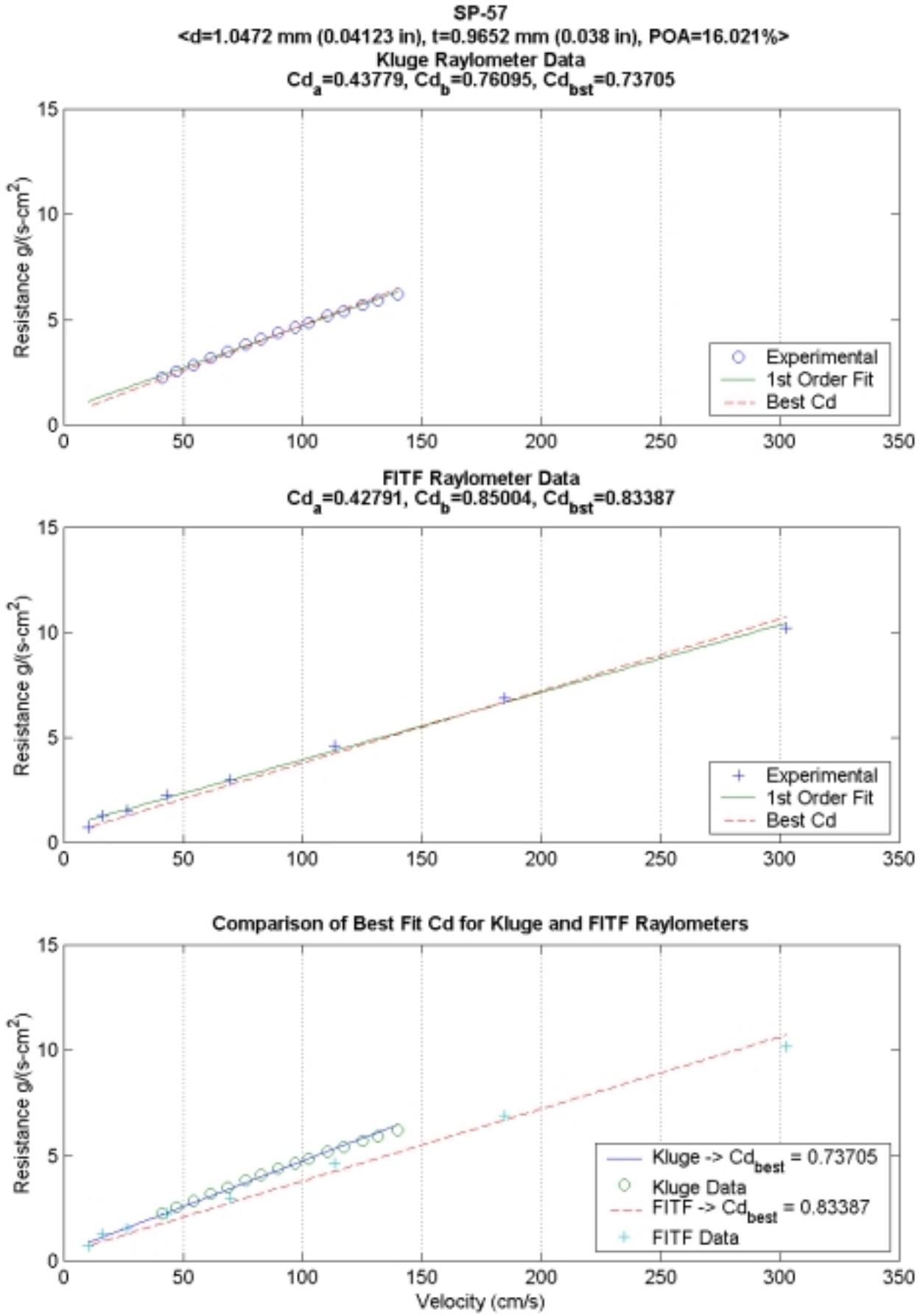
SP-57
<d=1.0472 mm (0.04123 in), t=0.9652 mm (0.038 in), POA=16.021%>
Kluge Raylometer Data
Cd_a=0.43779, Cd_b=0.76095, Cd_bst=0.73705
Resistance g/(s-cm^2)
Experimental
1st Order Fit
Best Cd
FITF Raylometer Data
Cd_a=0.42791, Cd_b=0.85004, Cd_bst=0.83387
Resistance g/(s-cm^2)
Experimental
1st Order Fit
Best Cd
Comparison of Best Fit Cd for Kluge and FITF Raylometers
Resistance g/(s-cm^2)
Kluge -> Cd_best = 0.73705
Kluge Data
FITF -> Cd_best = 0.83387
FITF Data
Velocity (cm/s)

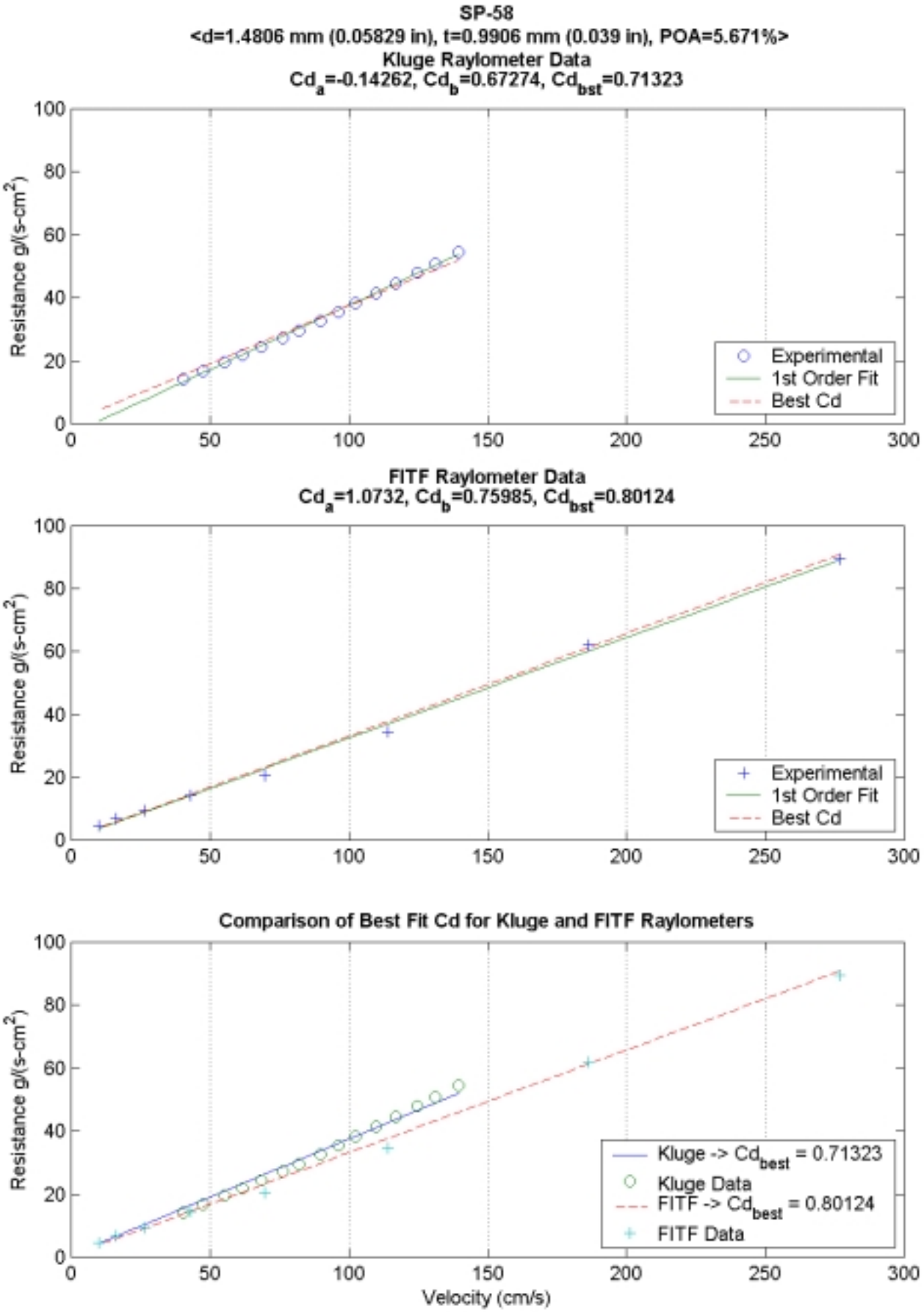
SP-58
<d=1.4806 mm (0.05829 in), t=0.9906 mm (0.039 in), POA=5.671%>
Kluge Raylometer Data
Cd_a=-0.14262, Cd_b=0.67274, Cd_bst=0.71323
Resistance g/(s-cm^2)
Experimental
1st Order Fit
Best Cd
FITF Raylometer Data
Cd_a=1.0732, Cd_b=0.75985, Cd_bst=0.80124
Resistance g/(s-cm^2)
Experimental
1st Order Fit
Best Cd
Comparison of Best Fit Cd for Kluge and FITF Raylometers
Resistance g/(s-cm^2)
Kluge -> Cd_best = 0.71323
Kluge Data
FITF -> Cd_best = 0.80124
FITF Data
Velocity (cm/s)

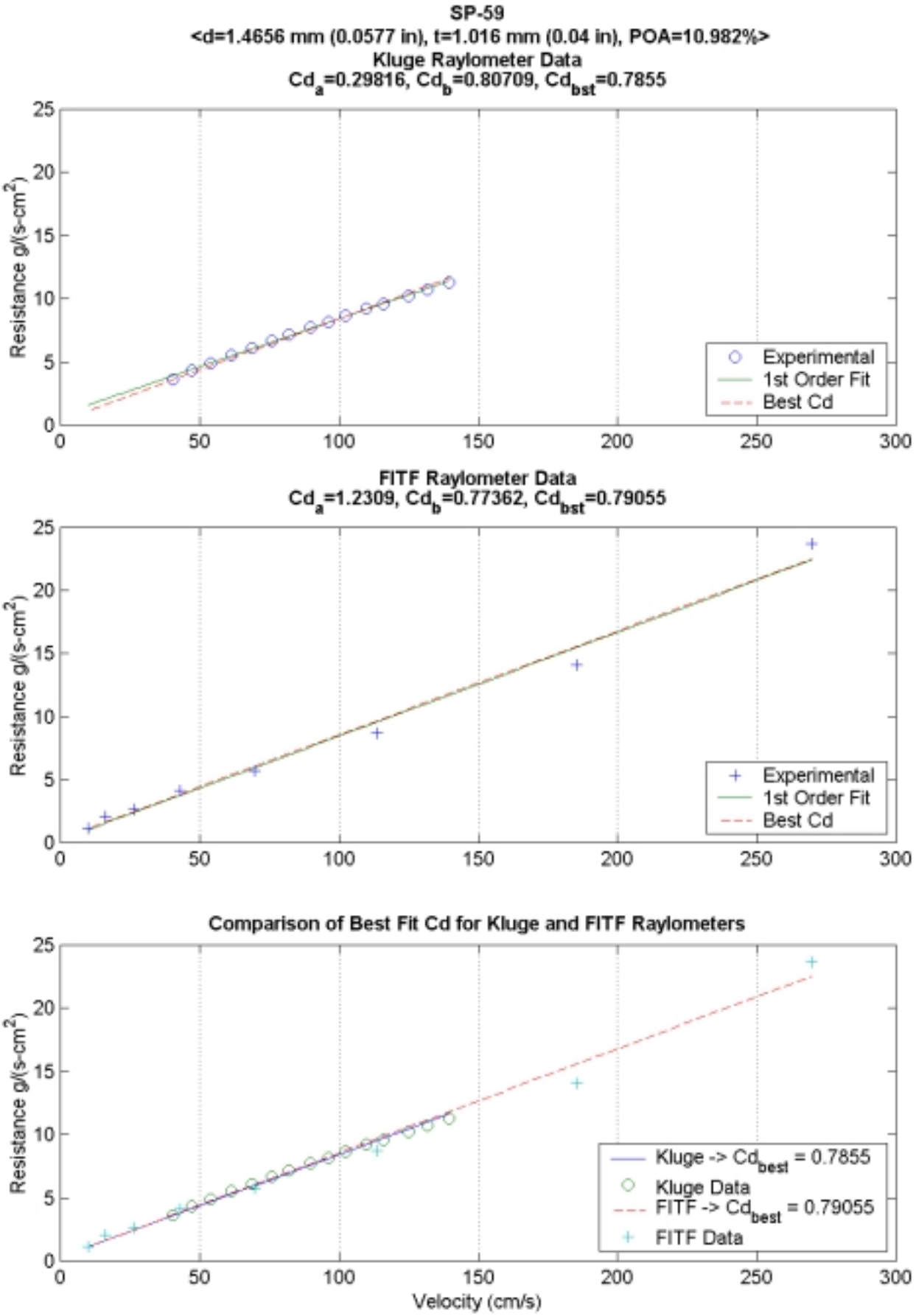
SP-59
<d=1.4656 mm (0.0577 in), t=1.016 mm (0.04 in), POA=10.982%>
Kluge Raylometer Data
Cd_a=0.29816, Cd_b=0.80709, Cd_bst=0.7855
Resistance g/(s-cm^2)
Experimental
1st Order Fit
Best Cd
FITF Raylometer Data
Cd_a=1.2309, Cd_b=0.77362, Cd_bst=0.79055
Resistance g/(s-cm^2)
Experimental
1st Order Fit
Best Cd
Comparison of Best Fit Cd for Kluge and FITF Raylometers
Resistance g/(s-cm^2)
Kluge -> Cd_best = 0.7855
Kluge Data
FITF -> Cd_best = 0.79055
FITF Data
Velocity (cm/s)

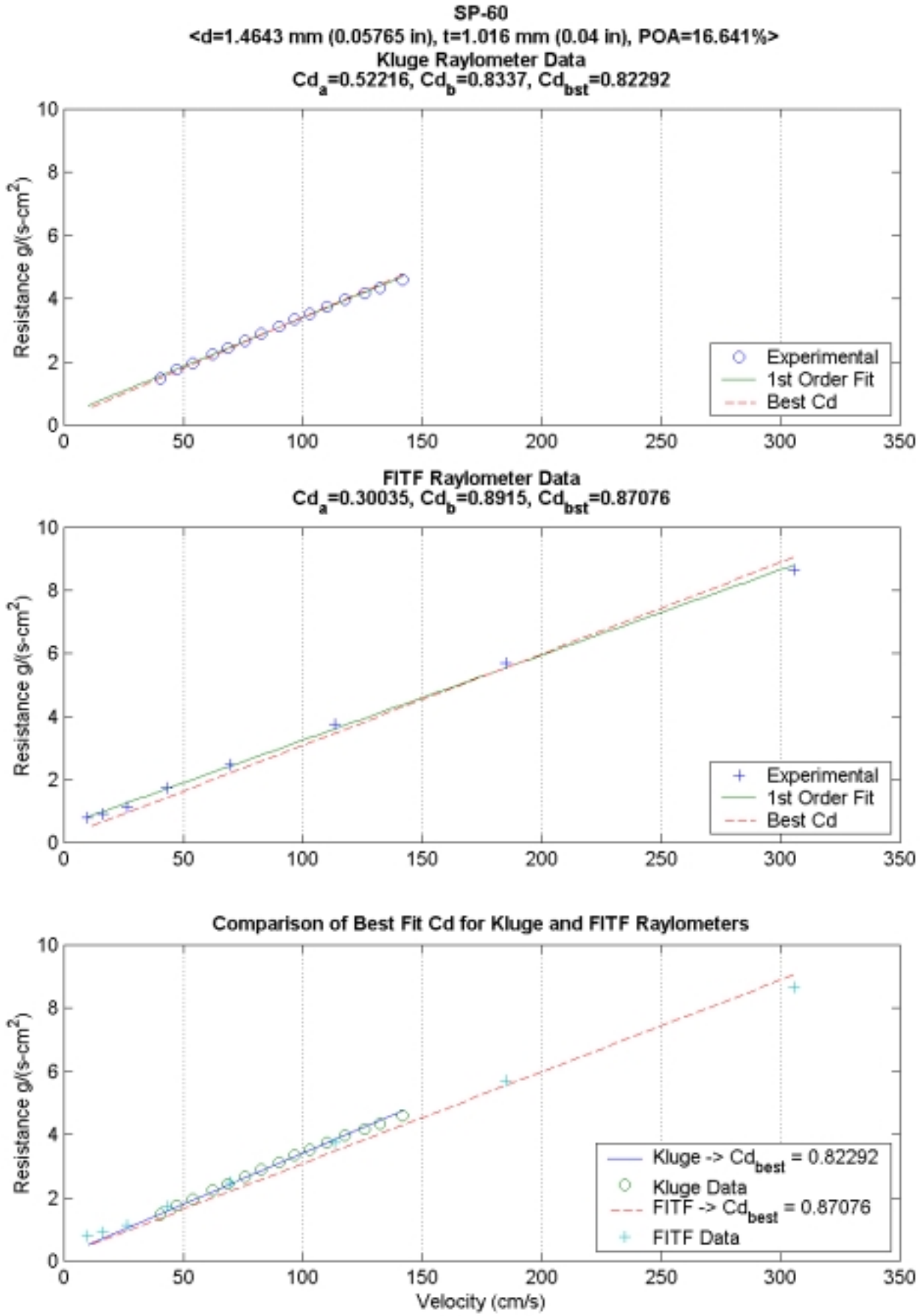
SP-60
<d=1.4643 mm (0.05765 in), t=1.016 mm (0.04 in), POA=16.641%>
Kluge Raylometer Data
Cd_a=0.52216, Cd_b=0.8337, Cd_bst=0.82292
Resistance g/(s-cm^2)
Experimental
1st Order Fit
Best Cd
FITF Raylometer Data
Cd_a=0.30035, Cd_b=0.8915, Cd_bst=0.87076
Resistance g/(s-cm^2)
Experimental
1st Order Fit
Best Cd
Comparison of Best Fit Cd for Kluge and FITF Raylometers
Resistance g/(s-cm^2)
Kluge -> Cd_best = 0.82292
Kluge Data
FITF -> Cd_best = 0.87076
FITF Data
Velocity (cm/s)

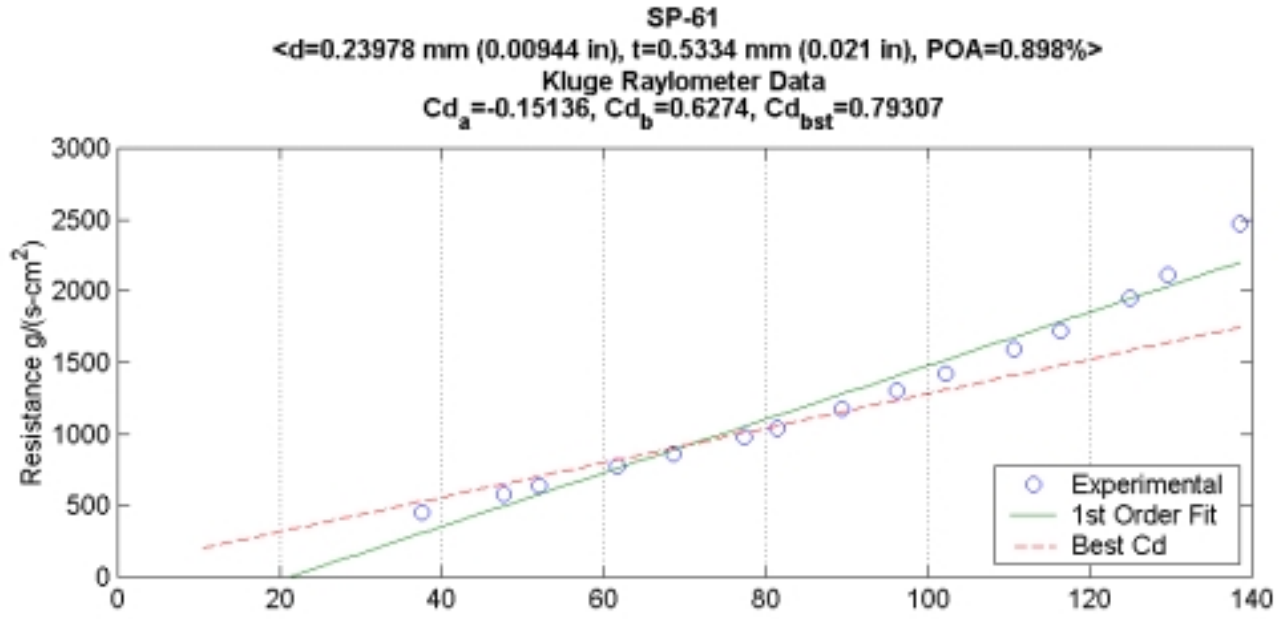
SP-61
<d=0.23978 mm (0.00944 in), t=0.5334 mm (0.021 in), POA=0.898%>
Kluge Raylometer Data
Cd_a=-0.15136, Cd_b=0.6274, Cd_bst=0.79307
Resistance g/(s-cm^2)
Experimental
1st Order Fit
Best Cd

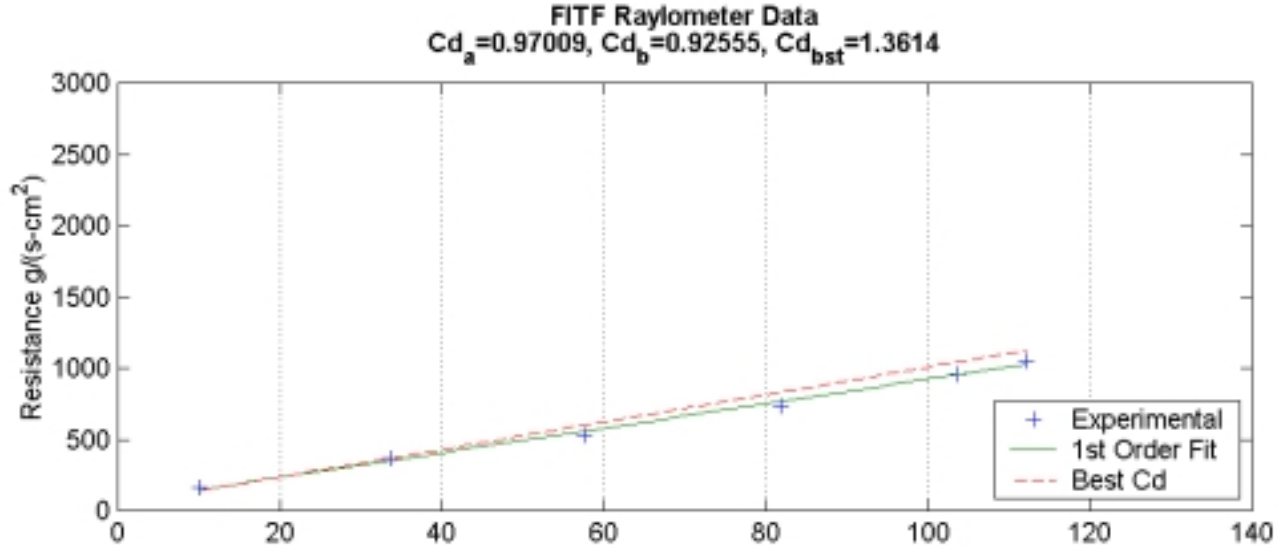
FITF Raylometer Data
Cd_a=0.97009, Cd_b=0.92555, Cd_bst=1.3614
Resistance g/(s-cm^2)
Experimental
1st Order Fit
Best Cd

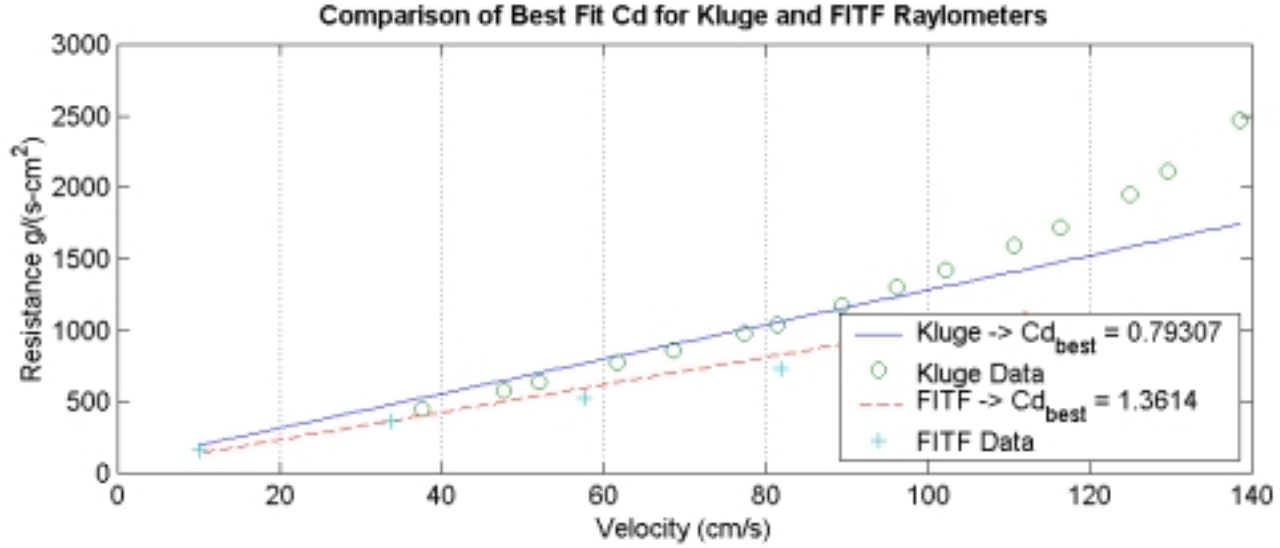
Comparison of Best Fit Cd for Kluge and FITF Raylometers
Resistance g/(s-cm^2)
Velocity (cm/s)
Kluge -> Cd_best = 0.79307
Kluge Data
FITF -> Cd_best = 1.3614
FITF Data

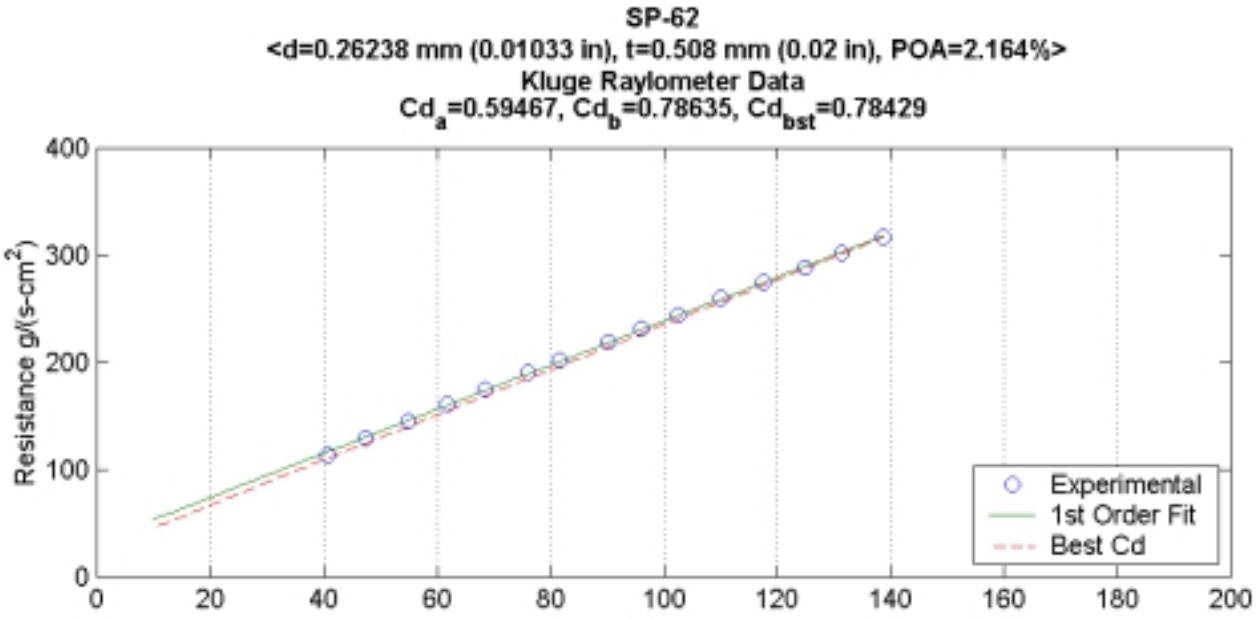
SP-62
<d=0.26238 mm (0.01033 in), t=0.508 mm (0.02 in), POA=2.164%>
Kluge Raylometer Data
Cd_a=0.59467, Cd_b=0.78635, Cd_bst=0.78429
Resistance g/(s-cm^2)
Experimental
1st Order Fit
Best Cd

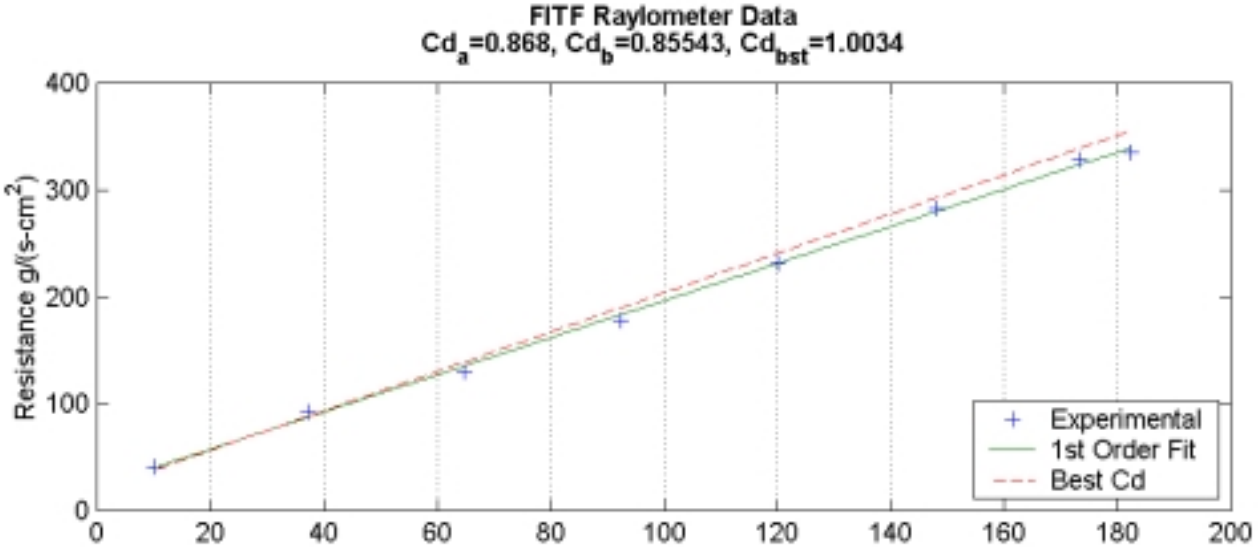
FITF Raylometer Data
Cd_a=0.868, Cd_b=0.85543, Cd_bst=1.0034
Resistance g/(s-cm^2)
Experimental
1st Order Fit
Best Cd

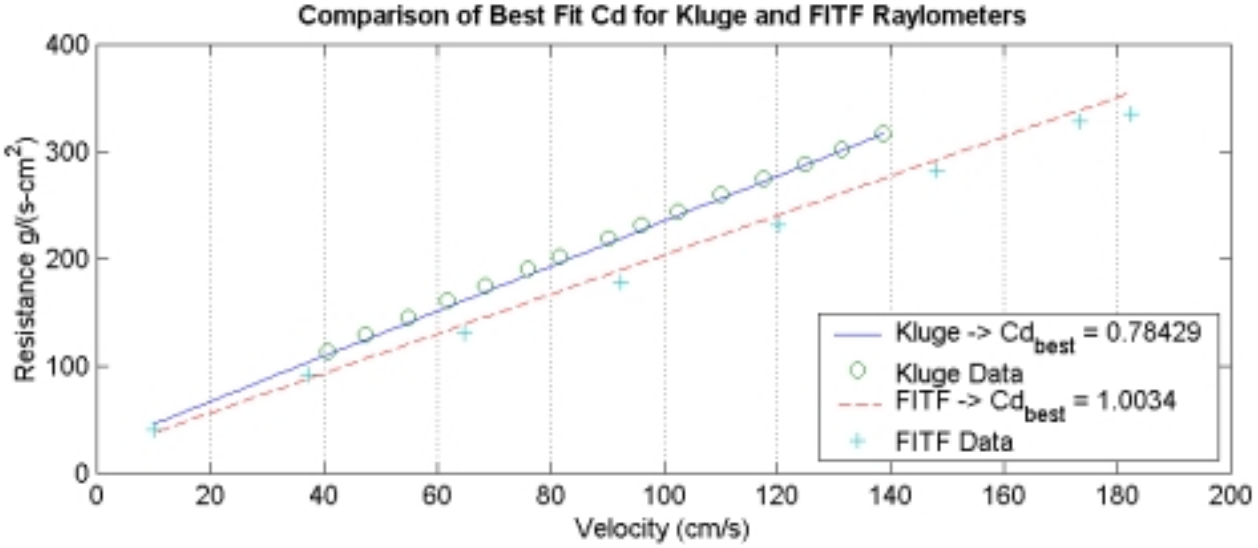
Comparison of Best Fit Cd for Kluge and FITF Raylometers
Resistance g/(s-cm^2)
Kluge -> Cd_best = 0.78429
Kluge Data
FITF -> Cd_best = 1.0034
FITF Data
Velocity (cm/s)

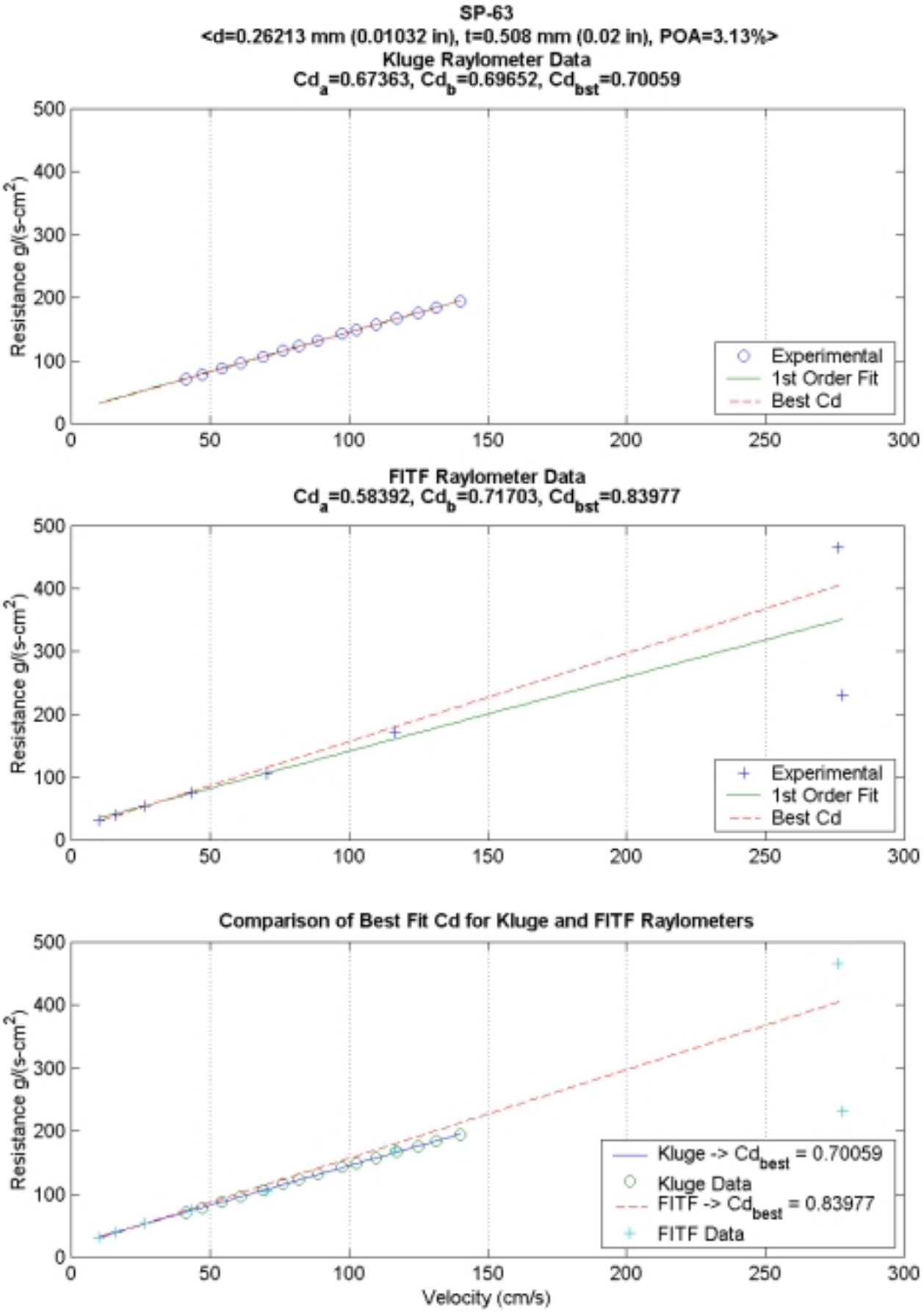
SP-63
<d=0.26213 mm (0.01032 in), t=0.508 mm (0.02 in), POA=3.13%>
Kluge Raylometer Data
Cd_a=0.67363, Cd_b=0.69652, Cd_bst=0.70059
Resistance g/(s-cm^2)
Experimental
1st Order Fit
Best Cd
FITF Raylometer Data
Cd_a=0.58392, Cd_b=0.71703, Cd_bst=0.83977
Resistance g/(s-cm^2)
Experimental
1st Order Fit
Best Cd
Comparison of Best Fit Cd for Kluge and FITF Raylometers
Resistance g/(s-cm^2)
Kluge -> Cd_best = 0.70059
Kluge Data
FITF -> Cd_best = 0.83977
FITF Data
Velocity (cm/s)

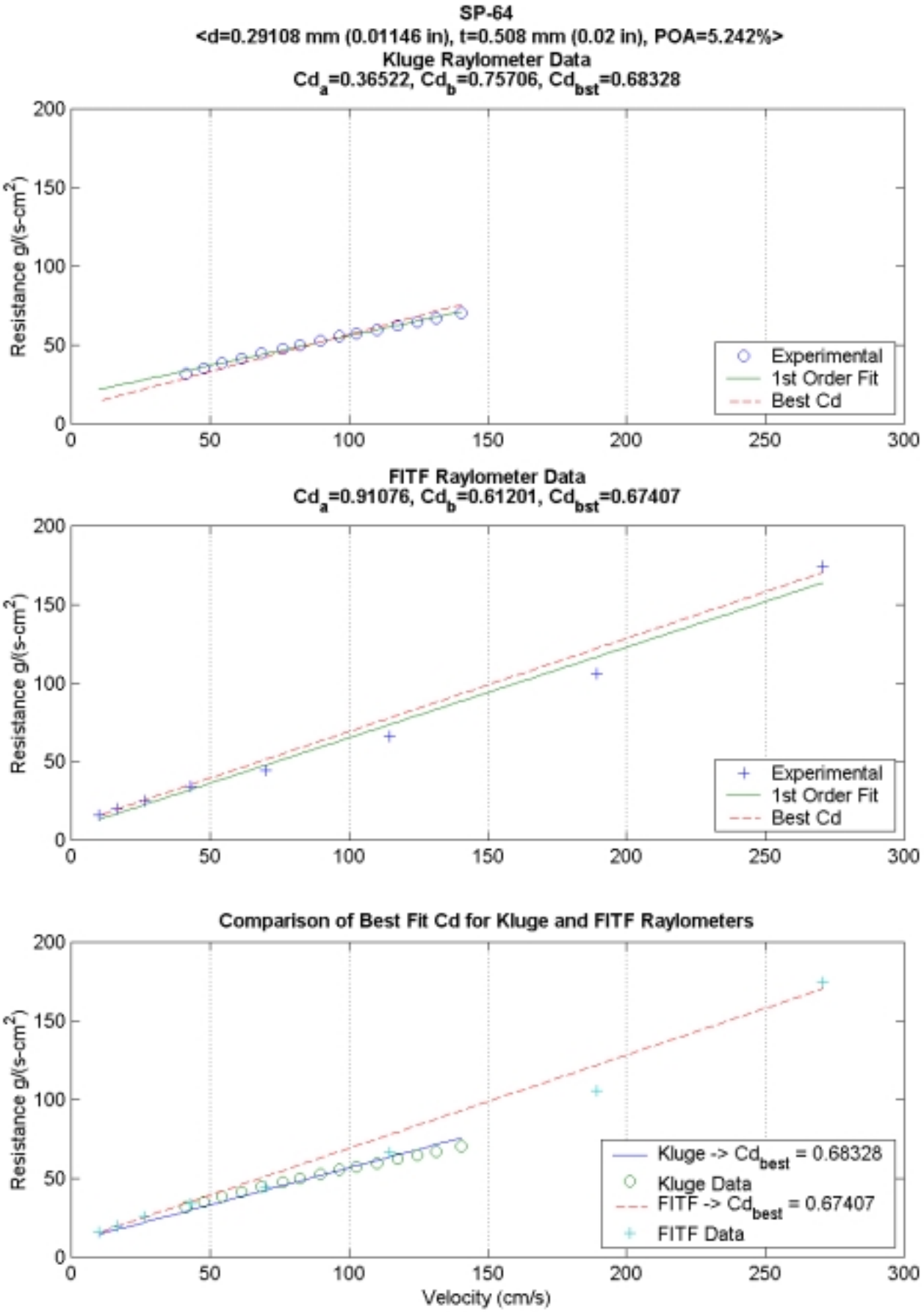
SP-64
<d=0.29108 mm (0.01146 in), t=0.508 mm (0.02 in), POA=5.242%>
Kluge Raylometer Data
Cd_a=0.36522, Cd_b=0.75706, Cd_bst=0.68328
Resistance g/(s-cm^2)
Experimental
1st Order Fit
Best Cd
FITF Raylometer Data
Cd_a=0.91076, Cd_b=0.61201, Cd_bst=0.67407
Resistance g/(s-cm^2)
Experimental
1st Order Fit
Best Cd
Comparison of Best Fit Cd for Kluge and FITF Raylometers
Resistance g/(s-cm^2)
Kluge -> Cd_best = 0.68328
Kluge Data
FITF -> Cd_best = 0.67407
FITF Data
Velocity (cm/s)

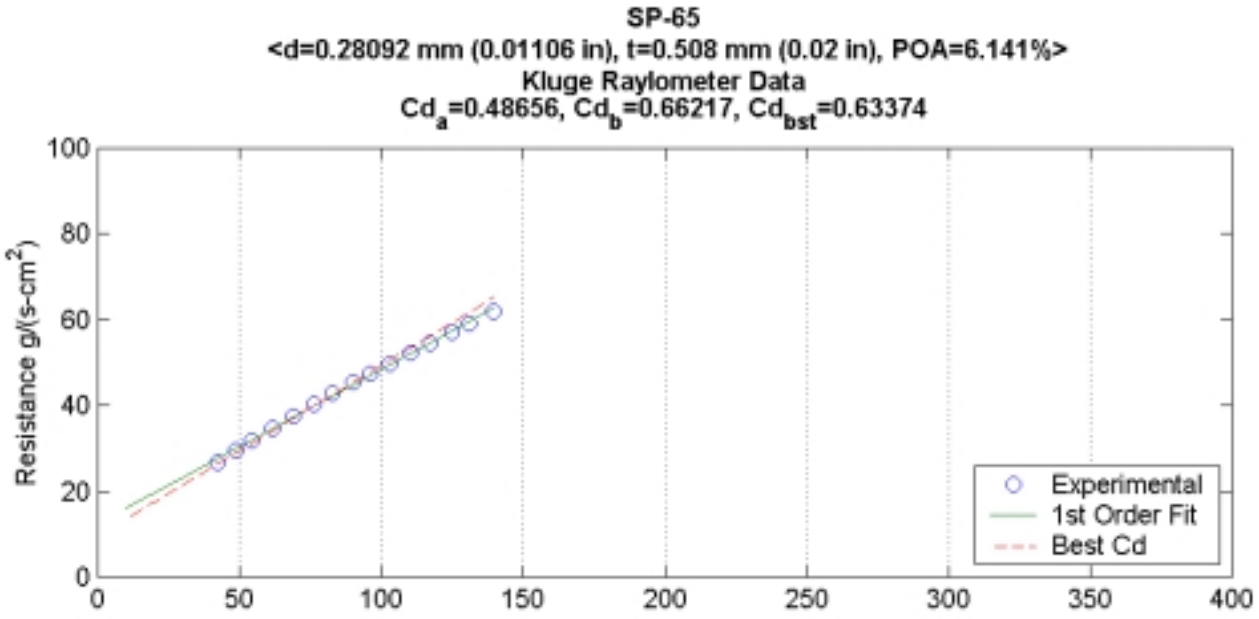
SP-65
<d=0.28092 mm (0.01106 in), t=0.508 mm (0.02 in), POA=6.141%>
Kluge Raylometer Data
Cd_a=0.48656, Cd_b=0.66217, Cd_bst=0.63374
Resistance g/(s-cm^2)
Experimental
1st Order Fit
Best Cd

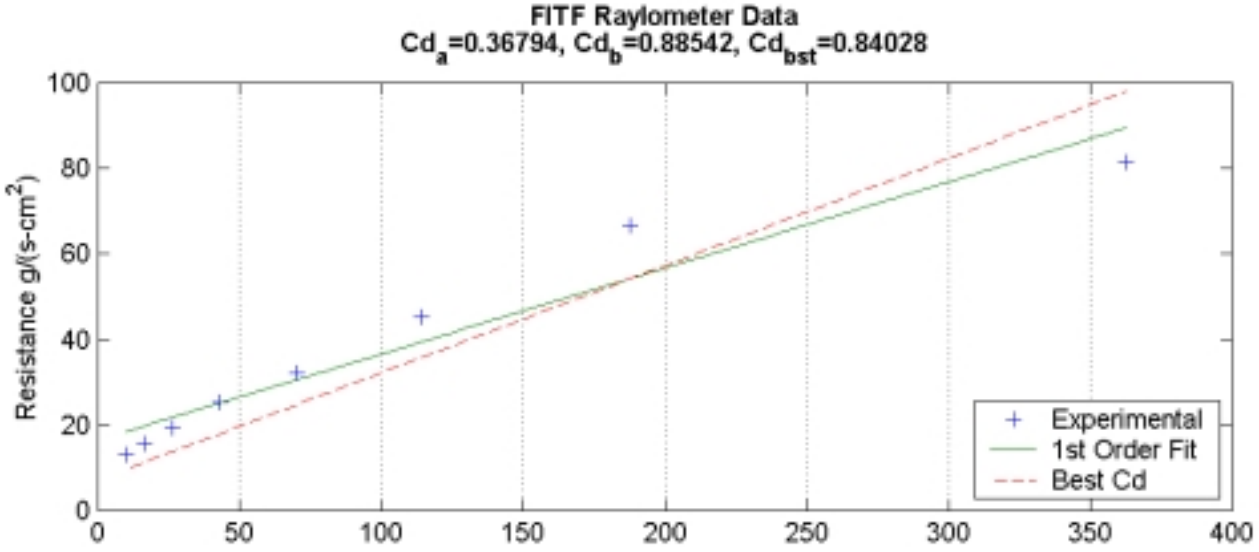
FITF Raylometer Data
Cd_a=0.36794, Cd_b=0.88542, Cd_bst=0.84028
Resistance g/(s-cm^2)
Experimental
1st Order Fit
Best Cd

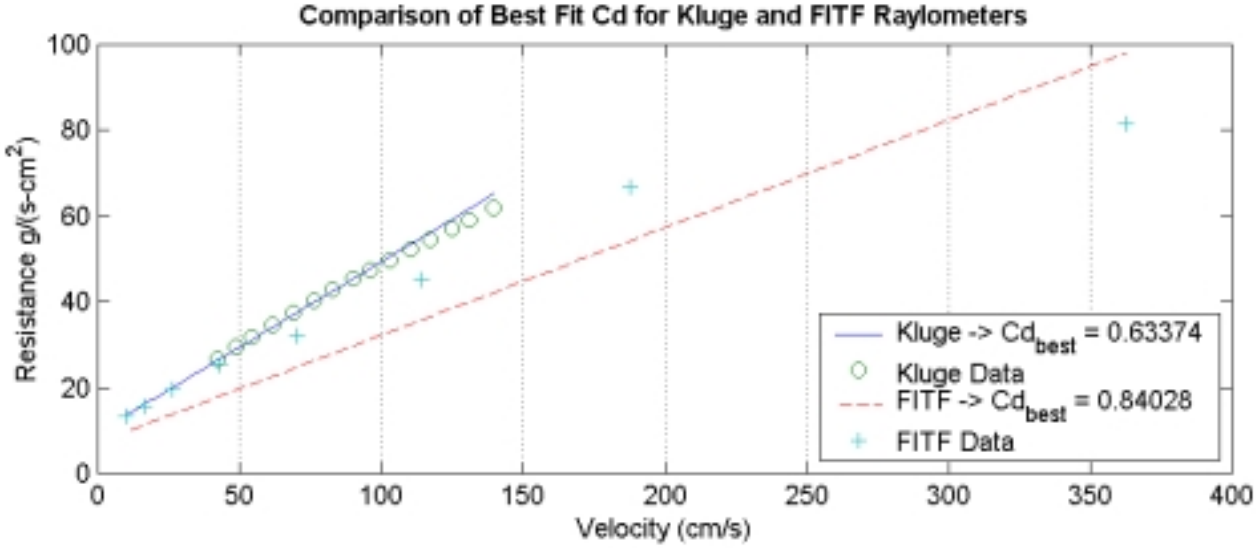
Comparison of Best Fit Cd for Kluge and FITF Raylometers
Resistance g/(s-cm^2)
Velocity (cm/s)
Kluge -> Cd_best = 0.63374
Kluge Data
FITF -> Cd_best = 0.84028
FITF Data

Appendix H: Experimental and PBFIF Model Impedance Database

The pages that follow provide plots of PBFIF model and experiment impedance results. These plots are not the complete database. To get the complete database contact Mike Jones in the Structural Acoustics Branch at NASA Langley Research Center.

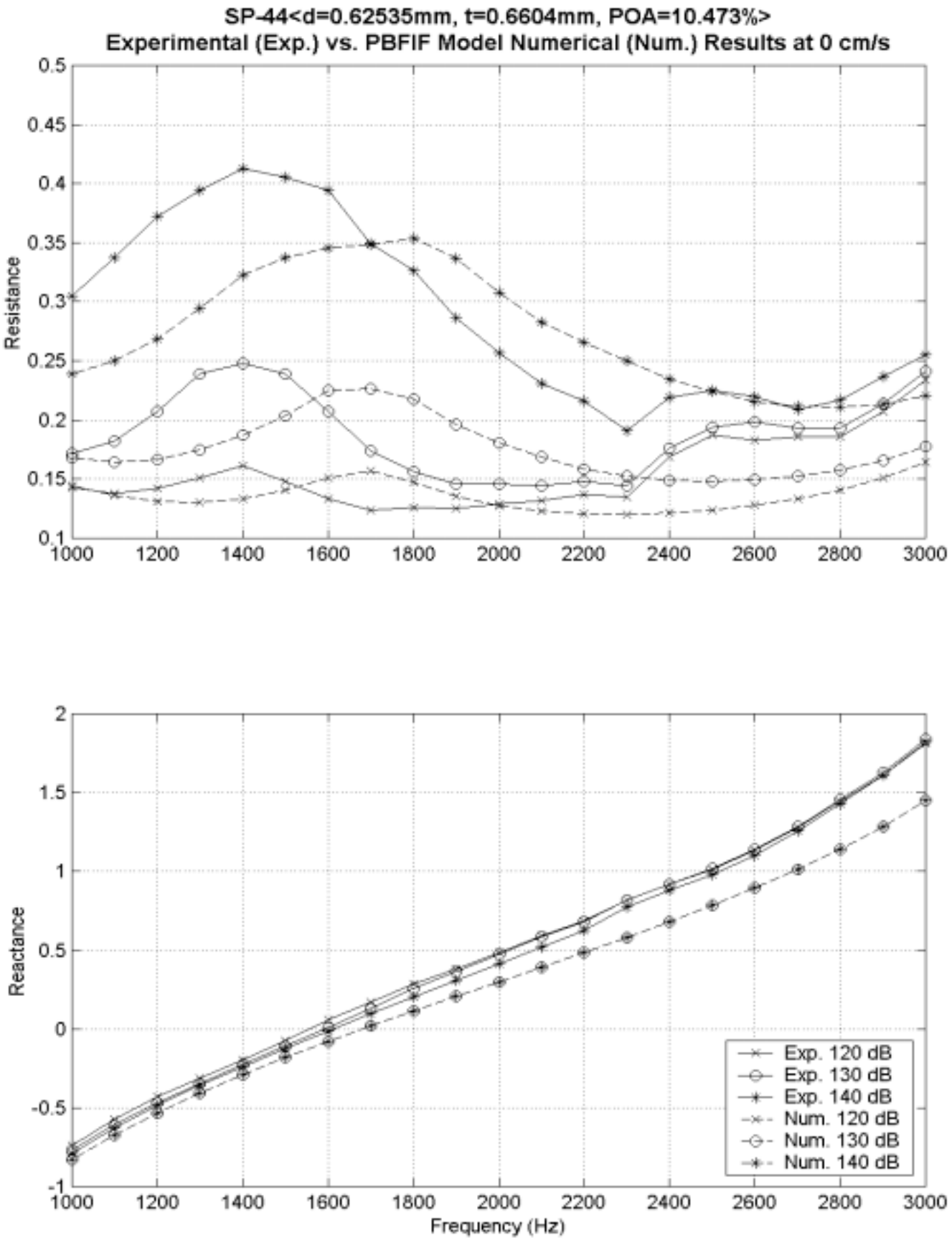
SP-44<d=0.62535mm, t=0.6604mm, POA=10.473%>
Experimental (Exp.) vs. PBFIF Model Numerical (Num.) Results at 0 cm/s
Resistance
Reactance
Frequency (Hz)
Exp. 120 dB
Exp. 130 dB
Exp. 140 dB
Num. 120 dB
Num. 130 dB
Num. 140 dB

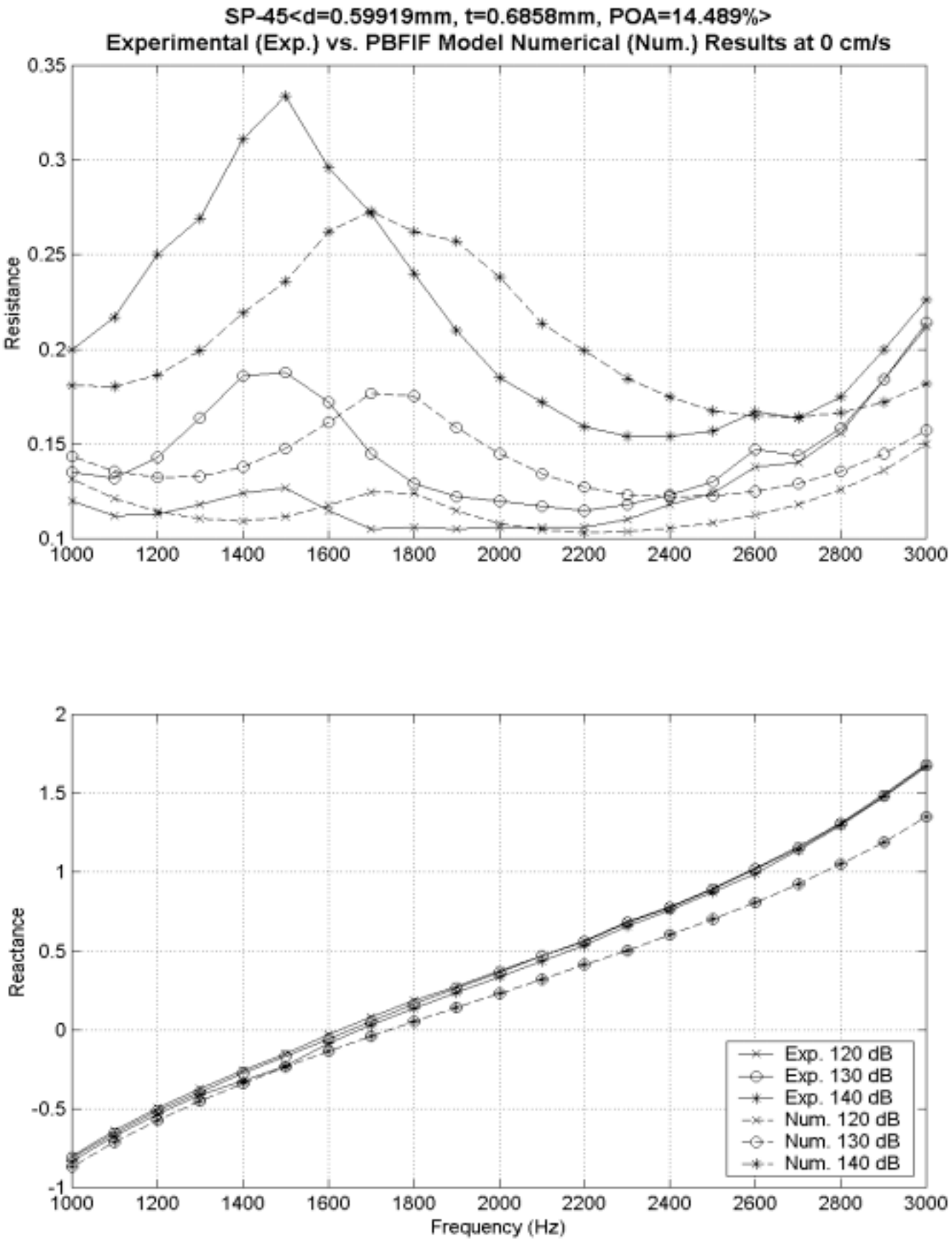
SP-45<d=0.59919mm, t=0.6858mm, POA=14.489%>
Experimental (Exp.) vs. PBFIF Model Numerical (Num.) Results at 0 cm/s
Resistance
Reactance
Frequency (Hz)
Exp. 120 dB
Exp. 130 dB
Exp. 140 dB
Num. 120 dB
Num. 130 dB
Num. 140 dB

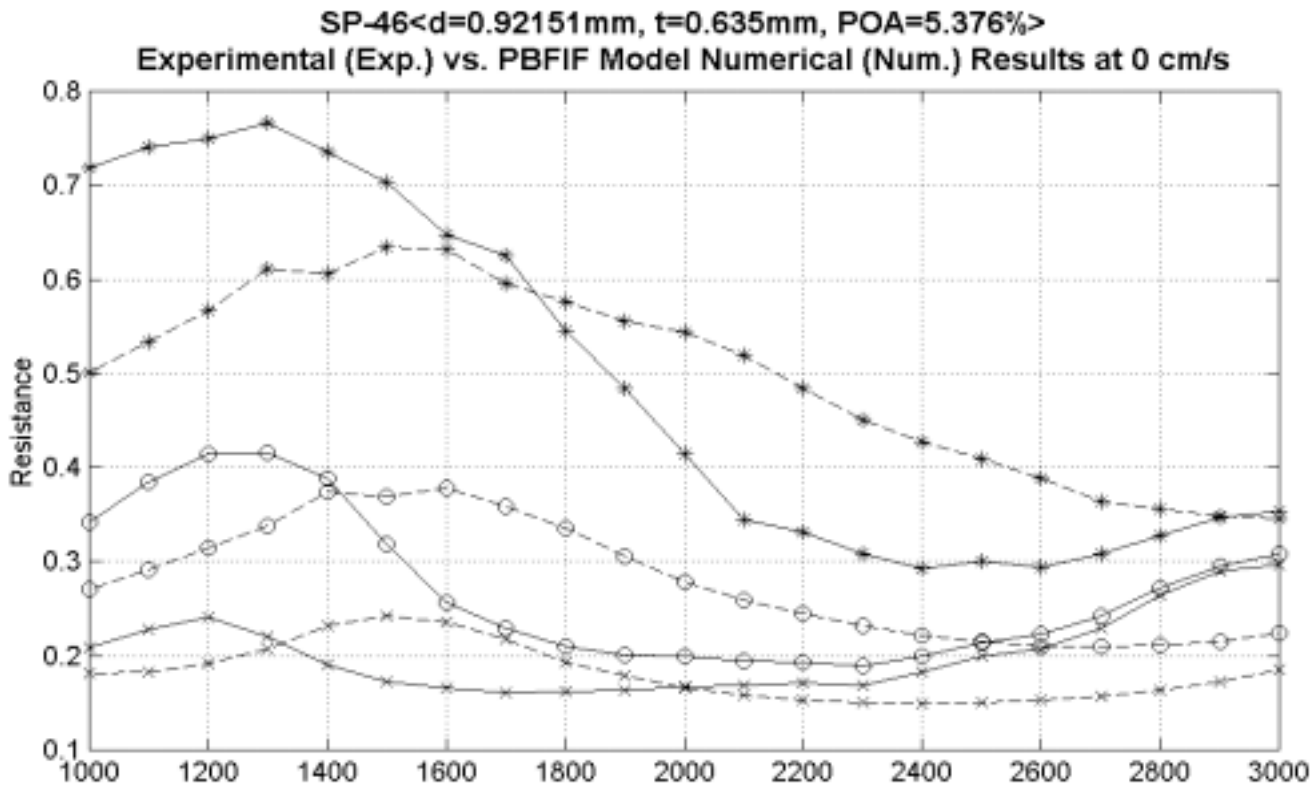
SP-46<d=0.92151mm, t=0.635mm, POA=5.376%>
Experimental (Exp.) vs. PBFIF Model Numerical (Num.) Results at 0 cm/s
Resistance
0.8
0.7
0.6
0.5
0.4
0.3
0.2
0.1
1000
1200
1400
1600
1800
2000
2200
2400
2600
2800
3000

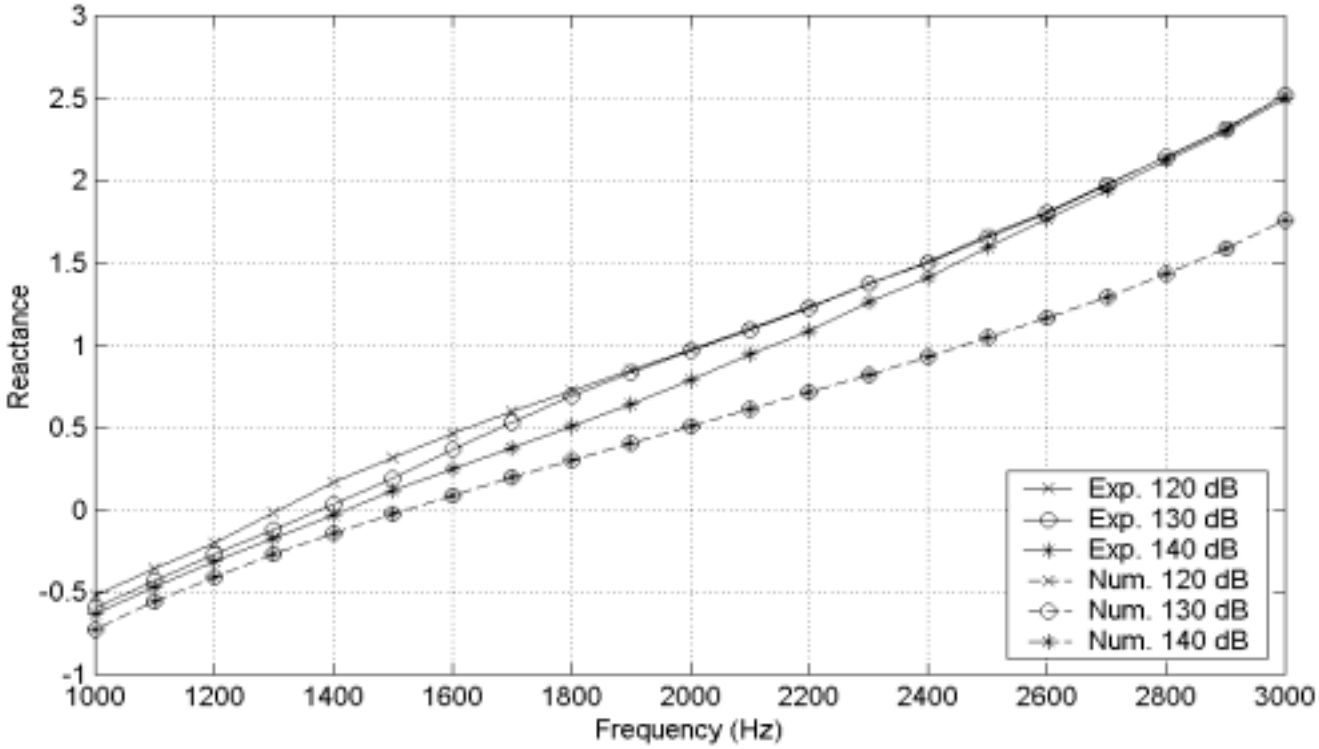
Reactance
3
2.5
2
1.5
1
0.5
0
-0.5
-1
1000
1200
1400
1600
1800
2000
2200
2400
2600
2800
3000
Frequency (Hz)
Exp. 120 dB
Exp. 130 dB
Exp. 140 dB
Num. 120 dB
Num. 130 dB
Num. 140 dB

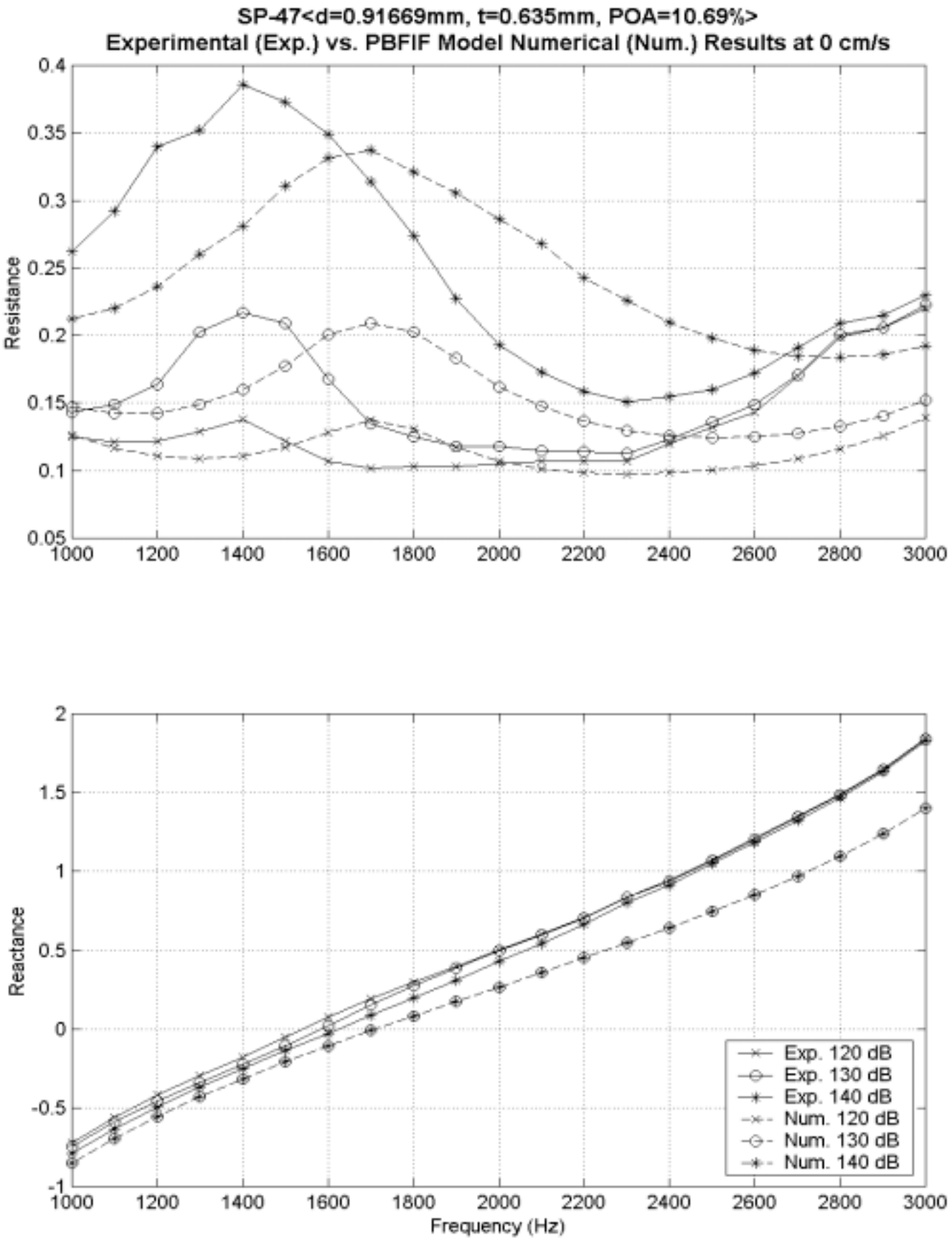
SP-47<d=0.91669mm, t=0.635mm, POA=10.69%>
Experimental (Exp.) vs. PBFIF Model Numerical (Num.) Results at 0 cm/s
Resistance
Reactance
Frequency (Hz)
Exp. 120 dB
Exp. 130 dB
Exp. 140 dB
Num. 120 dB
Num. 130 dB
Num. 140 dB

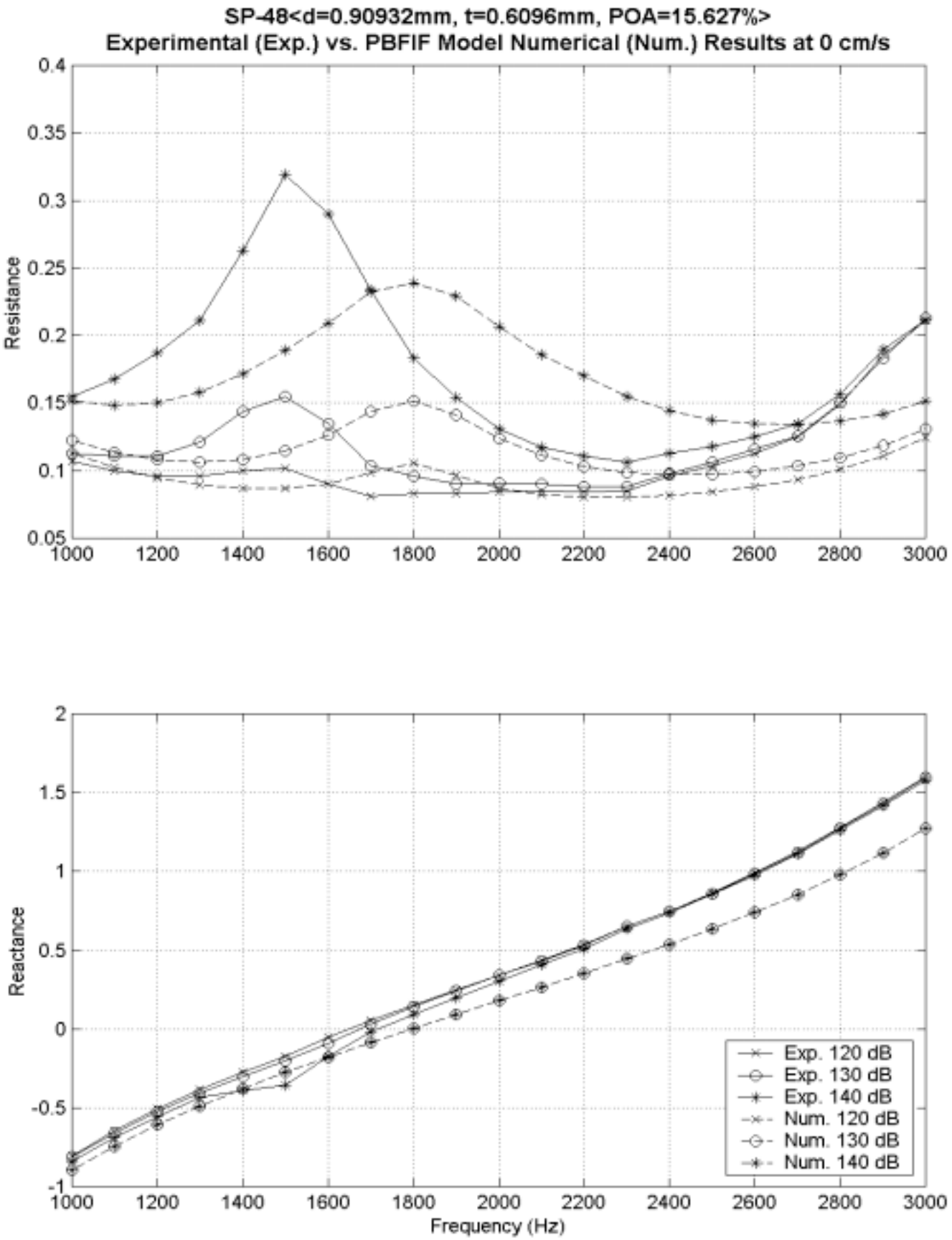
SP-48<d=0.90932mm, t=0.6096mm, POA=15.627%>
Experimental (Exp.) vs. PBFIF Model Numerical (Num.) Results at 0 cm/s
Resistance
Reactance
Frequency (Hz)
Exp. 120 dB
Exp. 130 dB
Exp. 140 dB
Num. 120 dB
Num. 130 dB
Num. 140 dB

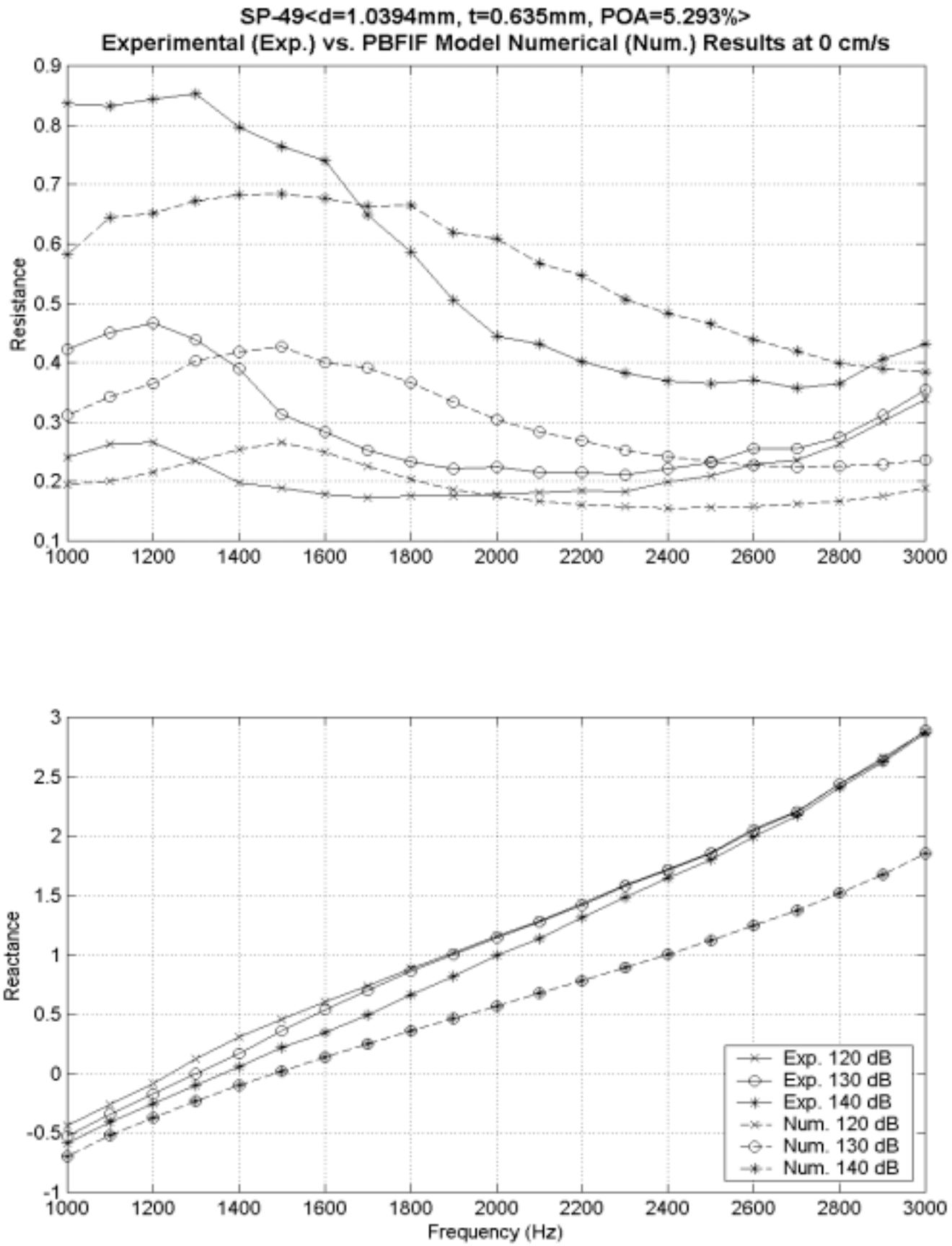
SP-49<d=1.0394mm, t=0.635mm, POA=5.293%>
Experimental (Exp.) vs. PBFIF Model Numerical (Num.) Results at 0 cm/s
Resistance
Reactance
Frequency (Hz)
Exp. 120 dB
Exp. 130 dB
Exp. 140 dB
Num. 120 dB
Num. 130 dB
Num. 140 dB

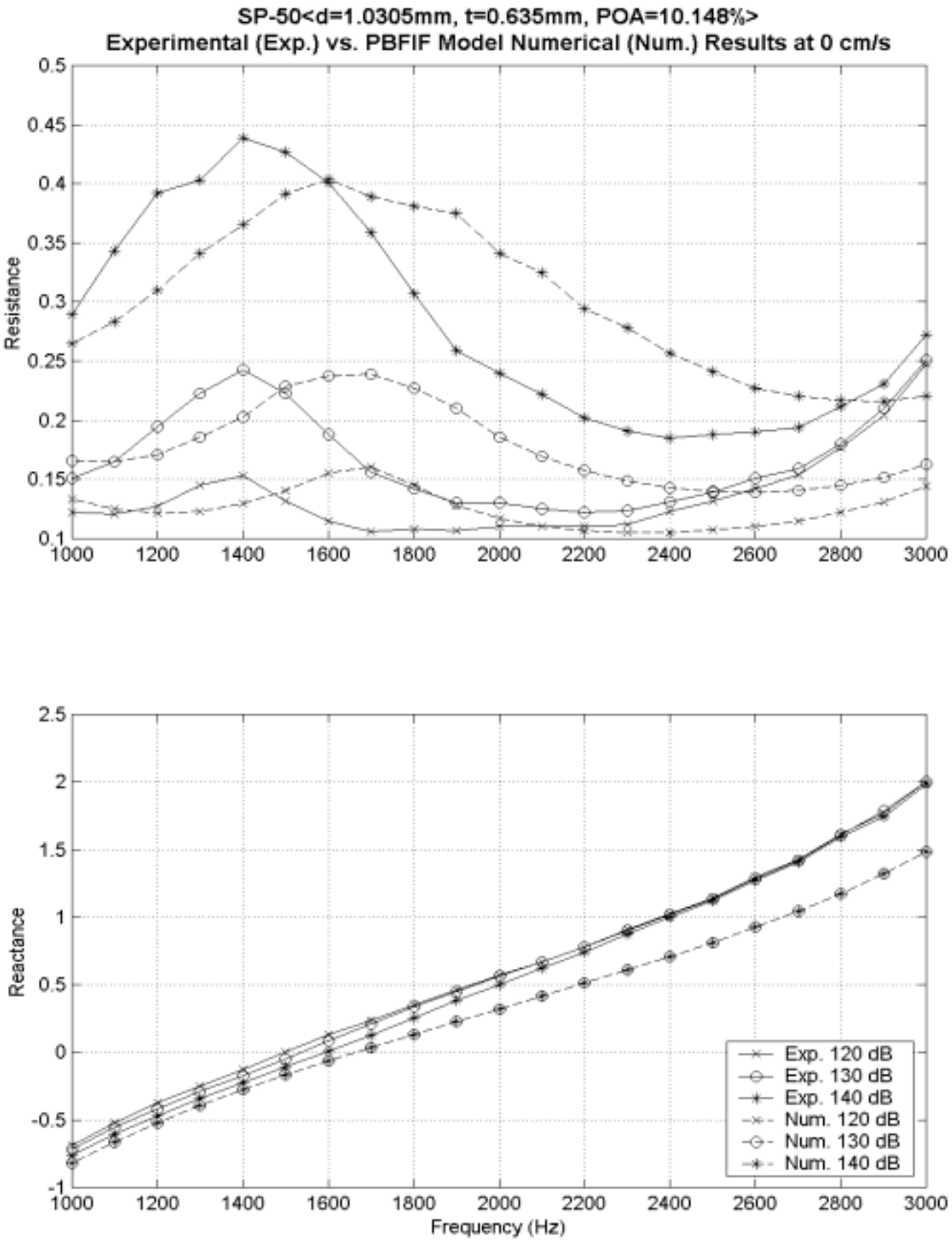
SP-50<d=1.0305mm, t=0.635mm, POA=10.148%>
Experimental (Exp.) vs. PBFIF Model Numerical (Num.) Results at 0 cm/s
Resistance
Reactance
Frequency (Hz)
Exp. 120 dB
Exp. 130 dB
Exp. 140 dB
Num. 120 dB
Num. 130 dB
Num. 140 dB

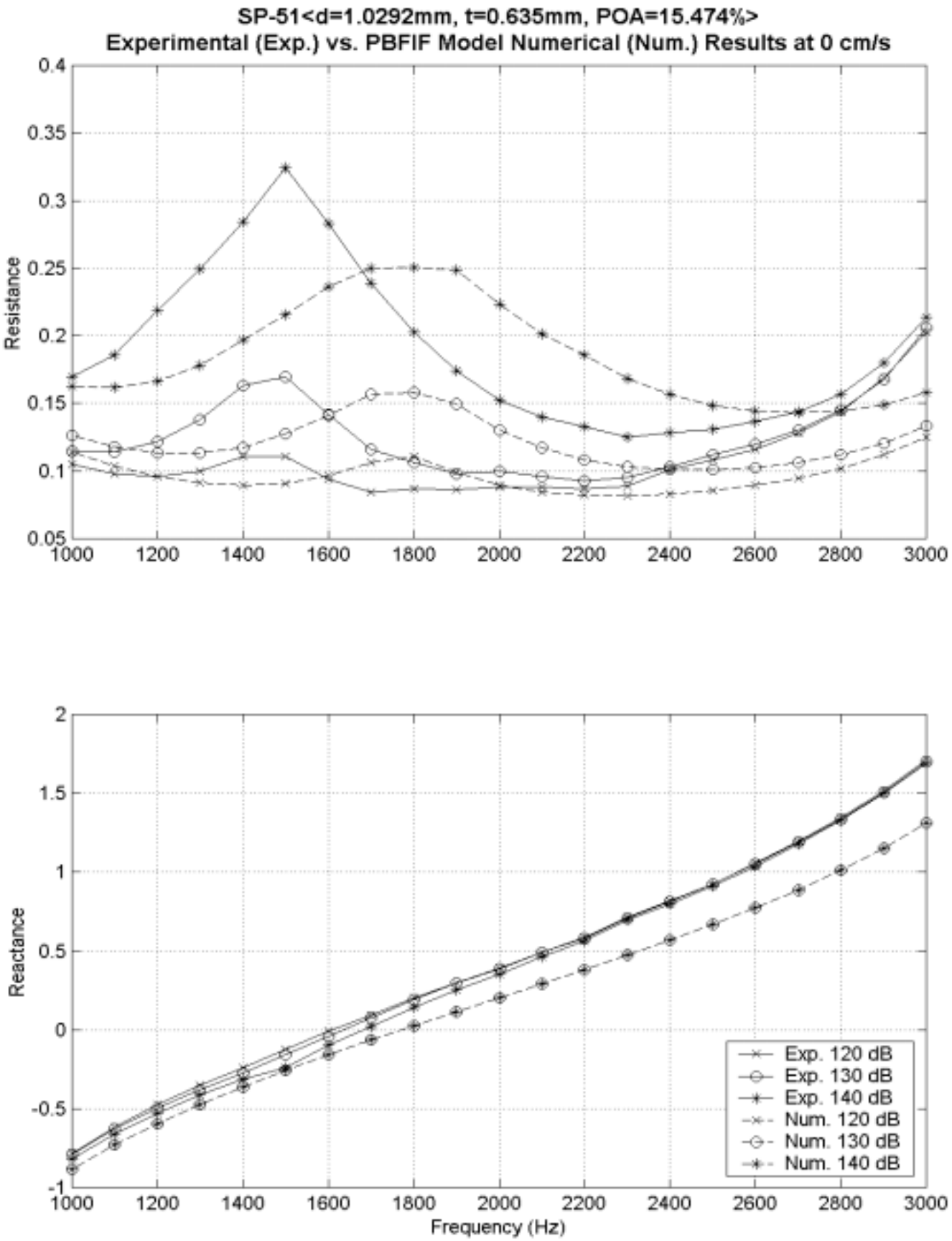
SP-51<d=1.0292mm, t=0.635mm, POA=15.474%>
Experimental (Exp.) vs. PBFIF Model Numerical (Num.) Results at 0 cm/s
Resistance
Reactance
Frequency (Hz)
Exp. 120 dB
Exp. 130 dB
Exp. 140 dB
Num. 120 dB
Num. 130 dB
Num. 140 dB

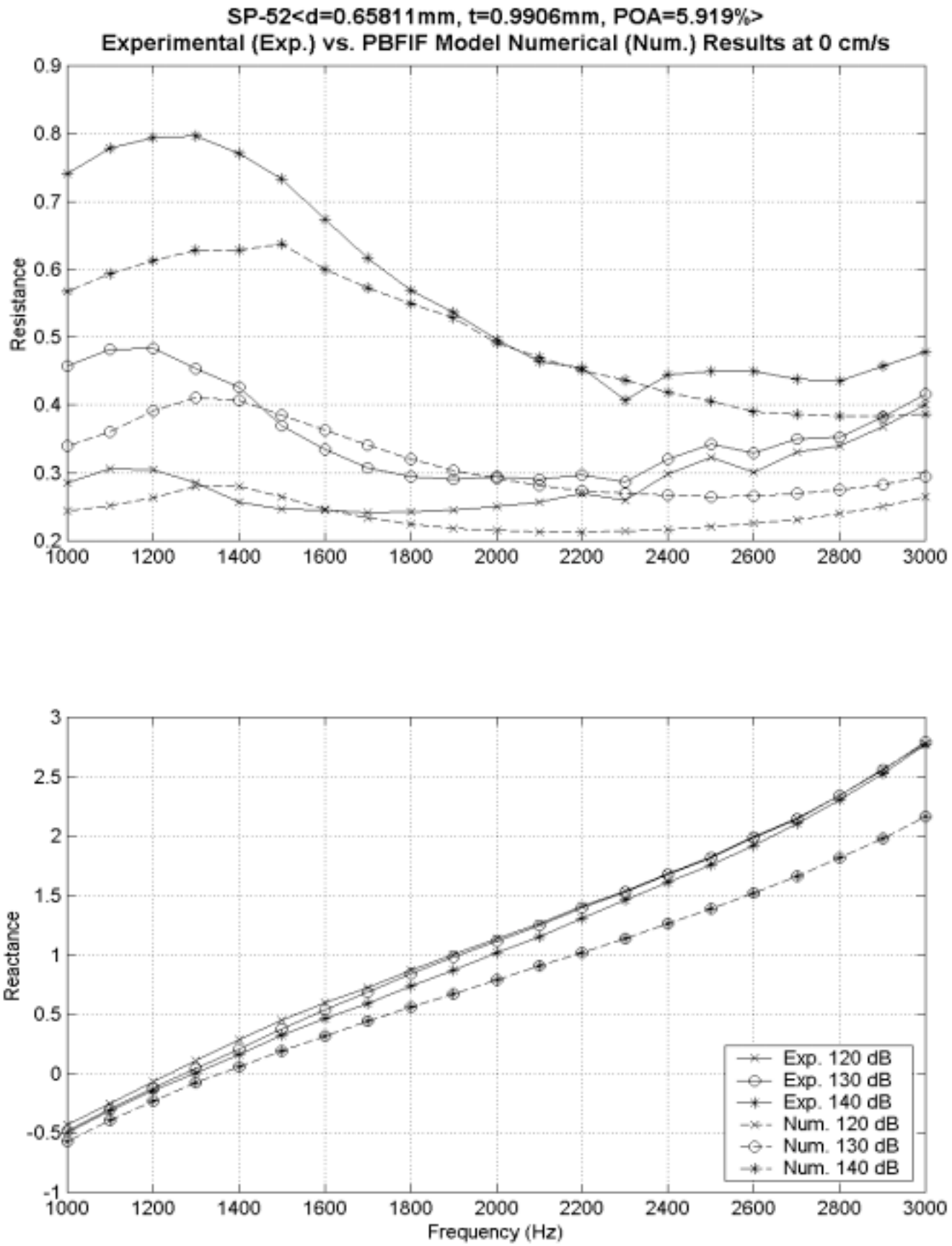
SP-52<d=0.65811mm, t=0.9906mm, POA=5.919%>
Experimental (Exp.) vs. PBFIF Model Numerical (Num.) Results at 0 cm/s
Resistance
Reactance
Frequency (Hz)
Exp. 120 dB
Exp. 130 dB
Exp. 140 dB
Num. 120 dB
Num. 130 dB
Num. 140 dB

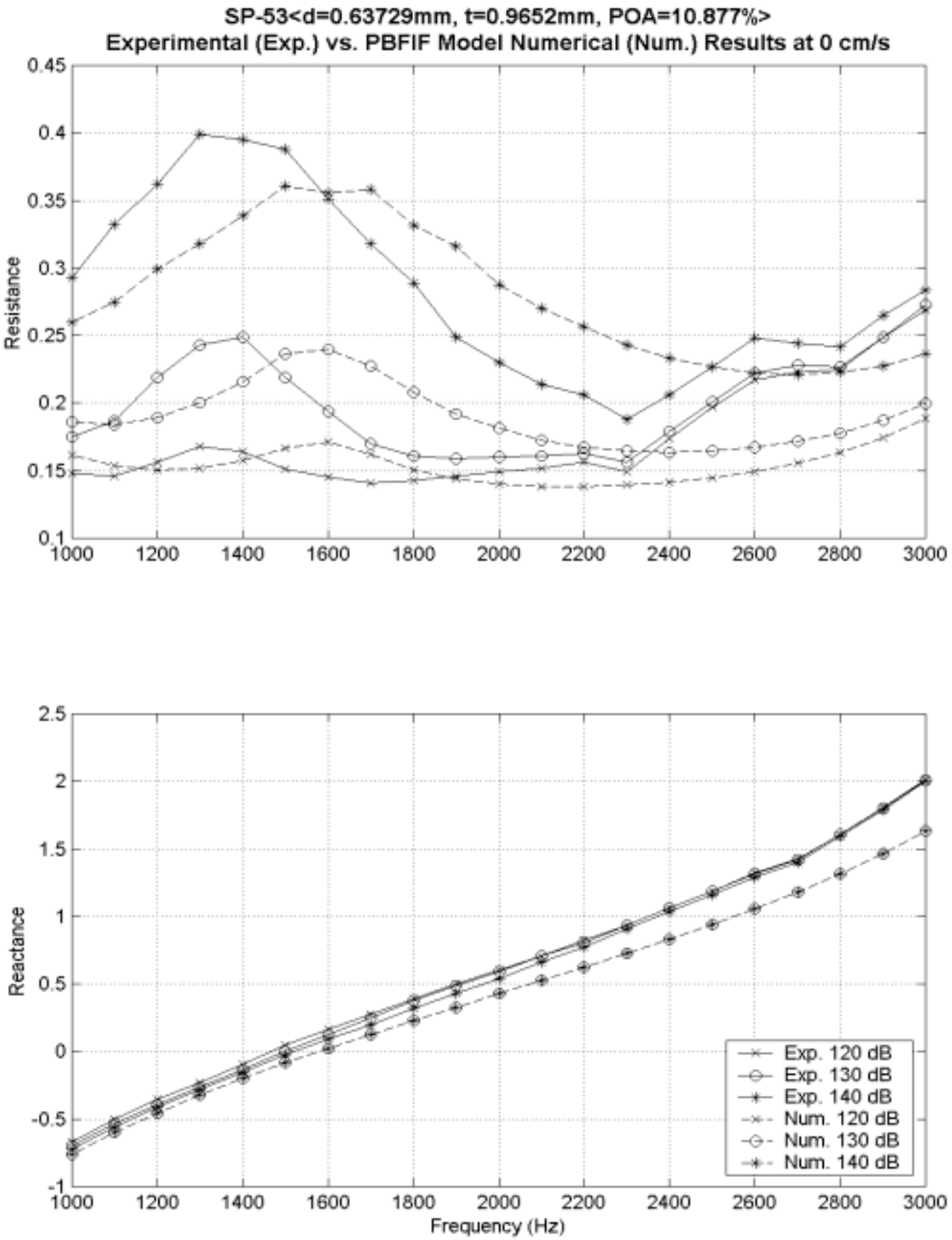
SP-53<d=0.63729mm, t=0.9652mm, POA=10.877%>
Experimental (Exp.) vs. PBFIF Model Numerical (Num.) Results at 0 cm/s
Resistance
Reactance
Frequency (Hz)
Exp. 120 dB
Exp. 130 dB
Exp. 140 dB
Num. 120 dB
Num. 130 dB
Num. 140 dB

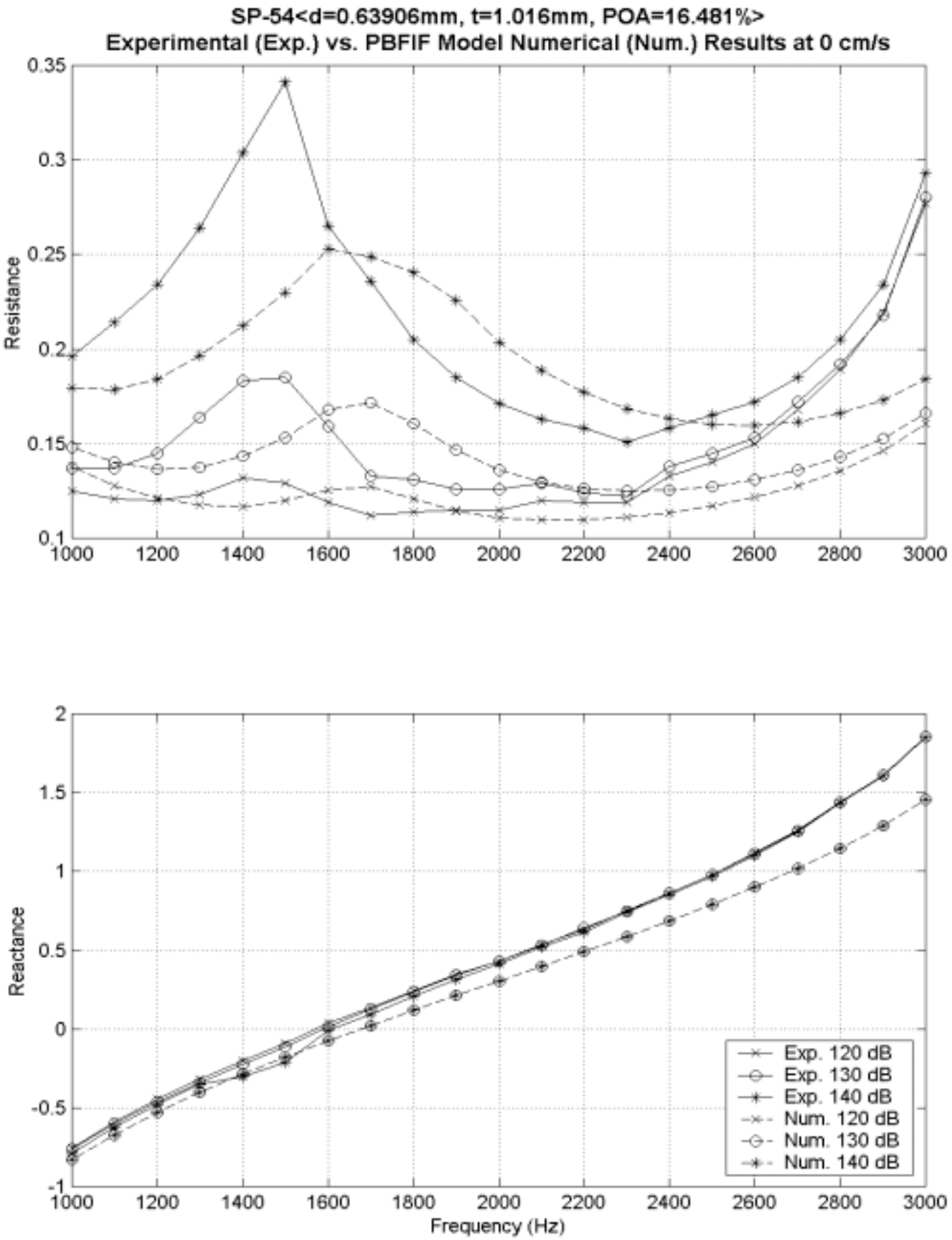
SP-54<d=0.63906mm, t=1.016mm, POA=16.481%>
Experimental (Exp.) vs. PBFIF Model Numerical (Num.) Results at 0 cm/s
Resistance
Reactance
Frequency (Hz)
Exp. 120 dB
Exp. 130 dB
Exp. 140 dB
Num. 120 dB
Num. 130 dB
Num. 140 dB

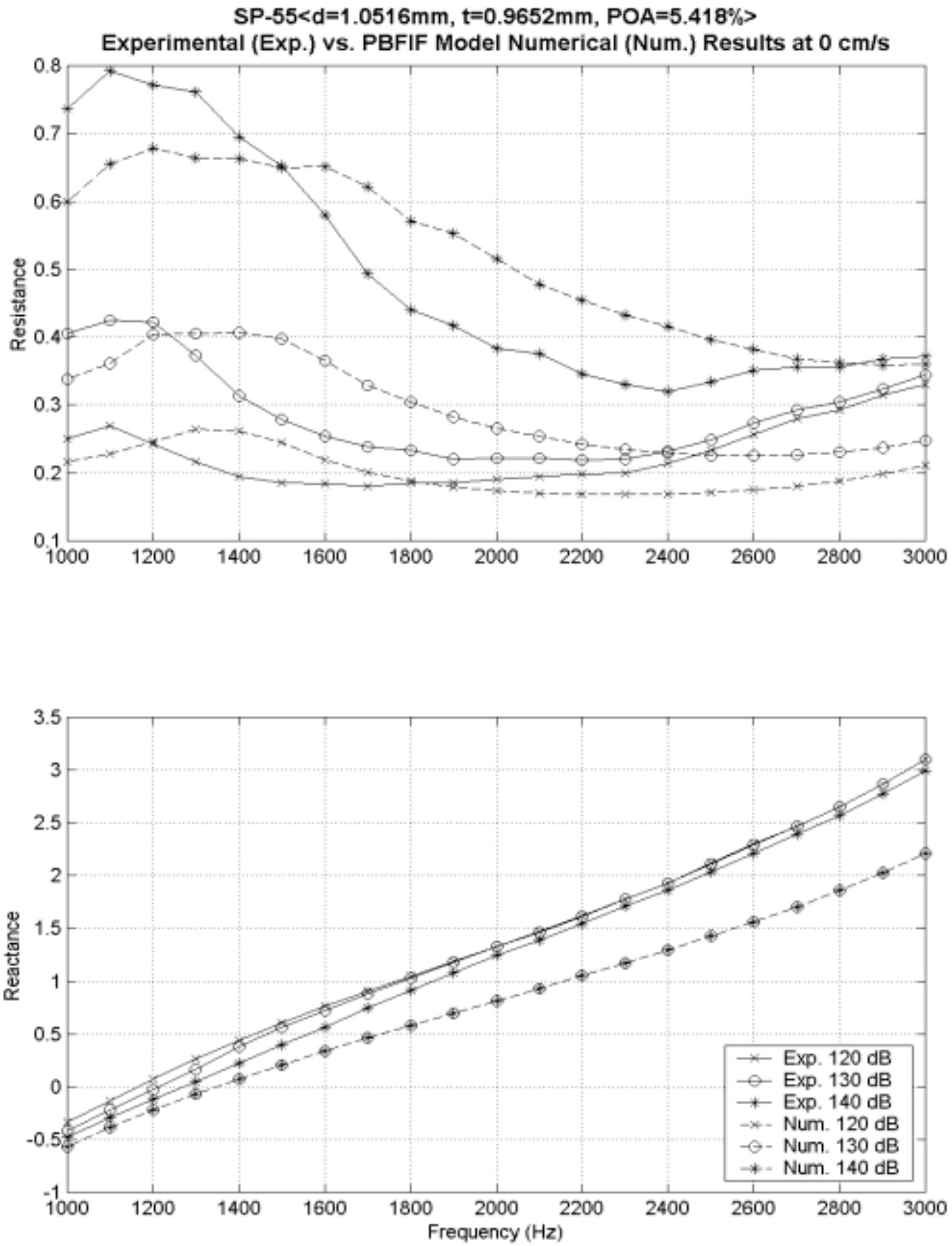
SP-55<d=1.0516mm, t=0.9652mm, POA=5.418%>
Experimental (Exp.) vs. PBFIF Model Numerical (Num.) Results at 0 cm/s
Resistance
Reactance
Frequency (Hz)
Exp. 120 dB
Exp. 130 dB
Exp. 140 dB
Num. 120 dB
Num. 130 dB
Num. 140 dB

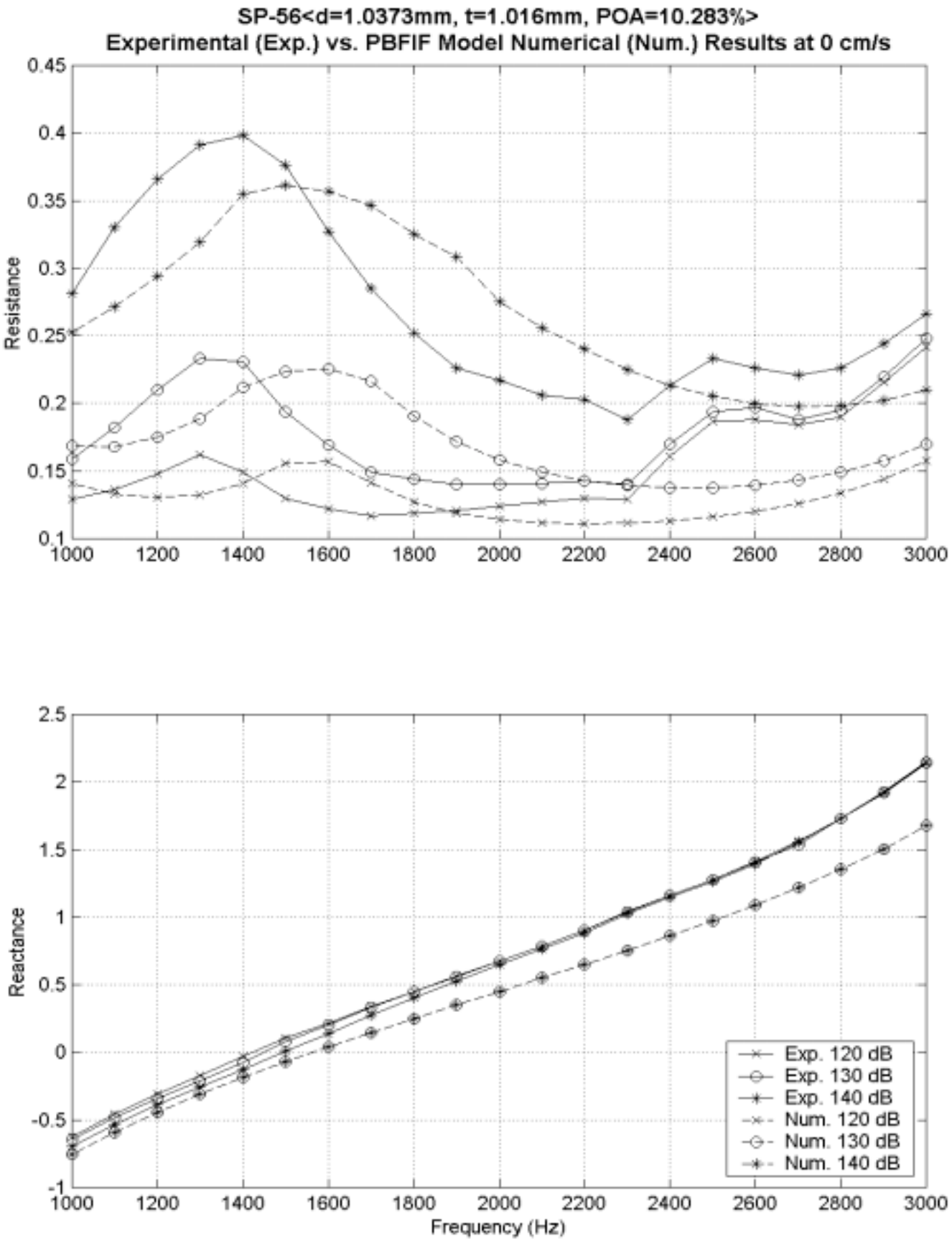
SP-56<d=1.0373mm, t=1.016mm, POA=10.283%>
Experimental (Exp.) vs. PBFIF Model Numerical (Num.) Results at 0 cm/s
Resistance
Reactance
Frequency (Hz)
Exp. 120 dB
Exp. 130 dB
Exp. 140 dB
Num. 120 dB
Num. 130 dB
Num. 140 dB

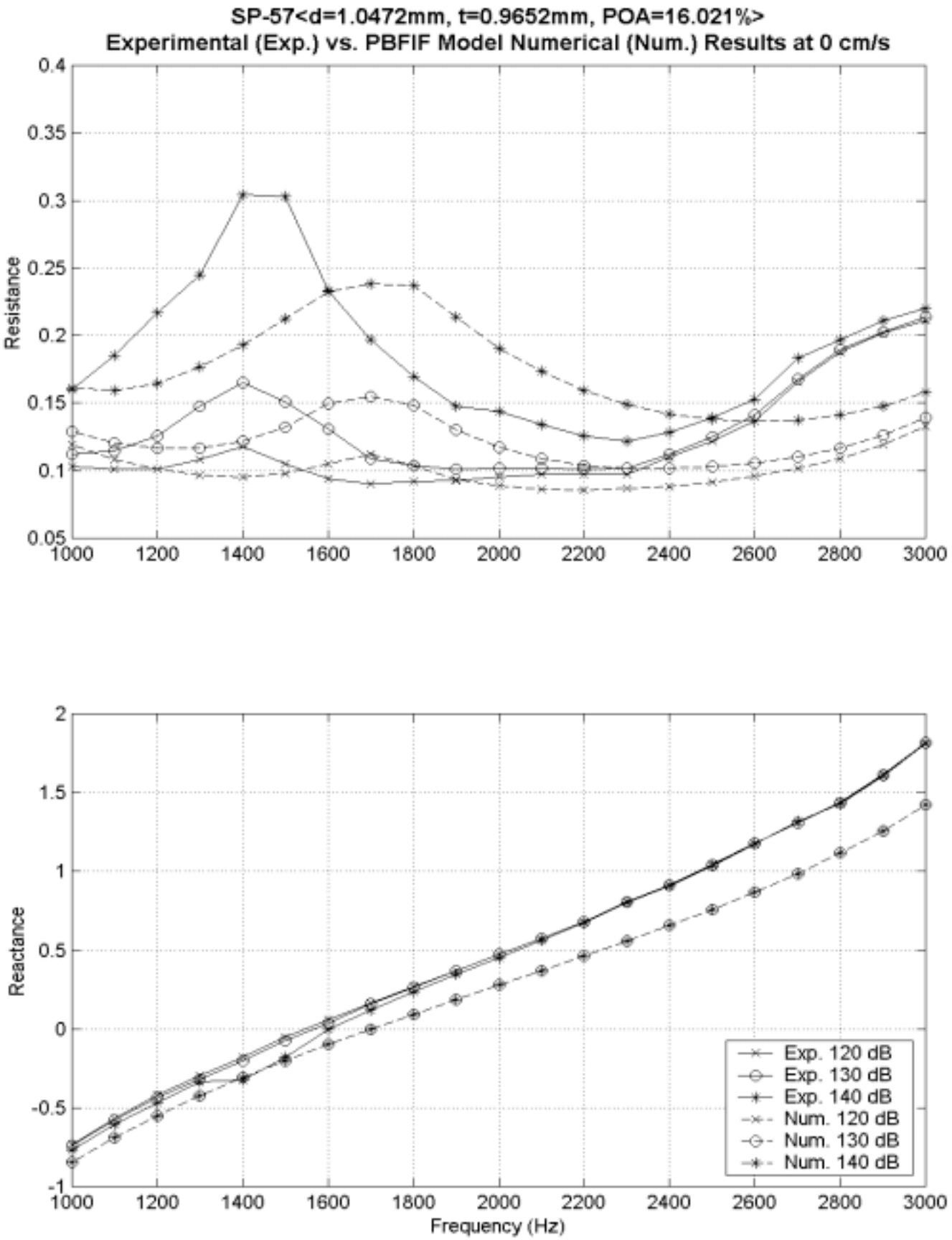
SP-57<d=1.0472mm, t=0.9652mm, POA=16.021%>
Experimental (Exp.) vs. PBFIF Model Numerical (Num.) Results at 0 cm/s
Resistance
Reactance
Frequency (Hz)
Exp. 120 dB
Exp. 130 dB
Exp. 140 dB
Num. 120 dB
Num. 130 dB
Num. 140 dB

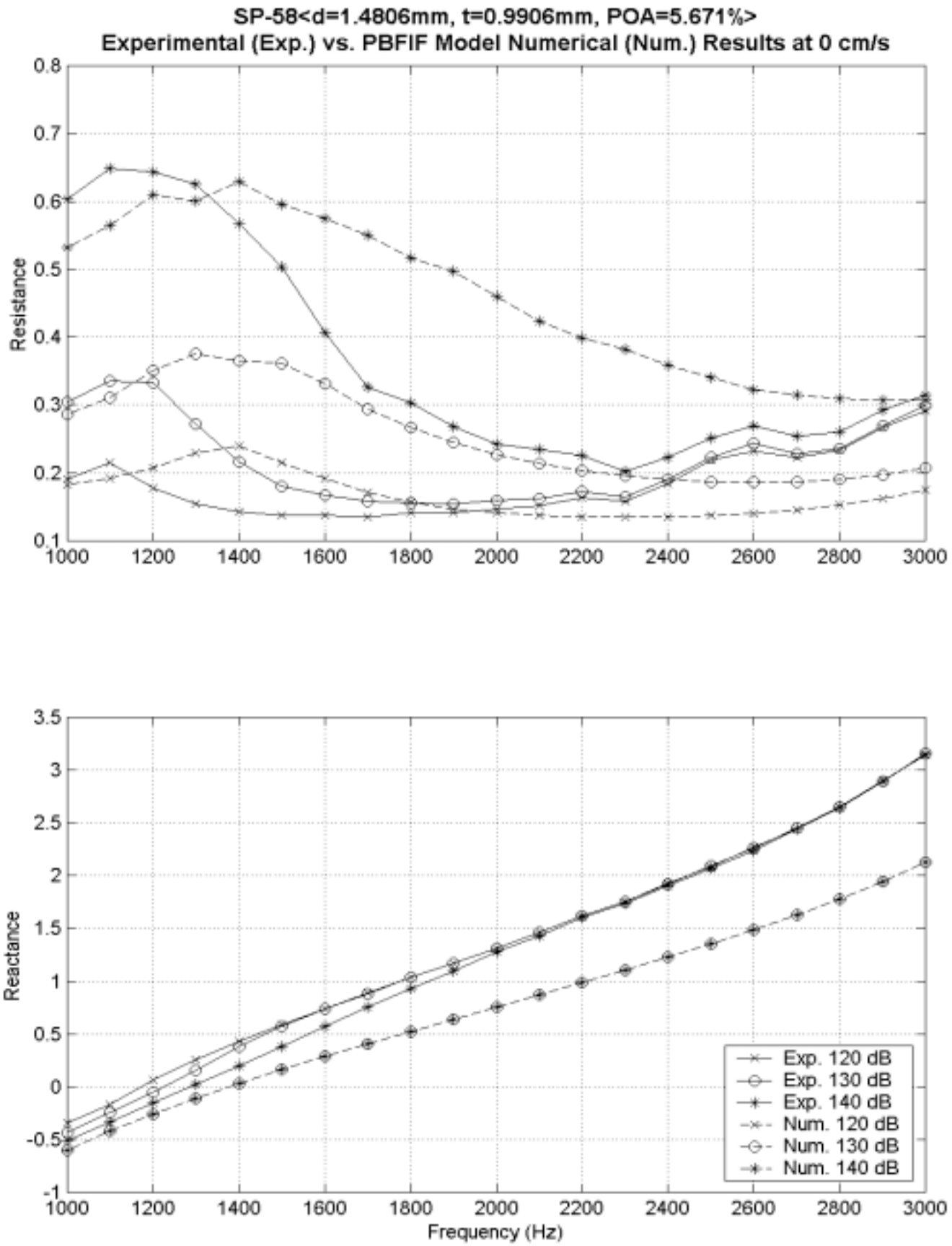
SP-58<d=1.4806mm, t=0.9906mm, POA=5.671%>
Experimental (Exp.) vs. PBFIF Model Numerical (Num.) Results at 0 cm/s
Resistance
Reactance
Frequency (Hz)
Exp. 120 dB
Exp. 130 dB
Exp. 140 dB
Num. 120 dB
Num. 130 dB
Num. 140 dB

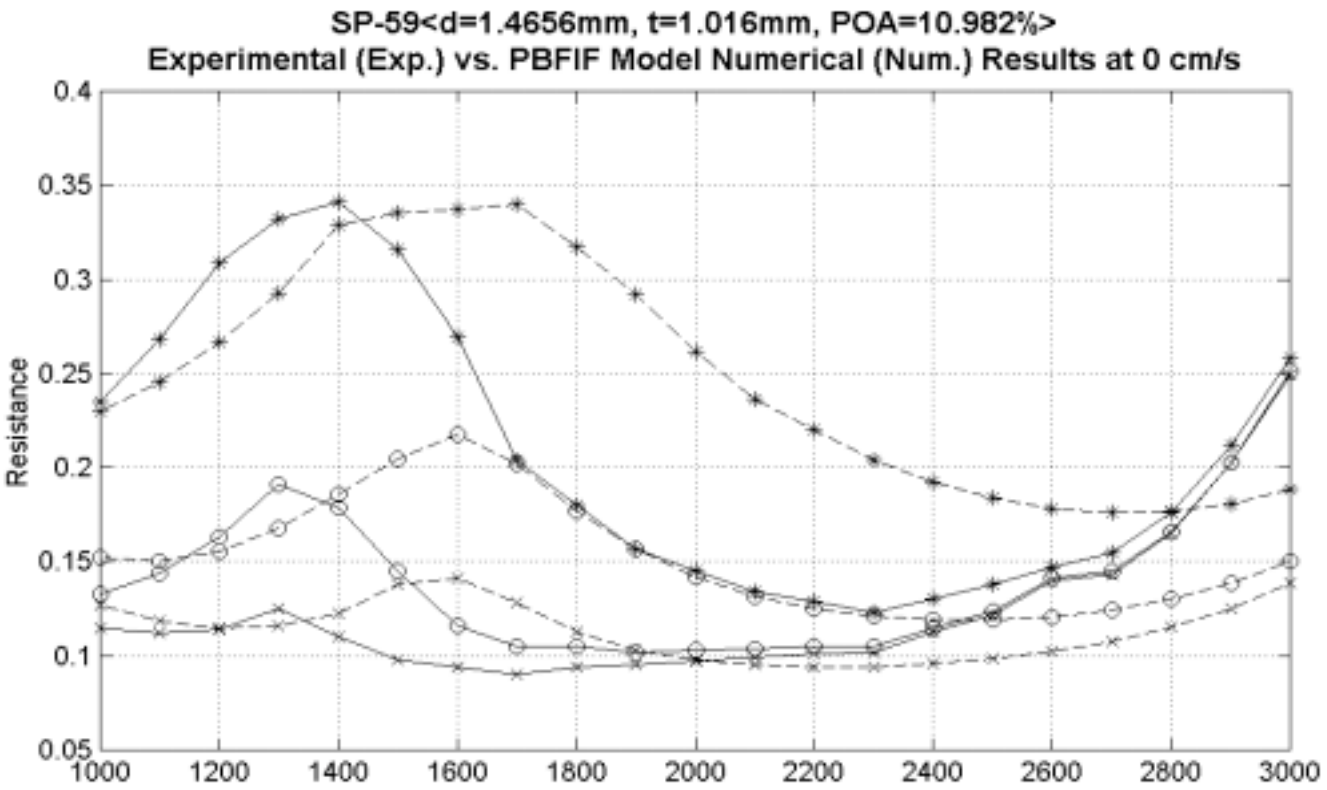
SP-59<d=1.4656mm, t=1.016mm, POA=10.982%>
Experimental (Exp.) vs. PBFIF Model Numerical (Num.) Results at 0 cm/s
Resistance
0.4
0.35
0.3
0.25
0.2
0.15
0.1
0.05
1000
1200
1400
1600
1800
2000
2200
2400
2600
2800
3000

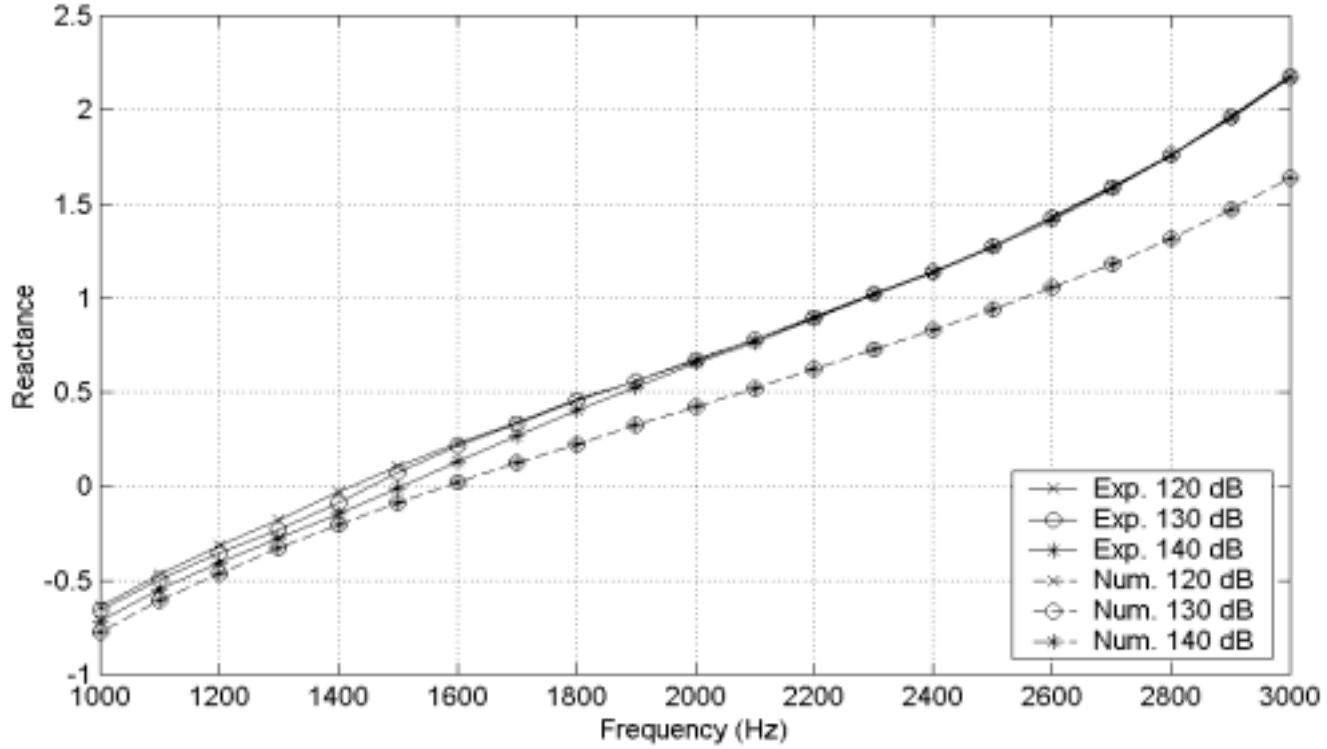
Reactance
2.5
2
1.5
1
0.5
0
-0.5
-1
1000
1200
1400
1600
1800
2000
2200
2400
2600
2800
3000
Frequency (Hz)
Exp. 120 dB
Exp. 130 dB
Exp. 140 dB
Num. 120 dB
Num. 130 dB
Num. 140 dB

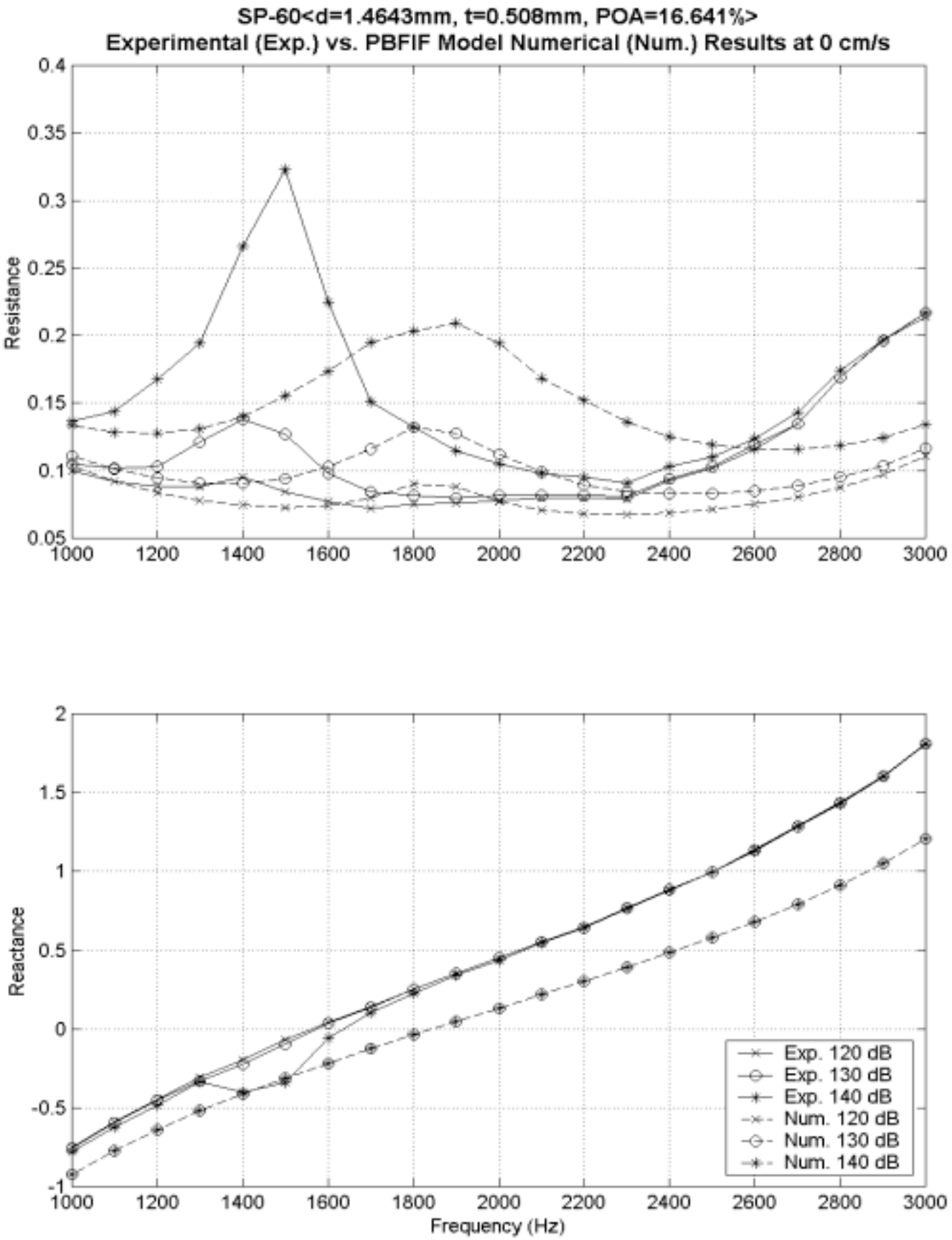
SP-60<d=1.4643mm, t=0.508mm, POA=16.641%>
Experimental (Exp.) vs. PBFIF Model Numerical (Num.) Results at 0 cm/s
Resistance
Reactance
Frequency (Hz)
Exp. 120 dB
Exp. 130 dB
Exp. 140 dB
Num. 120 dB
Num. 130 dB
Num. 140 dB

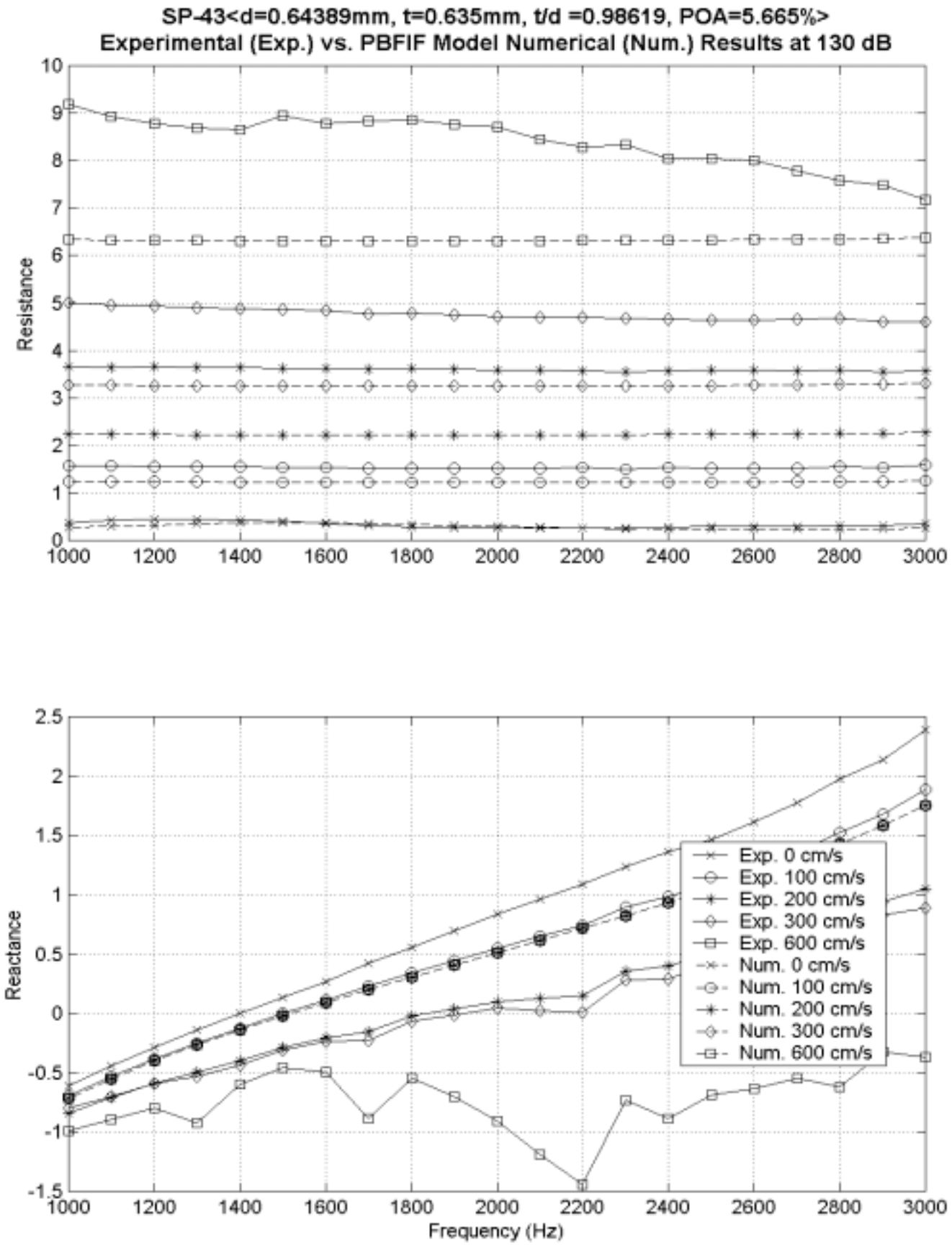
SP-43<d=0.64389mm, t=0.635mm, t/d =0.98619, POA=5.665%>
Experimental (Exp.) vs. PBFIF Model Numerical (Num.) Results at 130 dB
Resistance
Reactance
Frequency (Hz)
Exp. 0 cm/s
Exp. 100 cm/s
Exp. 200 cm/s
Exp. 300 cm/s
Exp. 600 cm/s
Num. 0 cm/s
Num. 100 cm/s
Num. 200 cm/s
Num. 300 cm/s
Num. 600 cm/s

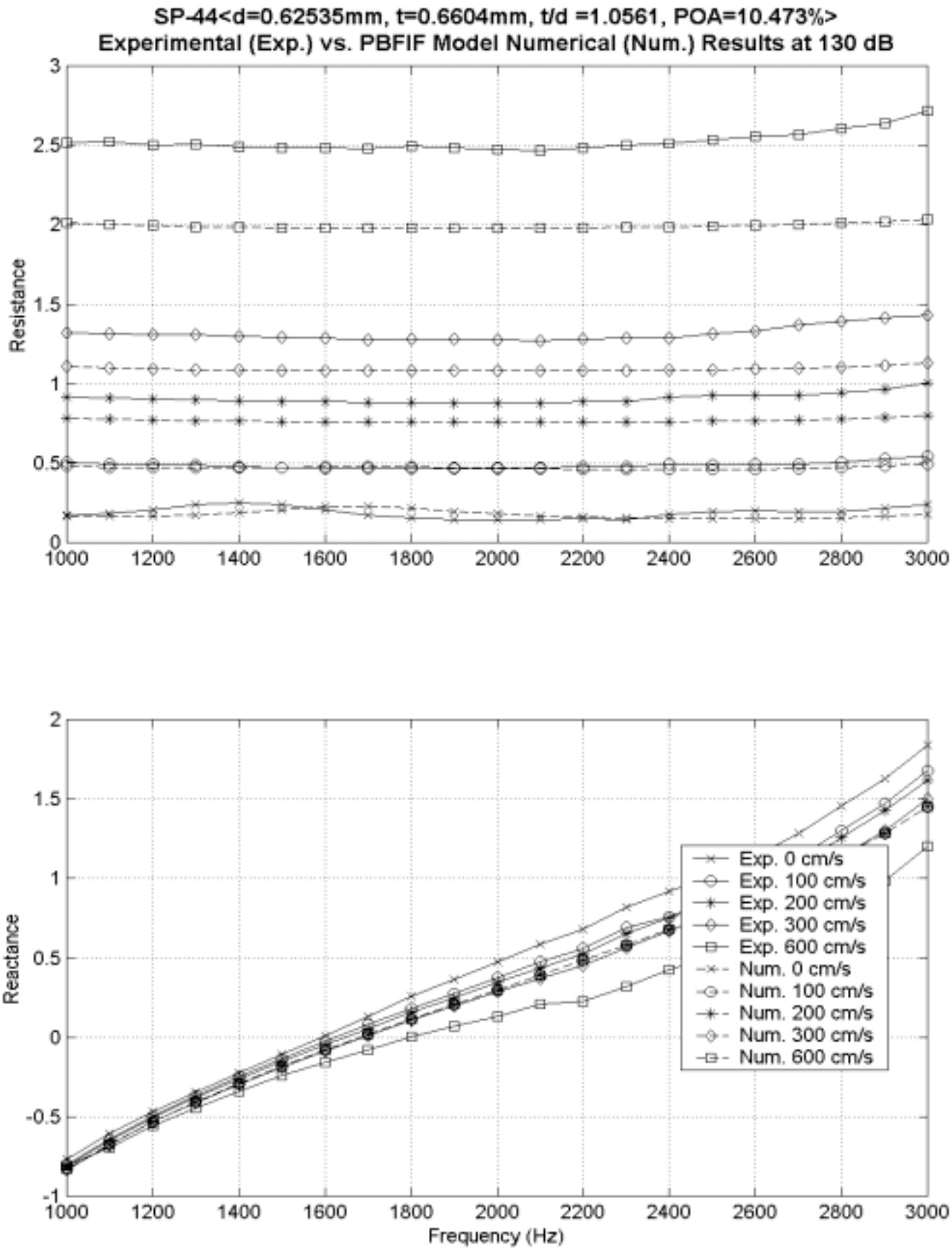
SP-44<d=0.62535mm, t=0.6604mm, t/d =1.0561, POA=10.473%>
Experimental (Exp.) vs. PBFIF Model Numerical (Num.) Results at 130 dB
Resistance
Reactance
Frequency (Hz)
Exp. 0 cm/s
Exp. 100 cm/s
Exp. 200 cm/s
Exp. 300 cm/s
Exp. 600 cm/s
Num. 0 cm/s
Num. 100 cm/s
Num. 200 cm/s
Num. 300 cm/s
Num. 600 cm/s

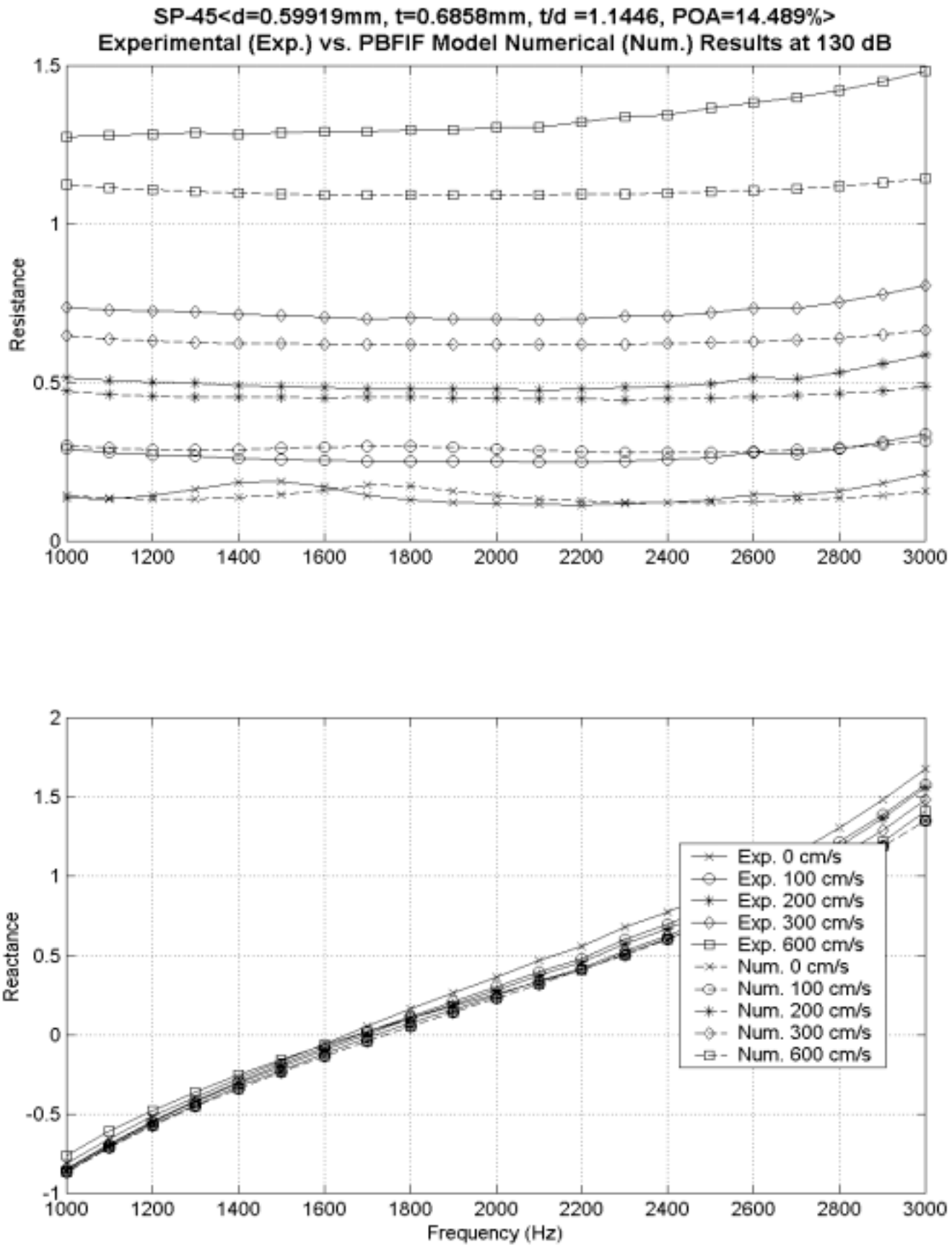
SP-45<d=0.59919mm, t=0.6858mm, t/d =1.1446, POA=14.489%>
Experimental (Exp.) vs. PBFIF Model Numerical (Num.) Results at 130 dB
Resistance
Reactance
Frequency (Hz)
Exp. 0 cm/s
Exp. 100 cm/s
Exp. 200 cm/s
Exp. 300 cm/s
Exp. 600 cm/s
Num. 0 cm/s
Num. 100 cm/s
Num. 200 cm/s
Num. 300 cm/s
Num. 600 cm/s

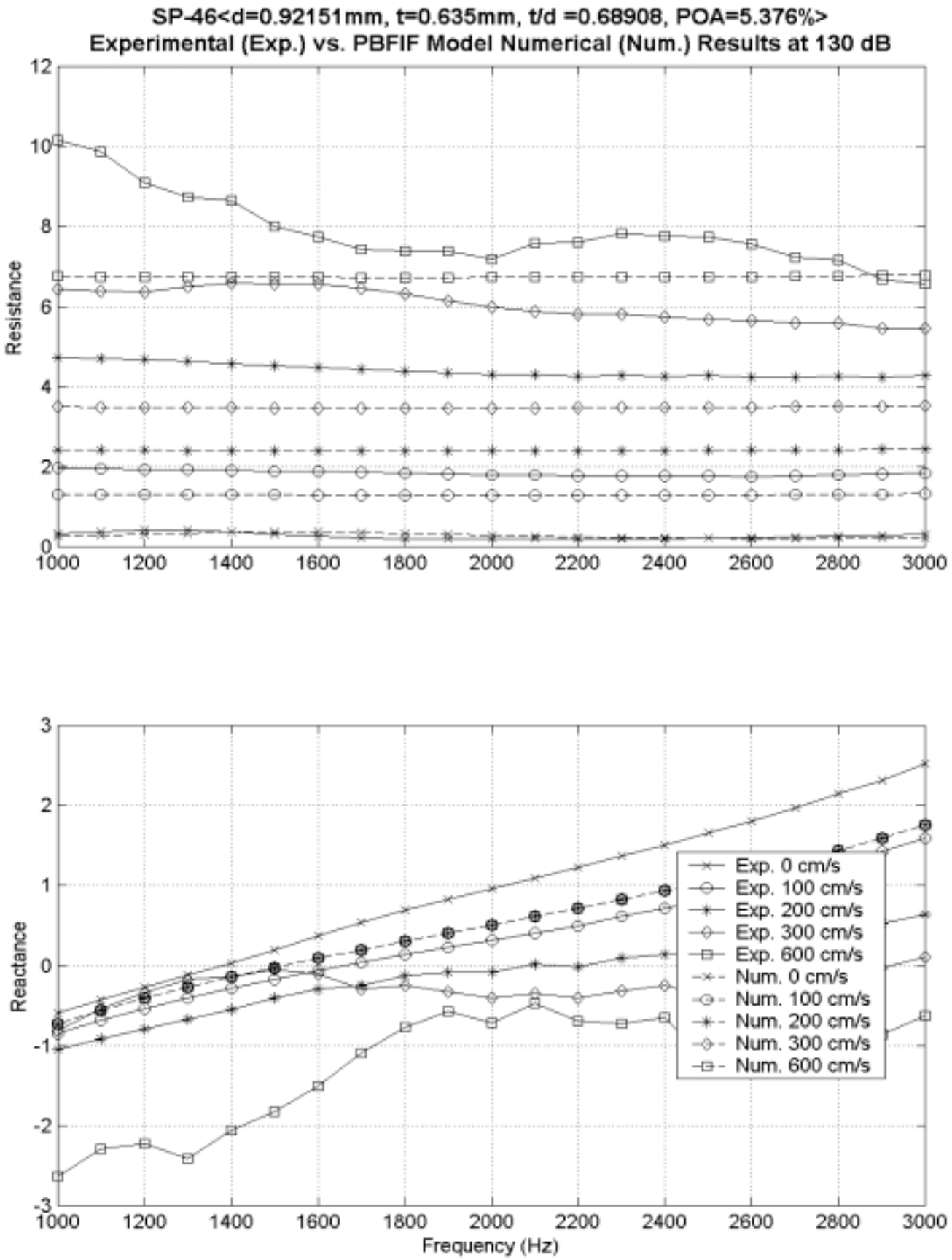
SP-46<d=0.92151mm, t=0.635mm, t/d =0.68908, POA=5.376%>
Experimental (Exp.) vs. PBFIF Model Numerical (Num.) Results at 130 dB
Resistance
Reactance
Frequency (Hz)
Exp. 0 cm/s
Exp. 100 cm/s
Exp. 200 cm/s
Exp. 300 cm/s
Exp. 600 cm/s
Num. 0 cm/s
Num. 100 cm/s
Num. 200 cm/s
Num. 300 cm/s
Num. 600 cm/s

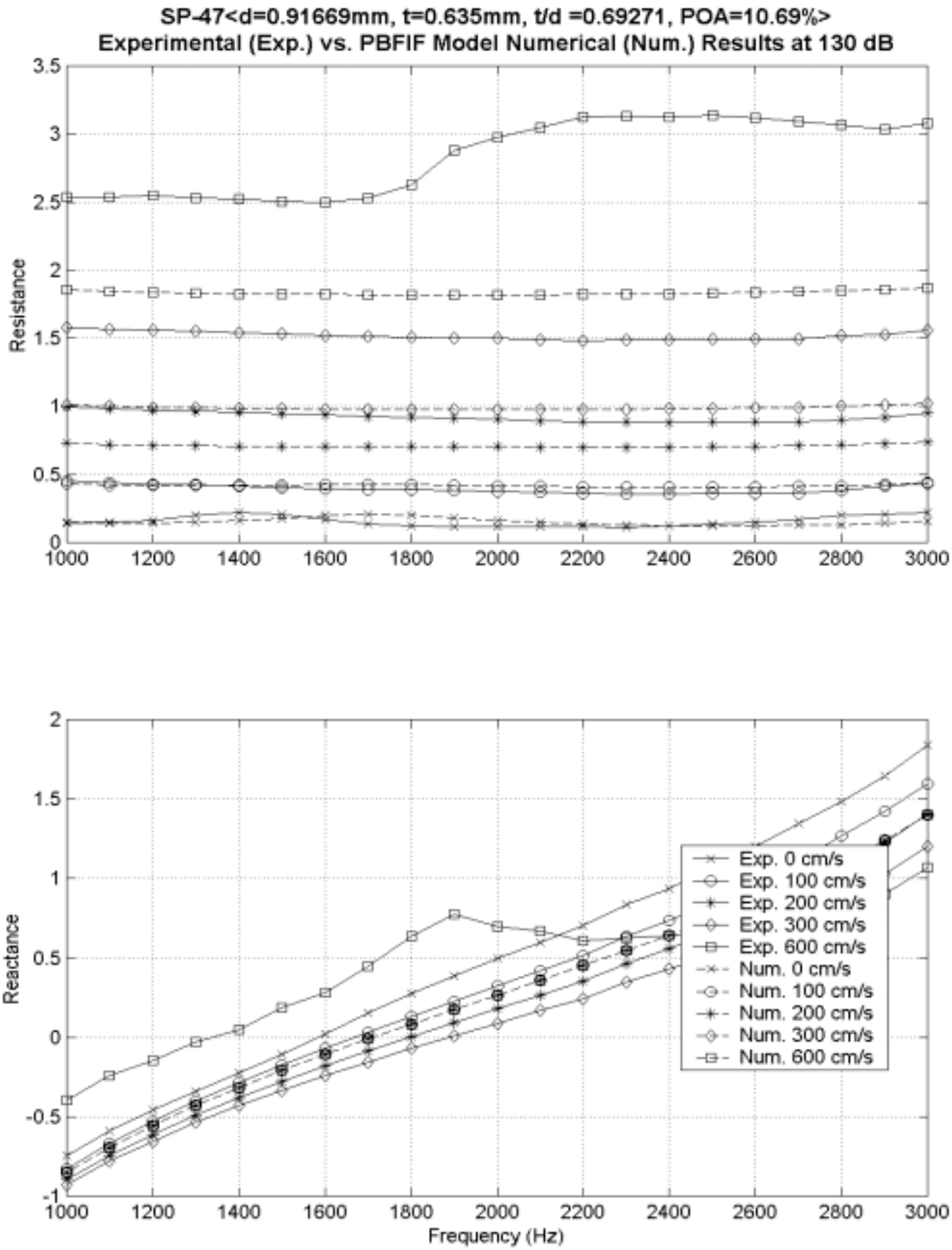
SP-47<d=0.91669mm, t=0.635mm, t/d =0.69271, POA=10.69%>
Experimental (Exp.) vs. PBFIF Model Numerical (Num.) Results at 130 dB
Resistance
Reactance
Frequency (Hz)
Exp. 0 cm/s
Exp. 100 cm/s
Exp. 200 cm/s
Exp. 300 cm/s
Exp. 600 cm/s
Num. 0 cm/s
Num. 100 cm/s
Num. 200 cm/s
Num. 300 cm/s
Num. 600 cm/s

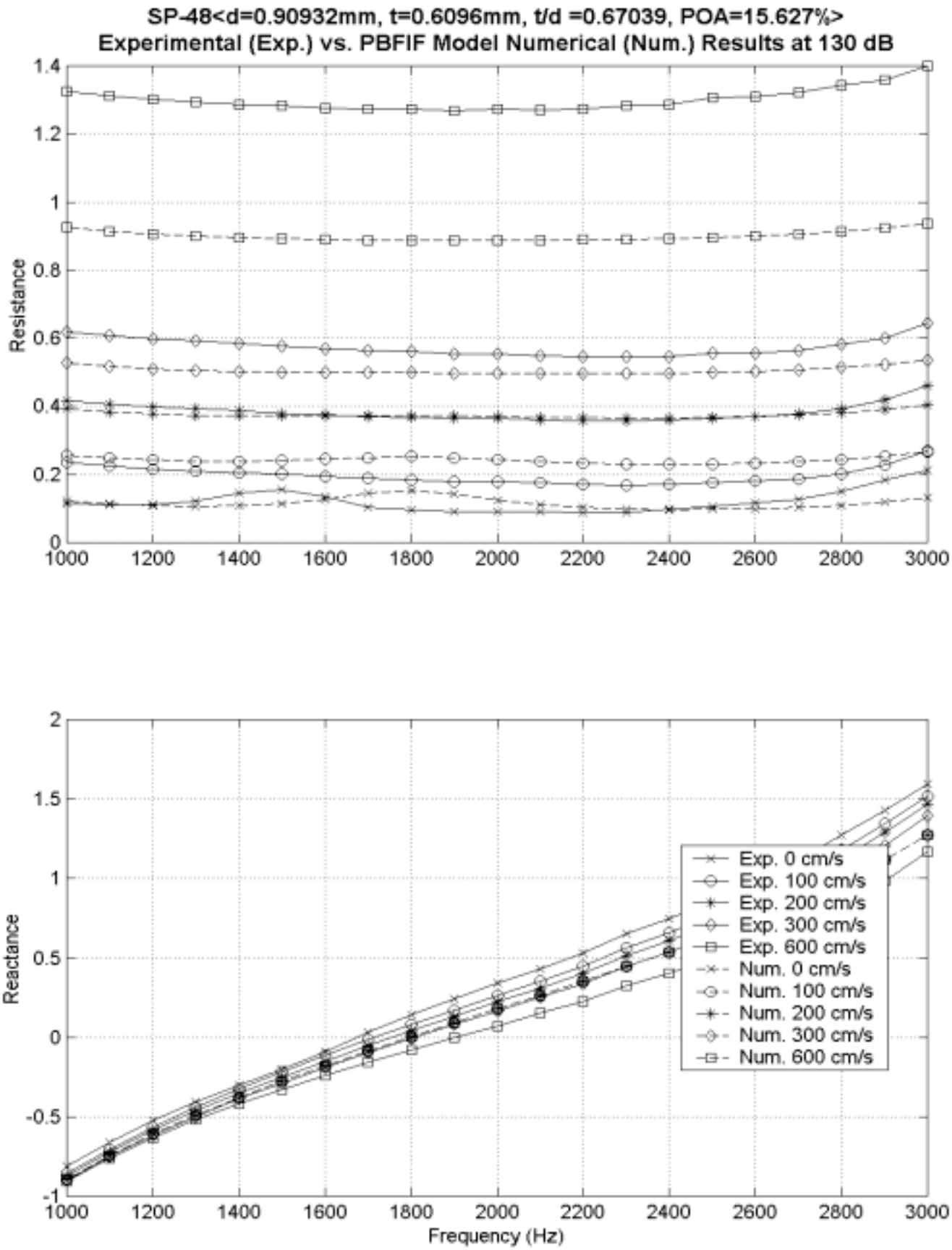
SP-48<d=0.90932mm, t=0.6096mm, t/d =0.67039, POA=15.627%>
Experimental (Exp.) vs. PBFIF Model Numerical (Num.) Results at 130 dB
Resistance
Reactance
Frequency (Hz)
Exp. 0 cm/s
Exp. 100 cm/s
Exp. 200 cm/s
Exp. 300 cm/s
Exp. 600 cm/s
Num. 0 cm/s
Num. 100 cm/s
Num. 200 cm/s
Num. 300 cm/s
Num. 600 cm/s

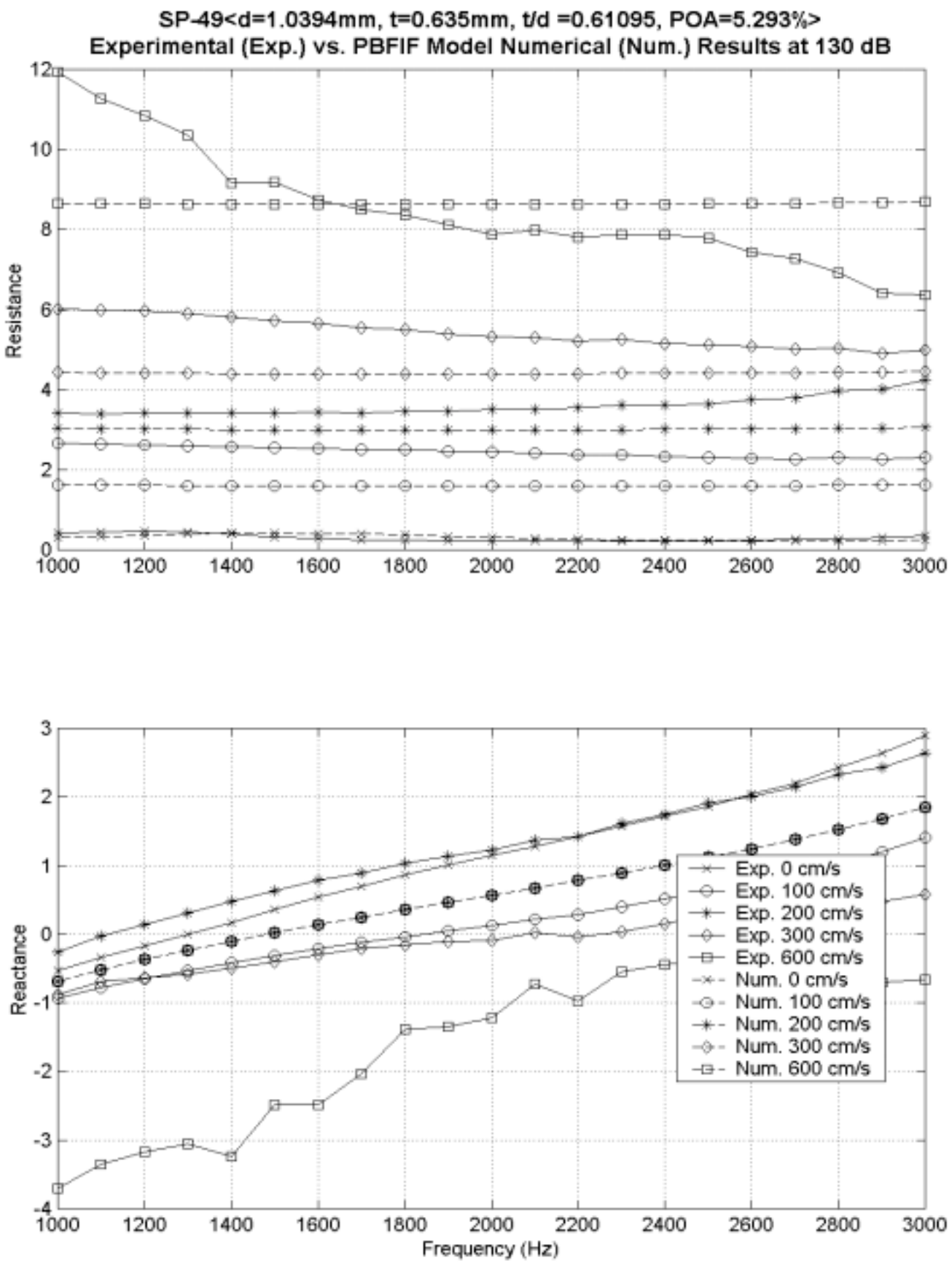
SP-49<d=1.0394mm, t=0.635mm, t/d =0.61095, POA=5.293%>
Experimental (Exp.) vs. PBFIF Model Numerical (Num.) Results at 130 dB
Resistance
Reactance
Frequency (Hz)
Exp. 0 cm/s
Exp. 100 cm/s
Exp. 200 cm/s
Exp. 300 cm/s
Exp. 600 cm/s
Num. 0 cm/s
Num. 100 cm/s
Num. 200 cm/s
Num. 300 cm/s
Num. 600 cm/s

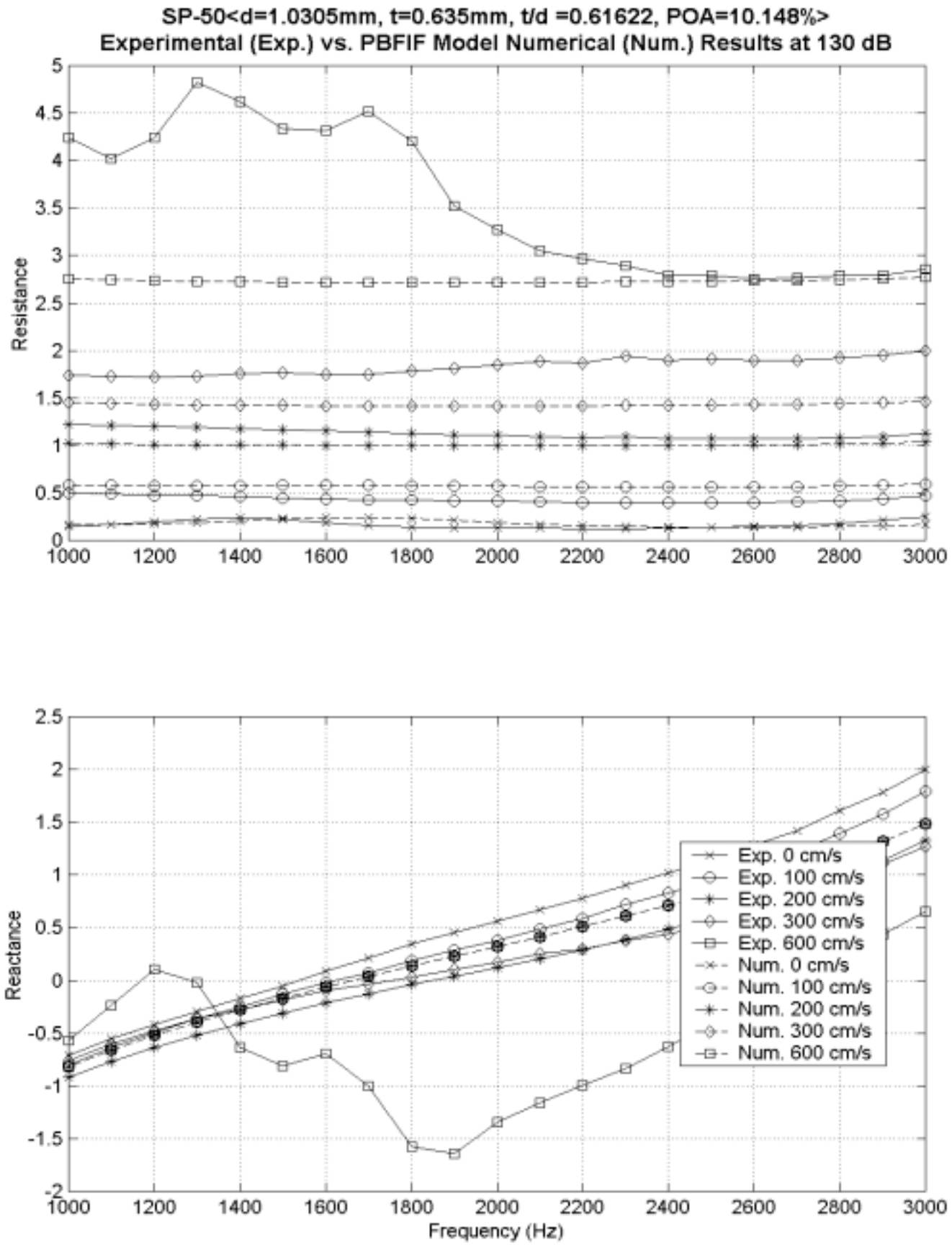
SP-50<d=1.0305mm, t=0.635mm, t/d =0.61622, POA=10.148%>
Experimental (Exp.) vs. PBFIF Model Numerical (Num.) Results at 130 dB
Resistance
Reactance
Frequency (Hz)
Exp. 0 cm/s
Exp. 100 cm/s
Exp. 200 cm/s
Exp. 300 cm/s
Exp. 600 cm/s
Num. 0 cm/s
Num. 100 cm/s
Num. 200 cm/s
Num. 300 cm/s
Num. 600 cm/s

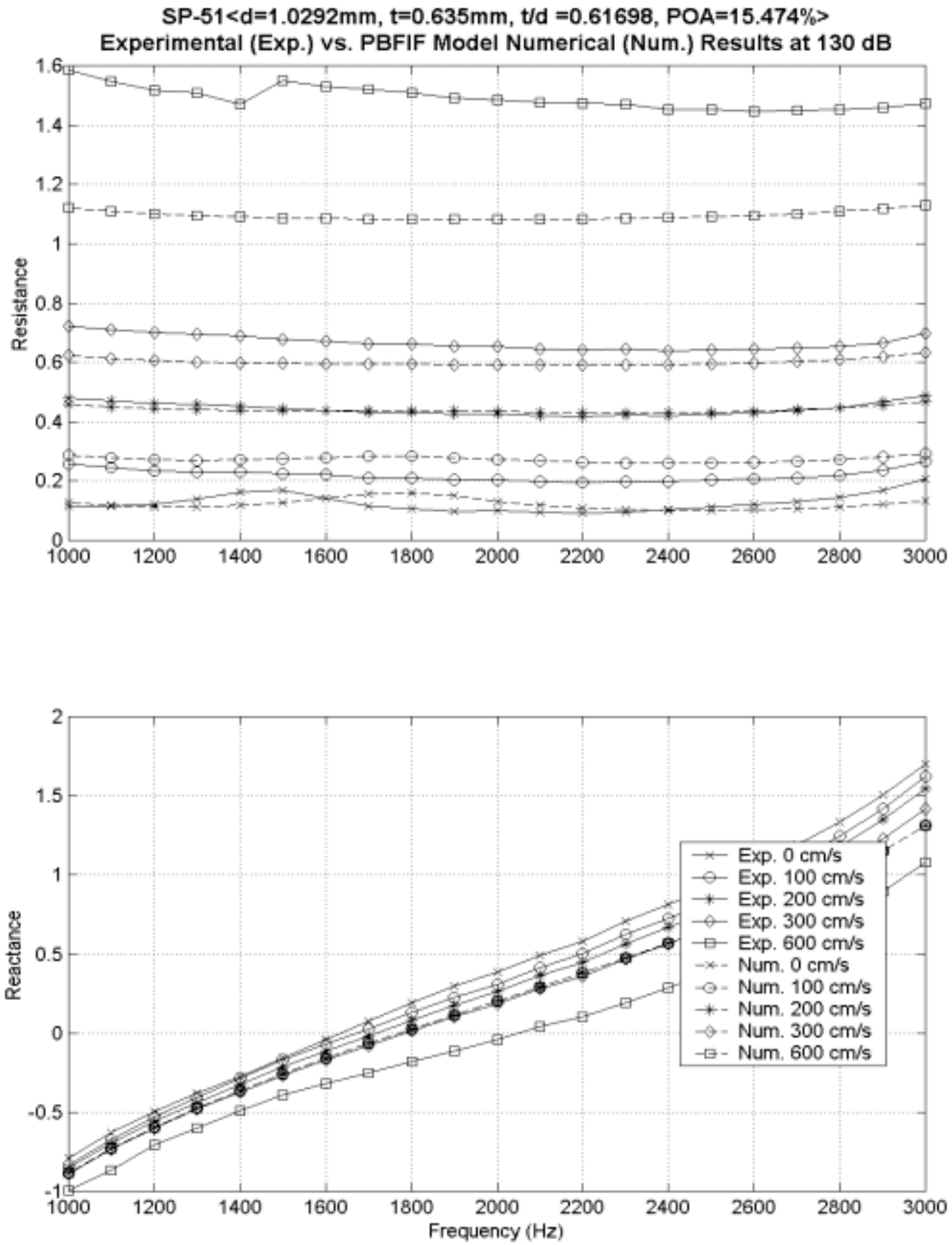
SP-51<d=1.0292mm, t=0.635mm, t/d =0.61698, POA=15.474%>
Experimental (Exp.) vs. PBFIF Model Numerical (Num.) Results at 130 dB
Resistance
Reactance
Frequency (Hz)
Exp. 0 cm/s
Exp. 100 cm/s
Exp. 200 cm/s
Exp. 300 cm/s
Exp. 600 cm/s
Num. 0 cm/s
Num. 100 cm/s
Num. 200 cm/s
Num. 300 cm/s
Num. 600 cm/s

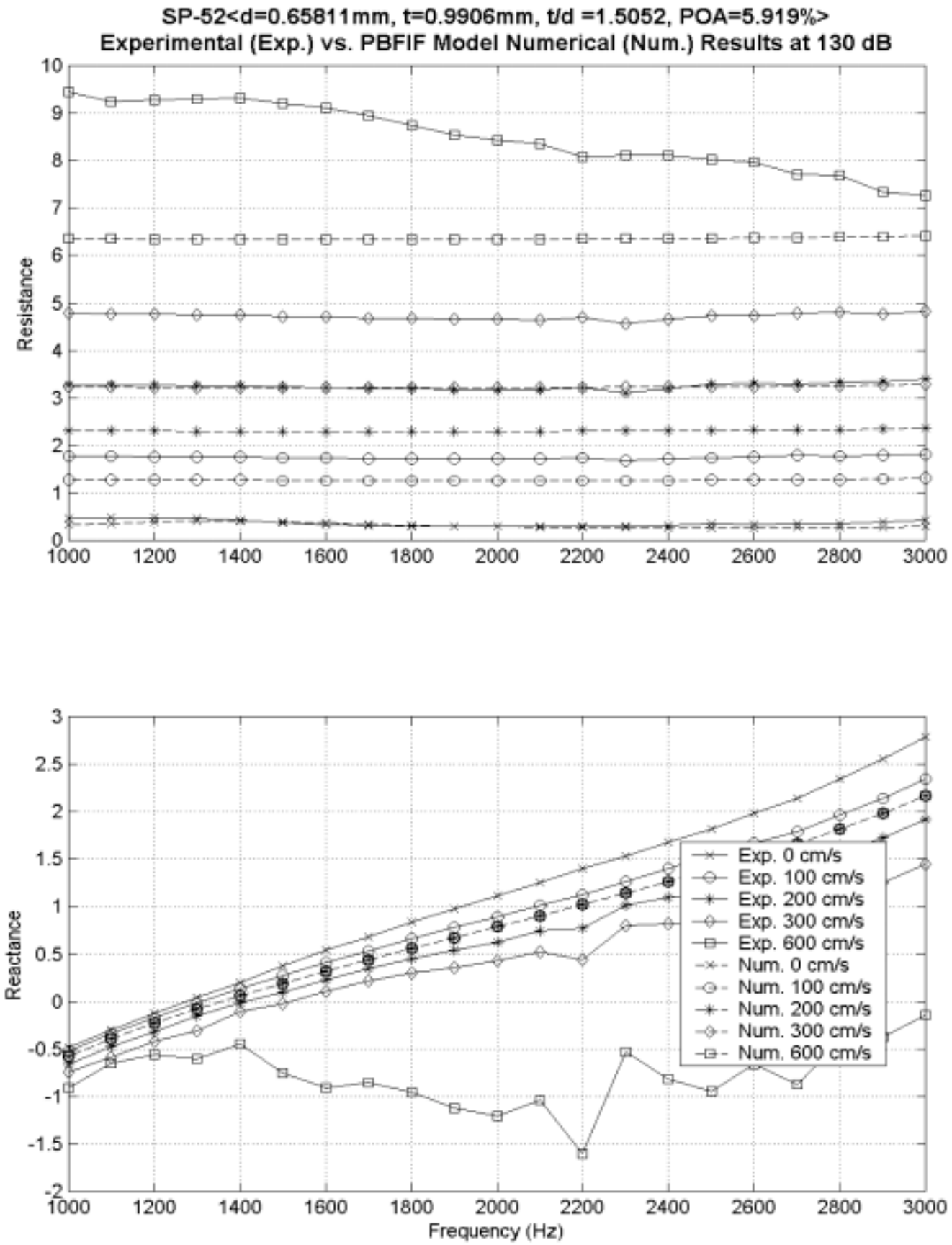
SP-52<d=0.65811mm, t=0.9906mm, t/d =1.5052, POA=5.919%>
Experimental (Exp.) vs. PBFIF Model Numerical (Num.) Results at 130 dB
Resistance
Reactance
Frequency (Hz)
Exp. 0 cm/s
Exp. 100 cm/s
Exp. 200 cm/s
Exp. 300 cm/s
Exp. 600 cm/s
Num. 0 cm/s
Num. 100 cm/s
Num. 200 cm/s
Num. 300 cm/s
Num. 600 cm/s

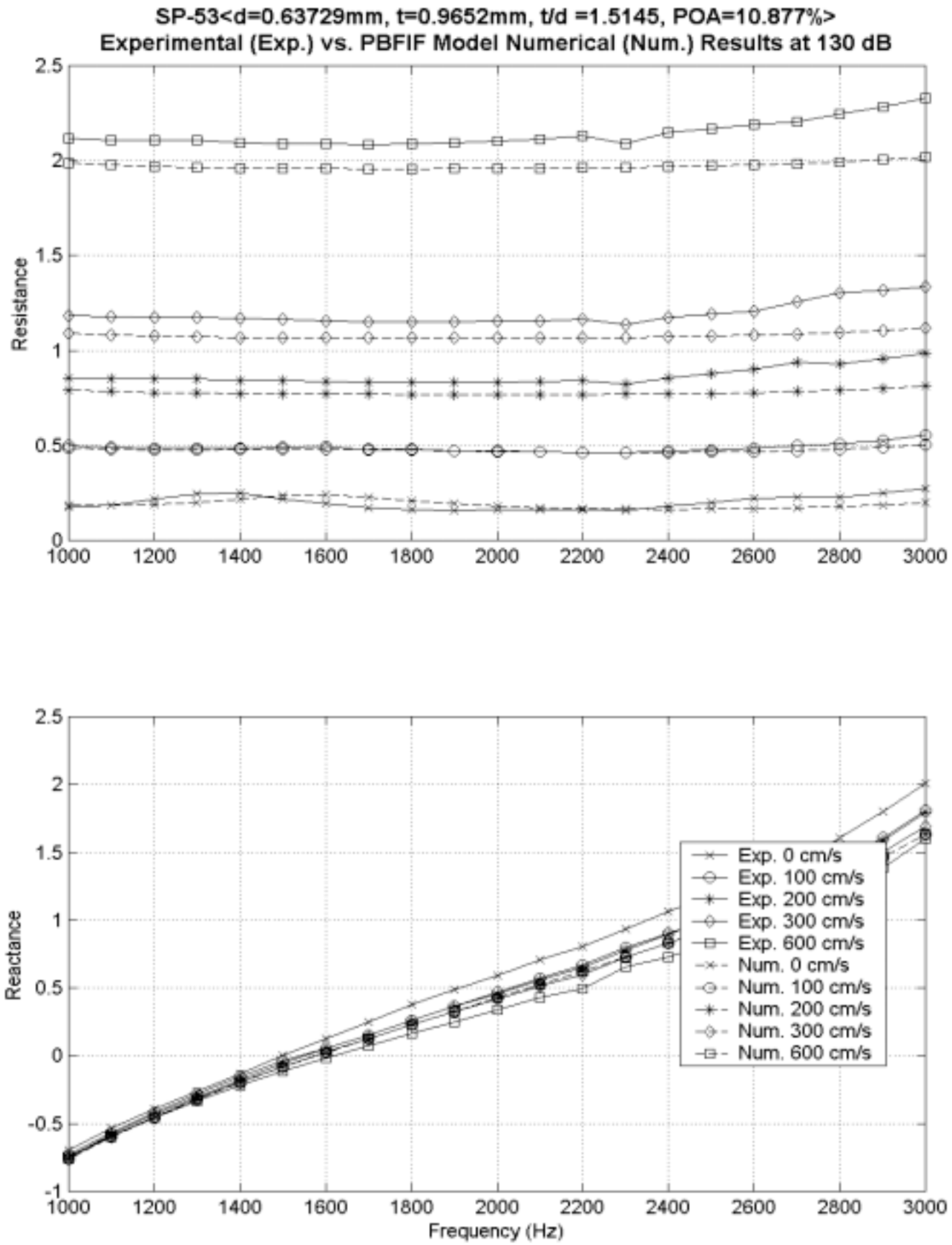
SP-53<d=0.63729mm, t=0.9652mm, t/d =1.5145, POA=10.877%>
Experimental (Exp.) vs. PBFIF Model Numerical (Num.) Results at 130 dB
Resistance
Reactance
Frequency (Hz)
Exp. 0 cm/s
Exp. 100 cm/s
Exp. 200 cm/s
Exp. 300 cm/s
Exp. 600 cm/s
Num. 0 cm/s
Num. 100 cm/s
Num. 200 cm/s
Num. 300 cm/s
Num. 600 cm/s

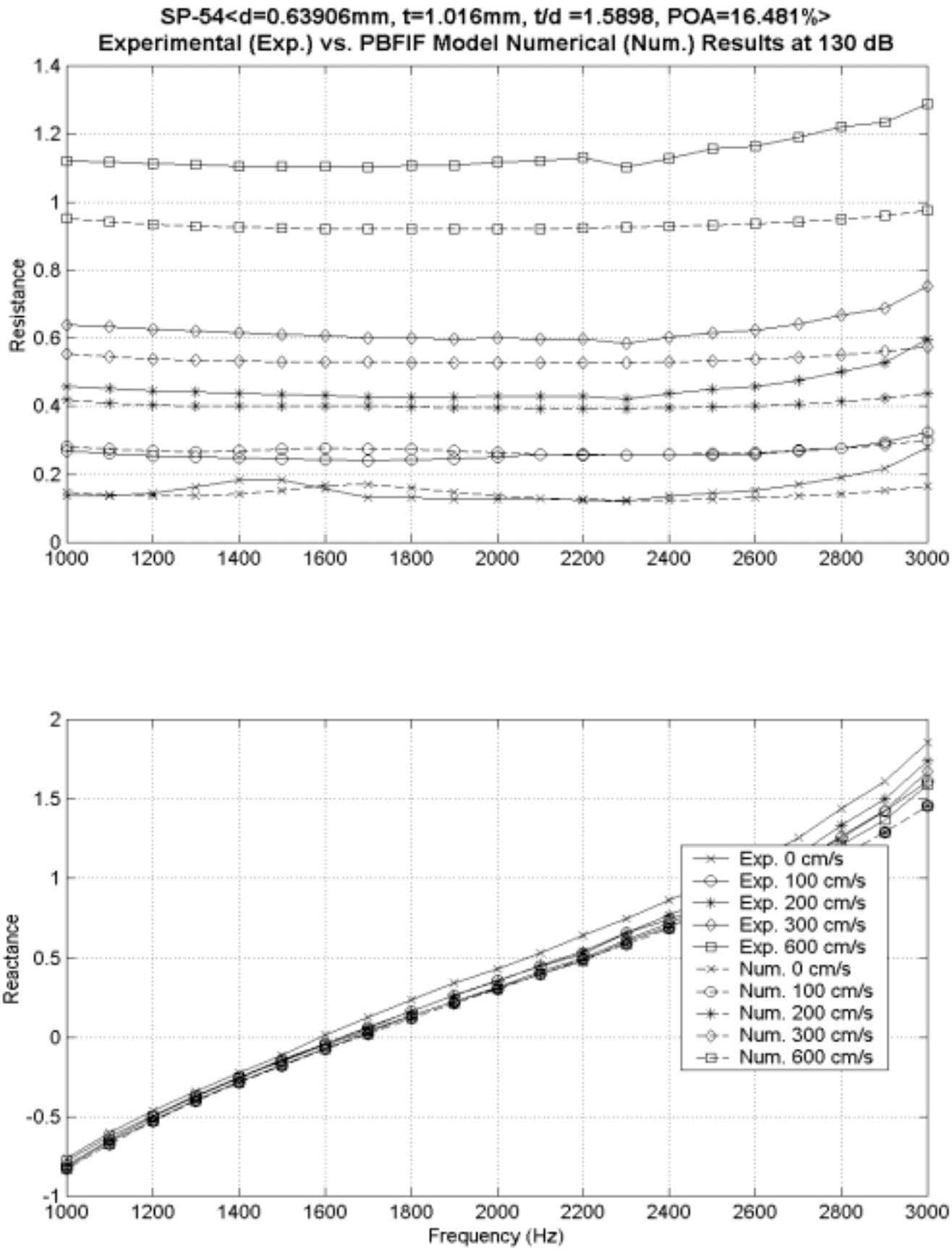
SP-54<d=0.63906mm, t=1.016mm, t/d =1.5898, POA=16.481%>
Experimental (Exp.) vs. PBFIF Model Numerical (Num.) Results at 130 dB
Resistance
Reactance
Frequency (Hz)
Exp. 0 cm/s
Exp. 100 cm/s
Exp. 200 cm/s
Exp. 300 cm/s
Exp. 600 cm/s
Num. 0 cm/s
Num. 100 cm/s
Num. 200 cm/s
Num. 300 cm/s
Num. 600 cm/s

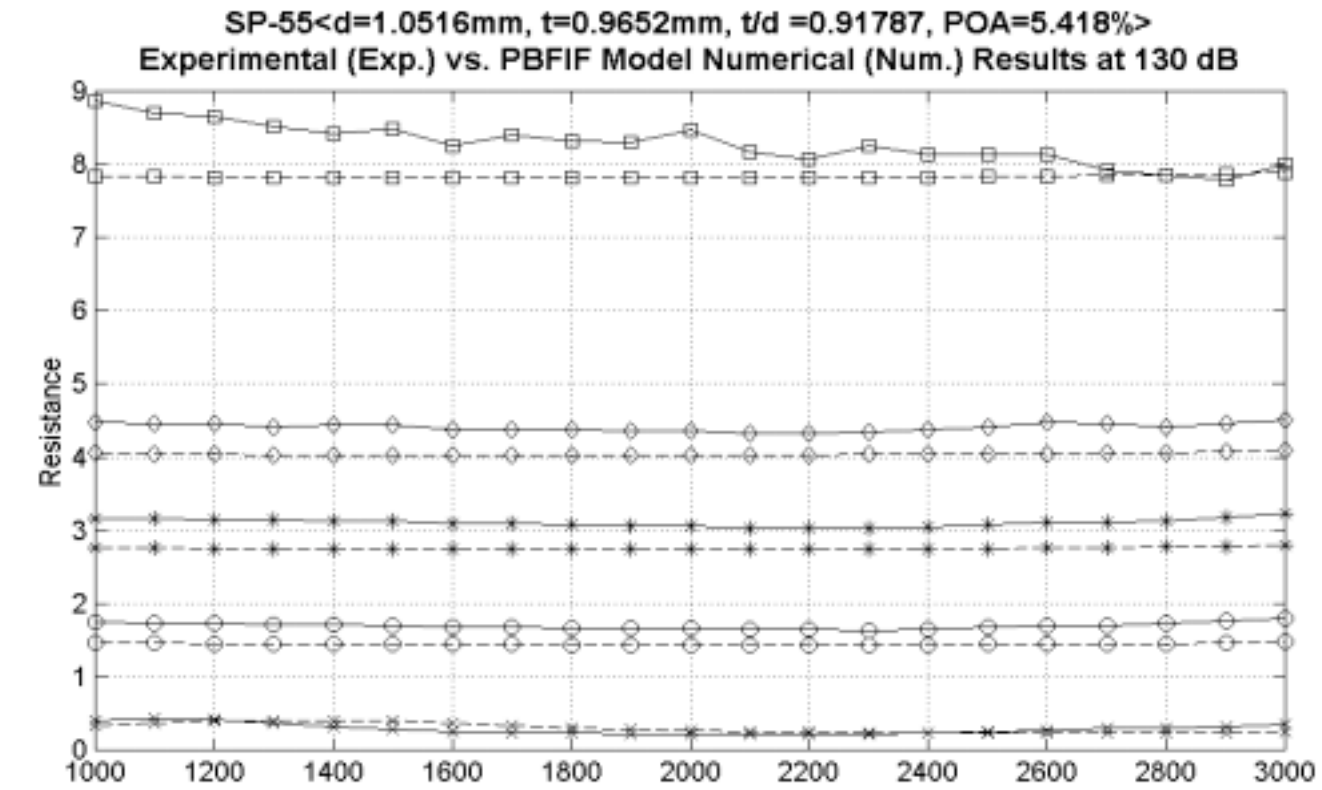
SP-55<d=1.0516mm, t=0.9652mm, t/d =0.91787, POA=5.418%>
Experimental (Exp.) vs. PBFIF Model Numerical (Num.) Results at 130 dB
Resistance
0
1
2
3
4
5
6
7
8
9
1000
1200
1400
1600
1800
2000
2200
2400
2600
2800
3000

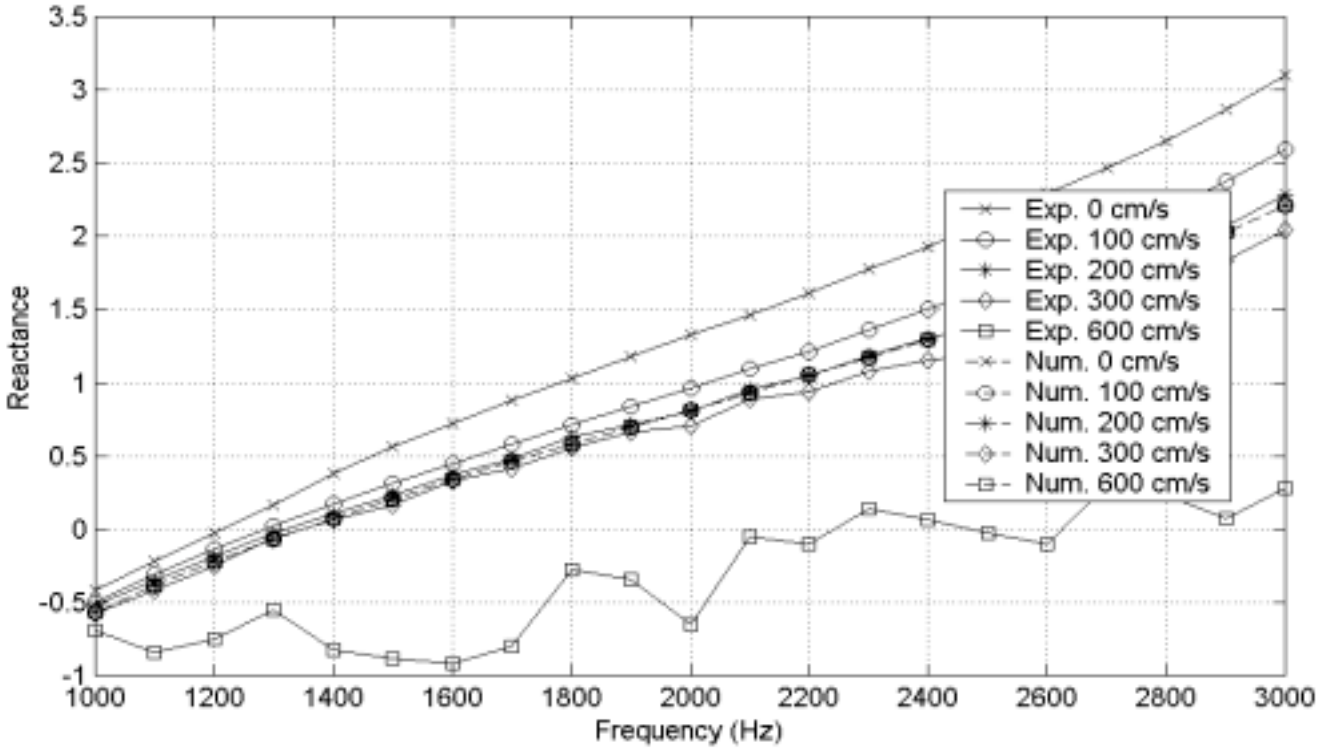
Reactance
Frequency (Hz)
-1
-0.5
0
0.5
1
1.5
2
2.5
3
3.5
1000
1200
1400
1600
1800
2000
2200
2400
2600
2800
3000
Exp. 0 cm/s
Exp. 100 cm/s
Exp. 200 cm/s
Exp. 300 cm/s
Exp. 600 cm/s
Num. 0 cm/s
Num. 100 cm/s
Num. 200 cm/s
Num. 300 cm/s
Num. 600 cm/s

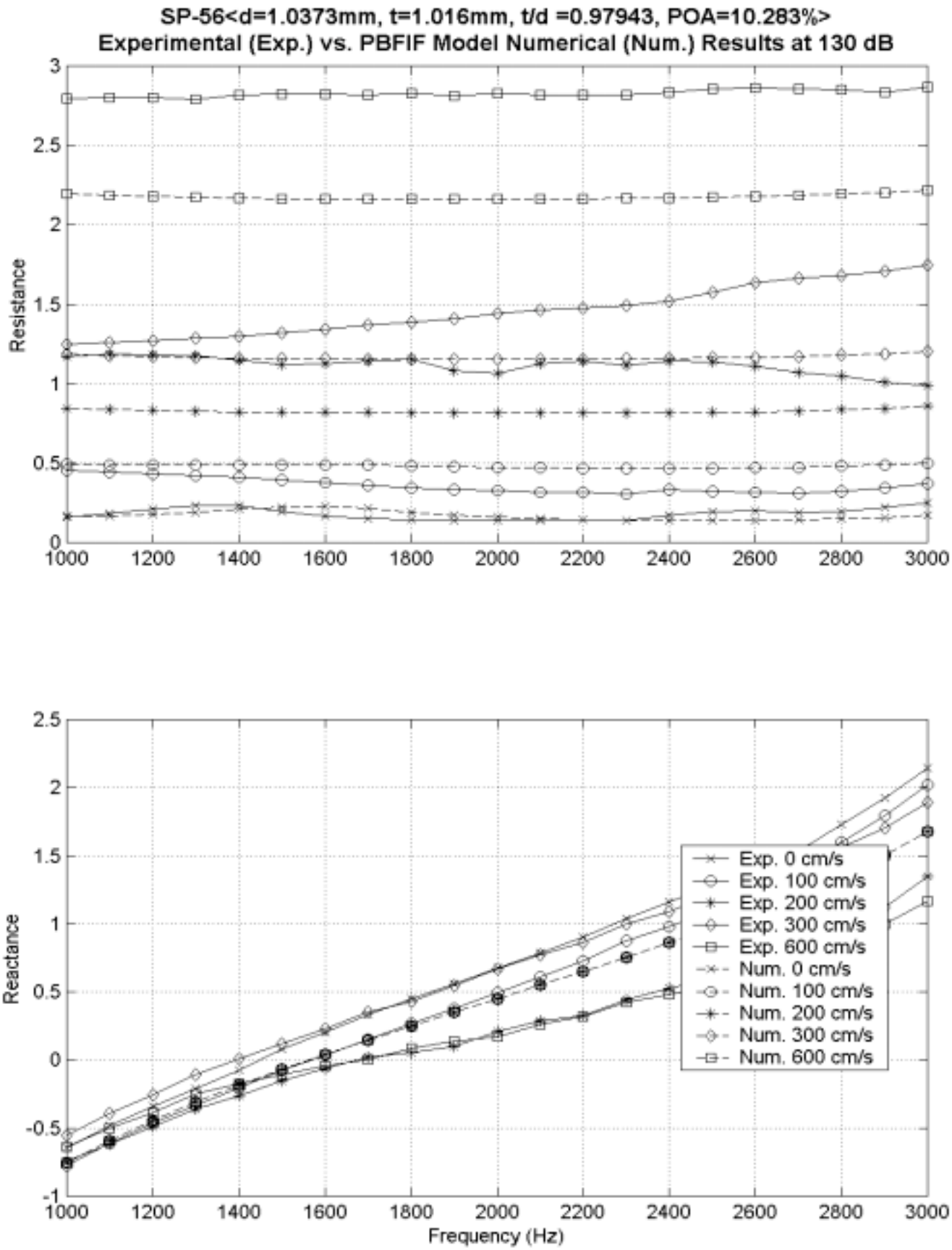
SP-56<d=1.0373mm, t=1.016mm, t/d =0.97943, POA=10.283%>
Experimental (Exp.) vs. PBFIF Model Numerical (Num.) Results at 130 dB
Resistance
Reactance
Frequency (Hz)
Exp. 0 cm/s
Exp. 100 cm/s
Exp. 200 cm/s
Exp. 300 cm/s
Exp. 600 cm/s
Num. 0 cm/s
Num. 100 cm/s
Num. 200 cm/s
Num. 300 cm/s
Num. 600 cm/s

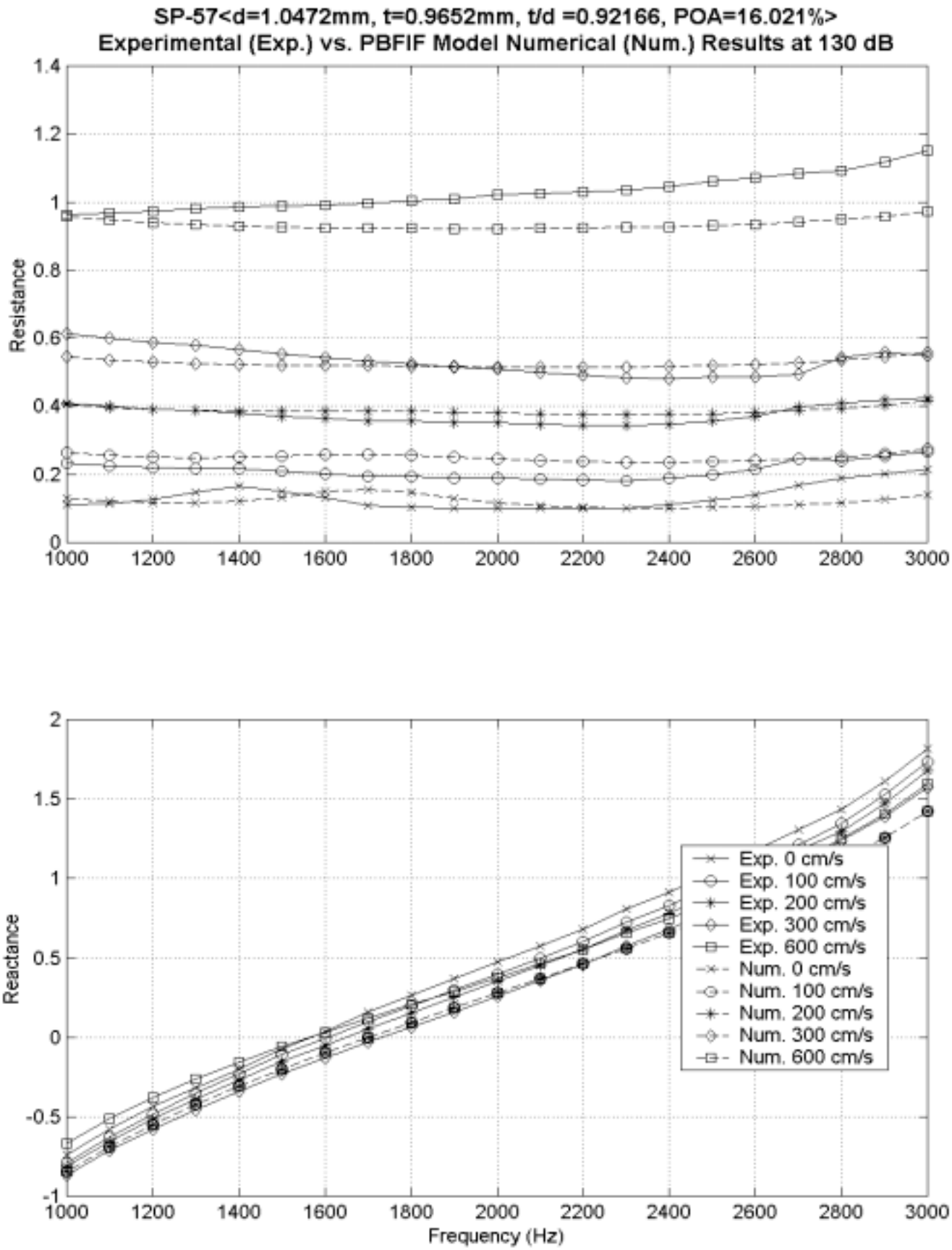
SP-57<d=1.0472mm, t=0.9652mm, t/d =0.92166, POA=16.021%>
Experimental (Exp.) vs. PBFIF Model Numerical (Num.) Results at 130 dB
Resistance
Reactance
Frequency (Hz)
Exp. 0 cm/s
Exp. 100 cm/s
Exp. 200 cm/s
Exp. 300 cm/s
Exp. 600 cm/s
Num. 0 cm/s
Num. 100 cm/s
Num. 200 cm/s
Num. 300 cm/s
Num. 600 cm/s

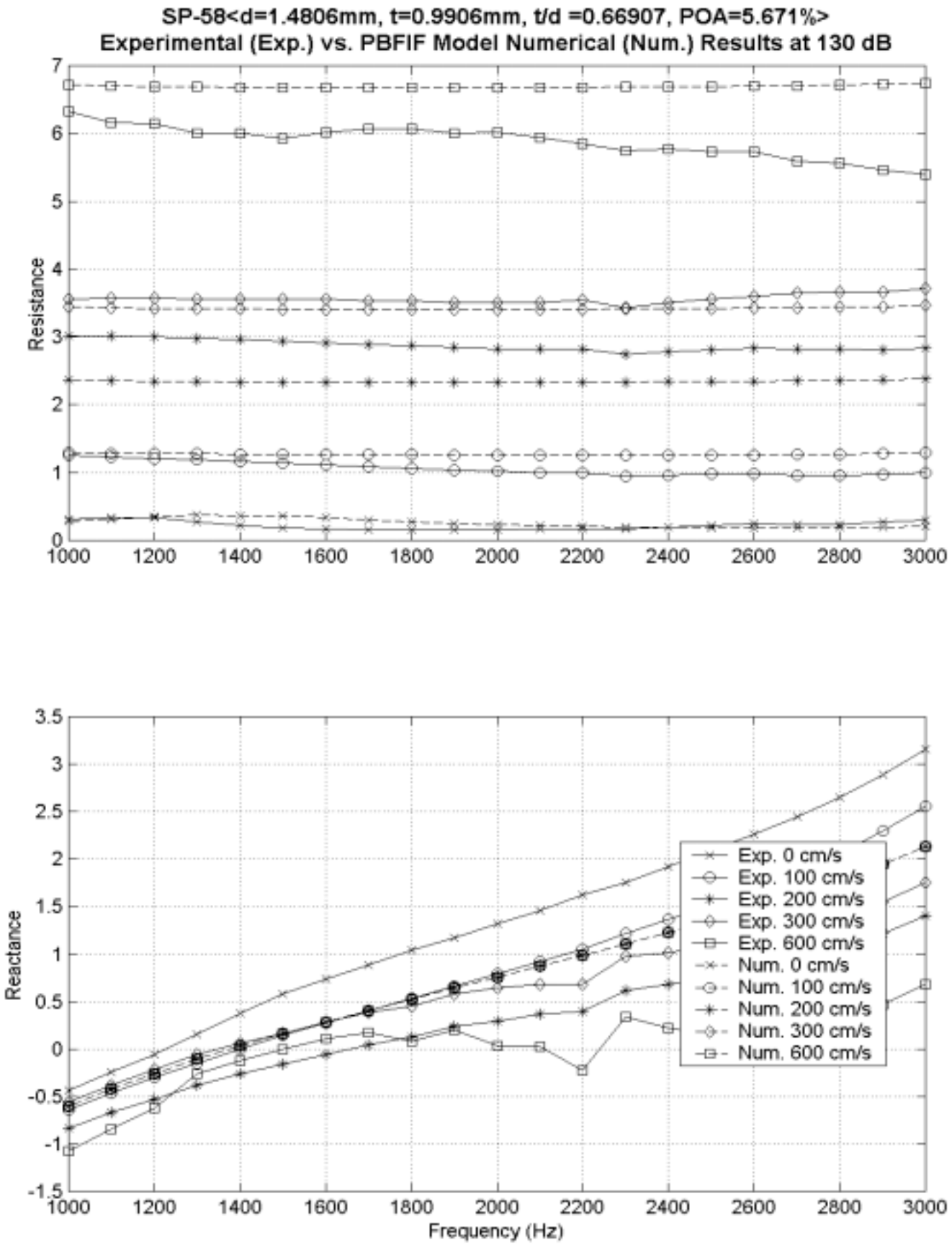
SP-58<d=1.4806mm, t=0.9906mm, t/d =0.66907, POA=5.671%>
Experimental (Exp.) vs. PBFIF Model Numerical (Num.) Results at 130 dB
Resistance
Reactance
Frequency (Hz)
Exp. 0 cm/s
Exp. 100 cm/s
Exp. 200 cm/s
Exp. 300 cm/s
Exp. 600 cm/s
Num. 0 cm/s
Num. 100 cm/s
Num. 200 cm/s
Num. 300 cm/s
Num. 600 cm/s

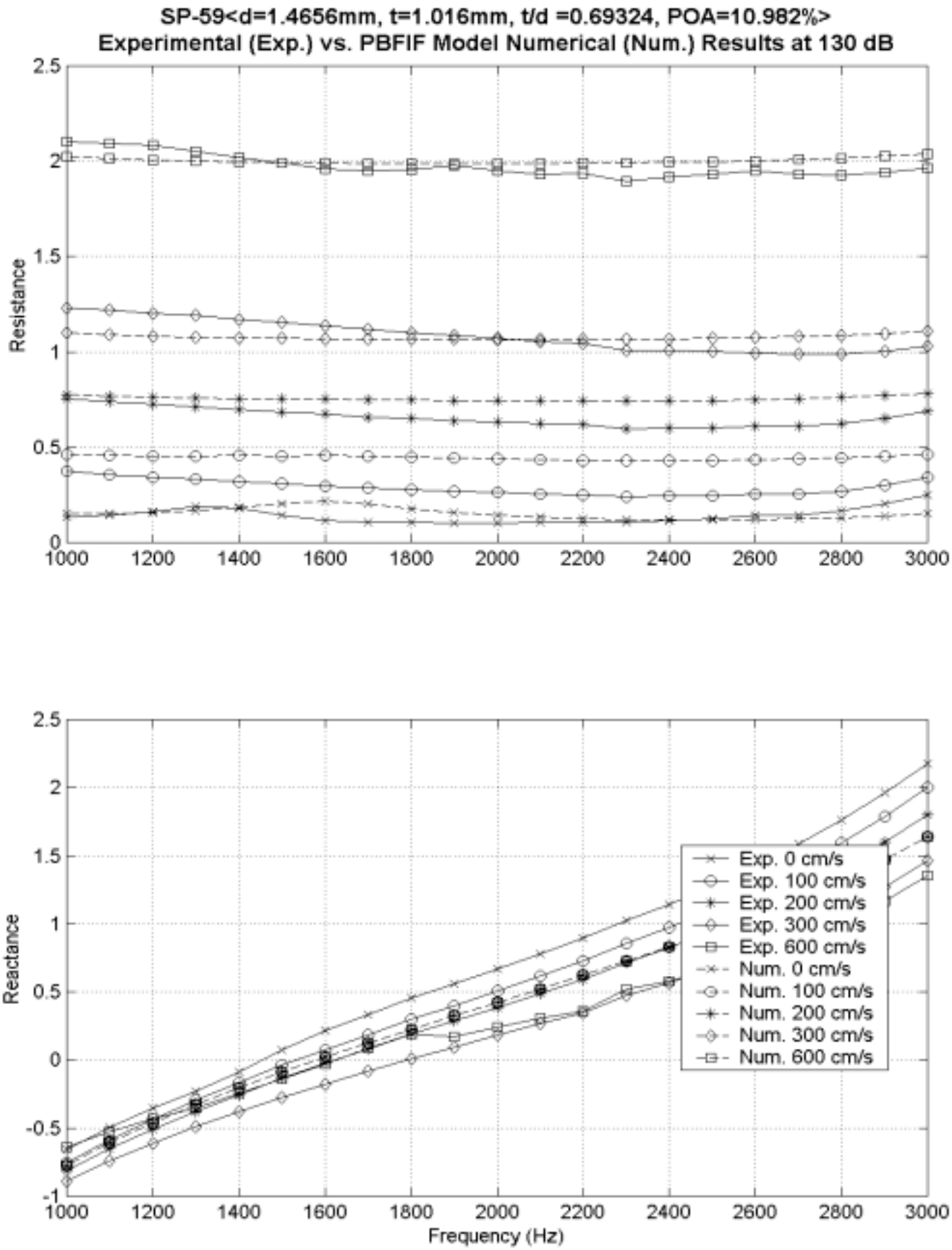
SP-59<d=1.4656mm, t=1.016mm, t/d =0.69324, POA=10.982%>
Experimental (Exp.) vs. PBFIF Model Numerical (Num.) Results at 130 dB
Resistance
Reactance
Frequency (Hz)
Exp. 0 cm/s
Exp. 100 cm/s
Exp. 200 cm/s
Exp. 300 cm/s
Exp. 600 cm/s
Num. 0 cm/s
Num. 100 cm/s
Num. 200 cm/s
Num. 300 cm/s
Num. 600 cm/s

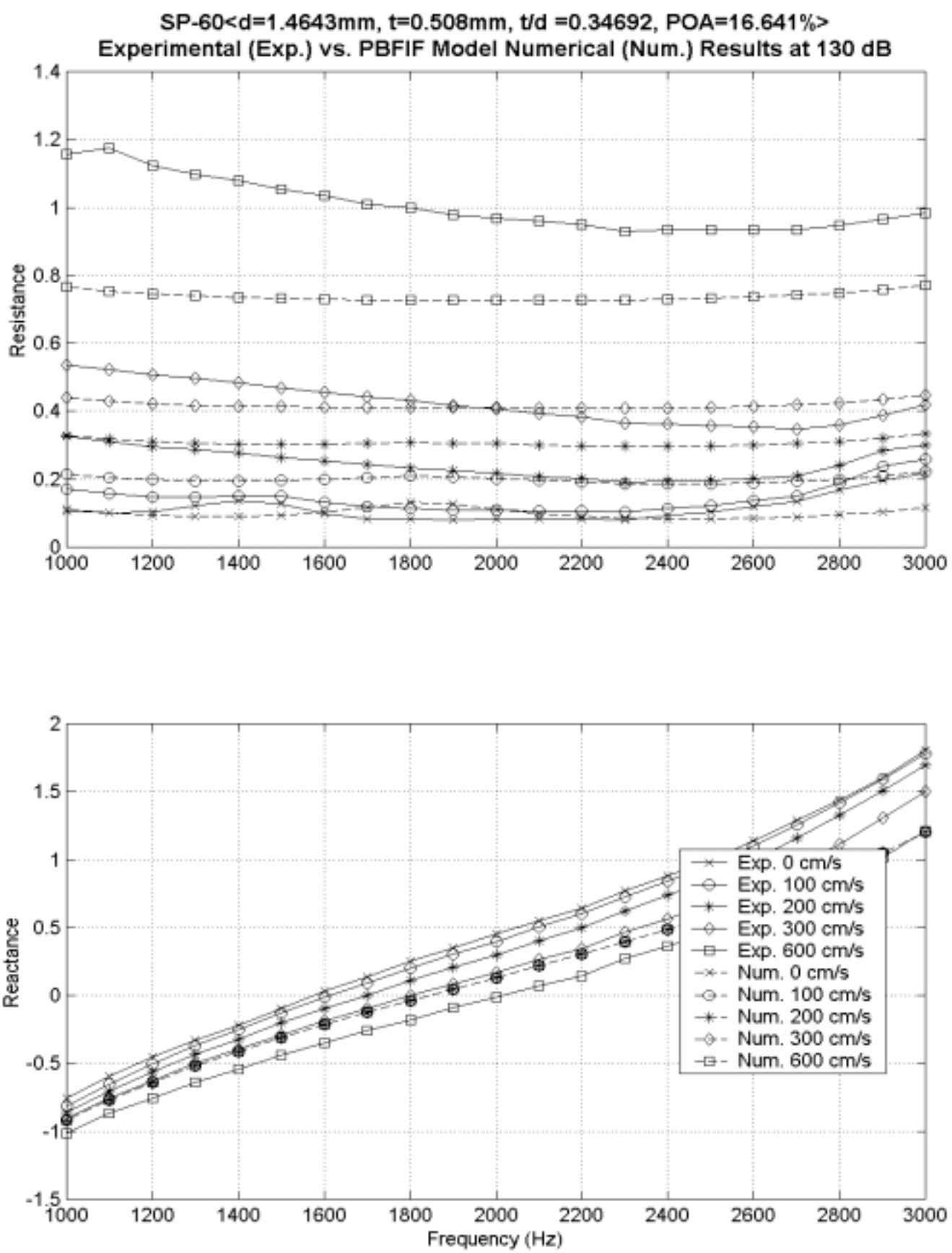
SP-60<d=1.4643mm, t=0.508mm, t/d =0.34692, POA=16.641%>
Experimental (Exp.) vs. PBFIF Model Numerical (Num.) Results at 130 dB
Resistance
Reactance
Frequency (Hz)
Exp. 0 cm/s
Exp. 100 cm/s
Exp. 200 cm/s
Exp. 300 cm/s
Exp. 600 cm/s
Num. 0 cm/s
Num. 100 cm/s
Num. 200 cm/s
Num. 300 cm/s
Num. 600 cm/s

Vita

Juan Fernando Betts was born on May 8, 1974 in Porto Alegre, Brazil. He was about a year old when his parents moved to Panama, where he lived most of his childhood. During his childhood his family moved from Panama, on three occasions, twice to Puerto Rico and once to Venezuela.

In 1991 he moved to United States, where he finished his last year of high school and then went to The George Washington University. Juan Fernando Betts graduated in 1996 with a Bachelor of Science degree in Mechanical Engineering (Pre-Medical Option) as a Magna Cum Laude and Norman B. Ames Graduate. During his senior year he was involved in a joint project with the Medical School doing Finite Element models of cerebral aneurysms during their surgical clipping process.

In the spring of 1996 he worked at Mantech Systems Engineering Corporation on the test plans for the Navy's AEGIS Defense System. He also worked that summer as a summer engineer for ANSER Research Institute in their space analysis division on the Air Force Space Vehicle Program.

In the fall of 1996 he became an SREB fellow and decided to pursue graduate studies at Virginia Tech, after declining an early admission he had been awarded to the George Washington Medical School. He finished a Master of Science degree in the spring of 1998 with a thesis titled "Finite Element Study of Plane Wave Acoustic Phenomena in Ducts."

In the summer of 1998 he started his Ph.D. at Virginia Tech on a Boeing Company and NASA Langley sponsored research project. Two years later he defended his dissertation titled "Experiments and Impedance Modeling of Liners Including The Effect of Bias Flow."